Dissertation zur Erlangung des Doktorgrades

der Fakultät für Geowissenschaften

der Ludwig-Maximilians-Universität München

Earthquakes and Coulomb Stress Evolution in a Diffuse Plate Boundary: Northern Basin and Range Province, USA

Alessandro Verdecchia

München
März 2016

Eingereicht am 01.03.2016
1. Gutachterin: Prof. Dr. Anke Friedrich
2. Gutachterin: Dr. Habil. Sara Carena
Tag der mündlichen Prüfung: 16.06.2016

Summary

Diffuse plate boundaries are characterized by deformation distributed over a wide area in a complex network of active faults, and by low strain rates. These characteristics make it difficult to understand the spatial and temporal distribution of seismicity. The northern Basin and Range Province (BRP) in the western United States is an excellent example of a diffuse plate boundary. Several surface-rupturing earthquakes have occurred in this area in the late Holocene, but the earthquake migration patterns has not been understood yet.

In order to explore the possible relationship among large earthquakes in the northern BRP, I used an approach based on modeling coseismic, postseismic and interseismic Coulomb stress changes. I first focused on the region around the Owens Valley (northwestern Eastern California Shear Zone) and examined the relationship among seven historically documented and instrumentally recorded $M_w \geq 6$ earthquakes that struck the region in the past 150 years. This study revealed that all the seven events are located in areas of positive stress changes (stress loading) produced by the previous earthquakes. The question remained as to whether the good agreement is only due to the small spatial (Owens Valley) and temporal (150 years) scales considered. I therefore expanded the study area to a vast region within the northwestern BRP, examining previously documented surface-rupturing earthquakes that occurred in the last 1400 years. My results show that in this case too, the majority of the source faults are located in areas of stress loading due to previous earthquakes.

Finally, in order to explore the potential effect of Coulomb stress changes on probabilistic seismic hazard calculations, I focused on the Wasatch Fault Zone, a ~350 km-long normal fault zone located in the easternmost part of the study region. By combining a physical model (Coulomb stress changes) with a statistical model

(probability calculations), I showed that large positive Coulomb stress changes (~ 10 bar) may significantly increase the probability of a large earthquake on at least three of the five main segments of the central Wasatch Fault Zone.

Table of Contents

List of Tables

List of Figures

Acknowledgments

First I would like to thank my advisor Sara Carena, who gave me the great opportunity to be a PhD student at LMU Munich, and taught me that good science is possible only with hard and meticulous work. Without her expertise and active support this thesis would not have been possible. Thank you to Prof. Anke Friedrich for her positive feedbacks and constructive criticism.

I thank Dr. Amir Abolghasen (LMU Munich) for introducing me to the code that I used in this work to calculate the postseismic stresses. Thank you to Dr. Bruno Pace (Universita' degli studi di Chieti-Pescara) and to Dr. Christopher DuRoss (U.S. Geological Survey) for offering their expertise on the time-dependent probability calculations the first, and on the Wasatch Fault Zone the second.

Special thanks to the Geology gang, and in particular to my officemate Stefanie Rieger, to Simon Kübler, Markus Hoffmann, and Christina Plattner for their scientific support, and mostly for making me feel welcome in Munich. Great thank also to our secretarial staff, Karin Hessinger and Jitka Unting helped me a lot in dealing with the fascinating German bureaucracy.

Least but not last, I thank my family and my girlfriend for their love and support. My parents, Enaudio and Mirella for their financial and moral support, and for always being my model and inspiration in life. Ivana, my girlfriend, is the real reason why I decided to become a PhD student, she transmitted me the passion for science, and she always helped me in taking the right decisions.

The Department of Earth and Environmental Sciences at LMU Munich provided most of the financial support. Part of this thesis was also funded by DFG grant CA-691/1-2 awarded to Sara Carena.

Introduction and Overview

Major earthquakes ($M_w \geq 7$) tend to occur repeatedly at expected locations on major plate boundary faults (e.g., San Andreas fault, North Anatolian fault, megathrusts in subduction zones), where high deformation rates are localized along a narrow zone [e.g., *Stein and Liu*, 2009]. However in regions like the Altiplano - Puna plateau in the Andes, the Tibetan plateau in China, the Apennines in Italy, or the Basin and Range Province, the motion of the nearby plate is accommodated in part by several systems of active faults distributed over a wider zone, resulting in a diffuse plate boundary [*Thatcher*, 1995; *Simkin et al*., 2006]. The combination of the complex network of faults with different slip rates and the lower seismicity rates in such regions makes it difficult to understand the spatial and temporal distribution of earthquakes.

This thesis aims at advancing our understanding of the migration and clustering patterns of earthquakes in the northern Basin and Range Province (BRP) (Figure 1), which is one of the most striking examples of a diffuse plate boundary. Here, between the northern Eastern California Shear Zone and Walker Lane to the west, and the Wasatch Fault Zone to the east (Figure 1), a network of currently active normal and strike-slip faults accommodates 25% of the ~ 50 mm/yr of relative motion between the Pacific and the North American plates (Figure 1) [*Bennett et al.*, 2003; *DeMets et al.*, 2010; *Wesnousky et al*., 2012]. At least 8 large historical earthquakes have occurred on the western part of the study area in the last 150 years (northern Eastern California Shear Zone, Walker Lane and Central Nevada Seismic Belt) and a further eleven surface-rupturing earthquakes have been recognized by paleoseismological studies in the same area. On the Wasatch Fault Zone, no large historical or instrumental event has been documented yet, but several paleoseismological investigations indicate that at

least 24 surface-rupturing earthquakes have occurred on various segments of the fault in the last 7000 years [e.g., *DuRoss et al.*, 2016, and references therein]. In addition to these paleoseismological and historical data, smaller instrumental seismicity [*Arabasz et al.*, 1992; *Waldhauser and Schaff*, 2008] shows that the northern Basin and Range Province as a whole is still seismically active.

Previous studies [*Wallace*, 1978, 1984b, 1987; *Koehler and Wesnousky*, 2011], have attempted to examine late Pleistocene seismicity patterns in the Basin and Range Province. These authors have combined data from historical earthquakes with paleoseismic investigations and concluded that no obvious pattern of migration of events across the whole region is observable. The general idea is that, in the Basin and Range Province, temporal seismicity clusters migrate regionally, each time activating a different belt of late Quaternary faults in a yet unknown migration pattern [*Wallace*, 1984b, 1987]

In order to determine if there are any specific earthquake patterns in this region, I used an approach based on the concept of Coulomb stress changes (ΔCFS) developed by *King et al.* [1994]. Earthquake interactions have been widely explored using this approach, and Coulomb stress changes appear to be reliable indicators when applied to earthquake forecasting on major plate boundary faults [e.g. *Stein et al.*, 1997; *Hubert-Ferrari et al.*, 2000; *Freed et al.*¸ 2007]. In addition, several studies have shown that the ΔCFS may have a significant effect on probabilistic seismic hazard calculations [*Toda et al.*, 1998; *Stein*, 1999; *Parsons*, 2005].

This method has already been used by several authors in the Basin and Range Province [*Hodgkinson et al.*, 1996; *Caskey and Wesnousky*, 1997; *Bell et al*., 2004]. However, these studies only focus on in-cluster seismicity patterns and are limited to

short periods of time (1915-1954 Pleasant Valley - Rainbow Mountain - Fairview Peak - Dixie Valley sequence).

In this thesis I modeled ΔCFS due to moderate-to-major instrumental, historical and paleoseismological earthquakes in the northern Basin and Range Province in order to answer the following questions:

(1) Is there any space-time relationship region-wide between earthquakes on specific faults, and location of previous and subsequent earthquakes?

(2) Can we use an approach based on ΔCFS to identify possible sources of future earthquakes in diffuse plate boundary regions?

(3) What is the effect of ΔCFS on probabilistic seismic hazard calculations for the Wasatch Fault Zone?

Following the introductory part of this dissertation I address these questions in three main chapters:

In Chapter 1 and 2, I modeled the evolution of coseismic, postseismic and interseismic ΔCFS in the westernmost part of the northern Basin and Range province at two different spatio-temporal scales. In Chapter 1, I examined seven historical and instrumental $M_w \geq 6$ earthquakes that struck the region around Owens Valley in the last 150 years. In Chapter 2, I expanded my study region to all of the northern Eastern California Shear Zone, Walker Lane and Central Nevada Seismic Belt, examining seventeen paleoseismological and historical surface-rupturing earthquake ($M_w \geq 6.5$) that occurred in the last 1400 years. Results from these studies reveal that in both cases coseismic and postseismic stress changes likely control the spatial and temporal distribution of earthquakes in the region. This finding allowed me to identify those faults that are the most likely to produce large earthquakes in the near future. Several faults in the region (e.g. White Mountain fault, Fish Lake Valley fault, Pyramid Lake

fault) have accumulated in the last 150 to 1400 years a total amount of stress (coseismic + postseismic + interseismic) comparable to the average stress drop in a major earthquake, and therefore they may be close to failure.

In order to study the impact of ΔCFS on probabilistic seismic hazard calculation in Chapter 3 I focused my attention on the eastern part of the Basin and Range Province, and more specifically on the central Wasatch Fault Zone (WFZ). This choice is based on the fact that a well-studied area with abundant geologic and paleoseismological data is needed in order to reduce the uncertainties connected with this kind of approach. The Wasatch Fault Zone matches the requirements. Using data based on paleoseismological investigations, I combined coseismic and postseismic ΔCFS accumulated by each of the five main segments of the fault with the probability of occurrence of a large earthquake ($M_w \geq 7$) for the next 50 years on each segment. Results from a comparison between probabilities calculated both with and without ΔCFS show that the probability of occurrence of a large earthquake on the central WFZ in the next 50 years may be underestimated, if an approach that does not take ΔCFS into account is adopted.

In this study I tested the reliability of Coulomb stress calculations when applied to currently active diffuse plate boundary regions at different spatial scales and time periods. Results from this thesis show that an approach based on coseismic, postseismic and interseismic stress calculations provides a better understanding of seismicity patterns in plate boundary regions characterized by distributed deformation. In particular it highlights the importance of time-dependent postseismic stresses in earthquake triggering at regional scales, and it contributes to identify possible sources of future major earthquakes and to quantify the seismic hazard connected to it. I believe that these findings will encourage the broader communities of active tectonics and

seismology to apply this approach to other examples of diffuse plate boundary regions around the world, where enough data are available for this purpose such as central and southern Italy or New Zealand.

Based on the results of my research, I propose some possibilities for future work. In Chapter 2 we explored the stress evolution in northern Eastern California Shear Zone, Walker Lane, and western Basin and Range Province. As next step it would be worthwhile to expand this study area to the west, and consider the effect on our model of plate boundary fault earthquakes (San Andreas fault, Cascadia subduction zone). Despite the location of these plate boundary faults relatively far from the studied diffuse plate boundary region, the magnitude of past events on the San Andreas fault (e.g. 1857, M_w 7.9 Fort Tejon earthquake, 1906, M_w 7.8 San Francisco earthquake), and on the Cascadia megathrust (e.g. 1700, M_w ~ 9.0, Cascadia earthquake) may have been large enough to affect the northern Eastern California Shear Zone and the Walker Lane in terms of coseismic and postseismic Coulomb stress changes. The thematic covered in Chapter 3 is still open for many future options which include the calculations of probability for different rupture scenarios (multisegment ruptures, segment spillovers), the quantification of the effect of laterally heterogeneous rheological models, and the creation of time-dependent fault-based seismic hazard maps for the Wasatch Fault Zone.

Finally, I believe that all the models proposed in this work will benefit from future new paleoseismological studies in the northern Basin and Range province. This work in fact highlights the important of fully recognizing paleoseismological earthquakes in the seismological record, which will hopefully encourage more investments in this direction.

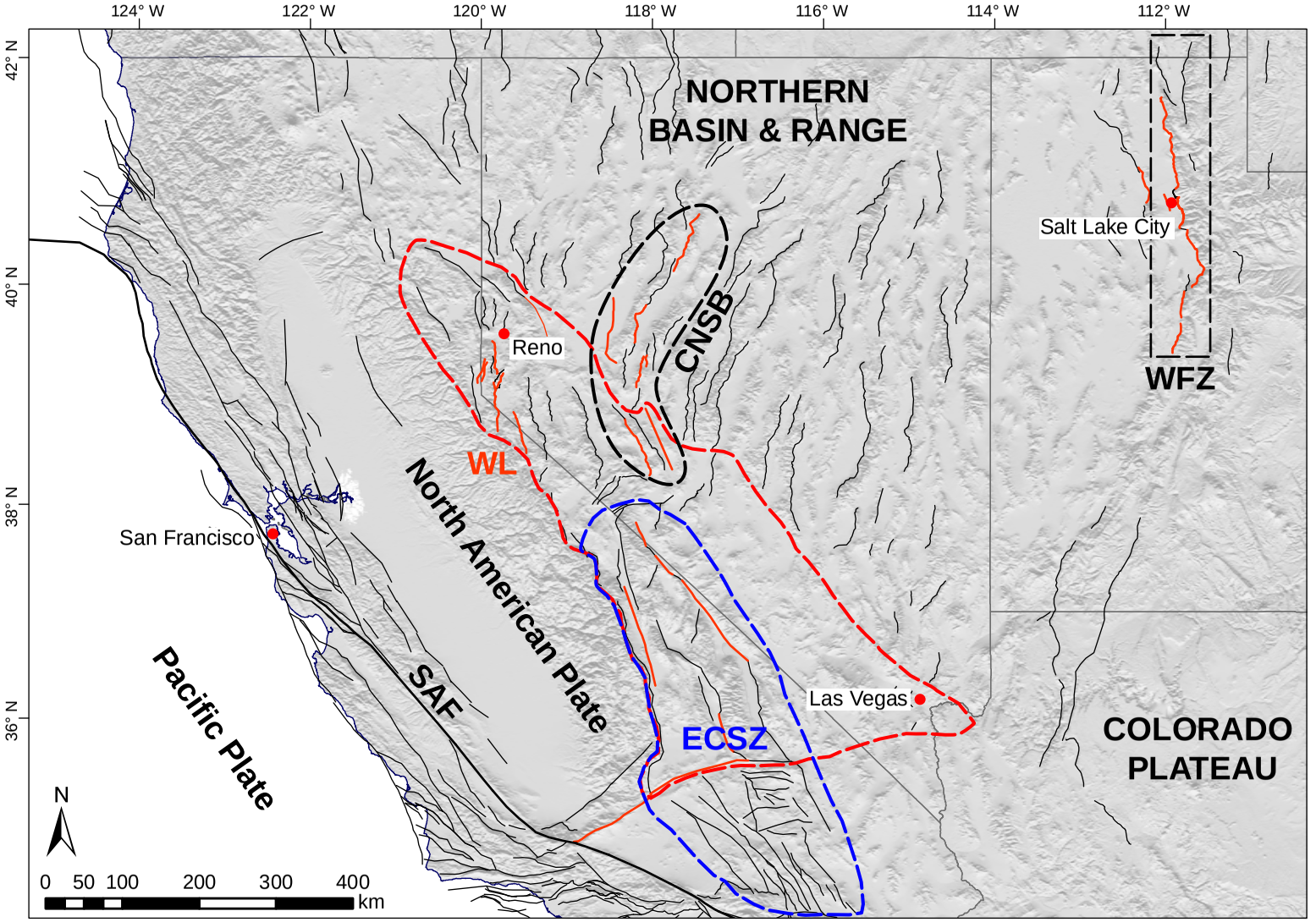

Figure 1. Map of active faults in northern Basin and Range Province and adjacent plate boundary area (California, Nevada, Utah), from U.S. Geological Survey National Seismic Hazard Maps [*Petersen et al*., 2014]. Thick red lines are the faults responsible for the surface-rupturing earthquakes modeled in this work. ECSZ=Eastern California Shear Zone [*Dokka and Travis*, 1990]; WL=Walker Lane Belt [*Stewart*, 1988]; WFZ=Wasatch Fault Zone; CNSB=Central Nevada Seismic Belt [*Wallace*, 1984]; SAF=San Andreas fault.

Chapter 1

One hundred and fifty years of Coulomb stress history along the California-Nevada border, USA.*

1.1 Abstract

The region north of the Garlock fault between the Sierra Nevada and Death Valley has experienced at least eight $M_w \geq 6$ earthquakes in historical times, beginning with the 1872, M_w 7.5, Owens Valley earthquake. Furthermore, since 1978, the Long Valley caldera has been undergoing periods of unrest, with earthquake swarms and resurgence. Our goal is to determine whether the 1872 Owens Valley earthquake and the caldera unrest have influenced the evolution of seismicity in the area. We model the evolution of coseismic, postseismic, and interseismic Coulomb stress change (ΔCFS) in the region due to both $M_w \geq 6$ earthquakes and caldera inflation in the last 150 years. Our results show that the 1872 Owens Valley earthquake has an important influence on subsequent events, strongly encouraging faulting in northern Owens Valley while inhibiting it elsewhere. There is also a correlation between caldera inflation and seismicity in northern Owens Valley, evidenced by the west-to-east migration of earthquakes from the Long Valley caldera towards the White Mountains immediately following the 1978 caldera inflation event. Finally, we show that a total ΔCFS increase of up to 30 bars in the last 150 years has occurred on part of the White Mountains fault, making it a possible candidate for the next major earthquake in this region.

---

*Published Paper: Verdecchia, A. and S. Carena (2015), One hundred and fifty years of Coulomb stress history along the California-Nevada border, USA, *Tectonics*, **34**, 213-231, doi:10.1002/2014TC003746.

1.2 Introduction

Between May 1980 and July 1986 the region located between the Sierra Nevada and the White Mountains (Figure 1.1) in northern Owens Valley, California, experienced several moderate-to-strong earthquakes (Figure 1.2). Although some of these earthquakes appear to be connected with the 1978 renewal of volcanic activity beneath Long Valley caldera [*Savage and Clark*, 1982], it is not clear whether these events may also be related to each other, to earlier seismicity, or whether they are just randomly distributed throughout the region.

The Owens Valley fault is in the Eastern California Shear Zone (ECSZ), which is part of a diffuse plate boundary zone that accommodates a large fraction (~ 10 mm/yr) of the relative Pacific-North America plate motion east of the San Andreas fault [e.g. *Dixon et al*., 2000; *Bennett et al.*, 2003]. The White Mountains (WM), Owens Valley (OV), Hunter Mountain-Panamint Valley (HM-PV) and Fish Lake Valley-Furnace Creek-Death Valley (FLV-FC-DV) faults are the main active structures that accommodate most of the dextral motion between the Sierra Nevada block and stable North America north of the Garlock fault (Figure 1.1) [*Frankel et al*, 2007a, *Ganev et al.*, 2010]. Although these faults are active and capable of major earthquakes ($M_w \geq 7$), only the Owens Valley fault has ruptured in historical times.

Pliocene-to-recent volcanism in Owens Valley and Long Valley is associated with the transtensional deformation in the ECSZ. The Long Valley caldera (Figure 1.1) is the result of an explosive eruption 760 ka ago that produced over 600 km^3 of rhyolitic ignimbrite (Bishop Tuff) [*Bailey*, 1989]. Although there have been no historical eruptions, the caldera has had several periods of unrest and resurgence in the last few decades.

In 1872 this region was affected by the M_w 7.5 Owens Valley earthquake. Large earthquakes have been shown to control the distribution of subsequent seismicity [e.g. *King et al*., 1994; *Stein*, 1999; *King and Cocco*, 2001]. Only a limited number of studies have been carried out on the interaction between earthquakes and volcanic events in the northern ECSZ. *Hough and Hutton* [2008] explained the large time gap (108 years) between the 1872 Owens Valley earthquake and the moderate seismicity south of Long Valley caldera in the 1980s with a stress shadow produced by the 1872 event. These authors, however, also acknowledged that these earthquakes may have occurred at that time simply because they were directly triggered by the magmatic processes acting within the caldera.

In order to evaluate possible correlations among earthquakes and between volcanic activity and earthquakes in the northern ECSZ, we first determined fault geometry using geological data and relocated seismicity. We then explored, through coseismic and postseismic Coulomb stress modeling, the influence of the 1872 M_w 7.5 Owens Valley earthquake on the distribution of seismicity that followed it. Finally, we calculated the total (coseismic + postseismic + interseismic) ΔCFS on large faults that have no historical earthquakes to evaluate whether it is comparable with the average stress drop expected in an earthquake. We show that the 1872 Owens Valley earthquake seems to control the general evolution of seismicity in space and time.

1.3 Data: Earthquakes and fault slip rates

Here we briefly discuss the sequence of earthquakes in the region of interest, the types and sources of the earthquake data and fault data we used, and the reasons for including or excluding specific data from the models.

1.3.1 Sequence of earthquakes, from 1872 to present

On March 26th, 1872, the largest earthquake (M_w 7.5, *Beanland and Clark*, 1994) ever recorded in the Eastern California Shear Zone (ECSZ) ruptured the Owens Valley fault. The rupture was ~110 km long, with dominant right-lateral strike-slip motion. Measured offsets indicate a coseismic right-lateral displacement up to 7 m and normal slip up to 2 m [*Beanland and Clark*, 1994].

Apart from aftershocks of the 1872 event, several $M_L \geq 6$ earthquakes have occurred in the same region up to the present day (Figure 1.2). Of particular interest is the sequence that began in 1978 with several M_L 3 to 4 earthquakes in and around Long Valley caldera that culminated with four $M_w \approx 6$ events occurred in late May 1980 [*Hill*, 2006]. Three of these moderate events nucleated within the Sierra Nevada block, where earthquakes seem to occur by simple shear on left-lateral strike-slip faults, in contrast with the activity on the south moat of the caldera, which is driven by the injection of magmatic fluids into the brittle crust from the adjacent inflating magma body [*Prejean et al*., 2002; *Hill*, 2006]. Although the focal mechanisms of the May 1980 events show a non-double-couple component (Figure 1.2), *Prejean et al.* [2002] supported by the aftershocks distribution, suggested that complex slip on multiple rupture planes may explain the non-double-couple nature of these three events, rather than magma injections.

In 1984 the earthquake swarm south of the caldera declined, but seismicity spread to the surrounding areas. On 23 November 1984 a M_w 6 earthquake occurred in Round Valley [*Priestley et al*., 1988], ~20 km southeast of the caldera. Two years later the activity shifted even further east with the Chalfant Valley earthquake sequence, with a M_w 5.7 foreshock followed ~24 hours later by the M_w 6.3 main shock [*Smith and Priestley*, 1988]. Further earthquake swarms occurred south of Long Valley caldera in

1989-1990, 1996, and 1997-1998 [*Hill et al.*, 2003], though none of these reached magnitude 6. The latest significant event that has occurred in the vicinity of Owens Valley to date is the May 26th, 1993, M_w 6.1 Eureka Valley earthquake (Figure 1.2).

1.3.2 Earthquake data used in this work

As source earthquakes for Coulomb stress modeling we used the updated CDMG Historical Earthquakes Catalog [*Petersen et al.*, 1996], which contains $M \geq 4$ events in northern California between 1769 and 2000. We selected only events with $M \geq 6$, because the effects of smaller earthquakes can be neglected at the scale of decades and tens of km, which are the scales relevant for our work. The only exception is the 1986 M_L 5.7 Chalfant Valley foreshock, which we included because of its proximity (spatial and temporal) to the Chalfant Valley main shock. We also excluded all the obvious aftershocks of the 1872 Owens Valley earthquake, because their location is not known precisely enough. However, because these aftershocks are one order of magnitude or more smaller than the main shock, their effect after over a century (i.e. by the 1980s, which is the time period we are interested in) would have been completely overprinted by the postseismic effects of the main shock. Therefore their exclusion does not substantially alter our results. To define the geometry of several of the source and receiver faults we used ~120,000 relocated hypocenters of earthquakes between 1984 and 2011 from the catalog of *Waldhauser and Schaff* [2008].

1.3.3 Fault slip rates and fault kinematics

The White Mountains - Owens Valley fault system (WM-OV), the Hunter Mountains - Panamint Valley (HM-PV) fault system, and the Fish Lake Valley - Furnace Creek-Death Valley (FLV-FC-DV) fault system represent the most continuous and prominent

structures that take up most of the 9.3 ± 0.2 mm/yr region-wide dextral motion determined from geodesy [*Bennett et al.,* 2003]. The FLV-FC-DV has geological slip rates of 3-9 mm/yr [*Klinger and Piety*, 2000; *Frankel et al*., 2007a, 2007b; *Willis et al.*, 2008] and geodetic rates of 2-8 mm/yr [*Bennett et al.*, 1997; *Dixon et al*., 2000; *McClusky et al*., 2001; *Del Pardo et al.*, 2012]. The HM-PV has geologic [*Zhang et al.*, 1990] and geodetic [*McClusky et al.*, 2001] slip rates of ~2.5 mm/yr. The geodetic and geologic rates of the OVF and WMF appear at first to disagree. *Bacon and Pezzopane* [2007] and *Kirby et al.* [2006] determined geologic slip rates of 1 mm/yr and 0.4 mm/yr for the Owens Valley fault and the White Mountains fault respectively. However, most of the geodetic rates calculated using elastic half-space models return values of 5 to 6 mm/yr for these same faults [*Dixon et al.,* 2000; *McClusky et al.,* 2001]. *Dixon et al.* [2003] and *Kirby et al.* [2006] explain this difference with the use of an inappropriate rheological model (elastic half-space). The long-term viscoelastic effect of the lower crust and upper mantle, and the corresponding postseismic effects of the Owens Valley earthquake, have been investigated by *Dixon et al.* [2000, 2003] using a viscoelastic coupling model. Their results show slip rates values of 2.1 ± 0.3 mm/yr for the Owens Valley fault and 3±2 mm/yr for the White Mountains fault, which are in reasonable agreement with the geologic slip rates above. In addition to these major faults, there are smaller east-dipping normal faults (e.g. Round Valley, Hilton Creek and Mono Lake faults) that bound the eastern escarpment of the Sierra Nevada. Geologic slip rates for these faults range between 0.8 and 1.5 mm/yr [*Berry*, 1997; *DePolo and Anderson*, 2000]. The Deep Springs fault (with a slip rate of ~ 0.8 mm/yr) and other minor NE-striking extensional structures transfer slip between Owens Valley and Panamint Valley in the west, and Death Valley in the east [*Reheis and Dixon*, 1996; *Lee et al*., 2001].

We used the geologic and geodetic slip rates above to calculate the interseismic Coulomb stress changes on the main active faults in the past ~150 years.

Knowledge of the kinematics of all source faults is required to carry out coseismic and postseismic Coulomb stress calculations. Except for the 1872 Owens Valley earthquake, none of the earthquakes that we considered produced a surface rupture or occurred on a known fault. For this reason, we used focal mechanisms to constrain the kinematics of all other ruptures. Focal mechanisms (Figure 1.2) suggest a left-lateral movement with a small normal component for the faults south of the Long Valley caldera [*Prejean et al*., 2002] and for the faults that caused the 1984 Round Valley earthquake [*Priestley et al.*, 1988] and the 1986 Chalfant Valley foreshock [*Smith and Priestley*, 2000]. The 1986 Chalfant Valley main shock is a dominantly right-lateral strike-slip event [*Smith and Priestley*, 2000], while the 1993 Eureka Valley earthquake is the only one that shows a nearly-pure normal faulting event [*Thio and Kanamori*, 1995].

1.4 Methods

1.4.1 Modeling Coulomb stress changes

In the last twenty years the concept of Coulomb stress changes in fault interactions has extensively been developed [e.g. *King et al., 1994*; *Stein et al.*, 1994, 1997; *Harris and Simpson*, 1998; *Stein*, 1999; *Parsons et al*., 2000; *Marsan*, 2003; *Ma et al.*, 2005; *Toda et al*., 2008]. Magma intrusions may also cause stress changes on nearby faults and promote or delay future earthquakes [*Tatcher and Savage*, 1982; *Nostro et al.*, 1998; *Hill et al.*, 2002].

The change in Coulomb failure stress (ΔCFS) on a receiver fault, due to a nearby fault rupture (source fault), is given by:

$$\Delta CFS = \Delta\tau - \mu'\Delta\sigma_n \quad [1.1]$$

Where $\Delta\tau$ is the change in shear stress calculated in a particular direction, μ' is the coefficient of effective friction, and $\Delta\sigma_n$ is the change in normal stress. The value of μ' we used in all plots is 0.4, and this choice is discussed in section 1.6.1. A positive ΔCFS indicates that the receiver fault has been brought closer to failure, while a negative ΔCFS means that the next rupture has been delayed. The processes of earthquake interactions can be classified as static (coseismic), quasi-static (postseismic, which are time-dependent) and dynamic [*Freed*, 2005]. Here we consider only static and quasi-static processes.

In coseismic stress models all the materials are considered elastic, while in postseismic stress models we need to differentiate the elastic upper and middle crust from the viscous lower crust and upper mantle. The limitation of the coseismic models is that only the instantaneous elastic stress can be modeled, and therefore we can correlate only earthquakes close in space and time. In the last decade the time-depended approach has thus been introduced to address long-distance and delayed earthquake triggering [e.g. *Chéry et al*., 2001; *Pollitz et al.*, 2003; *Lorenzo-Martín et al*., 2006; *Ali et al*., 2008; *Shan et al.,* 2013].

Regardless of the type of Coulomb stress models used, we need to know at the very least the location, size and focal mechanism of the earthquakes in the time period examined, and the 3-D geometry and kinematics of the active faults in the region. To calculate the postseismic response of the viscous lower crust and upper mantle, a

rheological model of the lithosphere is needed as well. Any uncertainties in the information above will propagate to the stress models, therefore care must be taken when making assumptions to compensate for missing data. For a complete overview of the stress evolution in a specific region we also need to determine the amount of strain accumulated on each fault during the interseismic period.

We carried out coseismic and interseismic ΔCFS calculations with the software Coulomb 3.3 [*Toda et al.,* 2011]. To calculate the interseismic ΔCFS we applied the "backslip" or "virtual dislocation" method [*Savage*, 1983; *Deng and Sykes*, 1997; *Papadimitriou and Sykes*, 2001] using long-term geological fault slip rates as input. For postseismic ΔCFS we used the code PSGRN/PSCMP [*Wang et* al., 2006], which is based on a multi-layered viscoelastic half-space.

1.4.2 3-D fault geometry

The first step in Coulomb stress modeling is defining the geometry of the faults used as both sources and receivers. We imported the relocated earthquake catalog for northern California [*Waldhauser and Schaff*, 2008] into the 3-D modeling and visualization software Gocad™. We then applied the techniques described by *Carena et al.* [2002, 2004] to fit surfaces to earthquake clouds in order to image in detail several active faults between the Sierra Nevada and the White Mountains (Figure 1.3). These faults include the ones that produced the 1980 sequence within the Sierra Nevada block, the 1984 Round Valley earthquake, and the 1986 Chalfant Valley foreshock and main shock. To obtain the 3-D geometry of the 1993 Eureka Valley earthquake fault we combined relocated earthquakes with the InSar-based results of *Peltzer and Rosen* [1995]. We constrained the geometry of the Owens Valley fault, for which no instrumental data are available, by using the surface rupture mapped by *Beanland and*

Clark [1994]. Due to the lack of deep constraints, we assumed a constant dip of 80°E for each fault segment, consistent with the geometry of the faults scarps measured by *Beanland and Clark* [1994], which show that NNW-trending faults segments have steeper dips (75°-90°) than the N-trending segments (60°-75°). Considering that the fault has an average strike of 160°, a constant dip of 80°E appears to be the most reasonable value to adopt for the Owens Valley fault.

1.4.3 Slip models for specific earthquakes

Because no finite fault model has been published for any of the earthquakes we considered, and because not enough good quality strong motion data are available even for the more recent events, we modeled the coseismic slip distribution for each event by using the reported moment magnitude (M_w) as a starting point. For all faults, we also assumed a slip distribution tapered at both ends in the slip direction, because the most realistic slip function for a propagating shear crack is a tapered one [e.g. *Scholz*, 2002]. The exceptions are the 1872 Owens Valley earthquake, and the 1986 Chalfant valley main shock, for which we used additional data to obtain a more accurate coseismic slip distribution.

For the 1980 Long Valley events and for the 1993 Eureka Valley earthquake we estimated an average coseismic slip for each earthquake based on the combination of earthquake magnitude [*Thio and Kanamori*, 1995; *Prejean et al.*, 2002] and 3-D geometry of the respective source faults. *Priestley et al.* [1988] for the 1984 Round Valley earthquake, and *Smith and Priestley* [2000] for the 1986 Chalfant Valley foreshock, used the same approach to determine the average coseismic slip. We therefore used their results in our models of these two earthquakes.

In the case of the Owens Valley earthquake, we divided the fault into twelve sections with different values of slip based on coseismic offsets along the fault trace mapped by *Beanland and Clark* [1994]. For lack of better constraints, we kept slip in each section constant in the dip direction.

For the 1986 Chalfant Valley earthquake main shock we produced a more detailed slip model based on the distribution of aftershocks (Figure 1.12). Following the idea that aftershocks occur in regions where high stress is induced by slip during the main shock [*Aki*, 1979; *Mendoza and Hartzell*, 1988; *Das and Henry*, 2003], we assumed that the part of the fault that slipped in the main shock is the one where the aftershocks density is lowest, surrounded by a higher-density zone of aftershocks. This anti-correlation of slip and aftershocks has been observed in many other events of magnitude between about 6 and 7 in which slip distribution could be determined independently of aftershock distribution, for example Morgan Hill 1984 [*Schaff et al.*, 2002], Landers 1992 [*Das and Henry*, 2003], Colfiorito 1997 [*Chiaraluce et al.*, 2003], Parkfield 2004 [*Johanson et al.*, 2006], L'Aquila, 2009 [*Valoroso et al.*, 2013]. We adjusted the actual slip distribution within the patch by matching the M_w predicted by our slip model to the observed M_w, using the same fault kinematics as the one determined by *Smith and Priestley* [2000]. Because this earthquake did not produce a surface rupture, slip was set to zero everywhere in the top few km of the fault. We based our slip model on the distribution of aftershocks in the time span between the July 21st main shock and the July 31st M_L 5.8 strongest aftershock, excluding all events following this aftershock because it is not possible to establish which of those still belong to the main shock.

1.4.4 Viscoelastic models

The rheological parameters of the lithosphere need to be defined before we can model postseismic stresses. Several authors have attempted to determine these parameters in the western United States using postseismic GPS [*Hetland and Hager*, 2003; *Pollitz*, 2003; *Gourmelen and Amelung*, 2005; *Johnson et al.*, 2007; *Hammond et al.*, 2009; *Hammond et al.*, 2010] and InSAR [*Gourmelen and Amelung*, 2005; *Hammond et al.*, 2009], with variable results. The main finding for the western United States is that, for time intervals up to 100 years, the upper mantle has an effective viscosity up to about two orders of magnitude less than the lower crust [*Thatcher and Pollitz*, 2008].

Most of these authors use models based on Maxwell rheology that represents a simplification different from a more realistic transient [e.g. *Pollitz*, 2003] or power-law rheology [*Freed and Bürgamnn*, 2004]. In addition as concluded by *Meade et al.* [2013], a Burgers rheology with at least two relaxation timescales better explains observed behaviors as rapid postseismic deformation and localized postseismic strain rates. In the other hand we believe that a model with linear viscosity does not influence the stress changes due to viscoelastic relaxation at a time scale of 100 years considered in this work.

In order to compare different time/stress curves to choose the most suitable rheological parameters for our study area, we simulated the stress redistribution over 600 years due to a random strike-slip earthquake, using different combinations of viscosity based on all the studies cited above. We supplemented the rheological models from literature with two additional models (Models 2 and 3 in Table 1.1), in order to explore the widest possible range of viscosity combinations (Figure 1.4). We chose a point located in an area of coseismic stress increase (black dot in Figure 1.4c), for

which we calculated ΔCFS over the 600 years interval. The eight different curves for different combinations of lower crust and upper mantle viscosities are shown in Figure 1.4b. For the first four models, most of the stress is released in the first 200 years, presumably due to the low values of viscosity used for the lower crust. In the subsequent three models, stress is released more slowly, and part of it continues to be transferred to the crust well beyond 200 years after the earthquake. The last model correspond to a Burgers rheology and, like the Model 4, describes a fast stress release in the first years of the seismic cycle.

Figure 1.4c compares coseismic stresses with the effect of postseismic stress redistribution after 50 and 100 years from the occurrence of the simulated event. We used Model 6 for this plot, and the difference between the instantaneous and the 100 years Coulomb stress release is substantial, both in terms of spatial distribution and of magnitude.

We therefore tested three different viscosity models (2, 4 and 6) in our final calculations (Tables 1.2 and 1.3). Models 2 and 6 represent the end members of the relaxations curves (Figure 1.4b), and Model 4 is an average between these two. In this way, we were able to cover a wide range of possible values of postseismic ΔCFS. The plots that show postseismic stresses in this paper, including figures in the auxiliary material, show results obtained by using Model 6. This choice, and in general the influence of the rheological parameters on our results are discussed in section 1.6.2. These simulations emphasize the importance of considering postseismic ΔCFS in earthquake interaction studies that cover, like in our case, a time period of 50 to 100 years.

1.5 Results

Beginning with the effects of the 1872 earthquake on the faults that produced the 1980-1986 sequence in northern Owens Valley, we determined both the relationship among all events up to 1993, and the present-day cumulative ΔCFS on several of the major faults in the Eastern California Shear Zone north of the Garlock fault. We also investigated the possible correlation between volcanic unrest in the Long Valley caldera and seismicity in northern Owens Valley.

1.5.1 The 1980-1986 earthquake sequence

The ΔCFS calculated on optimally-oriented faults can give an overview of the redistribution of stresses after an earthquake, and it is especially useful in the study of aftershocks distributions [e.g. *King et al.*, 1994; *Reasenberg and Simpson*, 1992; *Ma et al.*, 2005]. If we want to study the relationship between events occurring on known faults, however we need to resolve the ΔCFS for the geometry and kinematics of the specific fault (receiver fault) and earthquake considered. Below we describe our results for both known faults, and for the aftershocks distribution of the 1986 Chalfant Valley earthquake.

1.5.1.1 ΔCFS on known faults

The cumulative (coseismic + postseismic) ΔCFS for all the modeled faults in northern Owens Valley due to the 1872 M_w 7.5 Owens Valley earthquake, calculated for the time just before the initiation of the 1980 Long Valley earthquake sequence, is shown in Figure 1.5a. In these 108 years the cumulative ΔCFS increased on all the faults, with the largest increase ($\geq$ 1.5 bar) occurring near the lower tip of each fault (i.e. close to the bottom of the seismogenic zone).

The May 1980 Long Valley earthquake sequence increased stresses further on the 1984 Round Valley earthquake fault (Figure 1.5b). The 1984 Round Valley earthquake in turn modified the stress distribution on the 1986 Chalfant Valley foreshock and main shock faults (Figure 1.5c). Comparing Figure 1.5b and 1.5c, it is evident that the 1984 earthquake shifted the largest positive patch of ΔCFS on the Chalfant Valley fault from the southern to the northern half of the fault, where the main shock nucleated later on.

In Figure 1.6 we show the cumulative ΔCFS due to all the preceding events (including the M_w 5.7 foreshock) on the Chalfant Valley main shock fault. Although the foreshock clearly creates an heterogeneous stress change pattern on the main shock fault plane, the hypocenter of the July 21th 1986 Chalfant Valley earthquake falls in an area of ΔCFS > 3 bars.

In summary, the 1872 Owens Valley earthquake increased the stress on all the fault planes involved in the 1980 - 1986 earthquake sequence. Adding to the effect of the major event (Figure 1.5a), each single earthquake has also increased stress on the fault responsible for the subsequent event (Figure 1.5b, 1.5c, 1.6, and Table 1.2).

1.5.1.2 ΔCFS on optimally-oriented faults: The 1986 Chalfant Valley aftershocks distribution

More than 3600 aftershocks were recorded in the 10 days following the July 21th M_w 6.3 main shock. The largest aftershock (M_L 5.7) occurred on July 31st [*Smith and Priestley*, 2000]. We did not include aftershocks beyond July 31st in this part of the study because it is not possible to distinguish which of these are actually aftershocks of the M_L 5.7 aftershock itself, rather than of the main shock. We compared the position of the relocated aftershock hypocenters [*Waldhauser and Schaff*, 2008] with the coseismic

ΔCFS distribution in the volume surrounding the main shock source fault. For this purpose, we calculated the coseismic ΔCFS on optimally-oriented faults using a regional stress orientation of N20˚ for σ_1, N110° for σ_3, vertical σ_2, and magnitudes of 100 bars for σ_1, 30 bars for σ_2, and 0 for σ_3 [*Hardebeck and Hauksson*, 2001; *Townend and Zoback*, 2004].

Our results show that 81% of the aftershocks fall into the volume where ΔCFS > 0, with 80% where ΔCFS ≥ 0.3. The correlation can be appreciated in Figure 1.7, which shows how most of the events, including the largest (M_L 5.8) aftershock, are clearly located in areas of significant stress increase (≥ 1 bar).

1.5.2 Present-day cumulative and total ΔCFS on faults in and around Owens Valley

The White Mountains fault (WMF) and the Fish Lake-Furnace Creek fault (FLV-FC) are two of the largest faults in the Eastern California Shear Zone north of the Garlock fault. Both faults show geomorphological and paleoseismological evidence of having produced several major earthquakes during the Holocene [*DePolo et al.,* 1993; *Reheis*, 1994; *Klinger*, 1999; *Kirby et al*., 2006]. There are also several other smaller normal faults that are nonetheless capable of $M_w \geq 7$ earthquakes (Emigrant Peak, Deep Springs, Hilton Creek and Round Valley normal fault).

We calculated coseismic, interseismic (Figure 1.8) and postseismic ΔCFS on all the faults mentioned above. Calculation of cumulative ΔCFS (coseismic + postseismic) is for the period from the 1872 Owens Valley earthquake until the present time, i.e. 142 years. "Total ΔCFS" is the sum of coseismic, postseismic and interseismic ΔCFS for the same period.

Figure 1.9 shows cumulative ΔCFS for the WMF and the FLV-FC. The distribution of ΔCFS along the WMF varies from segment to segment. The northern part of the fault (Montgomery and Hammil sections of *DePolo* [1989]) has experienced a maximum cumulative stress increase of ~ 4 bar, while on the northernmost part of the Central section there is a stress drop of several bars, mostly due to the 1986 M_w 6.3 Chalfant Valley earthquake. The highest positive ΔCFS is in the southern part of the Central section. Here the coseismic and postseismic effects of the 1872 M_w 7.5 Owens Valley earthquake dominate, producing a cumulative stress increase of at least 30 bars. The southernmost segment (Inyo section of *DePolo* [1989]) falls in an area of stress drop due to the fact that this segment is parallel to and overlapping with the Owens Valley fault. According to our models, the WMF has also accumulated between 3 and 3.5 bars of interseismic ΔCFS in the last 142 years (Figure 1.8). The total ΔCFS increase on the Montgomery section of the WMF is therefore ~7 bars, and on the southern part of the Central section it is ~34 bars (Table 1.3).

The positive ΔCFS on the FLV-FC is mostly concentrated on the Cucomongo section [as named by *Brogan et al.*, 1991], where the two fault segments join to form an E-W striking compressional bend (Figure 1.9b). The cumulative ΔCFS changes from ~ -1.6 bar in the northern FLV and southern FC faults, to 2.5 bar in the southern FLV and northern FC faults. Adding to this the interseismic ΔCFS (Figure 1.8), the positive total ΔCFS in the area where the northern FC fault and the southern FLV fault join is ~10 bars.

The sequence of events that between 1980 and 1986 struck the northern Owens Valley contributed to produce an inhomogeneous stress distribution along the Round Valley fault (Table 1.3 and Figure 1.22). A ~10 km-long segment of this fault has experienced a stress increase of at least 4 bars, but most of the fault falls in an area of

cumulative stress drop. The interseismic ΔCFS of 2.1 bars is not enough to erase this stress shadow.

The Emigrant Peak and the Deep Springs faults are the only structures that have been consistently loaded along their entire length (Table 1.3, Figures 1.19 and 1.20). The cumulative ΔCFS increase on the Emigrant Peak fault is relatively small (~0.5 bars). The Deep Springs fault however shows a far more significant loading, with positive cumulative ΔCFS between 2 and 8 bars. The additional contribution from interseismic loading results in a maximum total ΔCFS of ~11 bars for this fault (Table 1.3). Unlike the other faults studied, the Hilton Creek fault has been subjected to a cumulative ΔCFS decrease along its entire length (Table 1.3, Figure 1.21), and the positive interseismic ΔCFS (~3.5 bars) in the time period considered is barely sufficient to erase this stress shadow.

1.5.3 Volcano-earthquake interaction in northern Owens Valley

In order to better understand the interaction between magmatic processes in the Long Valley caldera and the surrounding seismic activity, we calculated the coseismic ΔCFS produced by the 1978-1980 caldera inflation event. Location, depth (7.5 km) and volumetric expansion (0.068 km^3) of the modeled point source are from *Tizzani et al.* [2009]. The calculated coseismic ΔCFS on the faults south of the caldera (Table 1.2) shows that the inflation event loads the faults that ruptured in the1980-1983 earthquake sequence (Figure 1.10). Ours is a conservative estimate. *Savage and Clark* [1982] suggested an even greater volumetric expansion of the magma chamber, 0.15 km^3, which would increase both the areal extent and the magnitude of the positive ΔCFS lobes.

1.6 Discussion

1.6.1 Influence of effective fault friction on the results

The choice of effective coefficient of friction (μ') needs to be discussed, because as seen in equation [1.1], this parameter plays an important role in the normal stress component of ΔCFS. μ' can in principle have values anywhere between 0 and 0.85, with very low values corresponding to higher fluid pressure or to specific materials (e.g. some clays). Frictionless faults are physically unrealistic, but low values of effective friction, significantly lower than classic Byerlee's friction of ~0.8, are likely and have been hypothesized for faults in different tectonic settings [e.g. *Bird and Kong*, 1994; *Hardebeck and Hauksson*, 2001; *Carena et al*., 2002; *Hardebeck and Michael*, 2004; *Iaffaldano et al*., 2006; *Suppe*, 2007; *Carena and Moder*, 2009; *Suppe et al*., 2009; *Hsu et al*., 2009].

In order to test the effect of varying μ', we calculated coseismic and postseismic ΔCFS for three different values of μ' (0.2, 0.4, 0.8) (Tables 1.2 and 1.3, with μ' always calculated for rheological Model 6). Table 1.2 shows cumulative ΔCFS calculated on each earthquake hypocenter at the time just before the earthquake occurred. A graphical representation of the same calculations can be found in Figures 1.14 to 1.18.

As also observed by *King et al.* [1994], μ' controls mainly the magnitude of ΔCFS, rather than the overall pattern of stress loading lobes and stress shadows. Specifically, in our case it does not affect the sign of the Coulomb stress changes on the receiver faults, which turn out to be all located in areas of stress increase produced by previous events, independently of the value of μ' used in the calculations. This is an important finding, because our main purpose is to establish whether there is in general a positive correlation among events, rather than to determine by how many years

earthquakes have been delayed or brought forward by preceding events (in which case the specific values would be far more important). The magnitude of ΔCFS is therefore not particularly relevant to this study. Based on the considerations above, we carried out all our calculations with a value of effective friction of 0.4.

1.6.2 Effect of viscosity on the results

Postseismic viscous relaxation appears to play an important role in ΔCFS calculations over a time period of 150 years. Therefore, the choice of the viscosity values for the lower crust and upper mantle could influence the significance and stability of our results and needs to be justified. As described in section 1.4.4, we tested a wide range of possible rheological models (Tables 1.2 and 1.3). These tests show that the choice of the viscosity model does not influence the sign of the ΔCFS, but it does influence its magnitude. The smaller the viscosity of the lower crust, the faster the stress is released in the first 150 years.

We have thus drawn our general conclusions from simulations done using rheological model 6 (Table 1.2), because this is the most conservative of all of the models we considered. Model 6 transfers stresses back to the upper crust at a slower rate than most of the other models (Figure 1.4), therefore any resulting correlations among earthquakes are robust.

1.6.3 Significance of observed stress patterns

Our analysis of the interaction among the earthquakes of 1980 - 1986 in northern Owens Valley shows that small coseismic stress changes appear to control the eastward migration of the seismicity. The coseismic ΔCFS in the 1980 - 1986 earthquake sequence is often below 1 bar, however this appears sufficient to encourage

faulting. This is similar to what other authors have observed for example in Turkey (*Stein et al.*, 1997; *Nalbant et al.*, 1998), southern California (*Harris et al.*, 1995; *Deng and Sykes*, 1997; *Freed et al.*, 2007) and Mongolia (*Chéry et al*., 2001; *Pollitz et al.*, 2003). As discussed by these authors, ΔCFS increases in the order of 1 bar may well not be the main source of stress loading for faults, but if these faults are at failure already, any increase in ΔCFS may trigger earthquakes. The occurrence of such documented cases worldwide seems to point to the conclusion that at any given moment most faults are likely to be close to failure, and any small perturbations in the state of stress can trigger a rupture.

The correlation between the 1872 Owens Valley earthquake and the recent seismicity is not limited to promoting events in areas of increased cumulative ΔCFS. If we ignore the events clearly produced by the Long Valley caldera activity, and compare the cumulative ΔCFS distribution with the seismicity of the last 30 years, not only is most of the seismicity located in regions of ΔCFS increase (Figure 1.11a, b) but the area within the stress shadow has very little seismicity. In fact, none of the $M > 5$ earthquakes of the last 30 years fall into this area (Figure 1.11c), even though it contains many active faults capable of $M \geq 5$ events (Hunter Mountain - Panamint Valley fault, Ash Valley fault, Black Mountain strand of the Death Valley fault, Sierra Nevada frontal fault). This is a strong indication that the region has not recovered yet from the 1872 earthquake.

The analysis of Coulomb stress interaction between the 1986 M_w 6.3 Chalfant Valley earthquake and its relocated aftershocks shows that most aftershocks, even very close to the fault plane, fall into the volume of positive coseismic ΔCFS. It has been observed that the best correlation in terms of coseismic ΔCFS between main shock and aftershocks is at distances greater than a few kilometers from the fault [e.g. *Freed*,

2005], because events near the fault are often correlated to an unknown heterogeneous slip distribution on the main fault. The more realistic slip distribution model used here to calculate ΔCFS for this fault shows that indeed most aftershocks occur in areas of coseismic ΔCFS increase, regardless of distance from the fault. In the case of moderate-size earthquakes this is significant, because most of the aftershocks occur close to the main fault. The only aftershocks located off-fault at some distance here, which occurred on minor faults delimiting a small pull-apart basin between the Chalfant Valley fault and the White Mountains fault, also mostly fall in a region of coseismic ΔCFS increase (Figure 1.13).

If we now consider the present-day state of stress in the region, for most of the faults the interseismic ΔCFS is comparable to the cumulative ΔCFS (Table 1.3). The White Mountains (Central section) fault is an exception, with a cumulative ΔCFS at least ten times larger than the interseismic ΔCFS. The total ΔCFS, for this fault (30 - 40 bars) is similar to the average stress drop expected for moderate-to-major earthquakes [*Hanks,* 1977; *Scholz*, 2002]. This is an indication that the White Mountains fault may have accumulated enough stress on a long enough segment to produce an $M_w \geq 7$ earthquake. Unfortunately, there are insufficient paleoseismological studies concerning the most recent event on the Central section of the White Mountains fault. There are also limited data about large earthquakes in the wider region before 150 years ago. Therefore, while our results point in the direction of the White Mountains fault being a candidate for the next large event in the region, additional paleoseismological data would be needed to confirm this.

Considering the entire range of possible values of stress drop for moderate-to-major earthquakes, which is between 10 and 100 bars [*Kanamori and Anderson*, 1975; *Hanks,* 1977; *Scholz,* 2002], the Fish Lake-Furnace Creek and the Deep Springs fault

may also have accumulated enough stress to produce a large earthquake (Table 1.3). Paleoseimological studies have been carried out for some of the active faults in the ECSZ north of the Garlock fault. The most recent event has been dated to at least 300 years B.P. [*Klinger*, 1999] for the Furnace Creek fault, 600-1200 years B.P. for the Fish Lake fault [*Reheis*, 1994], 1200 years B.P. [*Reheis*, 1991] for the Emigrant Peak fault, and 2000 years B.P. or more for the Hilton Creek, Deep Springs and Round Valley fault [*Berry*, 1997; *Lee et al.*, 2001]. These ages and the interseismic ΔCFS rates tell us that, since their last event, these faults would have accumulated very high values of stress. There are however two problems with this interpretation. First of all, we lack information about possible major earthquakes just outside our region of interest before 150 years ago, which could have put any of these faults in stress shadow. This is a consideration especially important for those faults that are located at the edge of our study area. In addition, the backslip model used in calculating the interseismic ΔCFS is based on fault slip rates, which are in part (geologic rates) based on dating faulted features. Therefore in several cases the interseismic rates may be dependent on knowledge of the age and offset of the last event, which is often characterized by large error margins. This is a circular problem, which cannot be solved in the absence of long-term loading rates determined fully independently of geological fault slip rates. However our geological slip rate-based interseismic calculations for the FLV-FC-DV fault system are in agreement with the geodetic slip rate-based stress accumulation rates modeled by *Del Pardo et al.* [2012].

1.6.4 Model limitations

Similarly to other studies of this kind, our results are affected by some limitations connected with the chosen physical parameters, and by oversimplifications.

We already described in sections 1.6.1 and 1.6.2 the effect of our choice of effective friction coefficient (μ') and of viscosity (η), and argued that this choice does not change our results.

Postseismic ΔCFS calculations are closely tied to the rheological models used. Our modeling choice is based on the state of the art [as summarized by *Tatcher and Pollitz,* 2008] available for the western United States. Different, and possibly more realistic, results could come from having for example more detailed models of the lithosphere in this region both on the vertical and horizontal scale. In alternative, other types of rheologies may turn out to be equally valid [*Pollitz,* 2003], which could produce different results.

Also, although it is the most realistic slip function in absence of detailed information, a tapered slip distribution is not the same as the actual slip distribution observed in a specific earthquake. A more heterogeneous distribution produces significant changes in ΔCFS patterns, especially very close to the source fault. However, because in nearly all cases we are not modeling earthquakes occurring on or near the source fault plane, the lack of availability of detailed slip models is not relevant. The only case in which it becomes indeed relevant is in examining the 1986 Chalfant Valley earthquake aftershocks, in which case we used a more realistic slip model.

Another consideration comes from the geometry of the source and receiver faults. In particular, the fault responsible for the 1872 Owens Valley earthquake has been modeled with a constant dip of 80°E which in some segment of the fault may be slightly different. However we believe that such little changes would not significantly affect the ΔCFS produced by the 1872 earthquake.

The result of interseismic ΔCFS calculations are also dependent on the depth extent of the faults considered. As discussed by *Smith-Konter and Sandwell* [2009], the stress accumulation rate is inversely proportional to the locking depth. In our study area, however, the depth of the base of seismicity, which we consider a reasonable proxy for the base of the modeled faults, is mainly between 1 and 15 km. These small variations are not sufficient to alter our conclusions concerning total stress changes on modeled faults.

The last consideration comes from the possible oversimplification of the Long Valley caldera inflation model. First of all, the model assumes a homogeneous and linearly elastic material, which in volcanic regions may not always be the most appropriate assumption. Moreover, the shape of the inflating source may well not be spherical but probably more similar to a prolate ellipsoid [*Langbein*, 2003]. Further work in this direction would be needed to fully understand the role of caldera unrest, and our results should be viewed as very much preliminary in this context.

1.7 Conclusions

The correlation between the 1872 M_w 7.5 Owens Valley earthquake and the subsequent moderate-to-strong seismicity in the ECSZ north of the Garlock fault supports the hypothesis that large events may control the timing and distribution of future seismicity in the surrounding regions. Also, the west to east migration of seismicity in northern Owens Valley during 1978 – 1986 appears to be controlled by coseismic stress loading, and initiated by the inflation of Long Valley caldera. This control includes the aftershocks of the last event in the series (1986 Chalfant Valley earthquake), 80% of which fall in the volume of crust coseismically loaded by the main shock. Finally, the total ΔCFS calculated on the main active faults in the region for the

last 150 years shows that several faults capable of $M_w \geq 7$ earthquakes (White Mountains, Fish Lake-Furnace Creek, and Deep Springs faults) may be close to failure.

Table 1.1. Combinations of tested crust and mantle viscosities (η).

	Model 1[a]	Model 2	Model 3	Model 4[b]	Model 5[c]	Model 6[d]	Model 7[e]	Model 8[f]
	η (Pa s)	η (Pa s)	η (Pa s)	η (Pa s)	η (Pa s)	η (Pa s)	η (Pa s)	η (Pa s)
Lower crust	1×10^{18}	1×10^{19}	1×10^{19}	3.2×10^{19}	3.2×10^{19}	1×10^{20}	1×10^{20}	3.2×10^{19}
Upper mantle	1×10^{20}	1×10^{19}	1×10^{20}	3.2×10^{18}	1×10^{21}	3.2×10^{18}	1×10^{19}	1.6×10^{17}
					3.2×10^{18}			4.6×10^{18}

[a]*Hetland and Hager* (2003); [b]*Hammond et al.* (2010); [c]Upper mantle divided in two layers: 20 km of uppermost mantle and 45 km of upper mantle (*Johnson et al.*, 2007) ; [d]*Gourmelen and Amelung* (2005); [e]*Hammond et al.* (2009); [f] Burgers rheology assuming a viscoelastic lower crust and a biviscous upper mantle (*Pollitz*, 2003).

Table 1.2. ΔCFS at hypocenter immediately before the occurrence of each earthquake.

Earthquake[a]	M_w	Strike/Dip/Rake (degrees)[b]	Coseismic ΔCFS (bars)			Cumulative ΔCFS (bars)			Cumulative ΔCFS (bars)	
						Model6			Model2	Model4
			μ' 0.2	μ' 0.4	μ' 0.8	μ' 0.2	μ' 0.4	μ' 0.8	μ' 0.4	μ' 0.4
1872 OV	7.5	340/80/-170[c]								
1980 LV	6.2	10/80/-5[d]	0.92	0.67	0.18	1.68	1.3	0.53	2.5	2.15
1984 RV	5.9	32/85/-30[e]	2.56	1.97	0.83	3.82	3.25	2.16	4.88	4.48
1986a CV	5.7	200/50/-10[f]	0.1	0.21	0.42	0.46	0.7	1.15	1.68	1.37
1986b CV	6.3	150/55/-175[f]	3.1	2.56	1.63	4.39	3.67	2.38	5.2	4.85
1993 EV	6.1	182/45/-100[g]	1.48	2.1	3.32	3.19	4.06	5.81	4.33	4.27

[a] OV, Owens Valley; LV, Long Valley; RV, Round Valley; CV, Chalfant Valley; EV, Eureka Valley.. [b] Aki and Richards convention. [c]*Beanland and Clark* [1994]. [d]Modeled as one event on four different fault planes from *Prejean et al.* [2002]; [e]*Priestley et al.* [1988]; [f]*Smith and Priestley* [2000]; [g]*Thio and Kanamori* [1995]. Model2, Model4 and Model6 are listed in Table 1.1.

Table 1.3. Minimum / maximum present-day cumulative ΔCFS for different rheologies and effective friction coefficient (μ'), and interseismic ΔCFS, calculated on each fault.

Fault[a]	Strike/Dip/Rake (degrees)[b]	Cumulative (bars)			Cumulative (bars)		Interseismic (bars)
		Model6			Model2	Model4	
		μ' 0.2	μ' 0.4	μ' 0.8	μ' 0.4	μ' 0.4	μ' = 0.4
EP	190/60/-90	0.25/0.48	0.31/0.60	0.45/0.85	0.13/0.43	0.18/0.45	2.13
DS	211/60/-90	1.67/6.62	2.01/8.3	2.7/11.9	1.87/10	1.97/9.6	2.36
HC	339/55/-90	-3.5/-0.17	-4.15/-0.15	-5.39/-0.1	-3.57/0.54	-3.62/0.36	3.55
RV	350/45/-90	-6.2/3.8	-7.6/4.45	-10/5.6	-6.64/6.06	-6.8/5.63	2.13
WM (MS)	166/60/-140	-0.22/2.0	0.31/3.75	1.39/7.25	1.20/5.34	1/4.81	3.12
WM (HS)	166/60/-140	-22.9/-1.7	-25.9/-2.5	-32/-4.2	-21.6/-0.4	-22.7/-1.2	2.96
WM (CS)	166/60/-140	-2/29.7	-1.2/31.7	0.32/35.6	1.65/35	0.71/34.1	3.6
FLV	320/85/180	-1.91/-0.6	-1.59/-0.55	-0.97/-0.3	-2.76/-1.14	-2.46/-1.02	5.1
FLV-FC	320/85/180	-0.8/1.18	0.36/2.52	2.6/5.18	-0.34/2.78	-0.04/2.8	7.3
FC	320/85/180	-1.44/0.9	-1.92/1.3	-2.88/2	-2.82/2	-2.56/1.95	5.6

[a]EP, Emigrant Peak; DS, Deep Springs; HC, Hilton Creek; RV, Round Valley; WM (MS), White Mountains (Montgomery section); WM (HS), White Mountains (Hammil section); WM (CS), White Mountains (Central section); FLV, Fish Lake Valley; FC, Furnace Creek. Model2, Model4 and Model6 are listed in Table 1.1.[b] Aki and Richards convention.

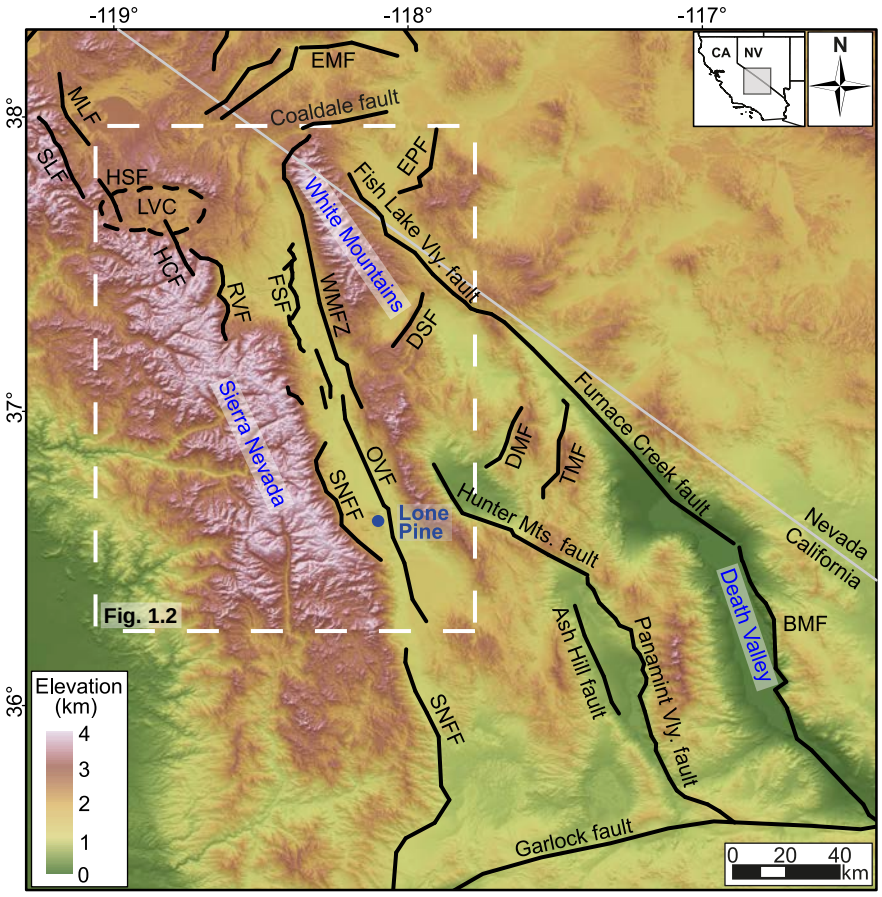

Figure 1.1. Map of the Eastern California Shear Zone north of the Garlock fault. Thick black lines are the main active faults from U.S. Geological Survey (USGS) Quaternary fault and fold database; dashed black line is the rim of the Long Valley caldera (LVC).
BMF=Black Mountains fault; DMF=Dry Mountain fault; DSF=Deep Springs fault; EMF=Excelsior Mountain fault; EPF=Emigrant Peak fault; FSF=Fish Slough fault; HCF=Hilton Creek fault; HSF=Hartley Springs fault; MLF=Mono Lake fault; OVF=Owens Valley fault; RVF=Round Valley fault; SLF= Silver Lake fault; SNFF=Sierra Nevada frontal fault; TMF=Tin Mountain fault; WMFZ=White Mountain fault zone.

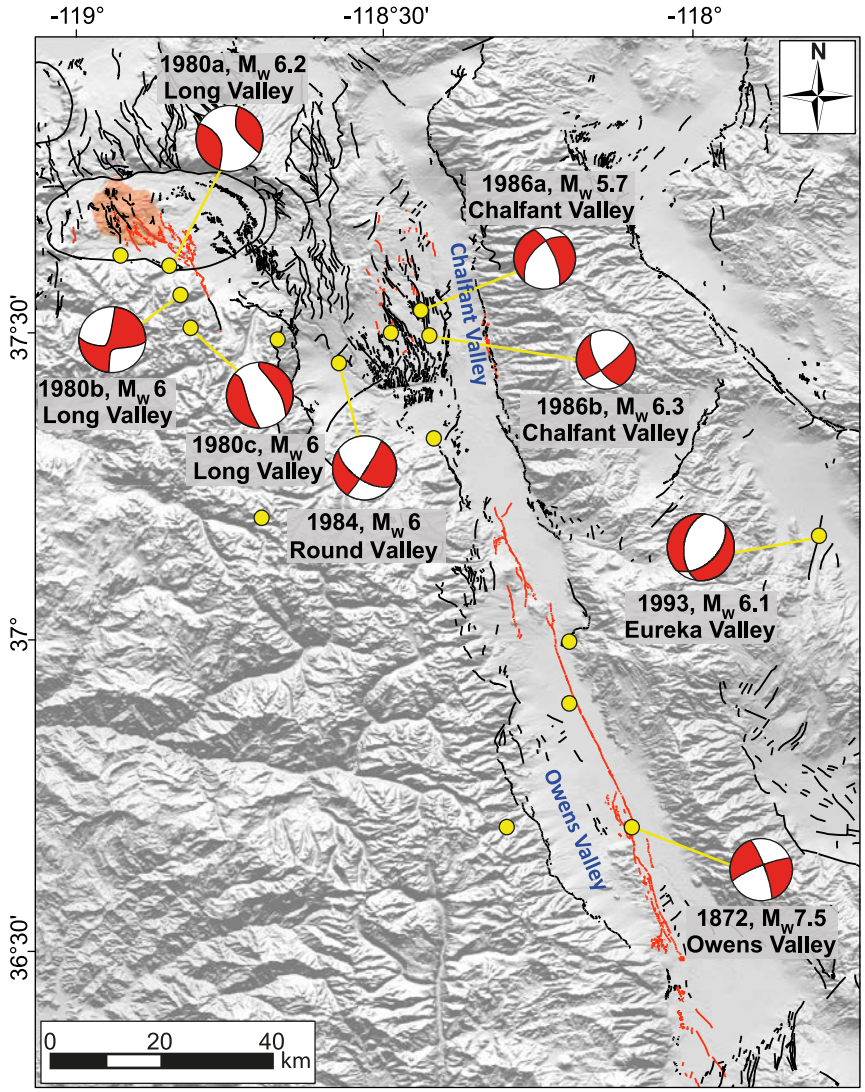

Figure 1.2. Map of Quaternary active faults (black lines) and faults that produced earthquakes in the last 150 years (red lines) from the U.S. Geological Survey (USGS) Quaternary fault and fold database. Earthquake (ML ≥ 5.5) locations for this and following figures are from the CDMG Historical Earthquakes Catalog [*Petersen et al.*, 1996]. Focal mechanisms are from *Beanland and Clark* [1994] (Owens Valley earthquake), *Julian and Sipkin* [1985] (Long Valley earthquakes), *Priestley et al.* [1988] (Round Valley earthquake), *Smith and Priestley* [2000] (Chalfant Valley main shock and foreshock) and *Thio and Kanamori* [1995] (Eureka Valley earthquake). The orange shading outlines the Long Valley caldera resurgent dome.

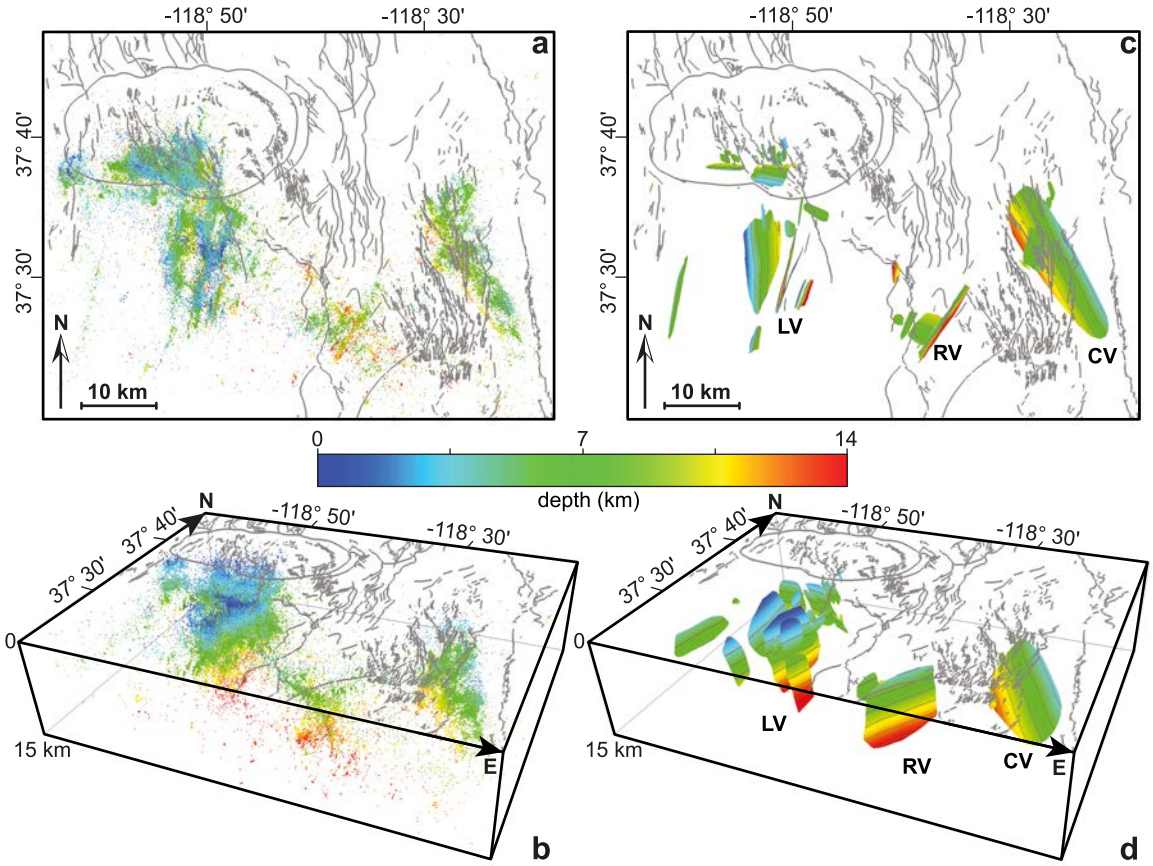

Figure 1.3. 3-D fault geometry in northern Owens Valley. (a) Map view and (b) perspective view of the earthquake hypocenters from *Waldhauser and Schaff* [2008]. (c) Map and (d) perspective view of the fault surfaces we modeled from these hypocenters. LV= Long Valley faults; RV= Round Valley fault; CV= Chalfant Valley fault.

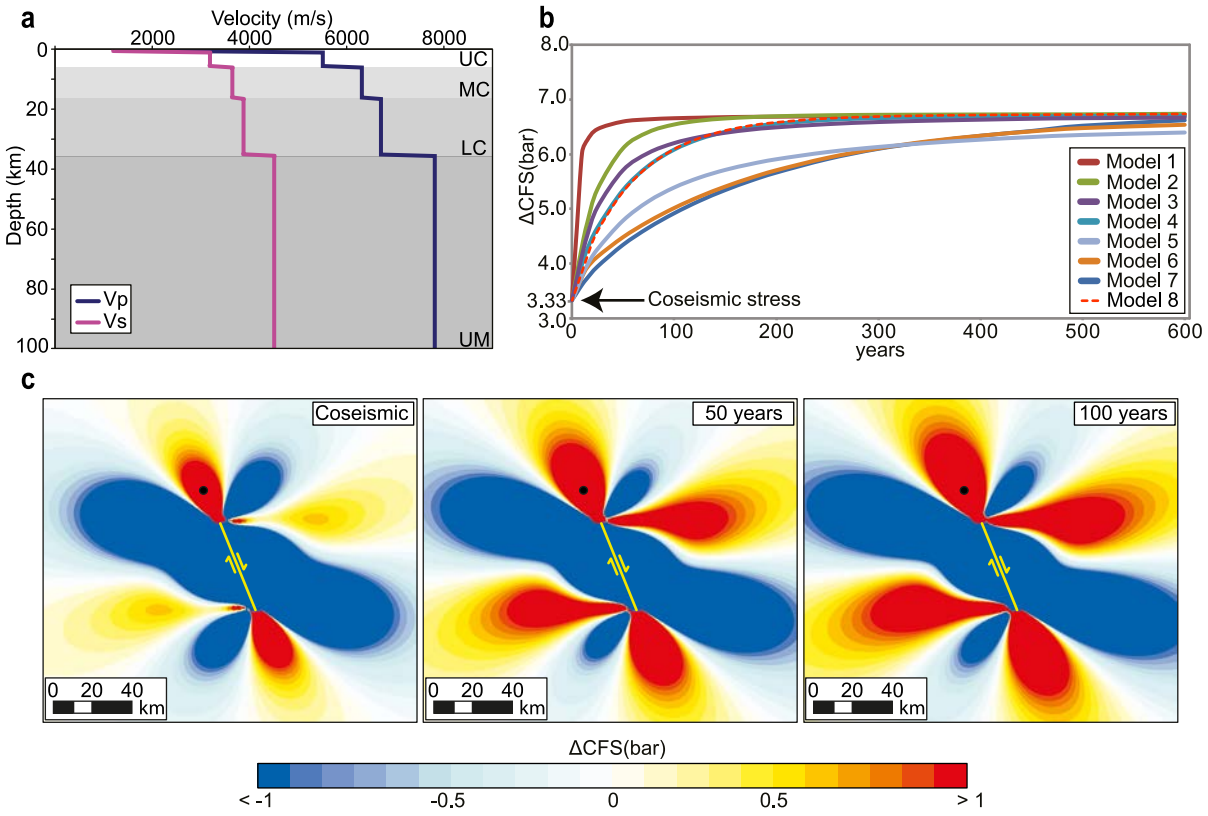

Figure 1.4. (a) Velocity model used for postseismic ΔCFS calculations [*Bassin et al.*, 2000]. (b) Observed postseismic stress changes for different viscosity values. (c) Simulation of an Mw 7.1 earthquake on a 45 km-long right-lateral strike-slip fault calculated at 10 km of depth. The black dot represents the observation point. For the list of parameters used for different models refer to Table 1.1. UC=upper Crust, MC=middle crust, LC=lower crust, UM=upper mantle.

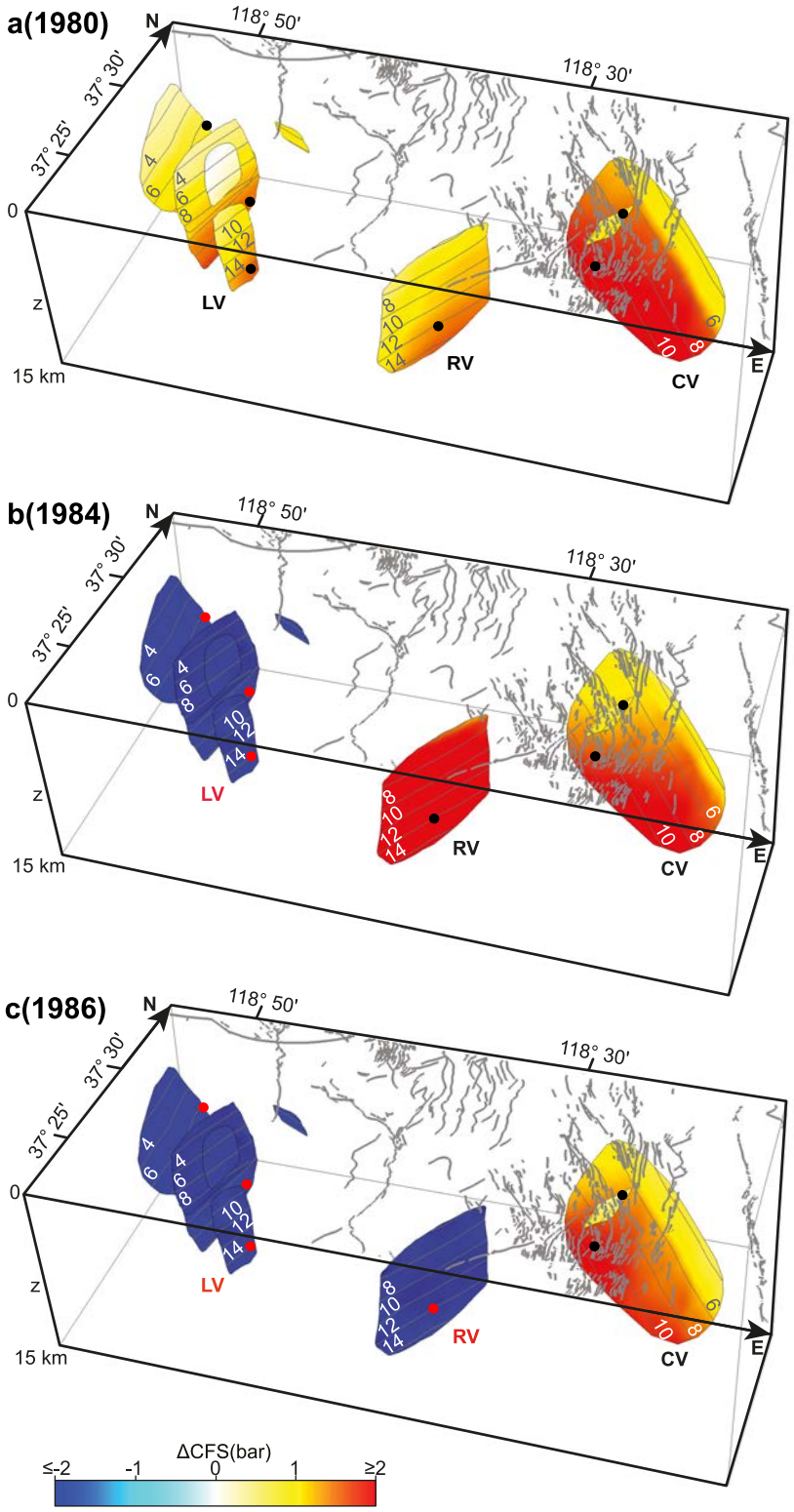

Figure 1.5. Cumulative ΔCFS on faults in northern Owens Valley. (a) ΔCFS due to the 1872 earthquake; (b) with the events of 1980 added, (c) and with the 1984 Round Valley event added. Contour lines on faults are in km b.s.l. LV= Long Valley faults; RV=Round Valley fault; CV=Chalfant Valley fault. Contour lines and numbers on the fault planes represent crustal depths. The small yellow patch located on the hanging-wall of the CV is the foreshock fault.

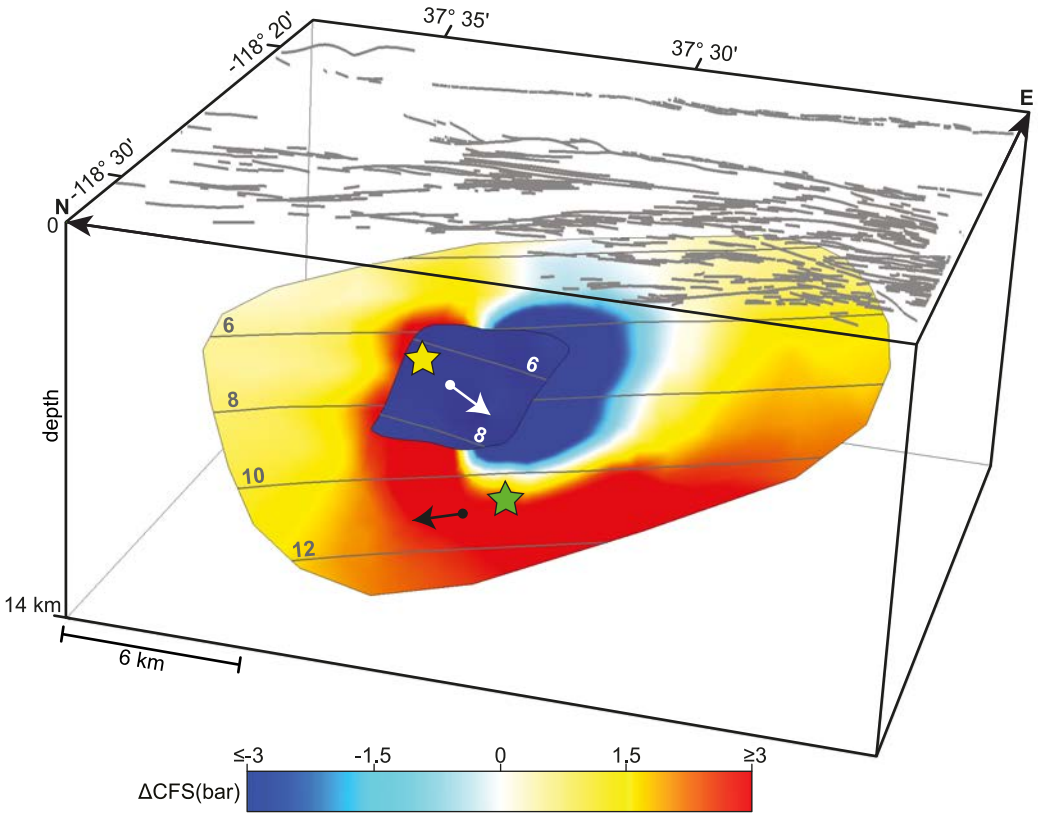

Figure 1.6. Cumulative ΔCFS on the Chalfant Valley main fault, due to all previous events in the region, including the foreshock. Yellow star shows the location of the July 20th, 1986, foreshock, and green star shows the location of the July 21st, 1986, main shock. Even though the foreshock partly unloaded the main fault segment, it contributed to increasing stress in the lowermost part of the main fault where the main shock nucleated just one day later. Arrows indicate slip direction of hanging wall.

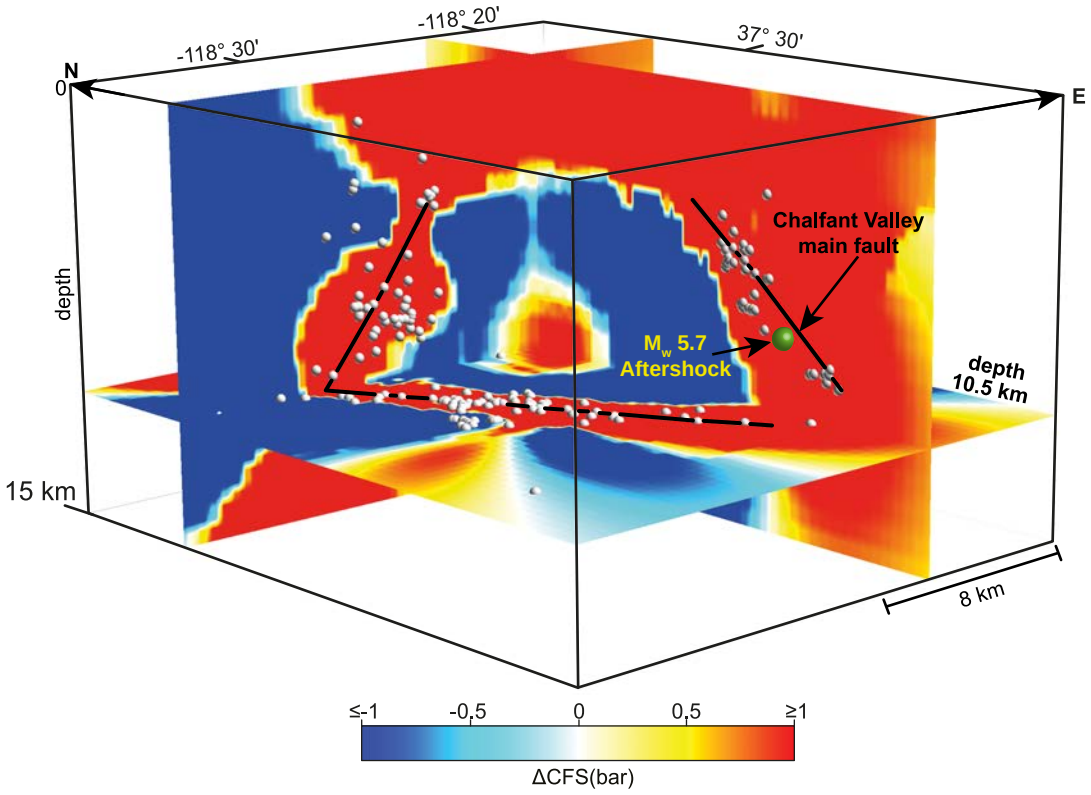

Figure 1.7. Coseismic ΔCFS from the 1986 Chalfant Valley main shock calculated on optimally-oriented faults, shown as slices through a ΔCFS volume. White spheres are aftershocks that occurred within 1 km of each slice in the 10 days between the main shock and the first strong aftershock (ML 5.8). 81% of all aftershocks occurred in areas of ΔCFS increase.

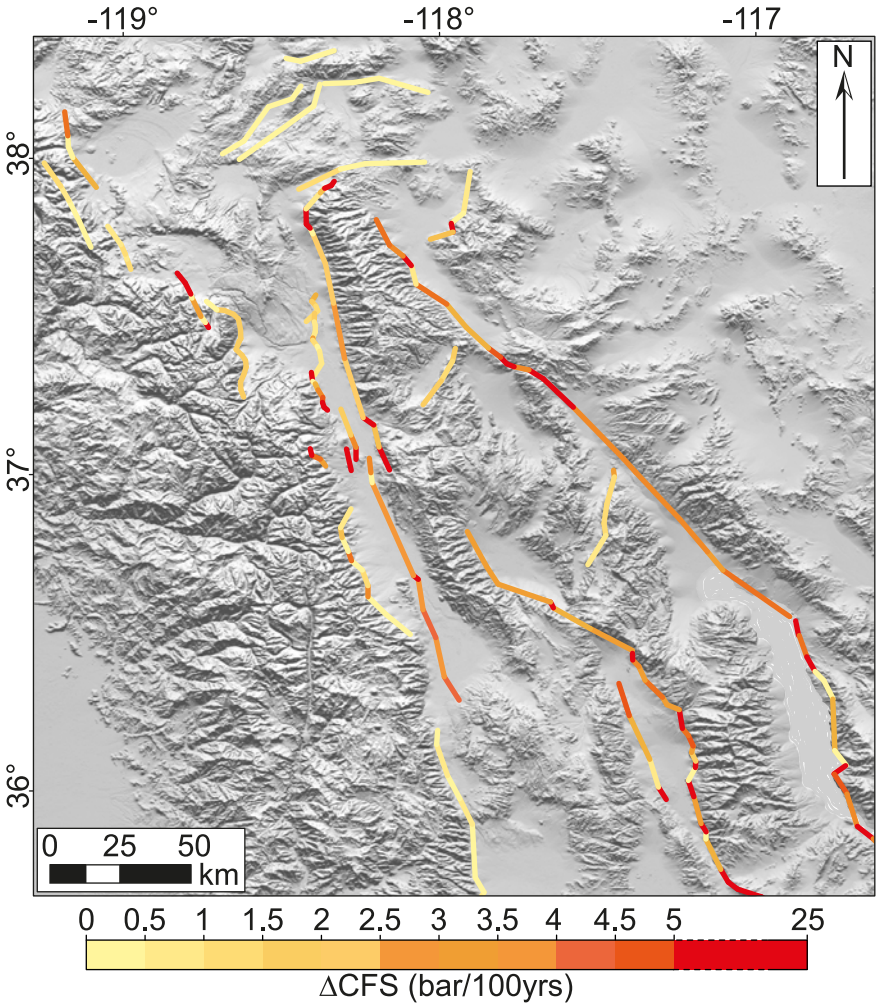

Figure 1.8. Interseismic ΔCFS due to 100 years of tectonic loading calculated with the back-slip method [*Savage*, 1983] on the orientation and kinematic of every modeled fault.

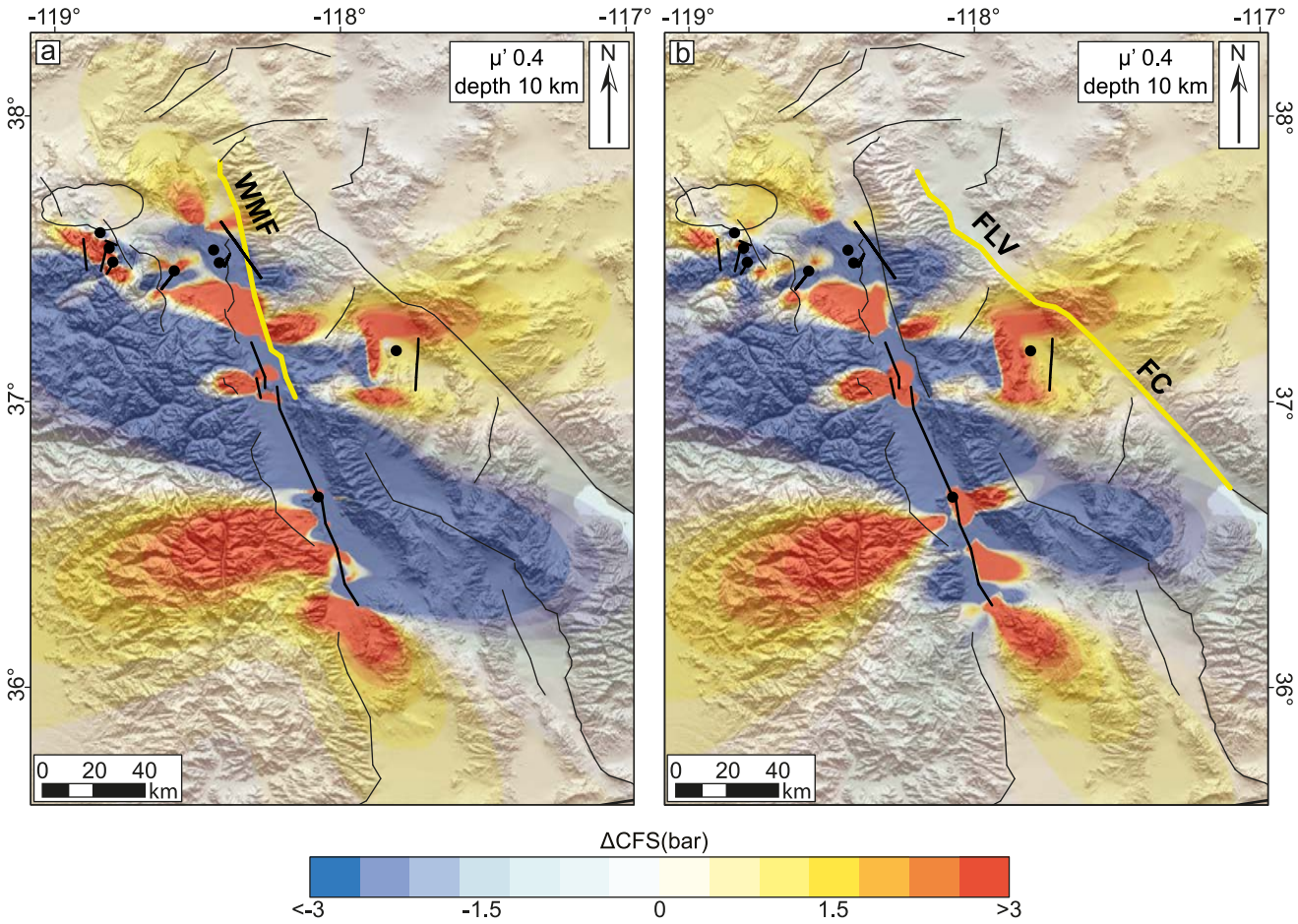

Figure 1.9. 142 years of cumulative ΔCFS from all the studied events combined, calculated (a) on the fault kinematic of the White Mountains fault (WMF) and (b) on the fault kinematic of the Fish Lake Valley-Furnace Creek fault (FLV-FC). Thick black lines are the surface traces (or surface projections) of source faults with corresponding earthquake epicenters (black dots), thick yellow lines are the receiver faults. Both receiver faults show significant areas of stress loading, exceeding 2 bars.

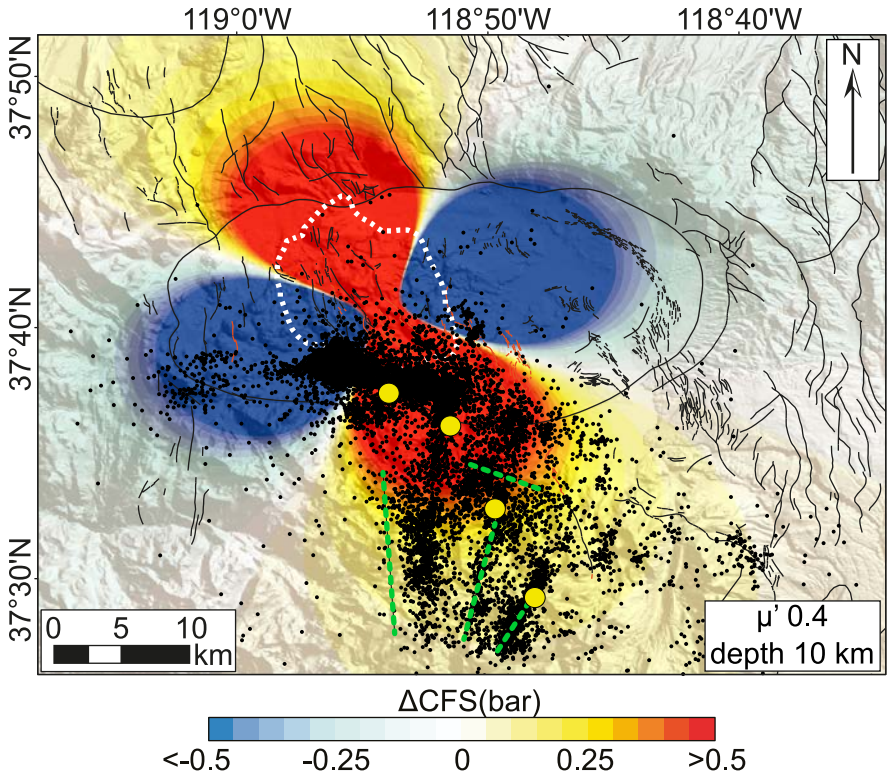

Figure 1.10. Coseismic ΔCFS calculated on an average orientation and kinematic of faults (dashed green lines) south of the Long Valley caldera due to 1978 Long Valley caldera inflation. 1980-1983 seismicity [*Prejean et al.*, 2002] shown as black dots. Yellow circles indicate the location of the three 1980, M ~ 6 earthquakes. Dashed white line is the perimeter of the resurgent dome.

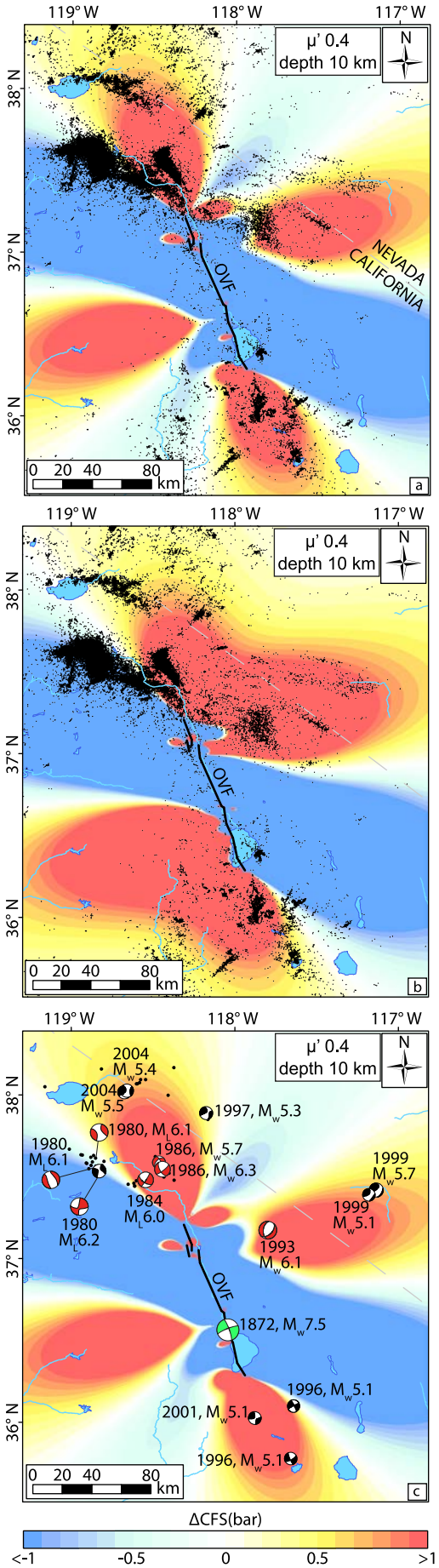

Figure 1.11. 108 years of cumulative ΔCFS due to the 1872 Owens Valley earthquake calculated on (a, c) optimal strike-slip and (b) optimal normal faults. Black dots in (a) and (b) represent the relocated 1984 - 2011 seismicity [*Waldahuser and Schaff*, 2008]. (c) shows the fault plane solutions of earthquakes with M ≥ 5 (from 1992 to 2014, NCEDC catalog, black; from 1980 to 1993, CDMG catalog, red), of the 1872 Owens Valley earthquake (CDMG, green), and the location of additional M ≥ 5 events in 1980 - 2014 for which no fault plane solution is available (small black circles). OVF = Owens Valley Fault.

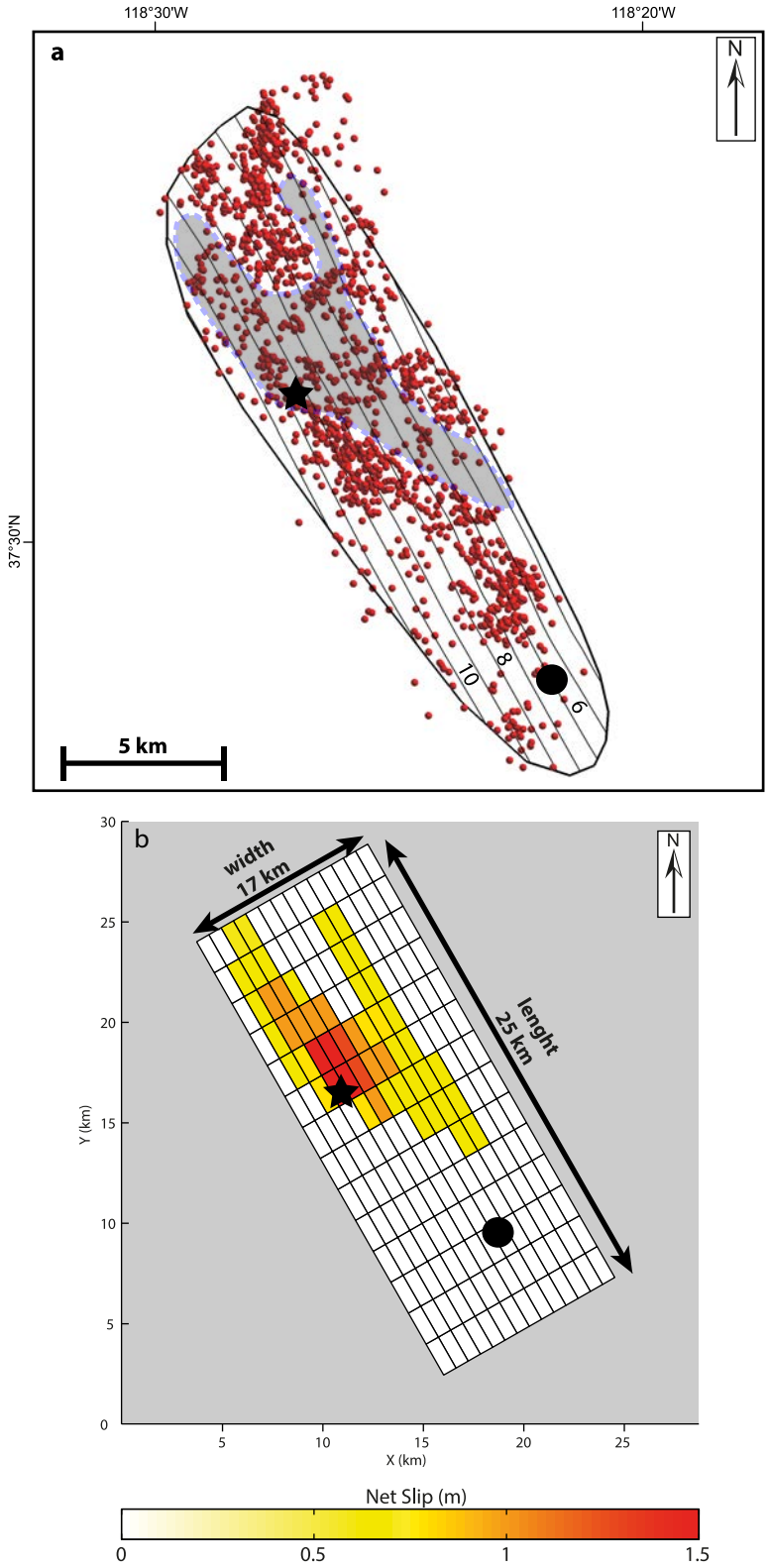

Figure 1.12. Slip distribution on the Chalfant Valley main fault inferred from aftershock pattern. (a) Aftershocks located within 500 m of each side of the fault, in the time interval between the main shock (black star) and the first large aftershock (black circle), and slip patch (grey). Contours on the fault are in km b.s.l. (b) Slip distribution based on aftershocks density and earthquake magnitude. Yellow star shows the location of the July 21th main shock. Earthquake data are from *Waldahuser and Schaff* [2008].

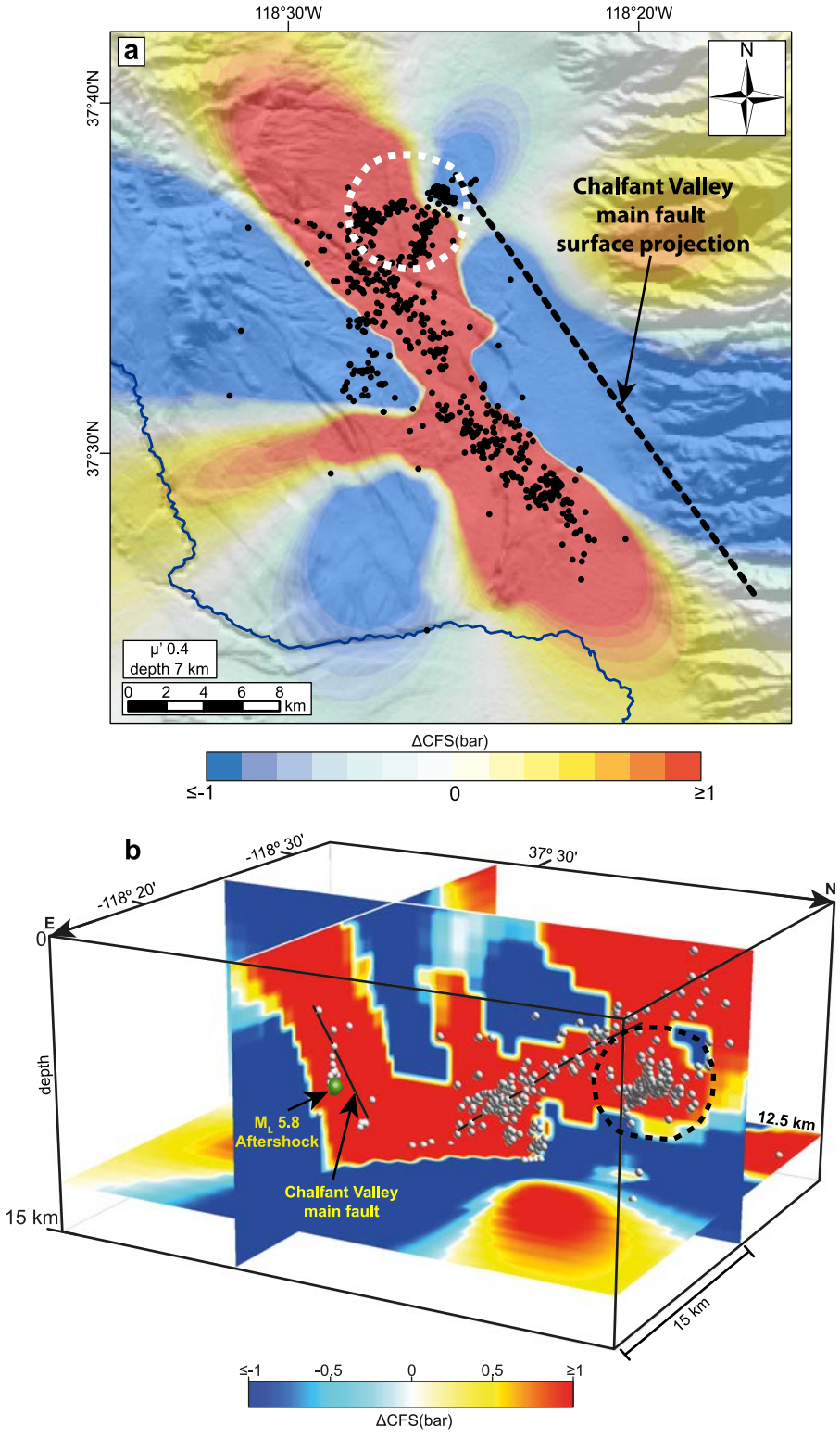

Figure 1.13. Coseismic ΔCFS from the 1986 Chalfant Valley main shock calculated on optimally-oriented faults, (a) map view, (b) slices through the ΔCFS volume. Black dots in (a) are the aftershocks that occurred in the time between the main shock and the first strong aftershock (10 days) at depth between 6.5 and 7.5 km. Spheres in (b) are aftershocks that occurred within 1 km of each slice shown, in the time between the main shock and the first strong aftershock (10 days). White (a) and black (b) dashed-line circles highlight the off-fault aftershocks. Earthquake hypcenter locations are from *Waldhauser and Schaff* [2008].

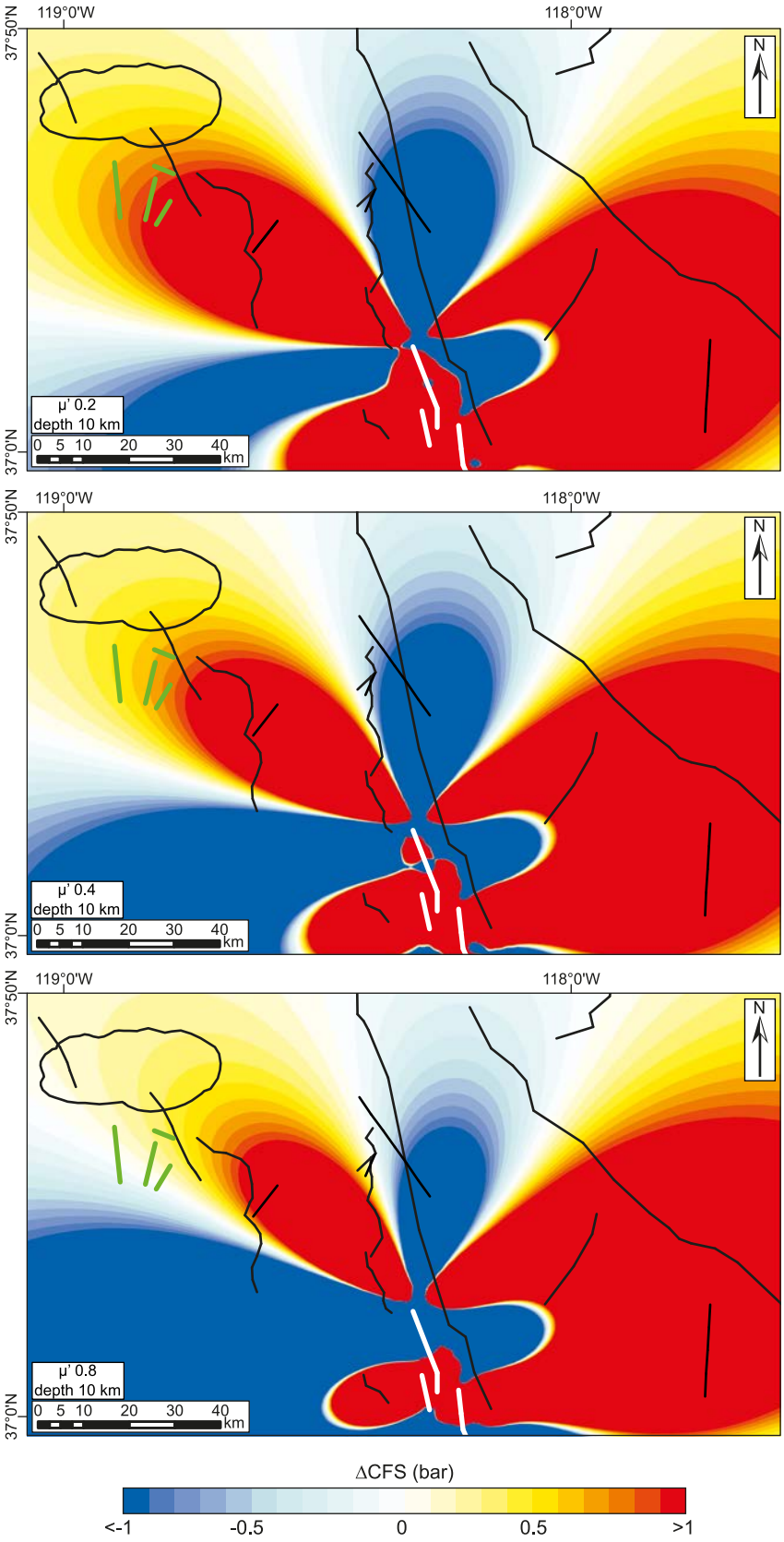

Figure 1.14. Coseismic ΔCFS calculated on the Long Valley caldera faults (green lines), due to the 1872 Owens Valley earthquake (white lines), for three different effective friction coefficients (μ').

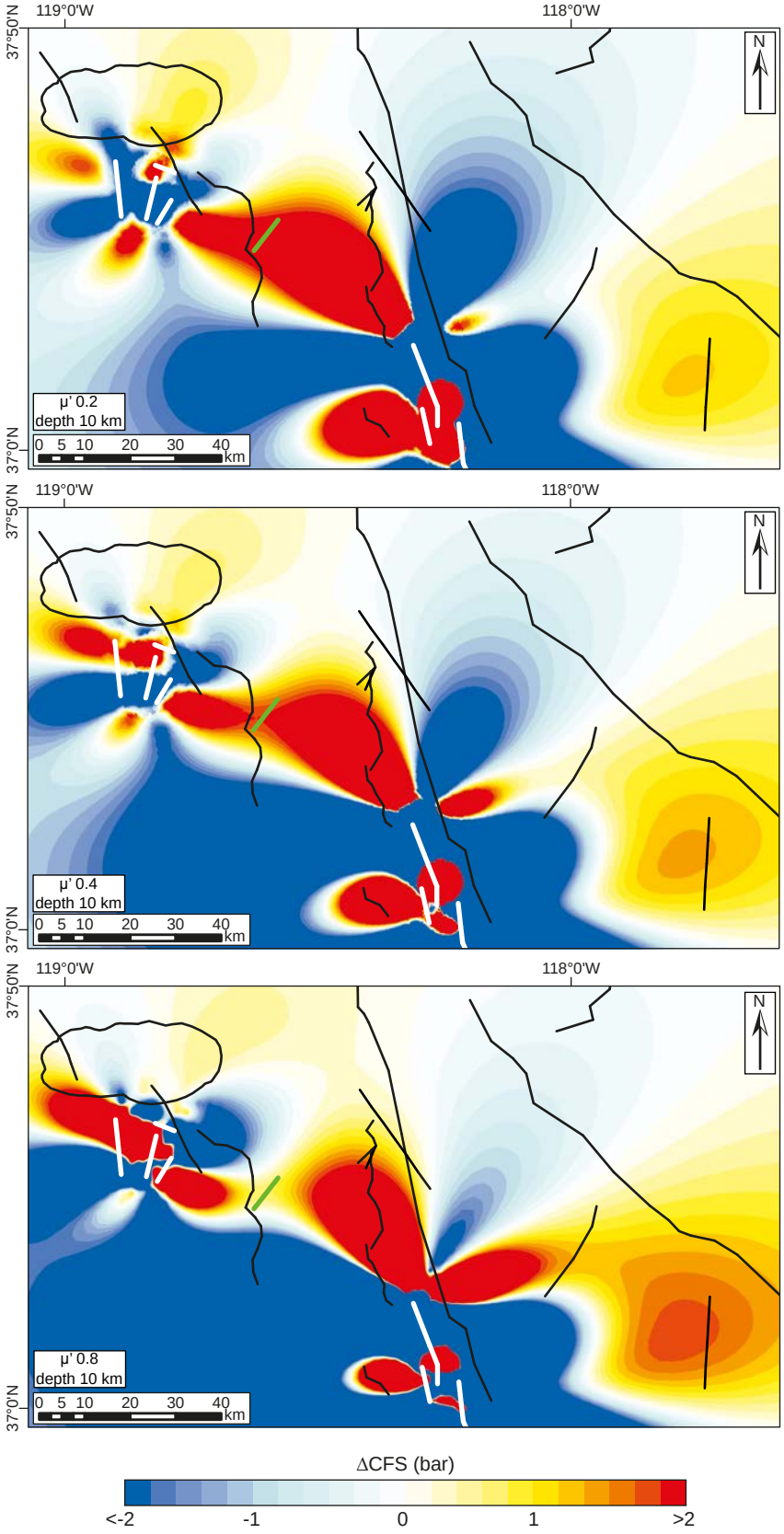

Figure 1.15. Coseismic ΔCFS calculated on the 1984 Round Valley fault (green line), due to all the preceding events (white lines), for three different effective friction coefficients (μ').

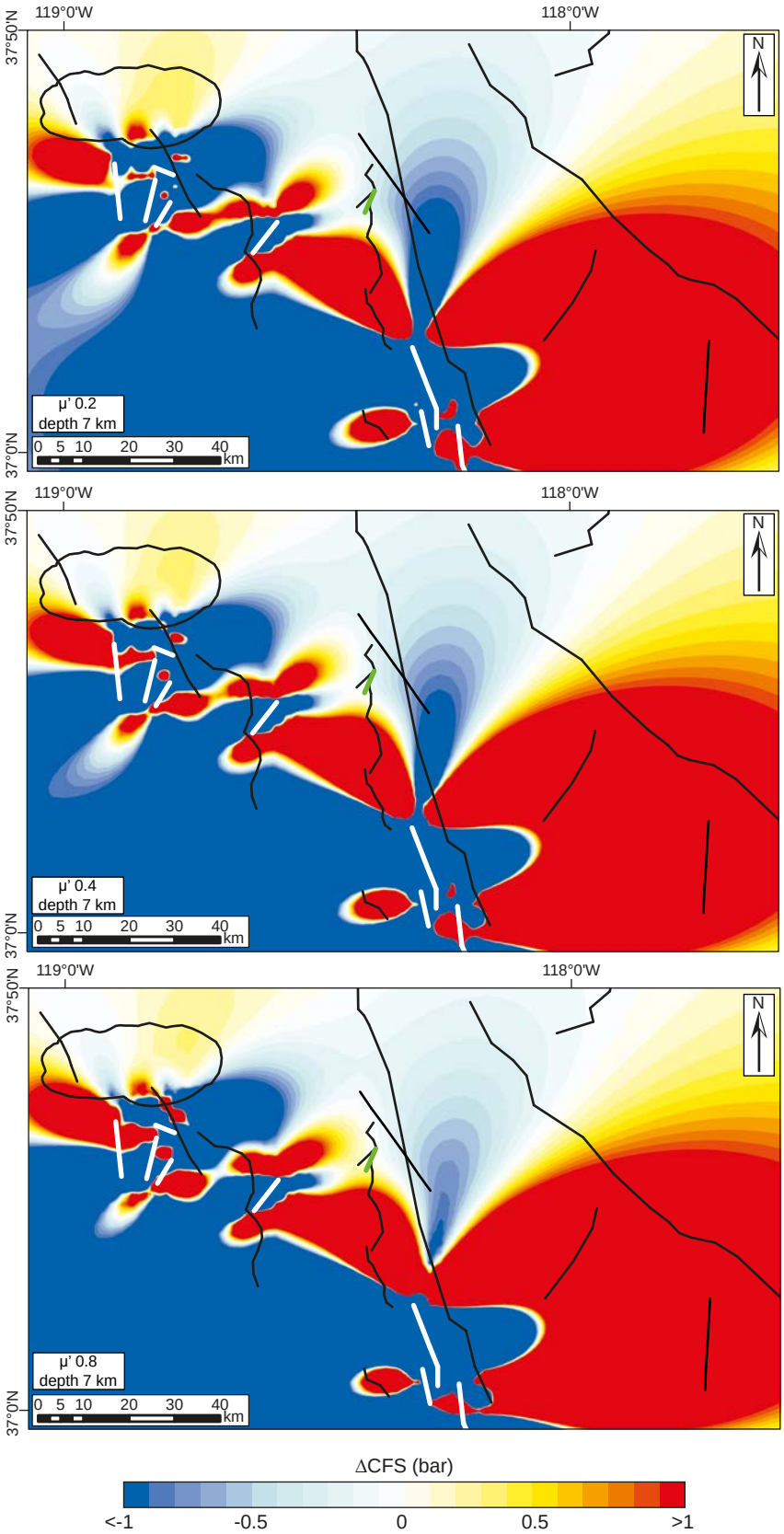

Figure 1.16. Coseismic ΔCFS calculated on the Chalfant Valley foreshock fault (green line) due to all the preceding events (white lines), for three different effective friction coefficients (μ').

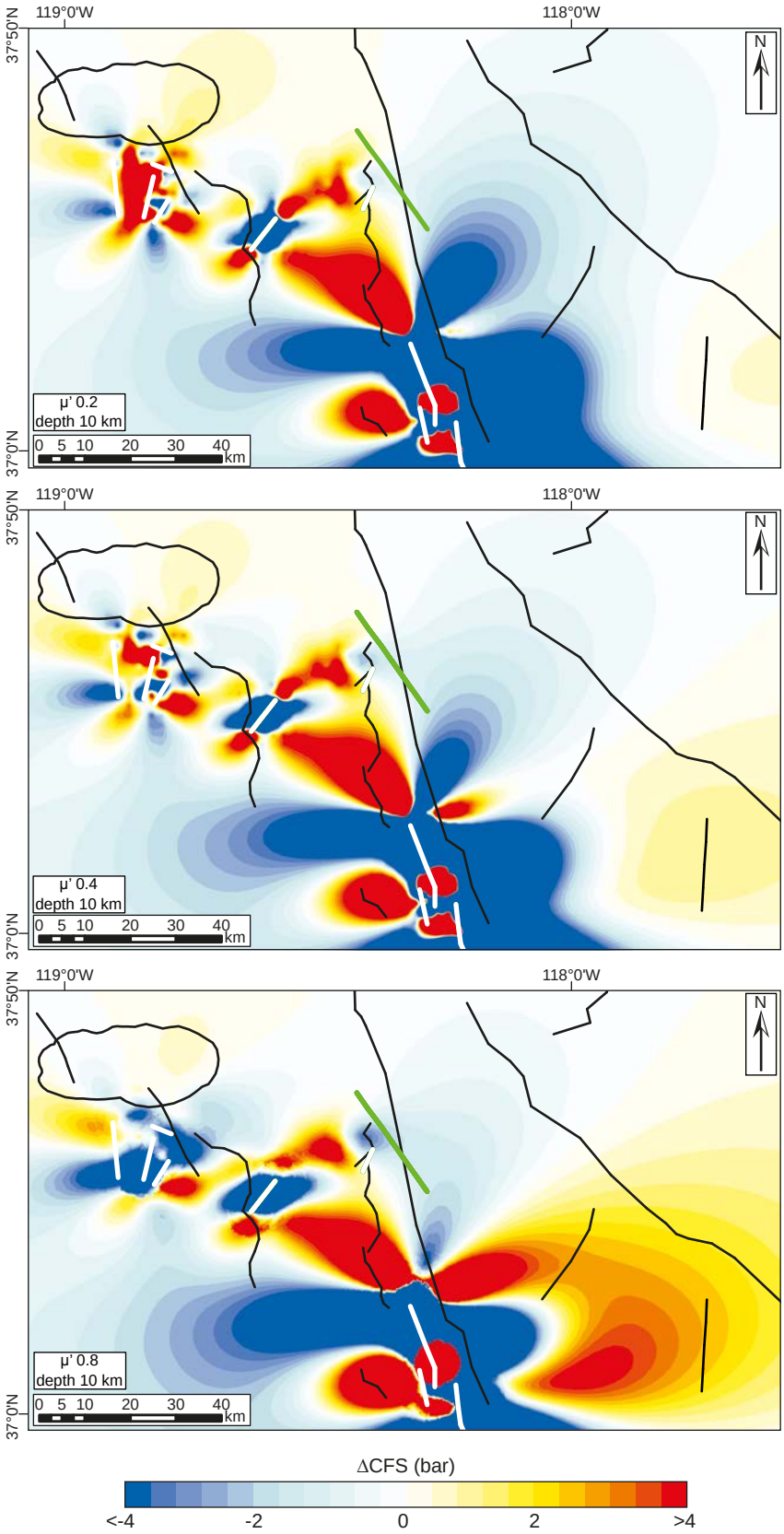

Figure 1.17. Coseismic ΔCFS calculated on the Chalfant Valley main shock fault (green line), due to all the preceding events (white lines), calculated for three different effective friction coefficients (μ').

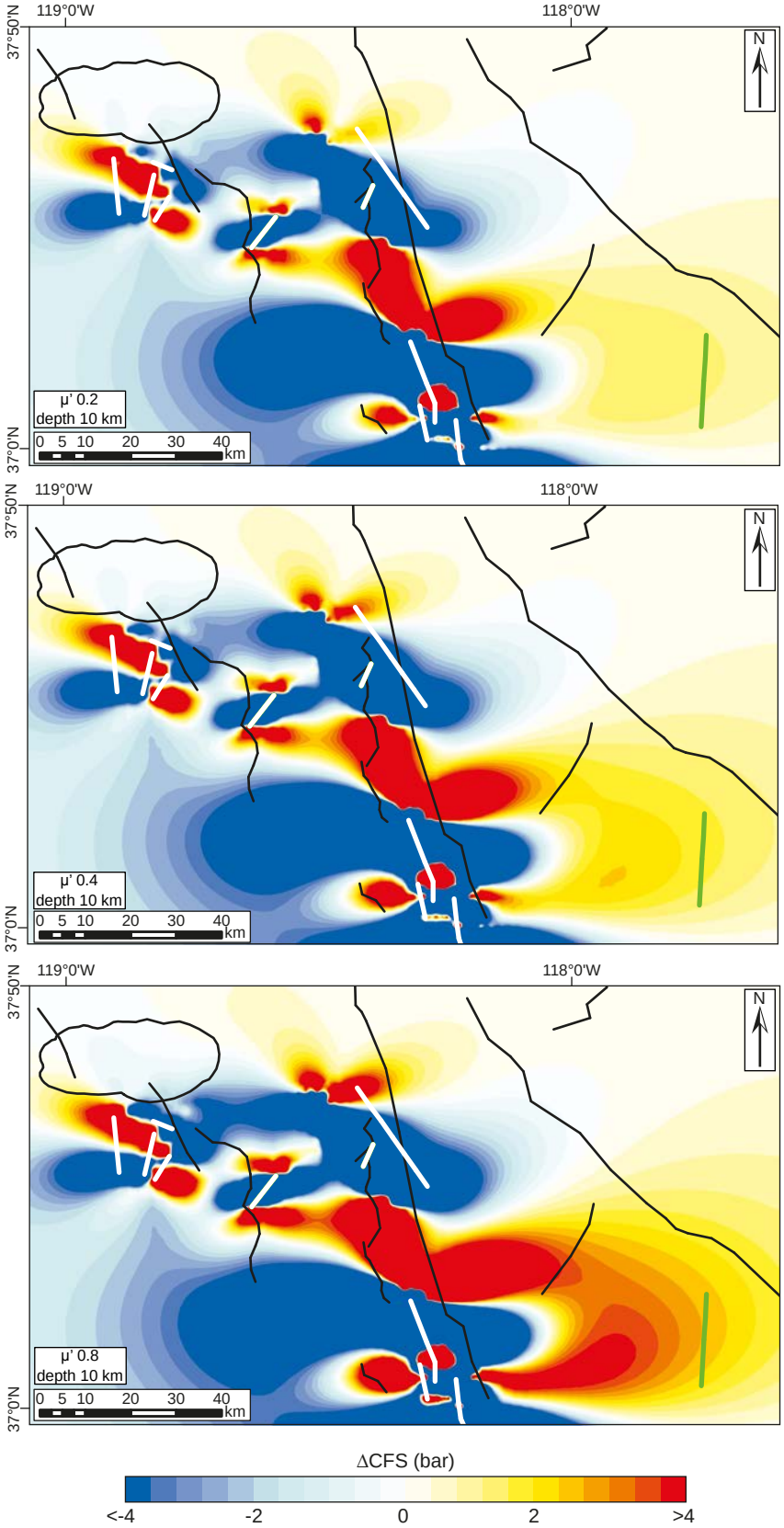

Figure 1.18. Coseismic ΔCFS calculated on the Eureka Valley fault (green line), due to all the preceding events (white lines), calculated for three different effective friction coefficients (μ').

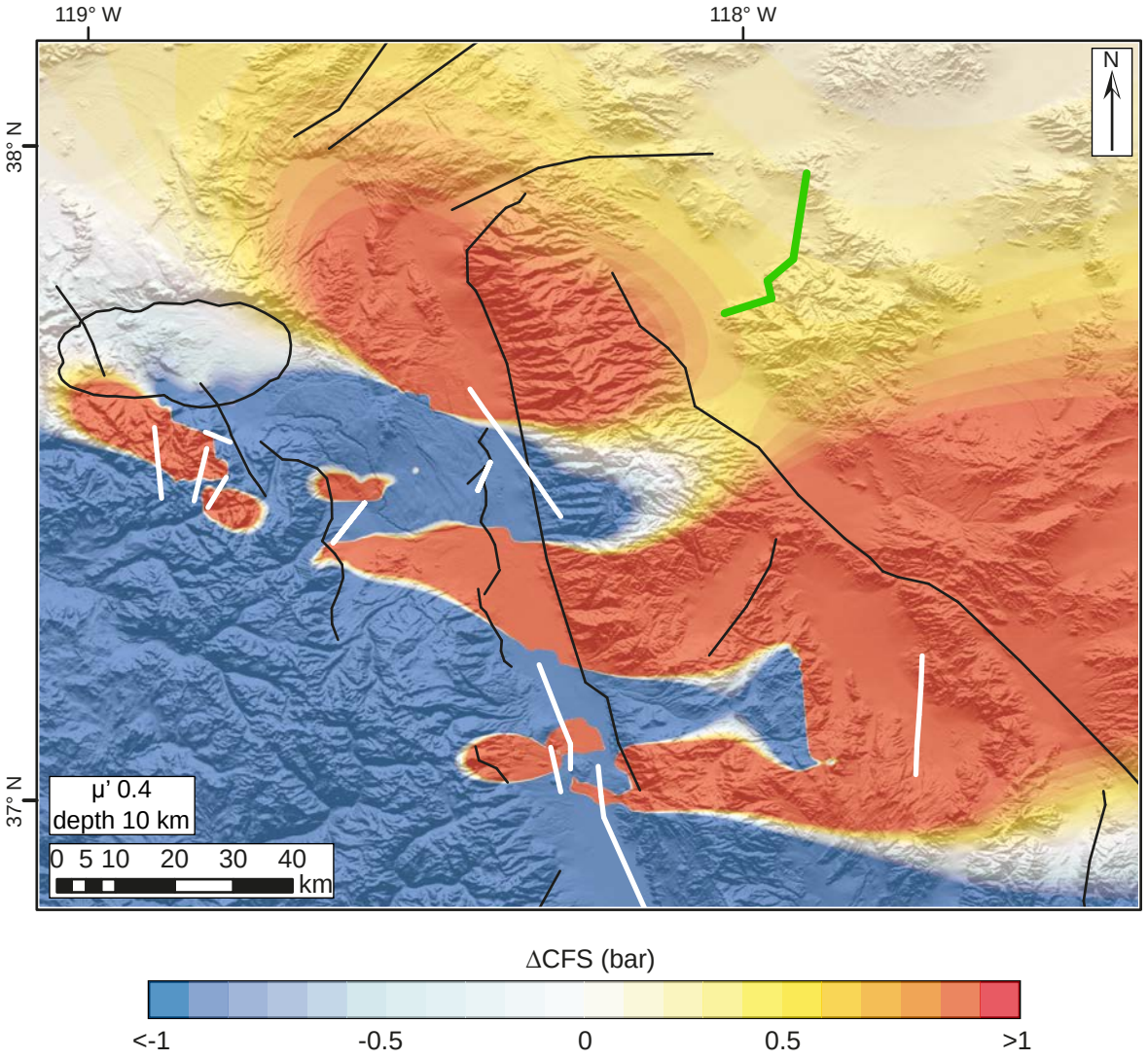

Figure 1.19. 142 years of cumulative ΔCFS from all the studied events combined, calculated on the Emigrant Peak fault (green line). Thick white lines are the surface traces (or surface projections, for blind faults) of source faults.

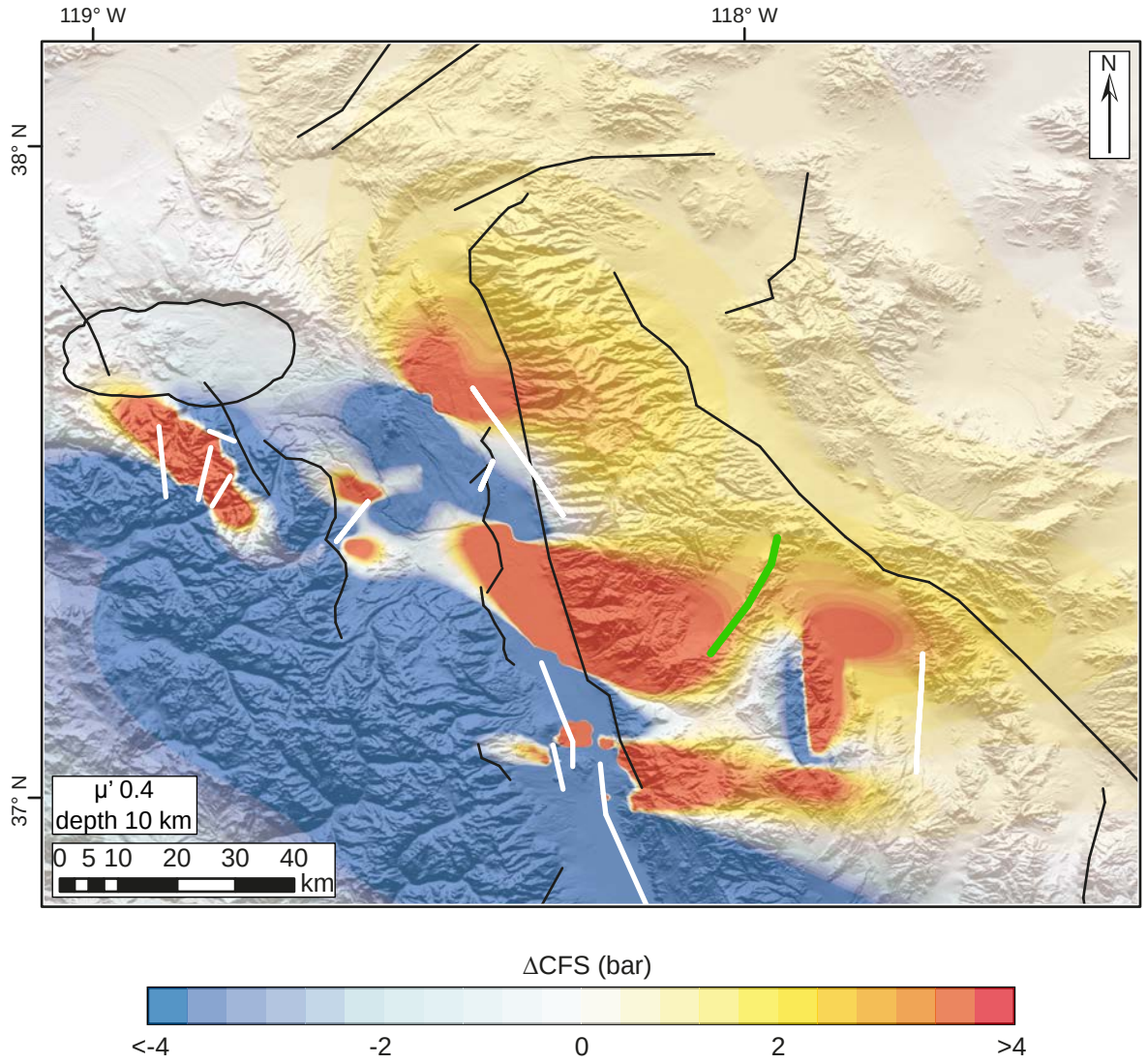

Figure 1.20. 142 years of cumulative ΔCFS from all the studied events combined, calculated on the Deep Springs fault (green line). Thick white lines are the surface traces (or surface projections, for blind faults) of source faults.

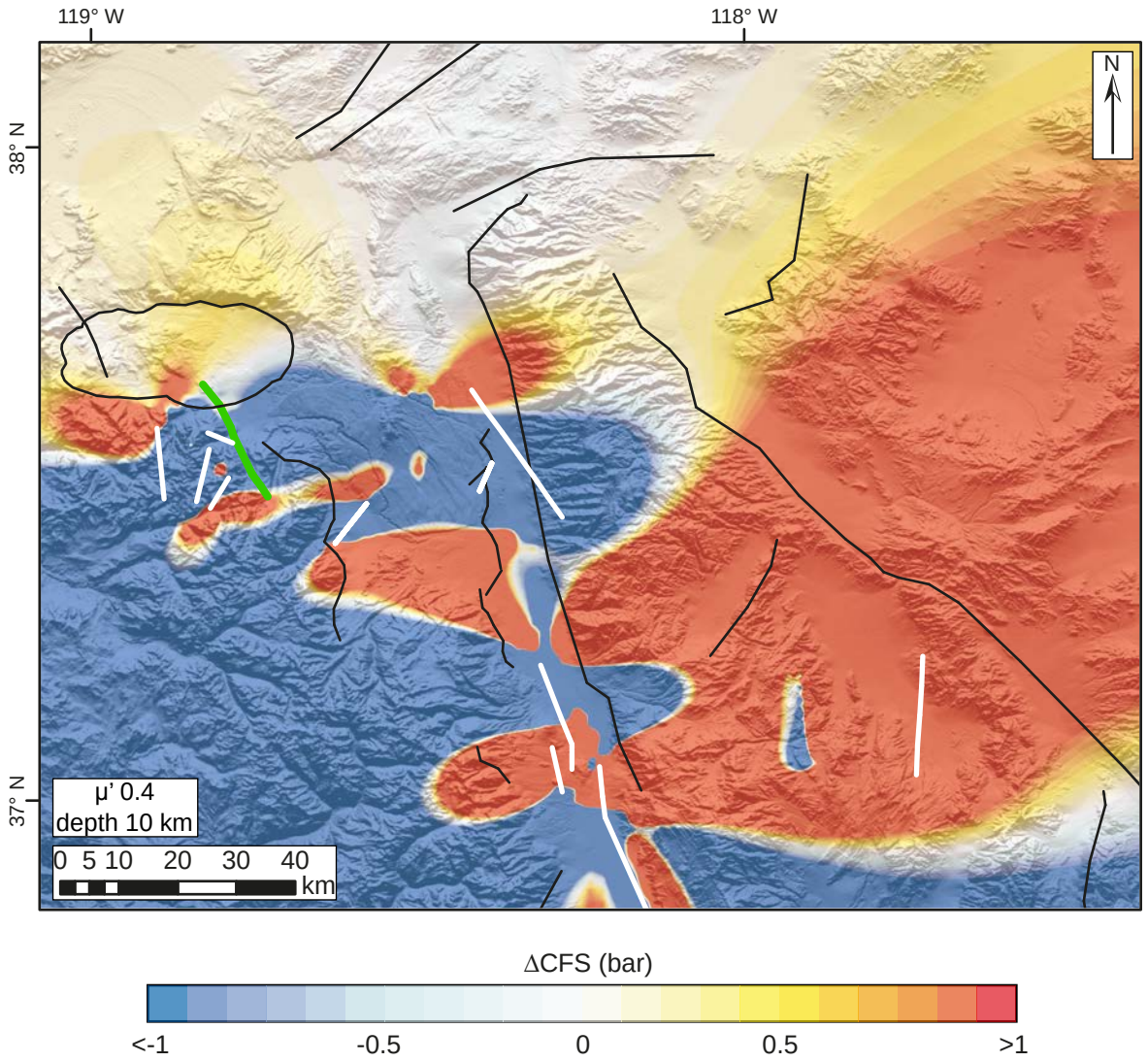

Figure 1.21. 142 years of cumulative ΔCFS from all the studied events combined, calculated on the Hilton Creek fault (green line). Thick white lines are the surface traces (or surface projections, for blind faults) of source faults.

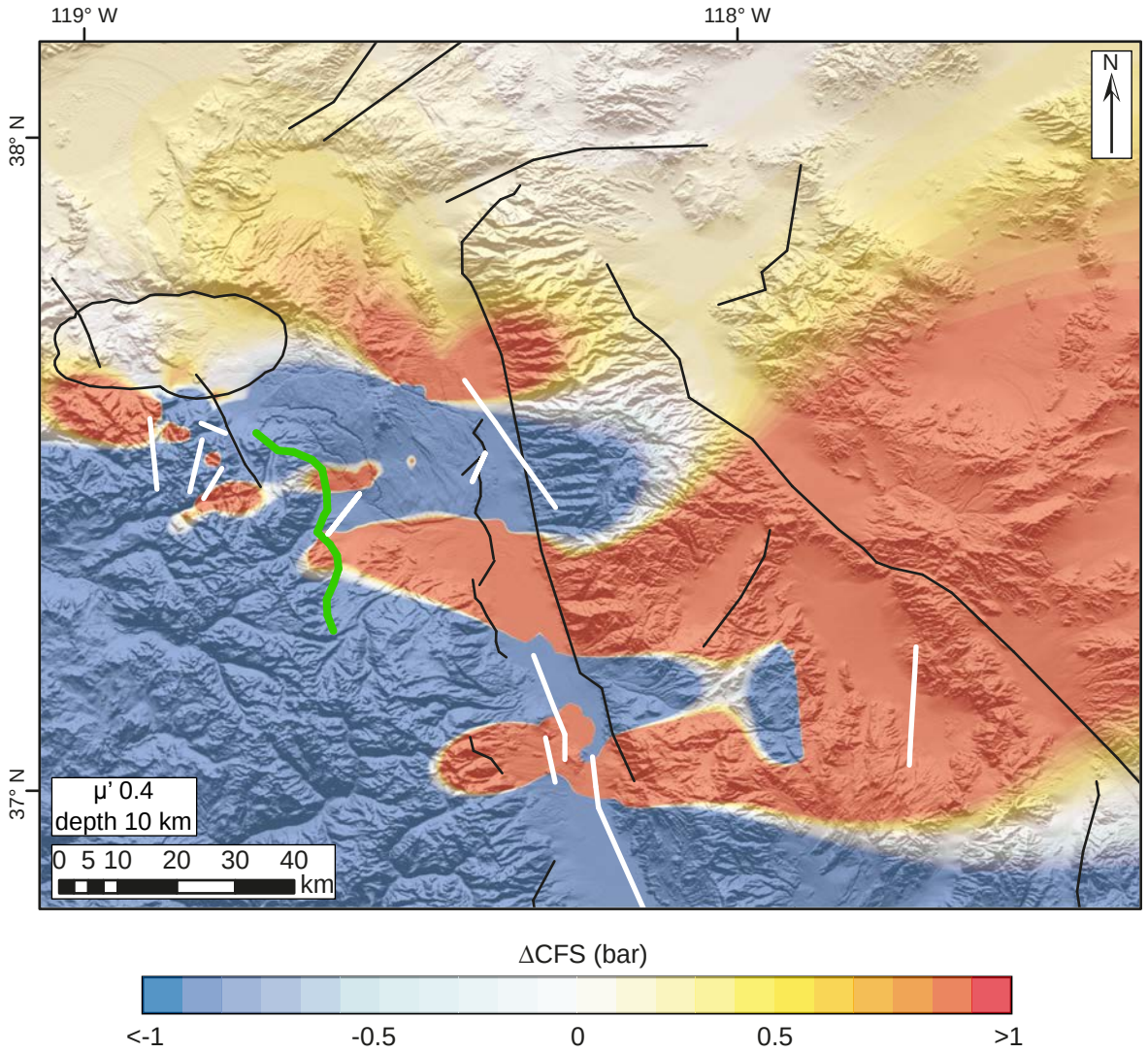

Figure 1.22. 142 years of cumulative ΔCFS from all the studied events combined, calculated on the Round Valley fault (green line). Thick white lines are the surface traces (or surface projections, for blind faults) of source faults.

Chapter 2

Coulomb stress evolution in a diffuse plate boundary: 1400 years of earthquakes in eastern California and western Nevada, USA.*

2.1 Abstract

Diffuse plate boundaries are characterized by deformation distributed over a wide area in a complex network of active faults, and by relatively low strain rates. These characteristics make it difficult to understand the spatial and temporal distribution of seismicity. The area east of the Sierra Nevada, between longitudes 121° W and 116° W, is part of a diffuse plate boundary. At least seventeen major surface-rupturing earthquakes have happened here in the last 1400 years. Our purpose is to determine whether these events influence each other, or whether they are randomly distributed in time and space. We model the evolution of coseismic and postseismic Coulomb failure stresses (ΔCFS) produced by these earthquakes, and we also model interseismic stresses on the entire fault network. Our results show that 80% of the earthquake ruptures are located in areas of combined coseismic and postseismic ΔCFS $\geq$ 0.2 bar. This relationship is robust, as shown by the control tests that we carried out using random earthquake sequences. We also show that the Fish Lake Valley, Pyramid Lake, and Honey Lake faults have accumulated 45, 37 and 27 bars respectively of total ΔCFS (i.e. coseismic + postseismic + interseismic) in the last 1400 years. Such values are

*Published Paper: Verdecchia A. and S. Carena (2016), Coulomb stress evolution in a diffuse plate boundary: 1400 years of earthquakes in eastern California and western Nevada, USA, *Tectonics*, .**35**, doi:10.1002/2015TC004091.

comparable to the average stress drop in a major earthquake, and these three faults may be therefore close to failure.

2.2 Introduction

Most plate boundaries are characterized by high deformation rates localized along a narrow fault zone, where major earthquakes ($M_w \geq 7$) tend to occur periodically at expected locations on a major plate boundary fault (e.g. San Andreas fault, North Anatolian fault, megathrusts in subduction zones) [*Stein and Liu*, 2009]. In diffuse plate boundaries, deformation is distributed across wider regions, and accommodated by several fault systems with variable slip rates [*Thatcher*, 1995; *Bennett et al.*, 2003]. As a consequence, earthquakes in diffuse plate boundaries occur in spatially and temporally complex patterns.

A good example of a diffuse plate boundary is the region east of the Sierra Nevada that encompasses the Eastern California Shear Zone (ECSZ), the Walker Lane, which are located in the westernmost part of the Basin and Range province (Figure 2.1). Here at least one-fifth of the ~ 50 mm/yr of right-lateral transform motion between Pacific and North America plates is accommodated along a northwest trending zone characterized by a combination of right-lateral strike-slip faults and normal faults [*Bennett et al.*, 2003; *DeMets et al.*, 2010; *Wesnousky et al*., 2012]. In this study we focus on the area north of the Garlock fault and east of the Sierra Nevada, which includes the ECSZ, the Walker Lane, and the Central Nevada Seismic Belt (CNSB), all located within the western Basin and Range Province (Figure 2.1 and 2.2). Six major earthquakes ($M_w \geq 7$) have occurred in this region in historical times, and at least another eleven surface-rupturing events that occurred in the last 1400 years have been recognized by paleoseismological studies (Figure 2.2).

Several authors showed that large earthquakes in this region interact in terms of Coulomb stress. *Hodgkinson et al.* [1996] and *Caskey and Wesnousky* [1997] found that each event in the 1954 Rainbow Mountain-Fairview Peak-Dixie Valley earthquake sequence precipitated the next one by positive coseismic static stress changes. *McAuliffe et al.* [2013] noted the similarity in ages between the most recent events on the Garlock and Panamint Valley faults, and proposed Coulomb stress interaction between these two faults as a reason. *Verdecchia and Carena* [2015] found that the 1872 M_w 7.5 Owens Valley earthquake strongly influenced the distribution of subsequent seismicity in the northern ECSZ.

All these previous studies however are restricted either to earthquakes that are part of the same spatio-temporal seismic cluster [*Hodgkinson et al.*, 1996; *Caskey and Wesnousky*, 1997], or to short periods of time (0 to 150 years) [*McAuliffe et al.*, 2013; *Verdecchia and Carena*, 2015]. The limited time range of recorded historical events makes the reconstruction and the interpretation of the evolution of seismicity patterns in the region challenging. In fact, no regional migration patterns have so far been recognized [*Wallace*, 1987], but no systematic study based on modeling the evolution of Coulomb stress changes due to major earthquakes in the region has been conducted either.

In order to address these issues, we model the coseismic and postseismic Coulomb failure stress changes (ΔCFS) due to seventeen ground-rupturing earthquakes in the last 1400 years. We also carry out tests to verify whether the results of our models are better than a random distribution. As a last step, in order to identify likely future sources of major earthquakes, we calculate the total (coseismic + postseismic + interseismic) Coulomb failure stress (ΔCFS_{tot}) accumulated by major faults that produced no large events in the last 1400 years. We show that the distribution of

earthquakes throughout the entire region is in fact not random, but rather earthquakes tend to occur in areas of positive cumulative (coseismic + postseismic) Coulomb stress (ΔCFS_{cum}).

2.3 Earthquakes and faults

We analyze earthquake interactions in this region over the past 1400 years because, unlike the San Andreas fault, where high deformation rates suggest recurrence intervals for large earthquakes of 100 to 300 years [*Field et al.*, 2013], most major faults in our study region rupture at intervals ≥ 1000 years [*Dixon et al.*, 2003; *Koheler and Wesnousky*, 2011].

Due to the fact that earthquakes recognized by paleoseismological methods are ground-rupturing, and therefore start at about M_w = 7, we do not consider events smaller than M_w = 6.5. Smaller events have anyway a limited effect in terms of areal extent and magnitude of stress changes.

In the next sections we present the data used to model the faults responsible for all the earthquakes used in this study. We consider only the most recent event for each fault except for the Fish Lake Valley Fault. For the latter we model also the penultimate event because these two events occurred on two separate segments of the fault. Each named earthquake below is accompanied by the acronym of its source fault to facilitate identification in the figures and tables.

2.3.1 Historical and instrumental earthquakes (1872 A.D. to present) and their source faults

The 1872 M_w 7.5 Owens Valley earthquake (OVF) [*Beanland and Clark*, 1994] and the 1915 M_w 7.5 Pleasant Valley earthquake (PSF) [*Wallace*, 1984a] are the two

oldest major historical events in the region. They also mark the southern and northern limit of a ~500 km long right-lateral transtensional zone where several major ground-rupturing earthquakes happened in the last 150 years (Figure 2.2).

The 1872 Owens Valley earthquake (OVF) created a ~110 km long rupture with right-lateral displacements up to 7 m [*Beanland and Clark*, 1994; *Haddon et al.*, 2016], whereas the 1915 Pleasant Valley earthquake (PSF) was a normal-slip event with little strike-slip motion forming coseismic fault scarps up to 5.8 m high [*Wallace*, 1984a]. The latter was followed 17 years later by the 1932 M_w 7.2 Cedar Mountain earthquake (CMF) (Figure 2.2), characterized by a complex pattern of right-lateral surface ruptures along a ~60 km long NNW-SSE striking zone [*Bell et al.*, 1999]. Finally, between July 6th and December 12th 1954, five M_w 6.4 to 7.2 events occurred in the Central Nevada Seismic Belt (CNSB). The first three events produced several right-lateral transtensional ruptures, forming a 70-km-long fault zone that includes the Rainbow Mountain Fault (RMF) and other previously unmapped structures [*Bell et al.*, 2004; *Caskey et al*., 2004]. Four months after the third event, the sequence moved to the east where a M_w 7.2 earthquake ruptured the ~35 km long Fairview Peak Fault (FPF) and other smaller structures, producing right-lateral offsets up to 2.9 m and fault scarps up to 3.8 m high [*Caskey et al*., 1996]. This was followed within a few minutes by the M_w 7.1 Dixie Valley earthquake (DVF), with maximum normal offsets of 2.8 m along a 42 km long fault rupture [*Caskey et al.*, 1996]. The 1954 Dixie Valley earthquake (DVF) is the last major event in the region of interest to date.

2.3.2 Paleoseismological earthquakes (587 A.D.-1715 A.D.) and their source faults

We collected data from several studies in order to define the age and the faults responsible for paleoseismological events that occurred in our study region in the last 1400 years (a detailed description of the data and the relevant references can be found in the appendix, section 2.8). The exact date of occurrence of each modeled earthquake is needed for the postseismic ΔCFS calculations. An exact date is of course not available for paleoearthquakes, which are characterized by large uncertainties. In such cases we take the mean value in the age range for the event and then subtract this value from the A.D. 1950 baseline. For the most recent event on the Antelope Valley fault, for example, we calculated the average (1363 years) within the 2σ uncertainty in the radiocarbon age (1312 and 1414 years B.P) for the most recent event identified by *Sarmiento et al.* [2011]. Then we subtracted this calculated value from the A.D. 1950 baseline, resulting in an absolute age of A.D. 587. In this way we can have a reasonable "year of occurrence" to use as input for stress calculations. Because most paleoearthquakes have a fairly large age uncertainty, we also had to verify how this might change our result. This is addressed in section 2.6.1. All modeled earthquakes with absolute year of occurrence, magnitude and fault kinematics are listed in Table 2.1.

2.3.3 Fault Slip Rates

Slip rate values are needed in order to calculate the interseismic ΔCFS (tectonic loading). A single fault however may have been assigned multiple slip rates by different authors. In particular, values derived from geodesy are often different from those derived from geology for the same fault. A justification for the selection of slip rates used in our models is therefore needed.

First of all, geologically and geodetically derived slip rates apply to different time scales: geologic rates are usually applicable to periods of 10^3-10^6 years, whereas geodetic rates are short-term (0-20 years). Geologic slip rates, in addition, may be strongly timescale-dependent. In the Basin and Range province this has been documented, for example, on the Wassuk Range fault [*Surpless and Kroeger*, 2015], for which variations in vertical displacement rate were documented across six temporal orders of magnitude, and on the Wasatch fault, where different rates are observed at 10^3, 10^5 and 10^6 time scales [*Friedrich et al.*, 2003]. Given that our period of interest is 1400 years, we use Holocene or Late Pleistocene geologic slip rates (10^3-10^4 years) to calculate the interseismic ΔCFS accumulated by the main active faults. Table 2.5 shows the slip rate values and their references used to model interseismic ΔCFS. The majority of these data were estimated from dated Quaternary landforms (alluvial fan, terrace surfaces, stream channels, etc.) that has been offset by the studied fault (Table 2.5). For a small number of faults, slip rate values were calculated based on the recognition of two or more paleoevents (Table 2.5). Slip rates values of several normal faults of the Basin and Range Province are based on an empirical relationship between vertical slip and maximum basal facet height developed by *dePolo* (1998). Finally for these faults for which no data are available, we use the geologic slip rates adopted for the construction of the United States National Seismic Hazard Maps [*Petersen et al.*, 2014].

Because only one slip rate value for each fault is needed to model interseismic ΔCFS, the numbers listed in Table 2.5 represent a mean in the uncertainties range of the slip rate values available for the modeled faults.

2.4 Methods

2.4.1 Modeling Coulomb failure stress changes

Earthquake interactions have been widely explored since the 1980's using the concept of Coulomb stress changes [e.g., *King et al.*, 1994; *Stein et al.*, 1994, 1997; *Harris and Simpson*, 1998; *Stein*, 1999; *Parsons et al.*, 2000; *Marsan*, 2003; *Ma et al.*, 2005; *Toda et al.*, 2008].

The change in Coulomb failure stress (ΔCFS) caused by an earthquake is:

$$\Delta CFS = \Delta\tau - \mu'(\Delta\sigma_n) \qquad [2.1]$$

Where $\Delta\tau$ is the change in shear stress calculated on the orientation and kinematics of either optimally oriented faults, or of specified faults, μ' is the coefficient of effective friction, and $\Delta\sigma_n$ is the change in normal stress. A receiver fault located in an area of positive ΔCFS will be brought closer to failure, whereas failure will be delayed on a fault located in an area of negative ΔCFS. Coulomb stress changes due to earthquakes can be static (coseismic), quasi-static (postseismic) or dynamic [*Freed* , 2005]. The latter represent a transient effect due to seismic waves propagation, and are believed to trigger seismicity only over a time period of days to months [*Freed*, 2005]. Because here we operate on a time span of 1400 years, we consider only static (time-independent) and quasi-static (time-dependent) stress changes.

Coseismic stress changes are most useful to correlate events relatively close in time (0 to 10 years). When two events are widely separated in time instead the postseismic effects due to relaxation of stresses in the lower crust and upper mantle can play an important role in the time-dependent redistribution of Coulomb stress, and therefore may become the dominant process at the time scale considered in this work (1400 years) [e.g. *Chéry et al*., 2001; *Pollitz et al.*, 2003; *Lorenzo-Martín et al*., 2006; *Ali et al*., 2008; *Shan et al.*, 2013; *Verdecchia and Carena*, 2015]. The interseismic ΔCFS for all faults of interest also needs to be determined. This is especially important in our case, because at the time scale considered most of the faults show at least some tectonic loading, which in a few cases may be comparable to the postseismic ΔCFS.

The input parameters necessary for all ΔCFS calculations are the location, size (or better, slip distribution), kinematics, and 3-D geometry of the source fault, and 3-D geometry and kinematics of the receiver faults. These parameters have uncertainties that can be addressed either by applying reasonable assumptions (e.g. for fault geometry and slip distribution), or by exploring the entire parameter space (e.g. friction coefficient, rheology). We calculated coseismic and postseismic ΔCFS using the code PSGRN/PSCMP [*Wang et al.*, 2006], which is based on a multilayered viscoelastic half-space. This code is composed of two routines. The first one (PSGRN) calculates the time-dependent Green functions of a given layered viscoelastic half-space for different dislocation sources at different depths. The second one (PSCMP) uses PSGRN results to calculate co- and postseismic deformation by linear superposition [*Wang et al.*, 2006]. We calculated interseismic ΔCFS instead using the elastic half-space based software Coulomb 3.3 [*Toda et al.*, 2011], applying the "back-slip" or "virtual dislocation" method [*Savage*, 1983; *Deng and Sykes*, 1997; *Papadimitriou and Sykes*, 2001; *Verdecchia and Carena*, 2015].

2.4.2 Fault geometry and slip models for specific earthquakes

Knowledge of geometry and slip models of source faults, and geometry and kinematics of receiver faults, is required for Coulomb stress modeling. These parameters can be obtained with a reasonable degree of detail for recent, instrumentally-recorded earthquakes. For paleoseismological earthquakes, we estimated the average slip for a given earthquake using empirical relationships among event magnitude, rupture length, width, area and surface displacement (e.g. *Wells & Coppersmith*, 1994). For some faults in particular (Antelope Valley, Benton Springs, Incline Village, Genoa, Panamint Valley, Furnace Creek) we used the measured coseismic offsets (described for each fault in the appendix, section 2.8) to better define input parameters as slip distribution and magnitude of the event. For the Genoa Fault and the Garlock Fault paleoseismological data for a single event exist at multiple localities along the fault trace. This allowed us to better define both the extent of the coseismic rupture, and the variation of coseismic slip along strike. For all other faults, we used a tapered slip distribution, with maximum values at the center of the fault tapering to zero at the tips along strike.

We modeled historical earthquakes by combining geological and seismological data. The surface rupture of the M_w 7.5 1915 Pleasant Valley earthquake has been mapped in detail by *Wallace* [1984a]. We used this information together with the focal mechanism determined by *Doser* [1988] to constrain the geometry and slip model of this rupture. The source fault of the M_w 7.2 1932 Cedar Mountain earthquake has been modeled using the surface faulting data of *Bell et al.* [1999] and the focal mechanism determined by *Doser* [1988]. We have constructed the geometry and slip models of the faults responsible for the 1954 Rainbow Mountain-Fairview Peak sequence from the focal mechanisms of *Doser* [1986] and the coseismic ruptures measurements of *Caskey*

et al. [2004] (Rainbow Mountain) and *Caskey et al.* [1996] (Fairview Peak). In order to define the geometry of the 1954 earthquake segment of the Dixie Valley Fault, we used the seismic profiles of *Abbott et al.* [2001] in combination with geological data (surface faulting) from *Caskey et al.* [1996]. The source fault parameters for the M_w 7.5 1872 Owens Valley earthquake are from *Haddon et al.* [2016], and are based on surface rupture data alone. Due to the lack of constraints at depth, for all source faults we used a constant dip angle. ΔCFS has always been calculated for the entire depth range considered (0 - 15 km), but here we are mainly interested in either the ΔCFS value at the hypocenter location (for historical earthquakes), or the maximum ΔCFS value along the fault (for paleoseismological earthquakes). We chose 10 km as an observation depth to be shown in all the figures, because the hypocenters of most of the moderate-to-large earthquakes in our study for which hypocentral depth is known are approximately at this depth.

2.4.3 Rheologic models

The postseismic ΔCFS, due to viscoelastic relaxation of lower crust and upper mantle, depends on the rheologic parameters used in the model. A Maxwell rheology [*Thatcher and Pollitz*, 2008], Burgers rheology [*Pollitz*, 2003] and power-law rheology [*Freed and Bürgmann*, 2004] have all been proposed for the western United States. The differences in postseismic ΔCFS among these models are however minor when calculated for time spans longer than 100 years [*Verdecchia and Carena*, 2015]. In this work we have therefore used a Maxwell rheology to calculate the postseismic ΔCFS in the region. On the basis of the range of rheological parameters of the lithosphere proposed for the western United States [*Tatcher and Pollitz*, 2008, and references therein], and of our prior work in this region [*Verdecchia and* Carena, 2015], we tested

three different models with a Maxwell rheology in our final calculations (Model 1, 2, and 3) (Table 2.2). Model 1 and Model 3 represent two end-members of relaxation time. In Model 1 most of the stress is quickly released in the first ~ 150 years, whereas for Model 3 relaxation times are much longer. Model 2 represents an average between the two end-members [*Verdecchia and Carena*, 2015]. In this model it becomes apparent that the viscosity value adopted for the lower crust (Table 2.2) strongly controls the rate at which stress is transferred back to the elastic crust. All the figures in this paper have been produced using Model 3. A brief explanation concerning the influence of choice of models on our results follows below.

2.4.4 Influence of effective fault friction and viscosity of the lower crust and upper mantle on the results

The coefficient of effective friction (μ') and the viscosity (η) of the lower crust and upper mantle play an important role in ΔCFS calculations. Effective friction, as it can be seen in equation (2.1), controls the value of the normal stress component. Viscosity instead influences the rate at which stresses are transferred to the upper crust. Both of these parameters may thus affect the stability of our results, and therefore they need to be considered.

In order to test the effect of varying μ' and η, we followed the same approach as *Verdecchia and Carena* [2015]. In addition to the three different rheological models discussed in section 2.4.3, we calculated ΔCFS_{cum} for three different values of μ' (0.2, 0.4, and 0.8) (Tables 2.1 and 2.3). In the supporting information (Figures 2.14, 2.15, and 2.16) graphical examples of ΔCFS_{cum} calculated with μ' of 0.2 and 0.8 are shown as well.

The result of these tests indicate that both μ' and η control mainly the magnitude of ΔCFS_{cum}, as also observed by *Verdecchia and Carena* [2015] on a 150 years time scale. Slightly different magnitudes of stress loading and stress shadows are observed for different values of μ', but this does not affect the sign of the Coulomb stress changes on the receiver faults. Based on the considerations above, we have drawn our general conclusions from simulations carried out using a value of effective friction of 0.4 and the rheology of Model 3, which represents the most conservative of all the rheological models considered.

2.5 Results

Starting with the 587 M_w 7.2 Antelope Valley earthquake, and ending with the 1954 M_w 7.2 Dixie Valley earthquake, we determined both the ΔCFS_{cum} for each of the seventeen studied faults immediately before the occurrence of each earthquake, and the present-day ΔCFS_{tot} on the major faults in the region. In order to make it easier to follow the description of our results below, we have divided the region in three sub-regions: (1) northern ECSZ (Figure 2.3), (2) central Walker Lane-Western Basin and Range (Figure 2.4), and (3) Northwestern Walker Lane (Figure 2.5). This subdivision takes into account the fact that, in terms of the stress transfer patterns obtained in this work, faults within the same sub-region strongly interact, whereas from one region to the next such interactions are less significant.

2.5.1 Cumulative ΔCFS in the northern ECSZ

The two surface-rupturing events on the Fish Lake Valley Fault (913 M_w 6.8 Leidy Creek segment and 950 M_w 6.7 Oasis segment) are the oldest earthquakes in our model that occurred in the northern ECSZ. The first event transferred ~ 2 bar of

positive ΔCFS_{cum} to the segment responsible for the second event (Table 2.1, Figure 2.11c), and together these two earthquakes increased stresses further on the Furnace Creek Fault, responsible for the 1715 M_w 7.2 earthquake (Figure 2.3a). The Furnace Creek event in turn produced a positive ΔCFS_{cum} in Owens Valley (Figure 2.3b), at the location where an M_w 7.5 earthquake occurred in 1872.

The ΔCFS_{cum} on the Garlock Fault just prior the 1453 M_w 7.7 event is small (0.2 bar) but still positive (Table 2.1, Figure 2.12b). The ΔCFS_{cum} of the 1453 earthquake largely contributed to the occurrence of the 1557 M_w 7.1 Panamint Valley earthquake, by producing a positive stress increase all along the fault with a maximum value of ~ 7 bars (Table 2.1, Figure 2.12c).

2.5.2 Cumulative ΔCFS in the central Walker Lane-Western Basin and Range

In the central Walker Lane the 1170 M_w 7.2 Benton Springs earthquake increased ΔCFS_{cum} on the northernmost part of the Cedar Mountain Fault, whereas negative ΔCFS_{cum} accumulated in the central and southern part of the same fault. The 1932 M_w 7.2 earthquake occurred [*Doser*, 1988] in the area of positive ΔCFS_{cum} (Figure 2.4a).Together with the 700 M_w 7.0 Pyramid Lake earthquake, the 1915 M_w 7.5 Pleasant Valley earthquake, and the 1932 M_w 7.2 Cedar Mountain earthquake, the 1170 Benton Springs earthquake also produced a large area of positive ΔCFS_{cum} in the region where the 1954 Rainbow Mountain-Fairview Peak-Dixie Valley earthquake sequence later occurred (Figure 2.4b). The 700 M_w 7.0 Pyramid Lake event also slightly increased ΔCFS_{cum} (~ 0.4 bar) at the location of the 1915 M_w 7.5 Pleasant Valley earthquake (Table 2.1, Figure 2.13a).

2.5.3 Cumulative ΔCFS in the Northwestern Walker Lane

The 587 M_w 7.2 Antelope Valley and the 700 M_w 7.0 Pyramid Lake earthquakes are the oldest events modeled in this study. The Antelope Valley earthquake first produced a small ΔCFS_{cum} increase (0.2-0.3 bar) on the Pyramid Lake Fault (Table 2.1, Figure 2.11a). Then the two events combined transferred significant positive ΔCFS_{cum} to the Carson Range and Lake Tahoe region (Figure 2.5a), where in 1375 the Incline Village Fault and the North Tahoe Fault ruptured together producing an M_w 7.1 earthquake. This earthquake then increased the stress on the central segment of the Genoa fault and on the northern part of the Mount Rose Fault, whereas it produced a stress drop on the northern segment of the Genoa Fault, and on the southern segment of the Mount Rose Fault (Figure 2.5b). These faults ruptured ~250 years later, possibly in two events very close to each other in time [*Ramelli and Bell*, 2009], with the first earthquake transferring positive ΔCFS_{cum} (~ 4 bars) on the fault segment responsible for the next event.

2.5.4 Present-day total ΔCFS in the northern ECSZ, Walker Lane, and Central Nevada Seismic Belt

In this region there are also several prominent faults that did not produce any major surface-rupturing event in the 1400 years considered in our study. Some examples are the Black Mountain [*Klinger and Piety*, 2001; *Sohn et al.*, 2014], Hunter Mountain [*Oswald and Wesnousky*, 2002], and White Mountain faults [*Kirby et al.*, 2006] in the northern ECSZ, the Wassuk Range [*Wesnousky*, 2005; *Bormann et al.*, 2012], Honey Lake [*Turner et al.*, 2008], and Mohawk faults [*Gold et al.*, 2014] in the Walker Lane, and the northern segment of the Dixie Valley fault [*Bell et al.*, 2004] in the Western Basin and Range (WBR). Here we calculated the ΔCFS_{tot} accumulated by

each of these faults in the last 1400 years by adding the interseismic ΔCFS (Figure 2.6, Table 2.3) to the ΔCFS_{cum} produced by all the studied events combined. We also calculated the ΔCFS_{tot} on the Pyramid Lake Fault and Fish Lake Fault for the last 1300 and 1000 years respectively (Table 2.3), because the age of the most recent event for these faults is comparable with their average recurrence interval [*Sawyer and* Reheis, 1999; *Briggs and Wesnousky*, 2004], and therefore they may be close to failure. According to our results, only four of the studied faults (Black Mountain, Honey Lake, Mohawk, and Pyramid Lake faults) have accumulated positive ΔCFS_{cum} along their entire length, whereas the rest are characterized by a heterogeneous ΔCFS_{cum} distribution. Figure 2.7a shows 1400 years of ΔCFS_{cum} for the Black Mountain Fault. This fault has accumulated a maximum of ~6 bars of ΔCFS_{cum} (Table 2.3), mostly due to the effect of the 1557 M_w 7.1 Panamint Valley earthquake. Adding to this the large interseismic ΔCFS, the ΔCFS_{tot} in the southern part of the fault is ~46 bars (Table 2.3).

The Honey Lake and the Mohawk faults have accumulated a maximum of 0.6 and 0.4 bars of positive ΔCFS_{cum} respectively (Table 2.3, Figure 2.7b, c), which represent a very small part of the ~30 bars of ΔCFS_{tot} calculated on the Honey Lake Fault and ~21 bars calculated on the Mohawk Fault. The interseismic loading forms also a large contribution to the ΔCFS_{tot} accumulated by the Pyramid Lake Fault (~ 37 bars, of which only ~ 1.5 bars are due to ΔCFS_{cum}) (Table 2.3, Figure 2.7d).

The Hunter Mountain Fault has been consistently unloaded along most of its length. Positive ΔCFS_{cum} were calculated only in a small region between the southern Saline Valley section and the northern Hunter Mountain section with maximum values of about 4.2 bars. Both the Hunter Mountain section and the Saline Valley section instead experienced a negative ΔCFS_{cum} of -2.2 bars and -7.2 bars respectively (Table 2.3, Figure 2.8a, b). However, the high interseismic ΔCFS entirely erased the stress

shadow, and loaded the Hunter Mountain Fault. The maximum ΔCFS_{tot} on this fault is ~36 bars in the region characterized by negative ΔCFS_{cum}, and ~45 bars in the region with positive ΔCFS_{cum} (Table 2.3).

The White Mountain Fault experienced ~10 bars of maximum positive ΔCFS_{cum} in its central segment (Table 2.3, Figure 2.8c) due to the 1872 M_w 7.5 Owens Valley earthquake. The addition of interseismic stress results in a ΔCFS_{tot} of ~ 30 bars. The southernmost part of the fault is instead located in a region of large stress drop due to the fact that it is parallel to the Owens Valley Fault, and as a result also the ΔCFS_{tot} in this segment of the fault is negative (Table 2.3).

The Wassuk Range Fault is equally characterized by an inhomogeneous distribution of ΔCFS_{cum} (Table 2.3, Figure 2.8d). While the northern part accumulated negative values of stress (~ -6 bars), the southern segment experienced a maximum ΔCFS_{cum} of ~ 4 bars. Adding the interseismic ΔCFS, the maximum ΔCFS_{tot} in the southern part of the fault is ~19 bars, and the minimum ΔCFS_{tot} in the northern part is ~ 9 bars.

The northern segment of the Dixie Valley Fault, located between the surface ruptures of the 1915 M_w 7.5 Pleasant Valley earthquake to the north and the 1954 M_w 7.2 Dixie Valley earthquake to the south, has accumulated a maximum positive ΔCFS_{cum} of ~10 bars (Table 2.3, Figure 2.8e). Due to its low slip rate, the contribution of the interseismic stress is only ~ 6 bars in the last 1400 years, which results in a ΔCFS_{tot} of ~16 bars (Table 2.3).

Finally, Figure 2.8f shows the ΔCFS_{cum} for the Fish Lake Valley Fault. The southern part of this fault has been loaded by the 1715 M_w 7.2 Furnace Creek earthquake, whereas a negative ΔCFS_{cum} (~-1 bar) characterizes the northern part.

Tectonic loading plays a major role in the ΔCFS_{tot} of the Fish Lake Valley Fault, which ranges between ~34 and ~45 bars.

2.6 Discussion

2.6.1 Significance of observed stress patterns

Our most significant result is that fifteen out of sixteen modeled receiver faults are either partially or entirely located in regions of positive ΔCFS_{cum} due to all previous events (Table 2.1). This finding indicates that changes in stress distribution due to major earthquakes may control the location of subsequent events over a 1400 years time scale.

The magnitude of positive ΔCFS_{cum} that we calculated varies from 0.2 to 10 bars. Such values are relatively small compared to average earthquake stress drops, suggesting that most faults are likely close to failure most of the time and as a consequence even small stress perturbations (< 1 bar) may affect the location of future events on suitably oriented faults. This has been already observed in the same region by *Verdecchia and Carena* [2015], and in other tectonically active regions worldwide by several other authors [*Stein et al.*, 1997; *Pollitz et al.*, 2003; *Freed et al.*, 2007; *Scholz*, 2010].

Not all of the faults in our study area have been the focus of paleoseismological studies that aimed at identifying the most recent event on each. As a consequence, it is possible that some large unidentified event would modify the ΔCFS_{cum} evolution that we calculated. This is an uncertainty that can only be addressed when relevant additional data become available in the future. Even if the most recent event on a fault is known, it is often characterized by large age uncertainties. Therefore the temporal

order of our events sequence may change depending on which age we choose within the uncertainty range of each event. In our study this applies to the oldest events (587 Antelope Valley, 700 Pyramid Lake, 913 Leidy Creek segment, and 950 Oasis segment earthquakes). However, as described in section 2.5, the first two events belong to the northwestern Walker Lane, and the other two to the northern ECSZ, and therefore the two pairs are too far and do not affect each other in terms of $\Delta CFS_{cum.}$ Changing the relative position of the events inside each pair will not alter our results, the Pyramid Lake earthquake will produce a small positive (~0.2 bar) ΔCFS_{cum} on the Antelope Valley fault, whereas in the original sequence it is the 587 Antelope Valley earthquake that increases the stress on the Pyramid Lake Fault. The Oasis segment earthquake will strongly encourage faulting on the Leidy Creek segment of the Fish Lake Fault, while the opposite is happening in the modeled sequence. In both cases the combining effect of the earthquakes on the two segments will eventually increase stress on the Furnace Creek Fault, responsible for the subsequent 1715 event. A similar consideration also applies to the pair formed by the 1453 Garlock and 1557 Panamint Valley earthquakes but, as also discussed by *McAuliffe et al.* [2013], these faults increase ΔCFS on each other, regardless of which of the two event struck first. Another case is that of the 1600 Mont Rose and the 1605 Genoa earthquakes. According to *Ramelli and Bell* [2009], these two earthquakes may have been very close in time, but the resolution of the data is not high enough to say which happened first. The order of these two earthquakes however does not affect our results, because one fault is the along-strike extension of the other, and therefore one fault loads the other regardless in which order the earthquakes occur.

An additional consideration concerning paleoseismological records is that in only a few cases (e.g. Genoa Fault, Garlock Fault) multiple paleoseismological sites

along a fault are available where a specific earthquake was recorded. This produces uncertainties in the extent of the coseismic rupture, which we mainly address by applying empirical relationships among event coseismic displacement, and magnitude [*Wells and Coppersmith*, 1994].

The presence outside of the study area of faults large enough to produce major earthquakes could change the state of stress on faults within the study area, affecting our results. An obvious example is the San Andreas Fault. *Freed et al.* [2007] found that the 1857 M_w 8.2 Fort Tejon earthquake likely transferred positive ΔCFS_{cum} to the Owens Valley region, and therefore contributed to the occurrence the 1872 Owens Valley earthquake. *McAuliffe et al.* [2013] suggested the possible interaction in terms of ΔCFS between the most recent event on the Garlock Fault [*Dawson et al.*, 2003; *Madugo et al.*, 2012], and the most recent event on the Mojave section of the San Andreas Fault [*Scharer et al.*, 2011]. Including these events from the San Andreas Fault will not change the significance of our results. In the first case, in fact, the effect of the 1857 Fort Tejon earthquake would further increase the ΔCFS on the Owens Valley Fault, already brought towards failure by the 1717 Furnace Creek earthquake. In the second case, a possible event on the Mojave section of the San Andreas Fault would transfer positive ΔCFS to the Garlock Fault increasing the ΔCFS_{cum} accumulated by this fault to values larger than 2.5 bars [*McAuliffe et al.*, 2013].

Several major faults in our study region do not seem to have produced any ground-rupturing events in the last 1400 years. If this is indeed real, as opposed to being the result of lack of sufficient information about the rupture history of these faults, it means that they have accumulated high values of ΔCFS_{tot}, comparable with the average stress drop expected for moderate-to-major earthquakes (10 to 100 bars [*Hanks*, 1977; *Scholz*, 2002]). As a consequence, if we think in terms of time-dependent

probability, these faults represent the most likely candidates for future major earthquakes in the region. Four large faults that appear not to have ruptured within the time range covered by this study are the Hunter Mountain Fault [*Oswald and Wesnousky*, 2002], the Black Mountain Fault [*Klinger and Piety*, 2001; *Sohn et al.*, 2014; *Frankel et al.*, 2016], the Honey Lake Fault [*Turner et al.*, 2008], and the White Mountains Fault [*Kirby et al.*, 2006] (Table 2.3, Figures 2.7 and 2.8). Because the most recent events on the Fish Lake Fault [*Reheis,* 1994*; Reheis et al.,* 1995] and Pyramid Lake Fault [*Briggs and Wesnousky*, 2004] occurred respectively ~1000 years and ~1300 years B.P., these two faults have also had enough time to accumulate significant values (10 to 100 bars) of ΔCFS_{tot}. Unfortunately for some of these faults there are limited paleoseismological data. The age of the most recent event on the White Mountains Fault and the Hunter Mountain Fault for instance is unknown. Scarp morphology analysis results from different sections of the Black Mountain Fault show different ages for the most recent event in each section. *Machette et al.* [1999] estimated an age of 500-840 years for the most recent faulting event on the northern section. *Klinger and Piety* [2001] found evidences for a Mid-Holocene event on the central section and for a 1000-2000 years old event on the southern section. *Frankel et al.* [2016] used optically-stimulated luminescence dating to define a maximum age of ~ 4.5 ka for the most recent event on the central part of the Black Mountain Fault (Badwater site). The authors concluded that the 6.4-m-tall scarp measured at the studied location could be the result of at least two surface-rupturing events. The Pyramid Lake, Fish Lake and Honey Lake faults are the only faults in this group for which trench studies have been completed. The available data and the relative uncertainties for the first two are described in detail in the appendix, section 2.8. The Honey Lake Fault has been studied by *Turner et al.* [2008] who reported one surface-rupturing earthquake

post ~4670 years B.P. Because of the limited stratigraphy at the study site, the authors however did not rule out the possibility of additional younger events.

Even considering the lack of detailed paleoseismological studies (especially for the White Mountains, Hunter Mountain, and Black Mountain faults), and the uncertainties in the age of the most recent event for all faults, we believe that these six faults are the most likely candidates for the next major earthquake in the region. The White Mountains Fault is the only one of these faults that falls into areas of both positive and negative ΔCFS_{tot} (Table 2.3). We speculate that, because its southern segment is still located in a region of negative ΔCFS_{tot}, a future rupture may be limited to the central and northern parts of this fault.

Discrepancies between geologic and geodetic slip rates have been widely observed in the Walker Lane and in the northern Eastern California Shear Zone [*Oskin et al.*, 2008; *Frankel et al.*, 2011; *Amos et al.*, 2013]. *Peltzer et al.* [2001] using InSAR data for the region where the Garlock Fault and the Eastern California Shear Zone intersect, observed deformation rates inconsistent with geological data, particularly in the region around the Little Lake Fault. The authors proposed that this ongoing rapid deformation could be the result of postseismic processes from the 1872 Owens Valley earthquake and the 1992 Landers earthquake. Although the 1992 Landers earthquake is not part of our study, our results (Figure 2.9a, b) show that the Little Lake Fault is located in a region of positive ΔCFS_{cum} produced by the 1872 Owens Valley earthquake and by the 1605 Garlock Fault earthquake. Concentrated postseismic ΔCFS produced by several source faults may therefore control the location of temporary rapid deformation and clustering of events, as it is presently happening around the Little Lake Fault. The cluster of events that occurred in 1954 in the Rainbow Mountain - Fairview Peak - Dixie Valley region may have been an analogue case in the past. In this region

several previous earthquakes had created a large area of positive ΔCFS_{cum} facilitating the occurrence of the 1954 sequence (Figure 2.4b).

2.6.2 Statistical significance of our results

In order to verify whether the results that most source faults are in areas of positive ΔCFS_{cum} can be obtained by chance, we performed 10 tests on random earthquake sequences. From our study region, we chose 67 active faults large enough to produce ground-rupturing earthquakes (these include also all those faults for which there is no record of any earthquakes in the last 1400 years). We then created ten sequences of 17 random source faults (i.e. earthquakes) with the same date of occurrence and event magnitude as those of our real sequence, and performed ΔCFS_{cum} calculations for each of the ten sequences. The results are shown in Table 2.4.

In the actual sequence, ~ 80% of the source faults are partially or fully located in areas of $\Delta CFS_{cum} \geq 0.2$, and ~ 70% are in areas of $\Delta CFS_{cum} \geq 0.4$. In none of the random tests these percentages could be reproduced. In fact, as expected for a random process, on average the events fell in areas of increased ΔCFS_{cum} only about 50% of the time.

For paleoseismological earthquakes the location of the epicenters is unknown, and thus an earthquake may in fact have occurred in a part of the fault that was unloaded. Therefore we also verified what happens if we restrict our tests just to the faults fully located in area of $\Delta CFS_{cum} > 0$. Once all source faults that are partly in stress shadow are excluded, the actual sequence shows that ~ 56% of the faults are located in area of positive ΔCFS_{cum} for their entire length. Again we were not able to reproduce the same percentages in the random tests, where the best result is 44% (and most of the other tests return 30% or less, see Table 2.4). From these tests it appears

that our results are robust, and the time sequence and areal distribution of major earthquakes in this region in the last 1400 years is unlikely to be random.

2.6.3 Effect of simplified slip distribution and fault geometry

In sections 2.4.3 and 2.4.4 we explained why our results are not really sensitive to the choice of rheological parameters in the model. The results, however, could in principle also be affected by oversimplifications due to lack of information concerning other parameters.

One possible issue is the slip distribution adopted for the source faults. We used a tapered slip distribution, which is different from reality, where the slip distribution is certainly more heterogeneous. The precise slip distribution however only affects the stress change pattern and values very close to the fault plane (a few km), and it is therefore relevant only in main shock-aftershocks interaction studies and for earthquakes occurring on or near the source fault. Neither of these two conditions applies to our study, therefore the assumption of a tapered slip distribution is a reasonable one.

The importance of fault geometry in ΔCFS calculations has already been explored by other works [e.g. *King et al.*, 1994; *Madden et al.*, 2013; *Wang et al.*, 2014; *Verdecchia and Carena*, 2015]. In our particular case the main concern is linked to the dominant fault kinematics in this region, where many of the faults have a dominant or significant normal component, As mentioned earlier in section 2.4.2, due to lack of data on fault geometry at depth we had to adopt a constant dip for the geometry of both source and receiver faults. Whereas this is not a problem for strike-slip faults, for which the dip most likely does not vary much with depth, it may not be the case for normal faults, which could have dip changes or a listric geometry still within the brittle crust.

In order to assess the impact of using a simple planar geometry for normal faults, we compared the coseismic stress change pattern produced by a 60° dipping fault with the one produced by a fault with a dip of 60° for the top 5 km and 30° for the bottom 7 km (Figure 2.17). In both cases we kept the earthquake magnitude and average slip constant. The along-strike positive lobes (Figure 2.17a and b) appear to be slightly larger in the case of the more complex geometry. The maximum values of coseismic ΔCFS however do not change significantly. In addition, a localized positive stress change is created in the region where the fault dip changes (Figure 2.17f), but the effect is so local that it would be relevant only for analyzing the aftershocks distribution, which is not the subject of our work. Therefore we opted for a high-angle, constant-dip geometry, which is also consistent with the few data on large historical earthquakes in the Basin and Range: the analyses of the 1954 Rainbow Mountain-Fairview Peak earthquakes [*Doser*, 1986], 1959 Hebgen Lake earthquake [*Doser*, 1985], and 1983 Borah Peak earthquake [*Stein and Barrientos*, 1985] all suggest a planar geometry of the source faults.

2.7 Conclusions

In order to better understand the relationships among large earthquakes in diffuse plate boundary regions, we modeled the evolution of coseismic and postseismic Coulomb stresses for seventeen ground-rupturing earthquakes that occurred in the northern ECSZ, Walker Lane, and Central Nevada Seismic Belt in the last 1400 years. Using geologic slip rates, we also determined the tectonic loading in the same period for all the major faults located in the study region.

Our results show that the majority of the source faults are partly or fully located in areas of positive stress loading produced by previous earthquakes. This indicates that

the spatial distribution of major earthquakes in the region is controlled by coseismic and postseismic stress redistribution processes. In addition, the present-day sum of coseismic, postseismic, and interseismic stress change for the Fish Lake Valley Fault, Honey Lake Fault, Pyramid Lake Fault, Hunter Mountain Fault, White Mountain Fault, and Black Mountain Fault, is comparable to the expected stress drop in a major earthquake. This finding suggests that these six faults may be close to failure at present but, especially for the last three, further paleoseismological studies would be needed to confirm the absence of events younger than 1400 years.

2.8 Appendix: Detailed description of the modeled source faults and their paleoseismological earthquakes, from the Antelope Valley earthquake to the Furnace Creek earthquake

2.8.1 Antelope Valley Fault

The Antelope Valley Fault (AVF) (Figure 2.2) is one of most prominent normal faults bounding the eastern flank of the Sierra Nevada. A trench excavated by *Sarmiento et al.* [2011] shows evidence for two paleoearthquakes in the last 6250 years, with the most recent event at about 1312-1414 years B.P. Based on measured coseismic offset of 3.6 m for this event, these authors determined a $M_w \geq 7.0$.

2.8.2 Pyramid Lake Fault

Right-lateral shear in the northern Walker Lane is mostly accommodated by the Pyramid Lake Fault (PLF) [*Briggs and Wesnousky*, 2004]. On this fault two surface-rupturing earthquakes have occurred since ~7630 year B.P., with the most recent event considered in this work occurring between 1705 ± 175 and 810 ± 100 years B.P. [*Briggs and Wesnousky*, 2004].

2.8.3 Fish Lake Valley fault zone

The Fish Lake Valley Fault (FLF) (Figure 2.2) is a ~70-km-long, right-lateral transtensional fault zone, and one of the faults with the highest slip rates in the ECSZ [*Frankel et al.,* 2007b]. Trenching work [*Reheis,* 1994*; Reheis et al.,* 1995] determined a most recent event age between 1500 and 600 years B.P. (FLFa in Table 2.1) for the northern part of the fault, and between 1160 and 830 years B.P. for the central and south part (FLFb in Table 2.1). Based on these data and on geomorphological investigations, *Sawyer and Reheis* [1997, 1999] divided the fault zone into four segments. According to the authors two of these four segments (Leidy Creek and Oasis segments) have ruptured independently in the last 1500 years.

2.8.4 Benton Springs Fault

Displacement from the Fish Lake Valley-Death Valley fault system is transferred north to the Walker Lane via the left-lateral strike-slip Excelsior Mountain (EMF) and Coaldale faults (CF) (Figure 2) [*Oldow*, 1992]. Here deformation accommodated by several NNW-SSE right-lateral strike-slip faults [*Bennett et al.*, 2003], including the Cedar Mountain Fault (CMF), responsible for the M_w 7.2 1932 earthquake, and the Benton Springs Fault (BSF). According to radiocarbon dating results from *Wesnousky* [2005], the BSF produced a surface-rupturing earthquake about 780 ± 35 years B.P with a normal offset of ~ 1m, suggesting a small normal component in the mainly right-lateral kinematics of the fault.

2.8.5 Faults of the Lake Tahoe basin

The West Tahoe Fault (WTHF), the North Tahoe Fault (NTF), and the Incline Village Fault (IVF) are the main active faults bounding the western side of the lake Tahoe half-graben (Figure 2.2) [*Brothers et al.*, 2009; *Wesnousky et al.*, 2012]. An onshore trench excavated by *Dingler* [2007] across the IVF indicates that the most

recent event occurred ~575 years B.P., with a coseismic normal vertical displacement of 3.1 m. Due to the short length of the fault compared to the coseismic displacement, the authors concluded that the fault may have ruptured in conjunction with the NTF, leading to a M_w ~ 7 earthquake. According to *Brothers et al.* [2009], the ~ 55 km-long WTHF has not produced any ground-rupturing events for at least the last 3600 years.

2.8.6 Garlock fault

The Garlock Fault (GAF) bounds our study area to the south. It extends for ~250 km from its intersection with the San Andreas fault, to the southern end of the Black Mountain Fault (BMF) (Figures 2.1 and 2.2). This left-lateral strike-slip fault can be divided into three main segments (western, central and eastern segment) [e.g. *McGill and Sieh*, 1991], and has been the focus of many paleoseismological studies in the last decade due to the fact that it has not generated any historical major ground-rupturing event. New investigations of the western segment by *Madugo et al.* [2012] reveal evidence of six surfaces ruptures in the past ~5600 years. These authors, citing the results of *Dawson et al.* [2003] on the central segment, suggest that the most recent event may have ruptured both the western and central segment, probably leading to an event with $M_w \geq 7.5$. Radiocarbon dating yielded a calibrated age of 310-500 years B.P. for the most recent earthquake on the GAF [*Dawson et al.*, 2003; *Madugo et al.*, 2012].

2.8.7 Panamint Valley fault

The Panamint Valley Fault (PVF) is, together with the Hunter Mountain Fault (HMF), one of the main right-lateral transtensional faults that accommodates large part of the dextral motion between the Sierra Nevada block and stable North America in the northern ECSZ (Figure 2.2) [*Frankel et al.*, 2007a,b; *Ganev et al.*, 2010]. Although this fault did not produce any major earthquakes in historical times, *Zhang et al.* [1990] recognized a 25 km-long zone of fault scarps associated with the most recent

prehistoric event. These authors, through geomorphological and paleoseismological analysis, defined an average coseismic displacement of ~3 m, indicating an M_w ~7 earthquake. A paleoseismological study by *McAuliffe et al.* [2013] found an age of 328-485 years B.P. for the most recent event.

2.8.8 Carson Range fault system

The Genoa Fault (GF) and the Mount Rose fault system (MRF) (Figure 2.2) are the main normal structures bounding respectively the southern and northern side of the Carson Range to the east. Paleoseismological studies by *Ramelli et al.* [1999] show evidence for two ground-rupturing earthquakes on the GF in the past 2000 years, with the last earthquake occurring 500-600 years B.P. Subsequent studies [*Ramelli and Bell*, 2009] on different trenches along the Carson Range fault system, including the Carson City fault and the MRF, yielded ages ~200 years younger, with the most recent event dated at ~390 ± 40 years B.P. Also, these authors concluded that both the GF and MRF may have ruptured as a sequence of clustered events similar to the 1954 Rainbow Mountain-Fairview Peak-Dixie Valley sequence, and excluded a 100-km-long single rupture.

2.8.9 Furnace Creek fault

Often referred to as the "Northern Death Valley Fault", the Furnace Creek Fault (FCF) extends for ~105 km in a continuous surface trace. With the FLF to the north and the BMF to the south (Figure 2.2), it forms the Death Valley fault system. The age of the last ground-rupturing event has been constrained by *Klinger* [1999], who dated recent laterally offset tephra layers, to sometime after 1640 and before 1790 A.D., with an estimated coseismic right-lateral slip of 3 ± 1 m.

Table 2.1. ΔCFS immediately before the occurrence of each earthquake[a].

	Earthquake[b] (A.D.)	M_w	Strike/Dip/Rake (degrees)[c]	Coseismic ΔCFS (bars)	Cumulative ΔCFS (bars)				
					Model3			Model1	Model2
				μ' 0.4	μ' 0.2	μ' 0.4	μ' 0.8	μ' 0.4	μ' 0.4
1	587 AV	7.2	344/60/-90	/	/	/	/	/	/
2	700 PL	7.0	340/85/180	0.06	0.19	0.24	0.35	0.29	0.27
3	913 LC	6.8	340/80/180	0.0	0.08	0.12	0.19	0.13	0.15
4	950 OS	6.7	319/75/180	1.5	2.00	1.9	1.74	2.42	2.17
5	1170 BS	7.2	150/85/-170	-0.2	-0.65	-0.60	-0.5	-0.75	-0.70
6	1375 IN	7.1	18/60/-90	0.30	0.88	1.12	1.61	1.05	1.08
7	1453 GA	7.7	75/90/0	0.01	0.21	0.18	0.27	0.22	0.23
8	1557 PV	7.1	158/80/-175	3.06	4.95	7.11	11.45	10.25	9.50
9	1600 MR	7.0	2/60/-90	3.04	5.34	6.53	8.57	7.08	6.97
10	1605 GN	7.2	1/60/-90	0.96	3.11	3.97	5.57	4.55	4.39
11	1715 FC	7.2	143/90/180	1.10	2.82	3.21	3.10	3.20	3.18
12	1872 OV	7.5	340/85/-172	-0.07	0.71	0.68	0.63	0.99	1.06
13	1915 PS	7.5	198/50/-90	0.02	0.30	0.36	0.47	0.36	0.40
14	1932 CM	7.2	343/85/-175	0.18	0.56	1.25	2.35	1.11	1.25
15	1954 RM	7.0[d]	8/55/-159	0.15	1.90	1.87	1.82	1.94	2.04
16	1954 FP	7.1	9/60/-140	0.13	0.82	0.80	0.77	1.22	1.10
17	1954 DV	7.2	37/35/-90	0.60	1.47	1.68	2.10	1.67	1.80

[a]Maximum calculated ΔCFS along the fault plane for the paleseimological events; ΔCFS at hypocenter for the historical earthquakes. [b] AV, Antelope Valley; PL, Pyramid Lake; LC, Leidy Creek segment; OS, Oasis segment; BS, Benton Spring; GA, Garlock; IN, Incline Village; PV, Panamint Valley; MR, Mont Rose; GN, Genoa; FC, Furnace Creek; OV, Owens Valley; PS, Pleasant Valley; CM, Cedar Mountain; RM, Rainbow Mountain; FP, Fairview Peak; DV, Dixie Valley. [c] Aki and Richards convention. [d]Modeled as a single event.

Table 2.2 Combinations of crust and mantle viscosities (η) tested.

	Thickness[a] (km)	Model 1 η (Pa s)	Model 2[b] η (Pa s)	Model 3[c] η (Pa s)
Upper - Middle crust	16	Elastic	Elastic	Elastic
Lower crust	19	1×10^{19}	3.2×10^{19}	1×10^{20}
Upper mantle	65	1×10^{19}	3.2×10^{18}	3.2×10^{18}

[a]*Bassin et al.* [2000].
[b]*Hammond et al.* [2010].
[c]*Gourmelen and Amelung* [2005].

Table 2.3. Minimum / maximum present-day cumulative ΔCFS (ΔCFS_{cum}) for different rheologies and effective friction coefficients (μ'), interseismic ΔCFS (ΔCFS_{int}), and minimum/maximum present-day total ΔCFS (ΔCFS_{tot}) calculated on each receiver fault.

Fault[a]	Strike/Dip/Rake (degrees)[b]	ΔCFS_{cum} (bar)			ΔCFS_{cum} (bar)		ΔCFS_{int} (bar)	ΔCFS_{tot} (bar)
		Model3			Model1	Model2		Model 3
		μ' 0.2	μ' 0.4	μ' 0.8	μ' 0.4	μ' 0.4	μ' 0.4	μ' 0.4
HM (SV)	336/85/-150	-3.9/-2.4	-5.2/-3.0	-8.4/-4.5	-5.1/-3.0	-5.0/-3.2	43.4[c]	38.2/40.4
HM (HM)	305/85/-150	-3.6/-0.5	-4.6/0.3	-7.4/2.0	-4.5/0.7	-4.4/0.7	37.8[c]	33.2/38.1
FLV	320/80/180	-1.7/8.5	-1.3/9.5	-0.5/8.6	-2.3/9.8	-1.9/9.1	35.0[d]	33.7/44.5
BM	165/60/-135	0.6/4.3	1.2/5.4	2.0/7.6	0.8/5.4	1.1/5.6	40.6[c]	41.8/46.0
WR	340/55/-90	-4.6/3.2	-5.7/3.9	-8.0/5.5	-6.3/4.4	-6.1/4.2	14.7[c]	9.0/18.6
HL	310/90/180	0.4/0.6	0.3/0.6	0.3/0.5	0.2/0.5	0.3/0.6	26.6[c]	26.9/27.2
WS	310/90/180	-0.3/0.9	-0.4/1.0	-0.5/1.1	-0.5/0.8	-0.4/0.9	5.6[c]	5.2/6.6
PL	340/85/180	0.6/1.8	0.5/1.6	0.3/1.5	0.2/1.6	0.4/1.9	35.1[e]	34.6/36.7
MFS	332/90/180	0.0/0.3	0.0/0.4	0.0/0.6	0.0/0.5	0.0/0.6	21.0[c]	21.0/21.4
DV (NS)	37/35/-90	-11.0/8.6	-11.0/9.7	-13.0/11.4	-10.0/11.3	-11.0/10.6	6.3[c]	-4.7/16.0
WM	166/60/-140	-63.9/17.9	-68.6/19.2	-73.5/17.7	-62.3/21.8	-63.3/21.5	19.6[c]	-49.1/38.8

[a]HM (SV), Hunter Mountain (Saline Valley section) ; HM (HM), Hunter Mountain (Hunter Mountain section); FLV, Fish Lake Valley; BM, Black Mountain; WR, Wassuk Range; HL, Honey Lake; WS, Warm Springs Valley; PL, Pyramid Lake; MFS, Mohawk; DV (NS), Dixie Valley (Northern Segment); WM, White Mountain. [b] Aki and Richards convention. [c] Calculated over 1400 years. [d] Calculated over 1000 years. [e] Calculated over 1300 years.

Table 2.4. Comparison of cumulative ΔCFS between the actual earthquake sequence and ten control tests on random faults and earthquakes.

Earthquake sequence	ΔCFS ≥ 0.2 bar	ΔCFS ≥ 0.4 bar	Full ΔCFS > 0[a]
Actual Sequence	13 (81%)	11 (69%)	9 (56%)
Test 1	9 (56%)	9 (56%)	6 (37%)
Test 2	9 (56%)	8 (50%)	5 (31%)
Test 3	7 (44%)	6 (37%)	4 (25%)
Test 4	7 (44%)	5 (31%)	5 (31%)
Test 5	8 (50%)	7 (44%)	5 (31%)
Test 6	8 (50%)	5 (31%)	4 (25%)
Test 7	10 (62%)	9 (56%)	7 (44%)
Test 8	10 (62%)	8 (50%)	6 (37%)
Test 9	6 (37%)	5 (31%)	5 (31%)
Test 10	5 (31%)	4 (25%)	3 (19%)

[a]Number of faults entirely located in areas of ΔCFS > 0 and percentage of total faults involved (total of 16 faults in all cases).

Table 2.5. Geologic slip rates used as input for interseismic Coulomb stress modeling.

Fault	Slip Rate (mm/yr)	Reference
Antelope Valley	0.8	Sarmiento et al. (2011)[a]
Ash Hill	0.5	Densmore and Anderson (1997)[b]
Benton Spring	1.0	Wesnousky (2005)[b]
Bettles Well/Petrified Springs	1.4	Wesnousky (2005)[b]
Black Mountains (Central Death Valley)	2.5	Klinger and Piety (2001)[b], Sohn et al. (2014)[b], Frankel et al. (2016)[b]
Bonham Ranch	0.4	dePolo (1998)[c]
Buena Vista Valley	0.2	dePolo (1998)[c]
Carson City	0.3	dePolo (2006)[a]
Cedar Mountains	0.4	Bell et al. (1999)[a]
Coaldale	0.1	Petersen et al. (2014)
Cortez Mountains	0.3	dePolo and Anderson (2000)[c]
Crescent Dunes	0.2	dePolo (1998)[c]
Deep Springs	0.8	Reheis and Sawyer (1997)[b]
Dixie Valley	0.6	Bell and Katzer (1990)[a]
Eastern Monitor Range	0.3	dePolo (1998)[c]
Eastern Pyramid Lake	1.5	Briggs and Wesnousky (2004)[b]
Emigrant Peak	0.8	Reheis and Sawyer (1997)[b]
Excelsior Mountains	0.2	Petersen et al. (2014)
Fairview Peak/Gold King/West Gate	0.3	Bell et al. (2004)[a]
Fish Lake Valley	3.1-4.5	Frankel et al. (2007a, 2007b)[b]
Fish Slough	0.5	Petersen et al. (2014)
Freds Mountain	0.3	dePolo and Anderson (2000)[c]
Furnace Creek (North Death Valley)	4.5	Frankel et al. (2007a, 2007b)[b]
Garlock	2.3-6.6	Ganev et al. (2012)[b], Madugo et al. (2012)[a]
Genoa-Kings Canyon	2.5	Ramelli and Bell (2009)[a]
Granite Springs	0.5	dePolo (1998)[c]
Grass Valley	0.3	dePolo (1998)[c]
Hartley Springs	1.0	dePolo and Anderson (2000)[c]
Hilton Creek	1.5	Berry (1997)[b]
Honey Lake	1.7	Turner et al. (2008)[b]
Hot Springs	0.2	dePolo and Anderson (2000)[c]
Hunter Mountain-Saline Valley	2.5	Oswald and Wesnousky (2002)[b]
Incline	0.3	Dingler et al. (2009)[b]
Indian Hills	0.2	dePolo (1998)[c]
Independence	0.5	Petersen et al. (2014)
Ione Valley	0.2	dePolo (1998)[c]
Kawich/Hot Creek Ranges	0.6	dePolo (1998)[c]
Last Chance	0.2	Petersen et al. (2014)
Little Fish	0.3	dePolo (1998)[c]
Little Lake	0.6-1.3	Amos et al. (2013)[b]
Little Valley	0.2	dePolo (1998)[c]
Lone Mountain	0.8	Lifton et al. (2015)[b]
Middlegate	0.2	Petersen et al. (2014)
Mohawk	0.6	Sawyer et al. (2013)[b], Gold et al. (2014)[b]
Mono Lake	1.9	dePolo and Anderson (2000)[c]
Mount Rose	1.5	Ramelli and dePolo (1997)[a]
Nightingale	0.3	dePolo (1998)[c]
North Tahoe	0.5	Dingler et al. (2009)[b]

Table 2.5 (Continued)

Fault	Slip Rate (mm/yr)	Reference
Owens Valley	2.1	Lee et al. (2001)[a], Haddon et al. (2016)[b]
Panamint Valley	2.5	Zhang et al. (1990)[b]
Peavine Peak	0.2	dePolo (2006)[a]
Peterson Mountain	0.3	dePolo and Anderson (2000)[c]
Pyramid Lake	2.5	Briggs and Wesnousky (2004)[b]
Queen Valley	0.4	Lee et al. (2009)[b]
Rainbow Mountain	0.4	Bell et al. (2004)[a]
Round Valley	0.8	Berry (1997)[b]
San Emidio	0.4	dePolo (1998)[c]
Sand Springs	0.5	Bell et al. (2004)[a]
Sheep Creek	0.3	dePolo (1998)[c]
Shoshone Range	0.3	dePolo (1998)[c]
Sierra Nevada Frontal South	0.5	Petersen et al. (2014)
Silver Lake	0.2	Sawyer and Bryant (1995)[b]
Simpson Park	0.3	dePolo and Anderson (2000)[c]
Singatse	0.3	dePolo (1998)[c]
Smith Valley	0.4	Wesnousky and Caffee (2011)[b]
South Death Valley	3.0	Sohn et al. (2014)[b]
Southwest Reese River	0.2	dePolo (1998)[c]
Spanish Springs	0.3	dePolo (1998)[c]
Tin Mountain	0.2	Petersen et al. (2014)
Toiyabe Range	0.3	dePolo and Anderson (2000)[c]
Warm Springs	0.2	Gold et al. (2013)[b]
Wassuk Range	0.9	Bormann et al. (2012)[b]
West Tahoe	0.7	Dingler et al. (2009)[b]
Western Humoldt Range	0.2	dePolo (1998)[c]
Western Toiyabe Range	0.3	dePolo and Anderson (2000)[c]
White Mountains	1.0	Lifton (2013)[b]

[a]Slip rates derived from multievents recognition.
[b]Slip rates calculated from the cumulative displacements of landforms of approximately known age.
[c]Slip rates based on empirical relationship between the maximum basal facet height and vertical slip rate.

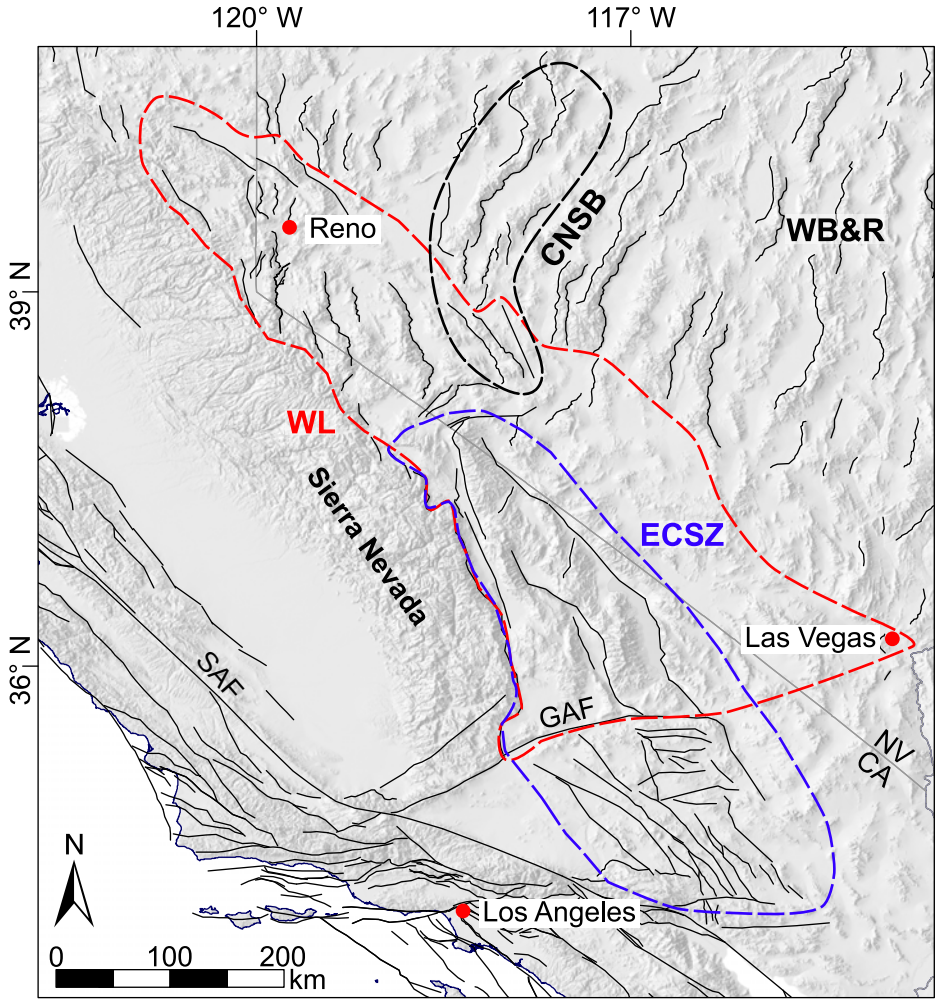

Figure 2.1. Map of active faults in California and central Nevada, from the U.S. Geological Survey National Seismic Hazard Maps [*Petersen et al.*, 2014]. CNSB = Central Nevada Seismic Belt [*Wallace*, 1984b]; ECSZ = Eastern California Shear Zone [*Dokka and Travis*, 1990]; WL = Walker Lane [*Stewart*, 1988]; WB&R = Western Basin and Range; SAF = San Andreas fault; GAF = Garlock fault.

Figure 2.2. Map of Quaternary active faults capable of M ≥ 7 earthquakes, from the U.S. Geological Survey National Seismic Hazard Maps [*Petersen et al.*, 2014]. Thick red lines represent faults that have produced a surface rupture event in the last 1400 years, and thick black lines the rest of the faults modeled in this work. Numbered red and yellow circles represent the sequence of historical and paleoseismological earthquakes respectively (listed in Table 2.1). For historical earthquakes, the red circle represents also the specific earthquake epicenter location from the CDMG Historical Earthquakes database [*Petersen et al.*, 1996]. Focal mechanisms are from *Beanland and Clark* [1994] (Owens Valley earthquake), *Doser* [1988] (Pleasant Valley and Cedar Valley earthquakes), *Doser* [1986] (Rainbow Mountain, Fairview Peak and Dixie Valley earthquakes). AVF= Antelope Valley fault; BMF=Black Mountains fault; BSF= Benton Springs fault; BRF=Bonham Range fault; CF=Coaldale fault; CMF=Cedar Mountain fault; DVF=Dixie Valley fault; EMF=Excelsior Mountains fault; EPF=Emigrant Peak fault; FPF=Fairview Peak fault; FLF=Fish Lake fault; FCF=Furnace Creek fault; GaF=Garlock fault; GF= Genoa fault; GVF=Grass Velley fault; HCF= Hilton Creek fault; HLF=Honey Lake fault; HMF=Hunter Mountain fault; IVF=Incline Village fault; LLF=Little Lake fault; LMF=Lone Mountain fault; MFS=Mohawk fault system; MRF=Mount Rose fault; NTF=North Tahoe fault; OVF=Owens Valley fault; PFF=Petrified Springs fault; PLF=Pyramid Lake fault; PSF=Pleasant Valley fault; PVF= Panamint Valley fault; RMF=Rainbow Mountain fault; RVF=Round Valley fault; SNFF=Sierra Nevada frontal fault; SVF=Smith Valley fault; WHF=West Humboldt fault; WMF=White Mountains fault; WRF=Wassuk Range fault; WSF=Warm Springs fault; WTHF=West Tahoe fault.

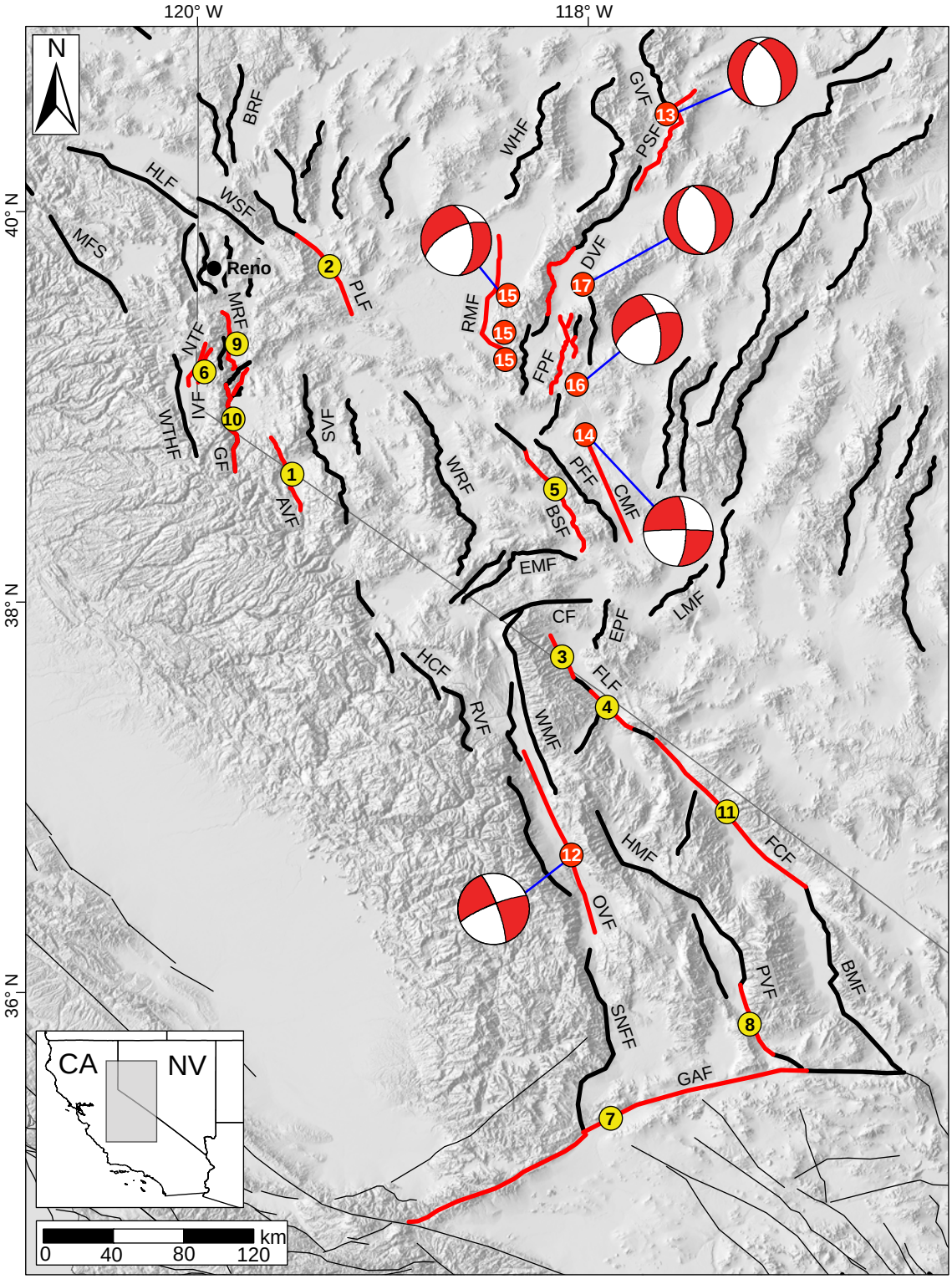
120° W
118° W
40° N
38° N
36° N
N
Reno
BRF
HLF
WSF
MFS
MRF
NTF
IVF
WTHF
GF
AVF
SVF
PLF
WHF
GVF
PSF
DVF
RMF
FPF
WRF
BSF
PFF
CMF
EMF
CF
EPF
LMF
HCF
RVF
FLF
WMF
HMF
FCF
OVF
PVF
BMF
SNFF
GAF
1
2
3
4
5
6
7
8
9
10
11
12
13
14
15
15
15
16
17
CA
NV
km
0
40
80
120

Figure 2.2

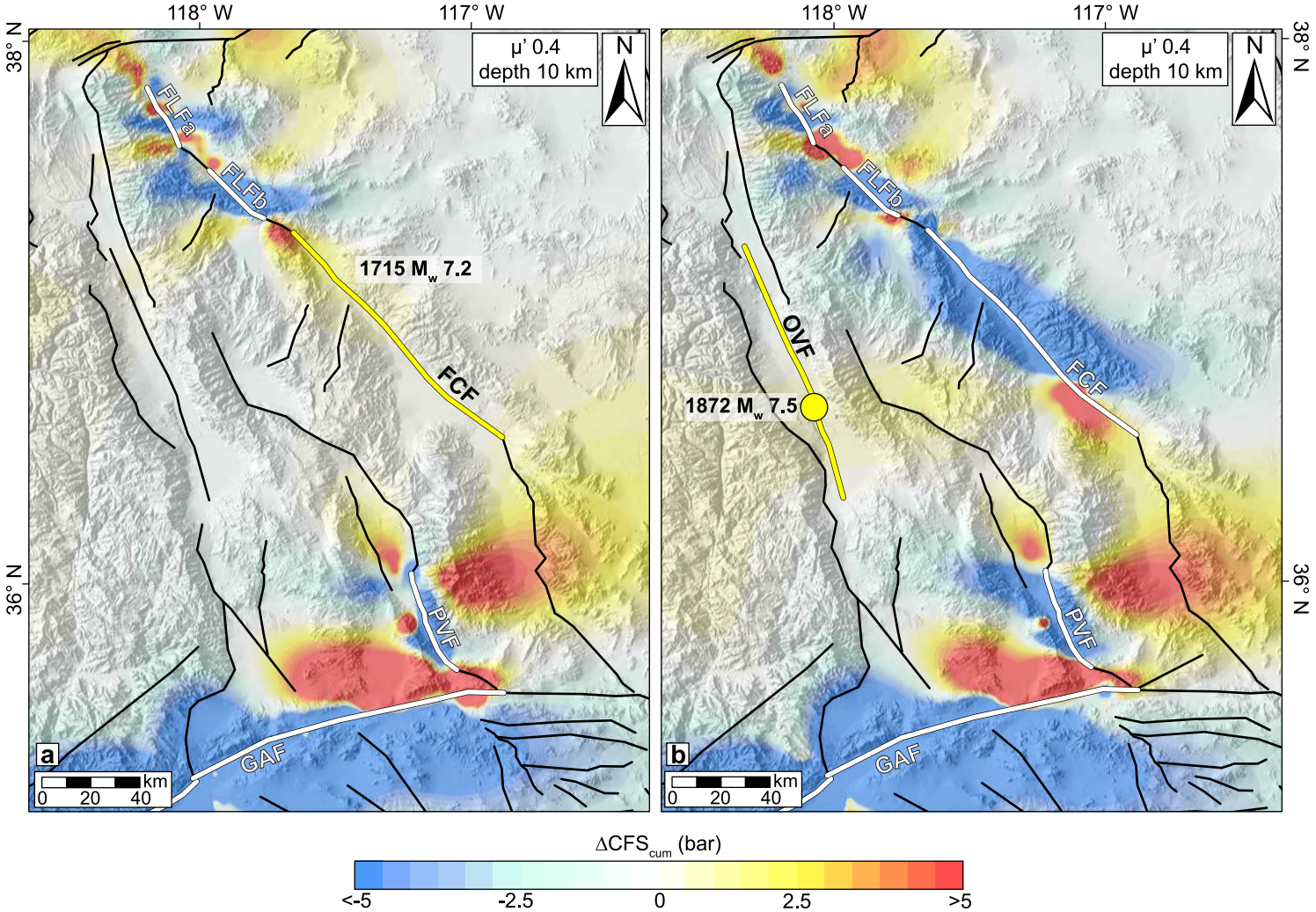

Figure 2.3. Cumulative ΔCFS due to all previous events resolved (a) on the kinematics of the Furnace Creek fault (FCF) just before the 1715 earthquake, and (b) on the kinematics of the Owens Valley fault (OVF) just before the 1872 earthquake (yellow circle = earthquake epicenter). Thick white lines are source faults; thick yellow lines are receiver faults. FLFa, Fish Lake Valley fault (Leidy Creek segment); FLFb, Fish Lake Valley Fault (Oasis segment); GAF, Garlock fault; PVF, Panamint Valley fault.

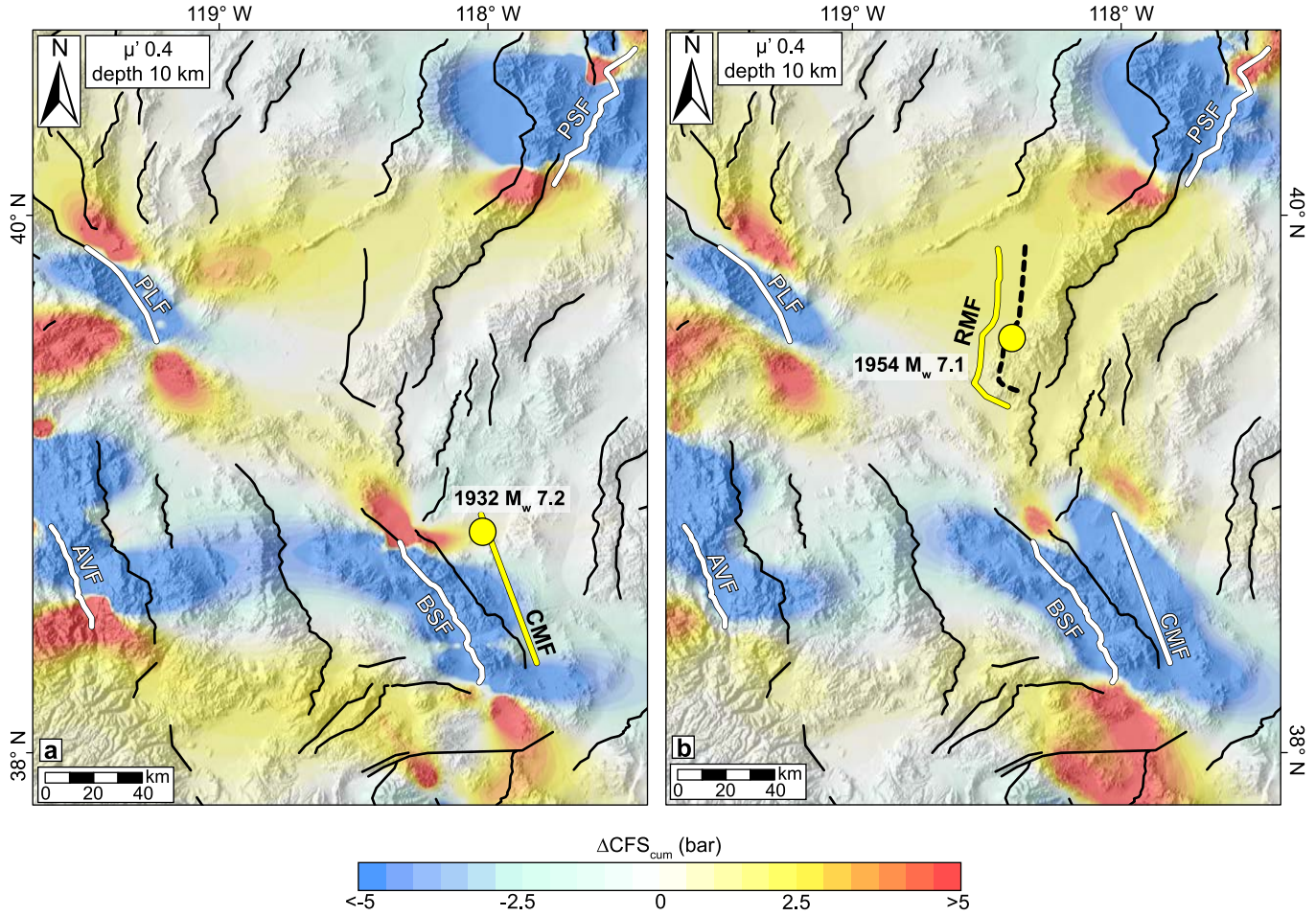

Figure 2.4. Cumulative ΔCFS due to all previous events resolved (a) on the kinematics of the Cedar Mountain Fault (CMF) just before the 1932 earthquake and (b) on the kinematics of the Rainbow Mountain Fault (RMF) just before the 1954 earthquake. Thick white lines are the source faults; thick yellow lines are the receiver faults; dashed black lines represent the depth contour of the receiver fault at calculation depth; yellow circles are the earthquake epicenters. AVF, Antelope Valley Fault; BSF, Benton Springs Fault; PLF, Pyramid Lake Fault; PSF, Pleasant Valley Fault.

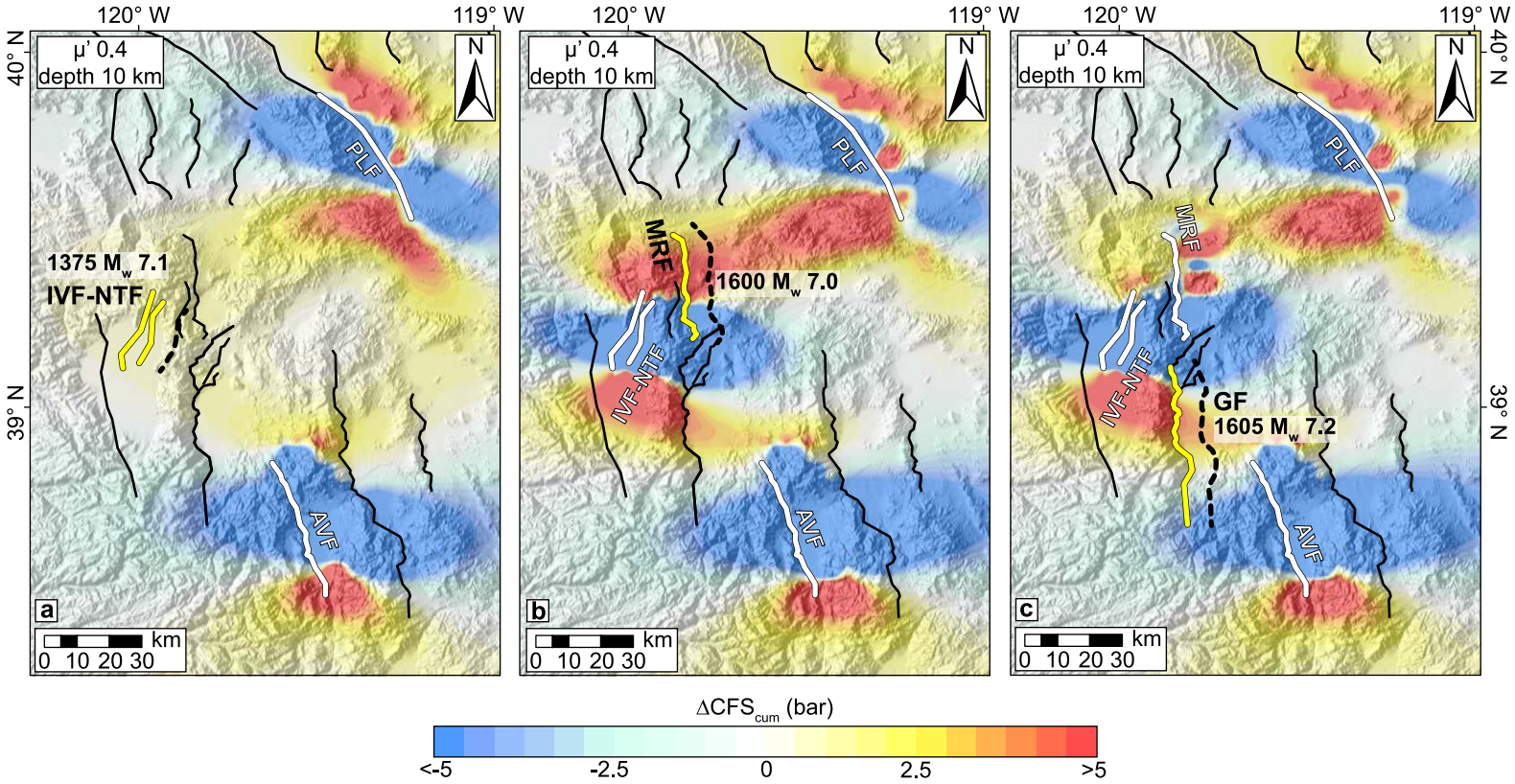

Figure 2.5. Cumulative ΔCFS due to all previous events resolved (a) on the kinematics of the Incline Village-North Tahoe fault (IVF-NTF) just before the 1375 earthquake, (b) on the kinematics of the Mount Rose fault (MRF) just before the 1600 earthquake, and (c) on the kinematics of the Genoa fault (GF) just before the 1605 earthquake. Thick white lines are source faults; thick yellow lines are receiver faults; dashed black lines represent the depth contour of the receiver fault at calculation depth. AVF, Antelope Valley fault; PLF, Pyramid Lake fault.

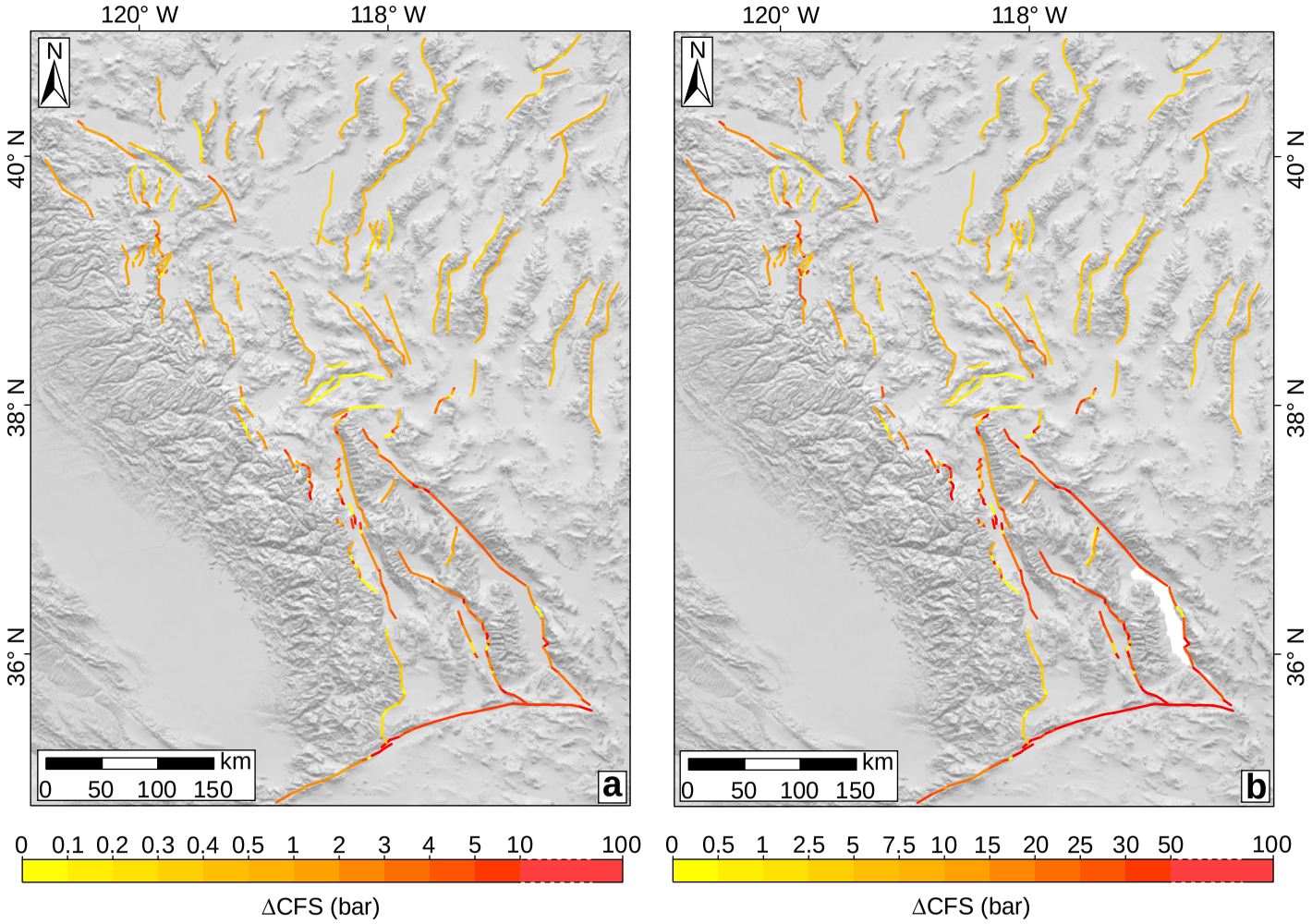

Figure 2.6. Interseismic ΔCFS (tectonic loading) for a time interval of (a) 100 years and (b) 1000 years, calculated with the back-slip method [*Savage*, 1983] on the orientation and kinematics of each modeled fault. For each segment, the maximum interseismic ΔCFS is shown, regardless of depth.

Figure 2.7. Cumulative ΔCFS from all the studied event combined, calculated (a) on the kinematics of the Black Mountains fault (BMF), (b) on the kinematics of the Honey Lake Fault (HLF), (c) on the kinematics of the Mohawk fault system (MFS) and (d) on the kinematics of the Pyramid Lake Fault (PLF). Thick white lines are the source faults; thick yellow lines are receiver faults; dashed black lines represent the depth contour of the receiver fault at calculation depth. AVF, Antelope Valley Fault; GF, Genoa fault; GAF, Garlock fault; IVF-NTF, Incline Village-North Tahoe fault; MRF, Mount Rose fault; PVF, Panamint Valley fault.

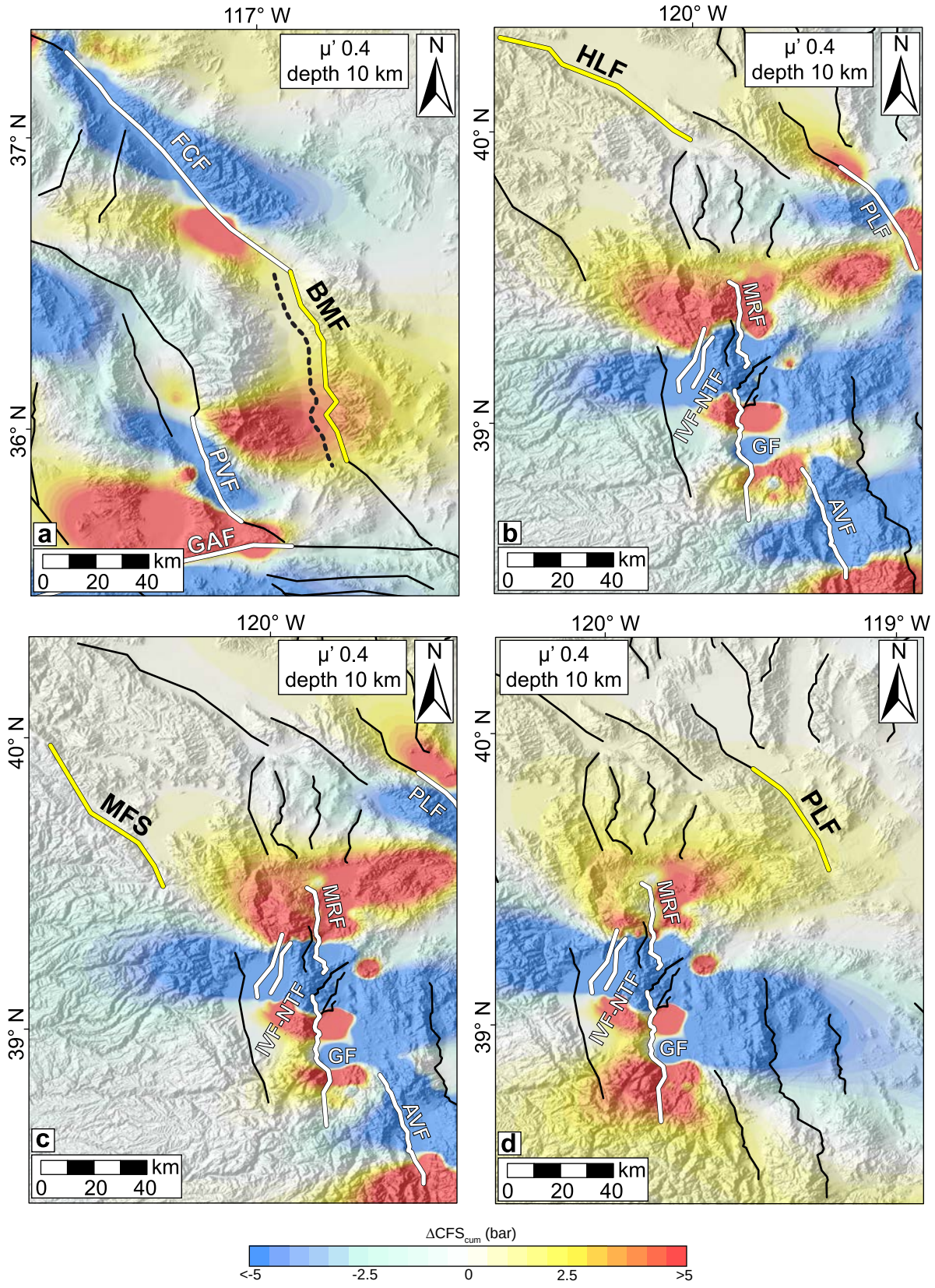
117° W
120° W
120° W
119° W
37° N
36° N
40° N
39° N
40° N
39° N
μ' 0.4
depth 10 km
N
FCF
BMF
PVF
GAF
HLF
PLF
MRF
IVF-NTF
GF
AVF
MFS
a
b
c
d
km
0 20 40
ΔCFS$_{cum}$ (bar)
<-5
-2.5
0
2.5
>5

Figure 2.7

Figure 2.8. Cumulative ΔCFS from all the studied event combined, calculated (a) on the kinematics of the Saline Valley section of the Hunter Mountain Fault (HMF(SV)), (b) on the kinematics of the Hunter Mountain section of the Hunter Mountain Fault (HMF(HM)), (c) on the kinematics of the White Mountains Fault (WMF), (d) on the kinematics of the Wassuk Range Fault (WRF), (e) on the kinematics of the Dixie Valley Fault (northern segment) (DVF(NS)), and (f) on the kinematics of the Fish Lake Valley Fault (FLF). Thick white lines are the source faults; thick yellow lines are the receiver faults; dashed black lines represent the depth contour of the receiver fault at calculation depth. BSF, Benton Springs Fault; CMF, Cedar Mountain Fault; DVF, Dixie Valley Fault; FCF, Furnace Creek Fault; FLFa, Fish Lake Valley Fault (Leidy Creek segment);, FLFb, Fish Lake Valley Fault (Oasis segment); FPF, Fairview Peak Fault; GAF, Garlock Fault; OVF, Owens Valley Fault; PSF, Pleasant Valley Fault; PVF, Panamint Valley Fault; RMF, Rainbow Mountain Fault.

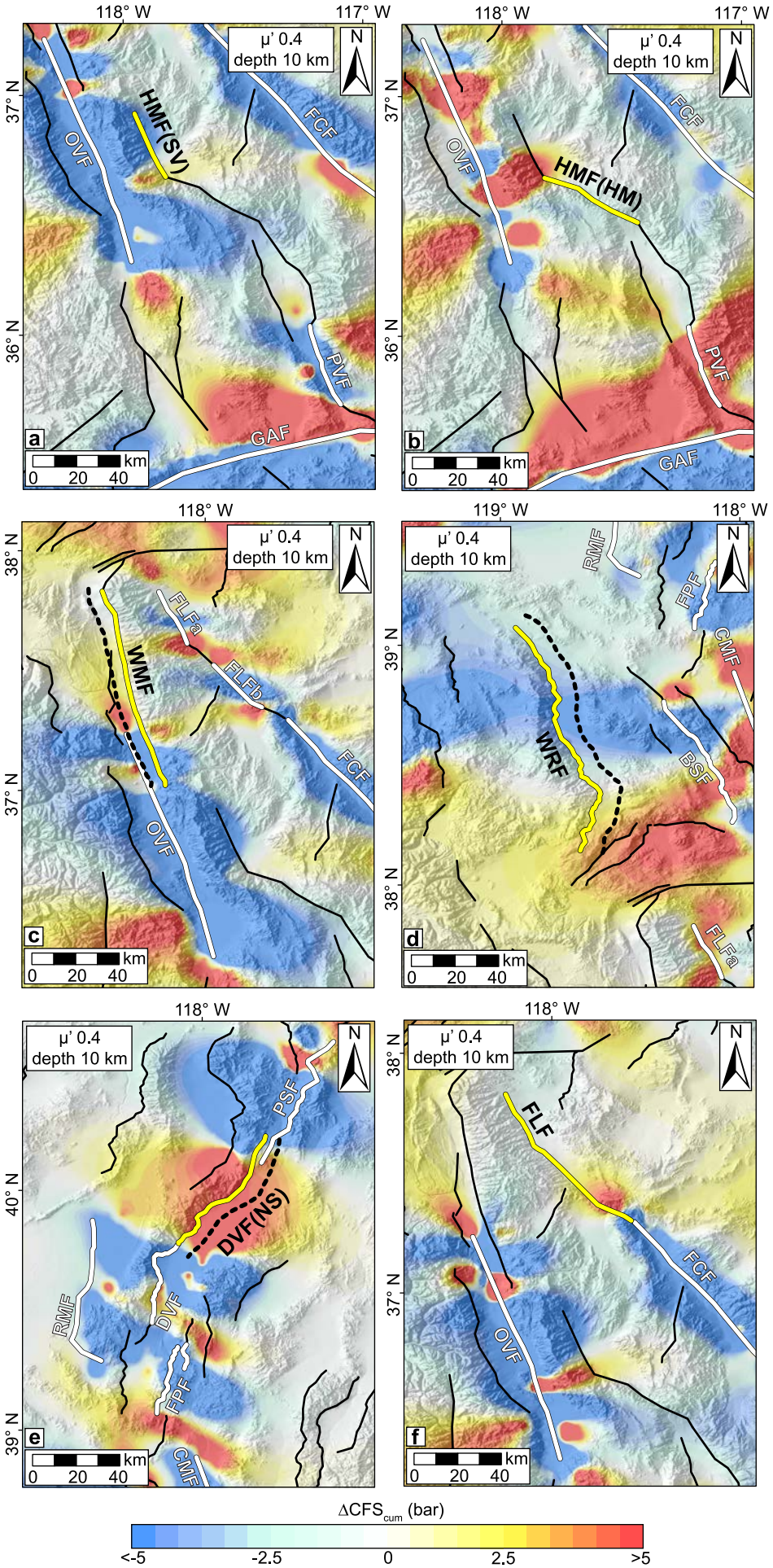
118° W
117° W
37° N
36° N
μ' 0.4
depth 10 km
N
HMF(SV)
OVF
FCF
PVF
GAF
a
km
0 20 40
HMF(HM)
b
38° N
WMF
FLFa
FLFb
c
119° W
RMF
FPF
CMF
WRF
BSF
d
39° N
PSF
DVF(NS)
DVF
e
FLF
f
ΔCFS$_{cum}$ (bar)
<-5
-2.5
0
2.5
>5

Figure 2.8

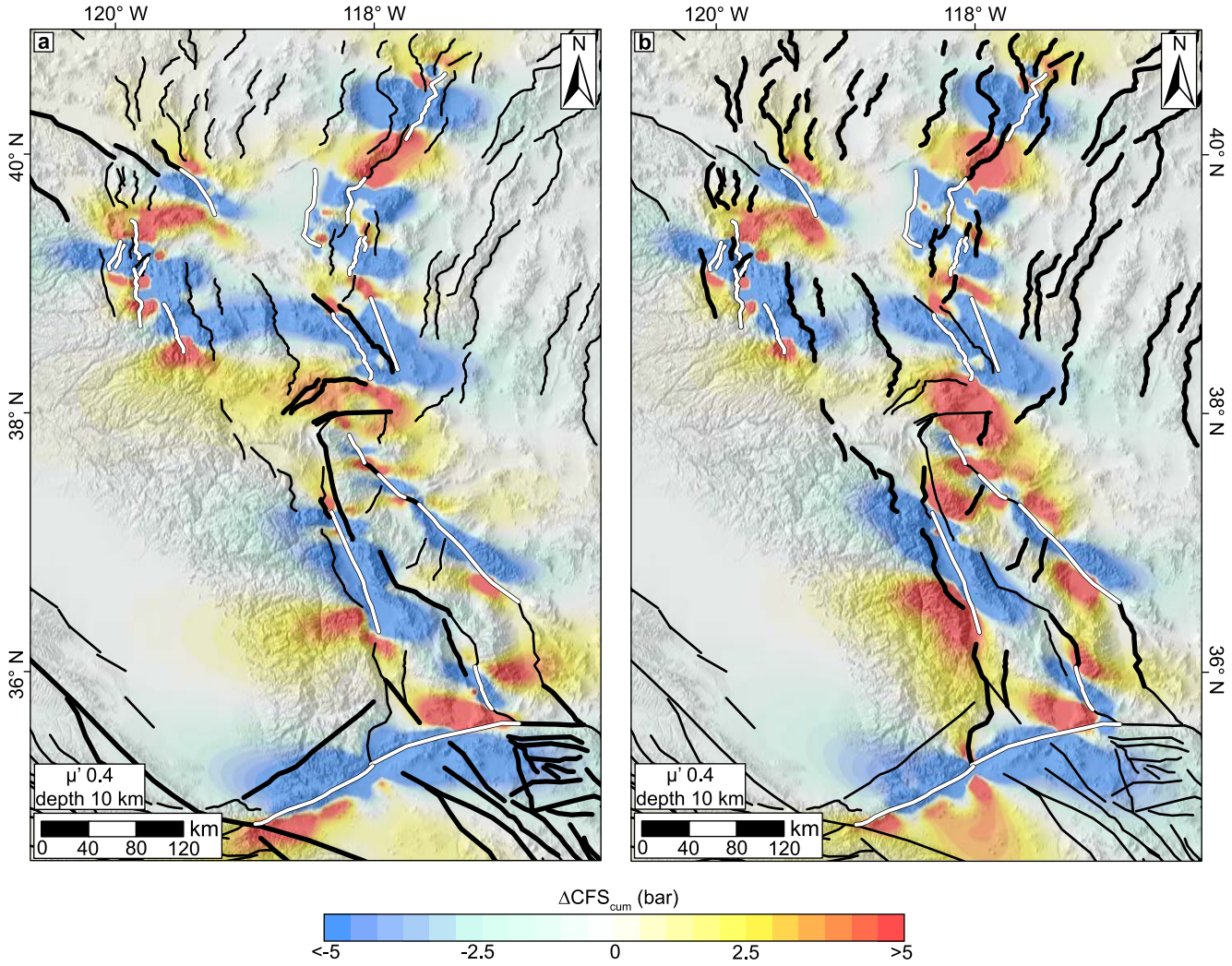

Figure 2.9. Present-day cumulative ΔCFS from all the studied events combined, calculated (a) on optimally oriented strike-slip faults, and (b) on optimally oriented normal faults. Thick white lines are the source faults. Thick black lines are the faults with dominantly strike-slip kinematics in Figure 2.9a, and dominantly normal kinematics in Figure 2.9b.

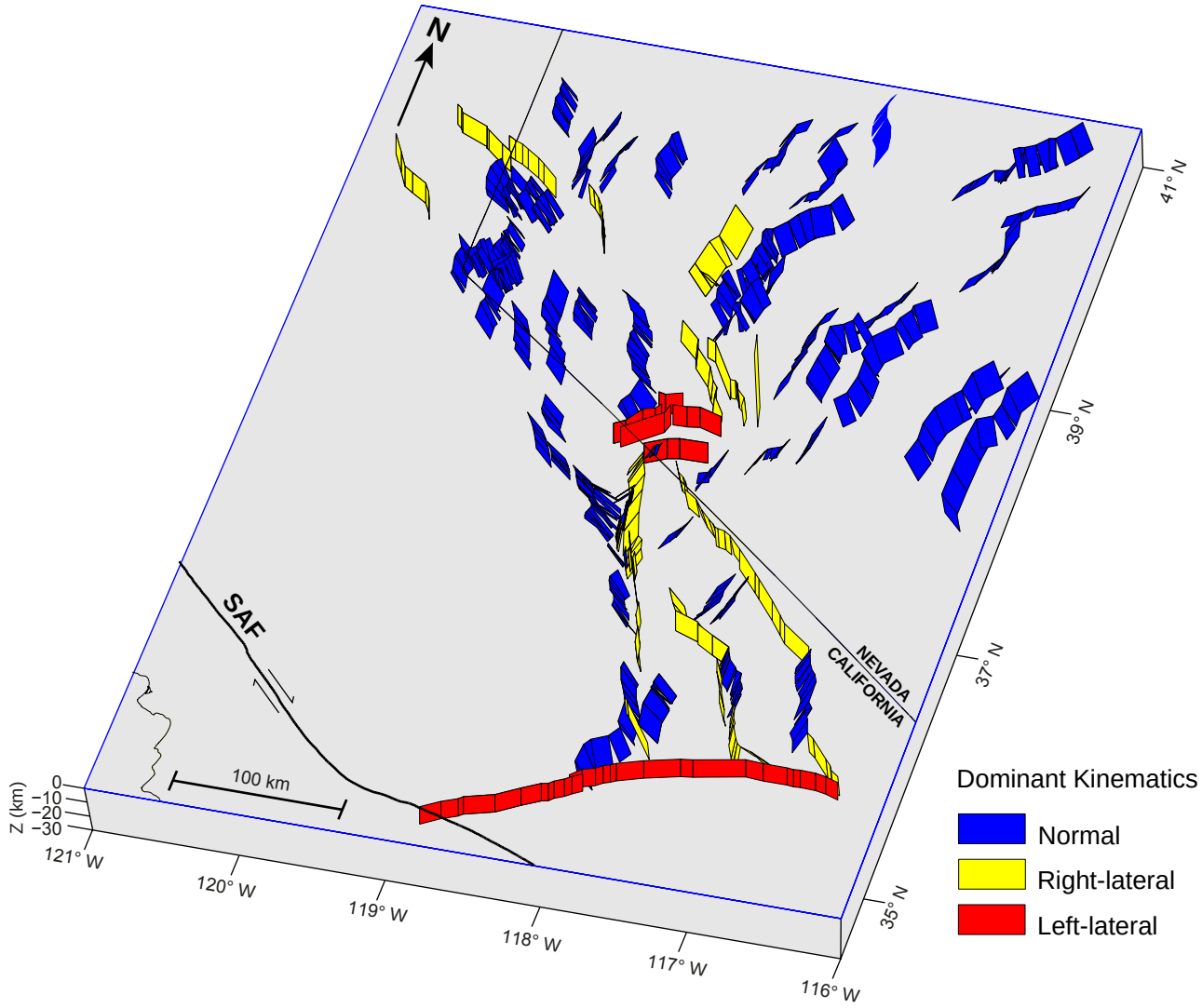

Figure 2.10. 3-D fault geometry in eastern California and western Nevada.

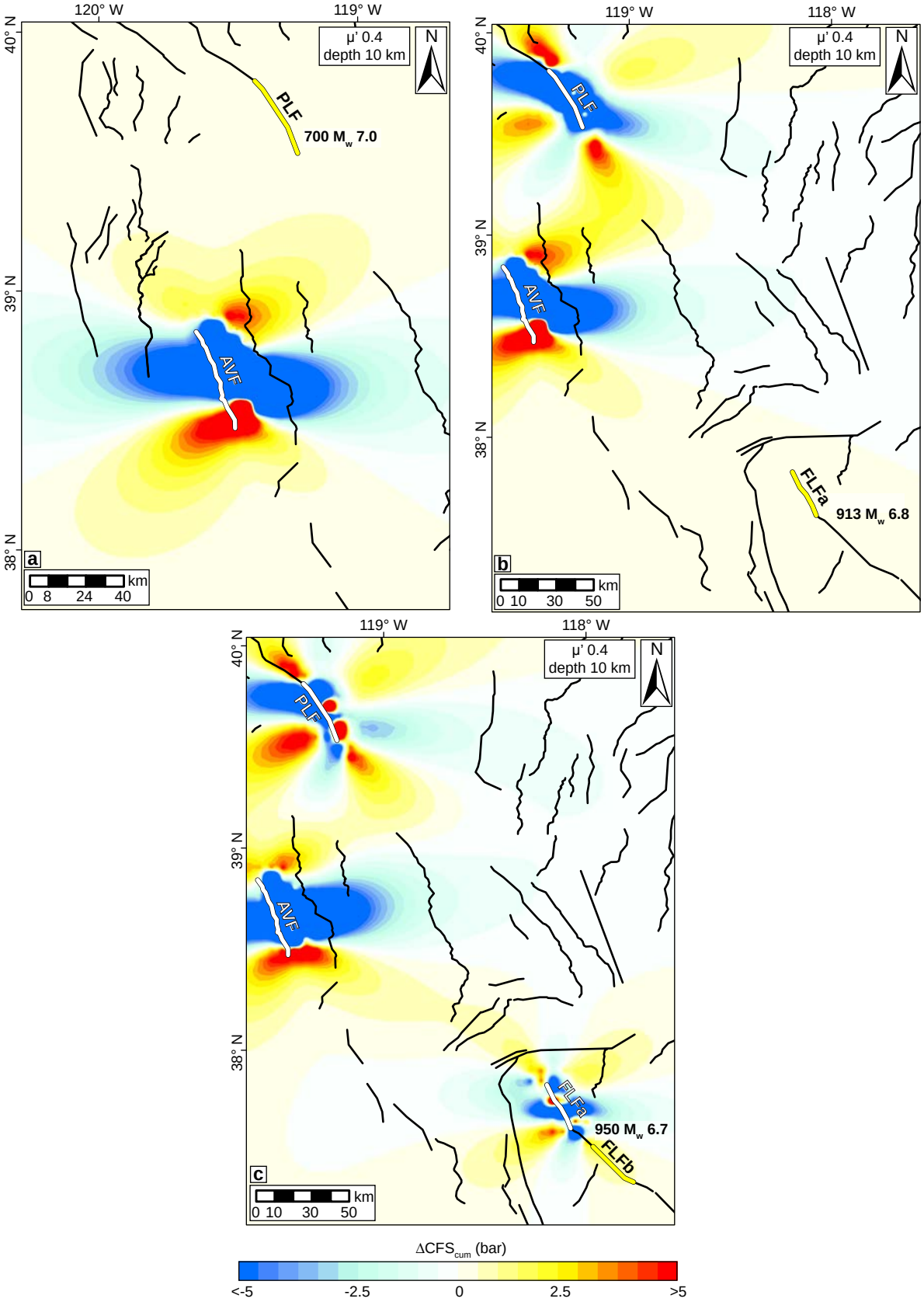

Figure 2.11. Cumulative ΔCFS due to all previous events resolved (a) on the kinematics of the Pyramid Lake fault (PLF) just before the 700 earthquake, (b) on the kinematics of the Fish Lake Valley Fault (Leidy Creek segment) (FLFa) just before the 913 earthquake, and (c) on the kinematics of the Fish Lake Valley Fault (Oasis segment) (FLFb) just before the 950 earthquake. Thick white lines are source faults; thick yellow lines are receiver faults. AVF, Antelope Valley fault.

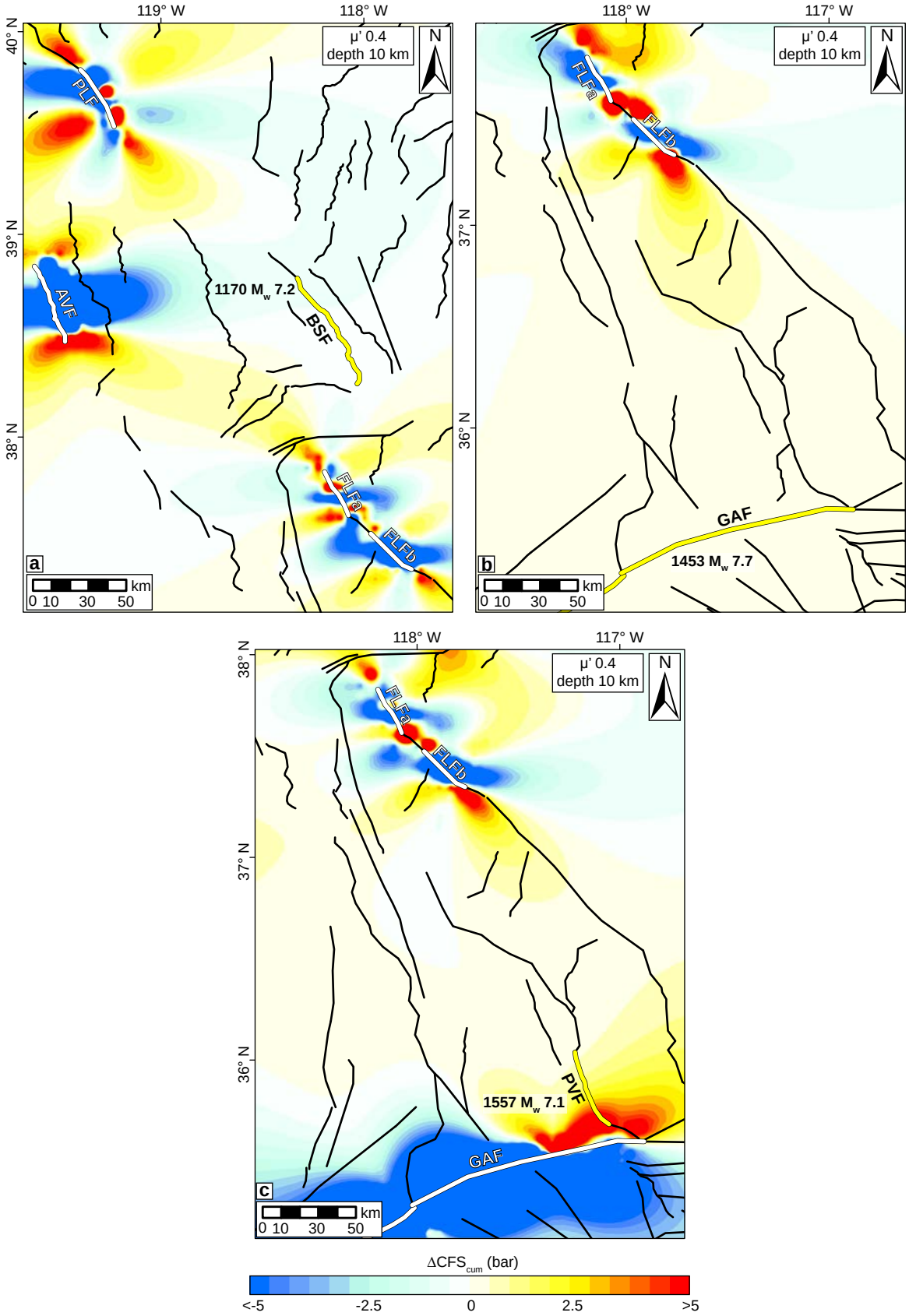

Figure 2.12. Cumulative ΔCFS due to all previous events resolved (a) on the kinematics of the Benton Spring fault (BSF) just before the 1170 earthquake, (b) on the kinematics of the Garlock fault (GAF) just before the 1453 earthquake, and (c) on the kinematics of the Panamint Valley fault (PVF) just before the 1557 earthquake. Thick white lines are source faults; thick yellow lines are receiver faults. AVF, Antelope Valley fault; FLFa, Fish Lake Valley fault (Leidy Creek segment); FLFb, Fish Lake Valley fault (Oasis segment); PLF, Pyramid Lake fault.

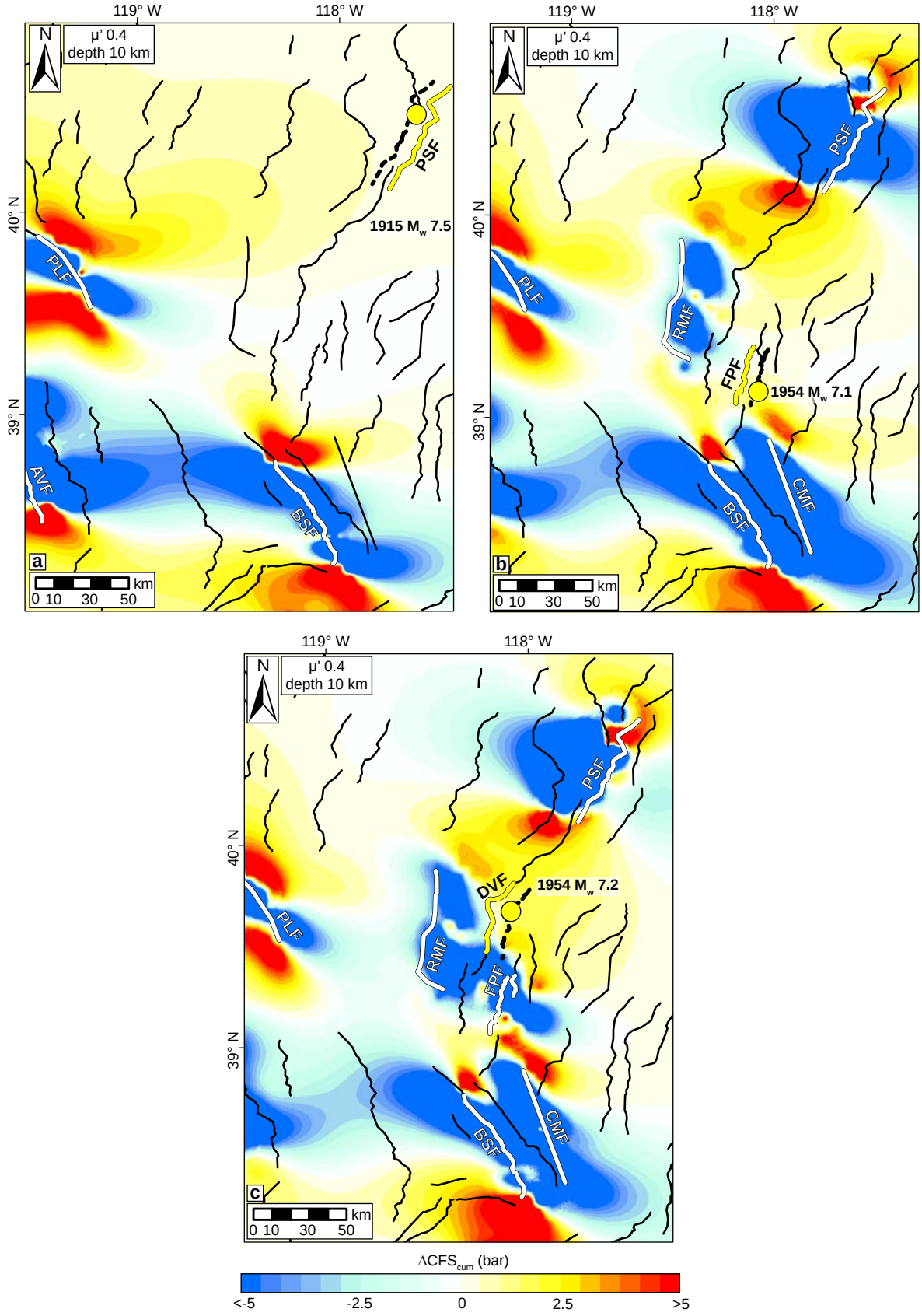

Figure 2.13. Cumulative ΔCFS due to all previous events resolved (a) on the kinematics of the Pleasant Valley fault (PSF) just before the 1915 earthquake (yellow circle), (b) on the kinematics of the Fairview Peak fault (FPF) just before the 1954 earthquake (yellow circle), and (c) on the kinematics of the Dixie Valley fault (DVF) just before the 1954 earthquake (yellow circle). Thick white lines are source faults; thick yellow lines are receiver faults, dashed black lines represent the depth-countour of the receiver fault at calculation depth. AVF, Antelope Valley fault; BSF, Benton Spring fault; CMF, Cedar Mountain fault; PLF, Pyramid Lake fault; RMF, Rainbow Mountain fault.

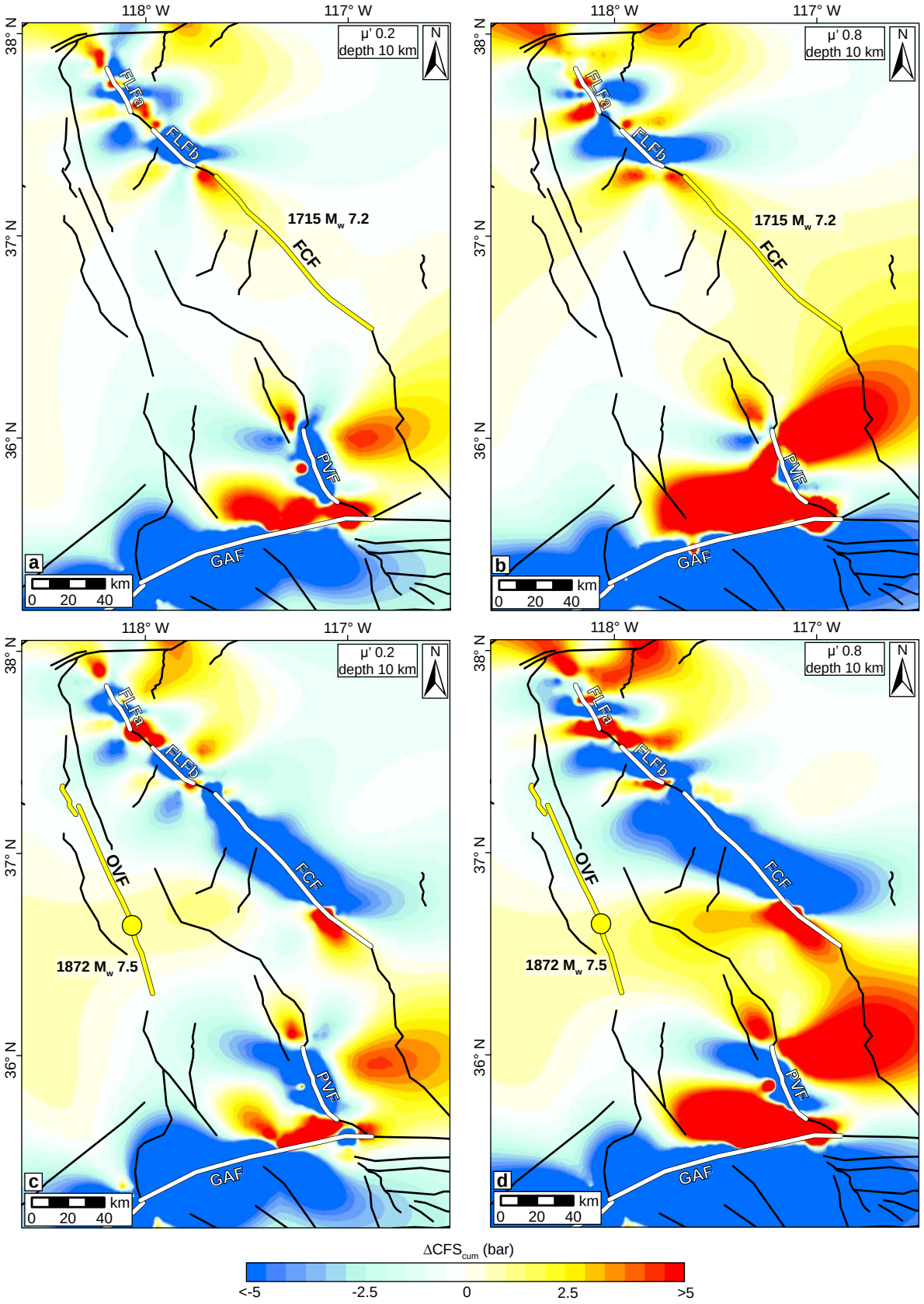

Figure 2.14. Cumulative ΔCFS due to all previous events resolved (a, b) on the kinematics of the Furnace Creek fault (FCF) just before the 1715 earthquake, and (c, d) on the kinematics of the Owens Valley fault (OVF) just before the 1872 earthquake (yellow circle), calculated for two different effective friction coefficients (μ'). Thick white lines are source faults; thick yellow lines are receiver faults, yellow circles are earthquake epicenters. FLFa, FIsh Lake Valley fault (Leidy Creek segment); FLFb, FIsh Lake Valley fault (Oasis segment); GAF, Garlock fault; LCF, Leidy Creek fault segment; OSF, Oasis fault segment; PVF, Panamint Valley fault.

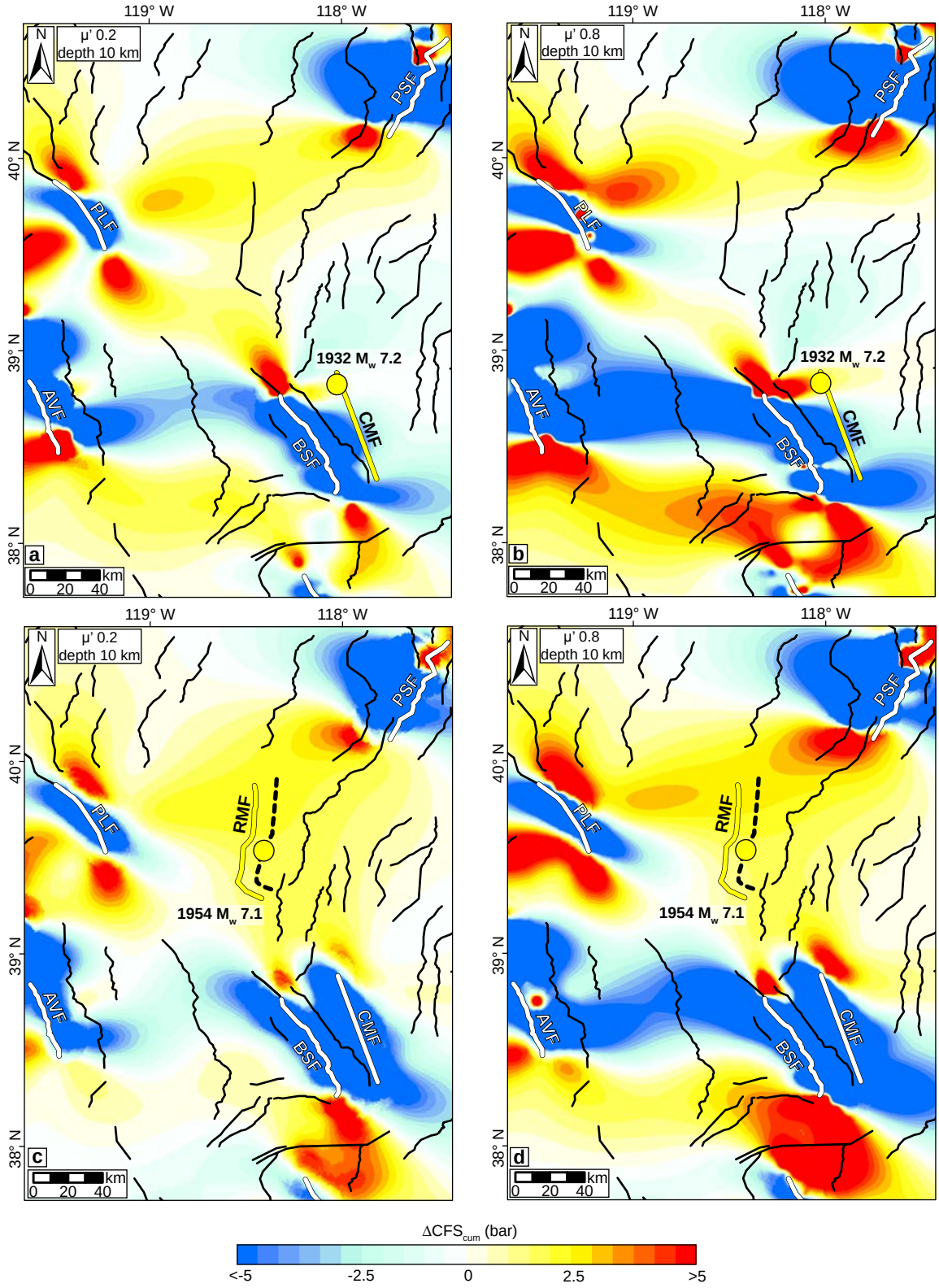

Figure 2.15. Cumulative ΔCFS due to all previous events resolved (a, b) on the kinematics of the Cedar Mountain fault (CMF) just before the 1932 earthquake (yellow circle), and (c, d) on the kinematics of the Rainbow Mountain fault (RMF) just before the 1954 earthquake (yellow circle), calculated for two different effective friction coefficients (μ'). Thick white lines are source faults; thick yellow lines are receiver faults, dashed black lines represent the depth-countour of the receiver fault at calculation depth, yellow circles are earthquake epicenters. AVF, Antelope Valley fault; BSF, Benton Springs fault; PLF, Pyramid Lake fault; PSF, Pleasant Valley fault.

Figure 2.16. Cumulative ΔCFS due to all previous events resolved (a, b) on the kinematics of the Incline Village-North Tahoe fault (IVF-NTF) just before the 1375 earthquake, (c, d) on the kinematics of the Mount Rose fault (MRF) just before the 1600 earthquake, and (e, f) on the kinematics of the Genoa fault (GF) just before the 1605 earthquake, calculated for two different effective friction coefficients (μ'). Thick white lines are source faults; thick yellow lines are receiver faults, dashed black lines represent the depth-countour of the receiver fault at calculation depth. AVF, Antelope Valley fault; PLF, Pyramid Lake fault.

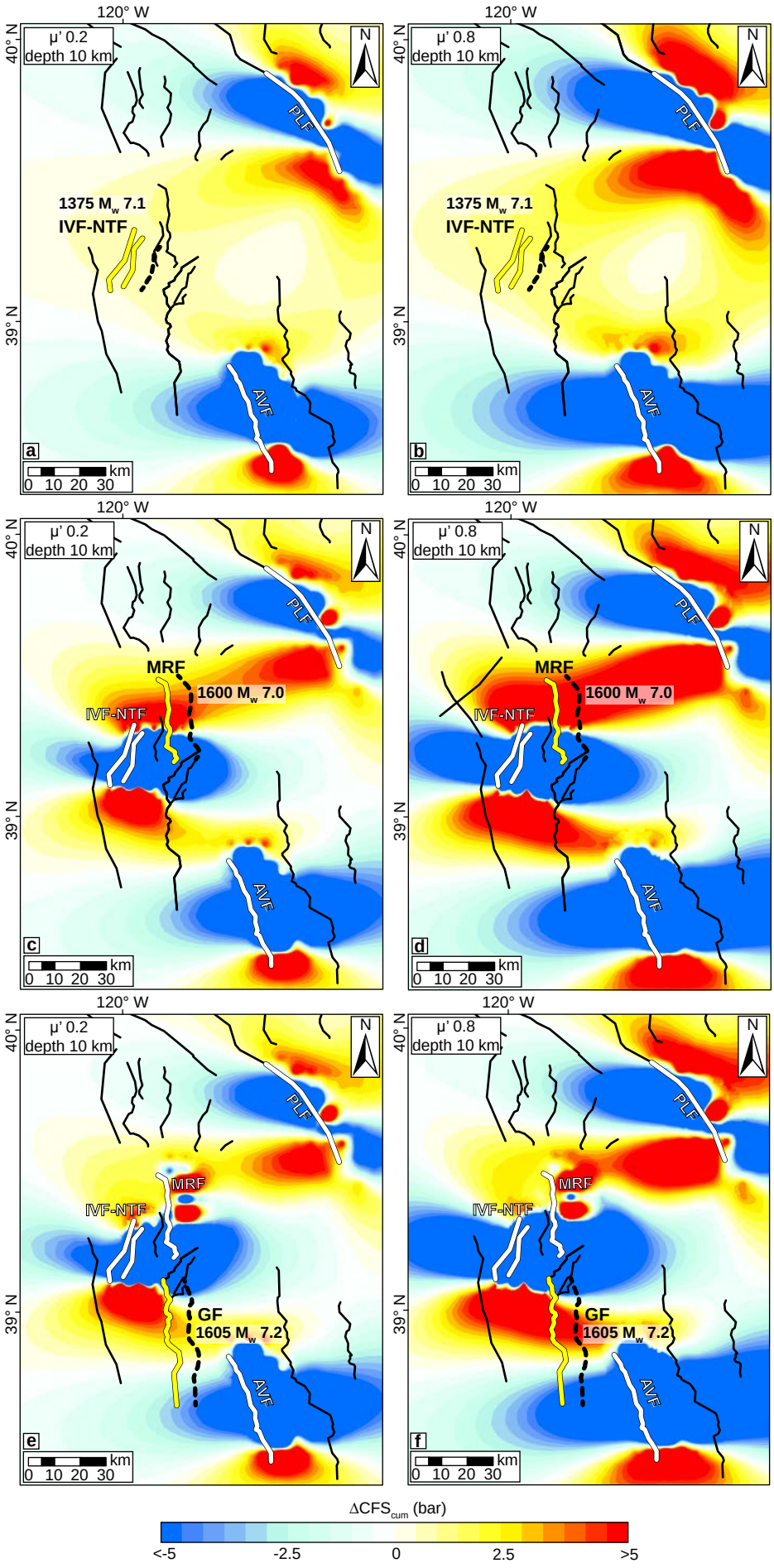
120° W
40° N
39° N
μ' 0.2
depth 10 km
μ' 0.8
N
PLF
AVF
1375 M_w 7.1
IVF-NTF
MRF
1600 M_w 7.0
GF
1605 M_w 7.2
a
b
c
d
e
f
km
0 10 20 30
ΔCFS$_{cum}$ (bar)
<-5
-2.5
0
2.5
>5

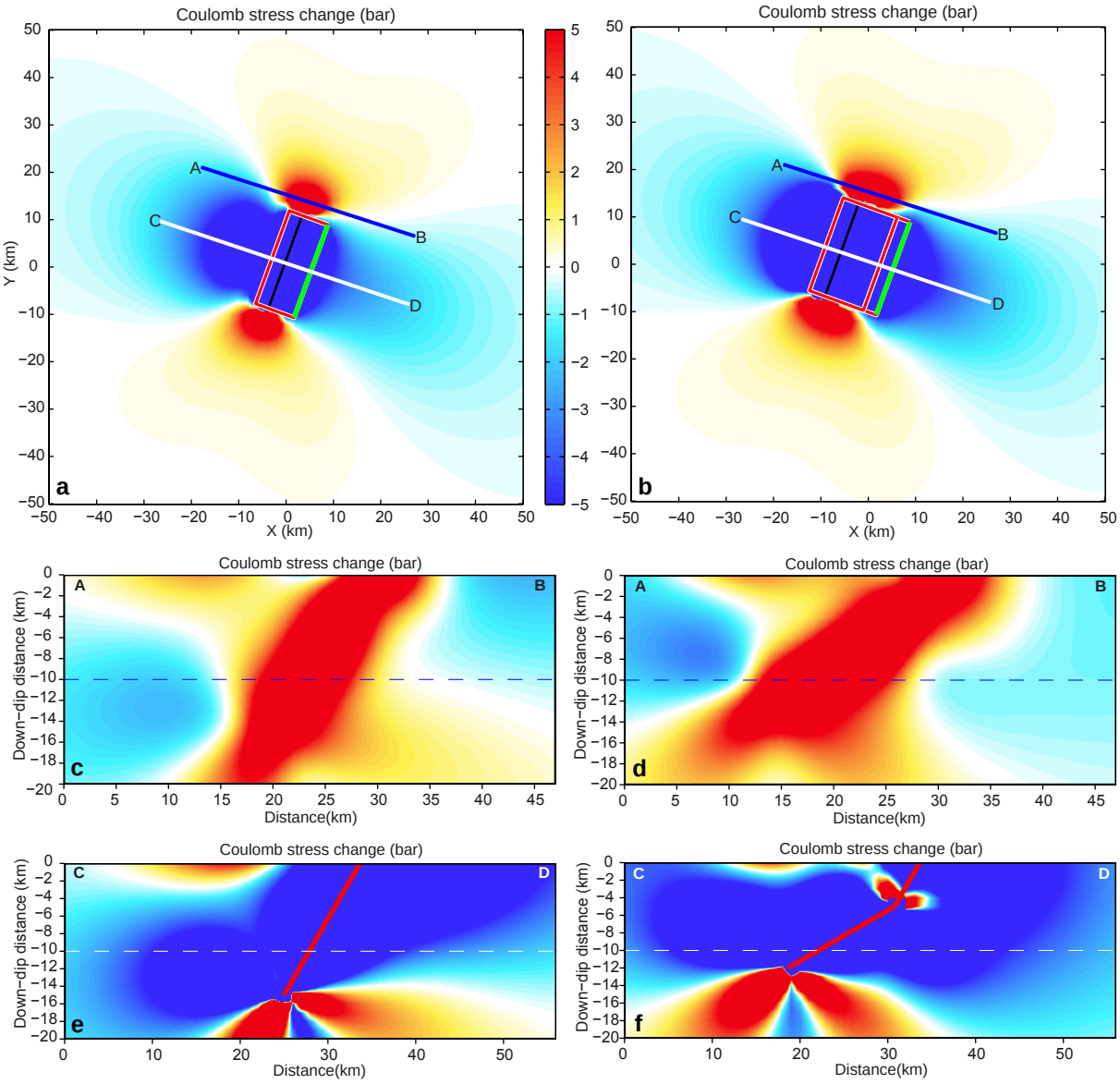

Figure 2.17. Coseismic ΔCFS due to a Mw 6.8 earthquake considering (a, c, e) a 60° dipping normal fault and (b, d, f) a normal fault with a dip of 60° for the first 5 km and 30° for the last 7 km. Map views (a, b) are calculated at 10 km depth.

Chapter 3

The effect of stress changes on time-dependent earthquake probability: an example from the central Wasatch Fault Zone, Utah, USA

3.1 Abstract

Static and quasi-static Coulomb stress changes produced by large earthquakes can modify the probability of occurrence of subsequent events on neighboring faults. In order to better understand and minimize the uncertainties in this kind of approach, which is based on physical (Coulomb stress changes) and statistical (probability calculations) models, we focused our study on the Wasatch fault zone (WFZ), a well-studied active normal fault system having abundant geologic and paleoseismological data. Paleoseismological trench investigations of the WFZ indicate that at least 24 large, surface-faulting earthquakes have ruptured the fault's five central, 35–59-km long segments since ~7 ka. Our goal is to determine if the stress changes due to selected paleoevents have significantly modified the present-day probability of occurrence of large earthquakes on each of the segments.

For each segment, we modeled the cumulative (coseismic + postseismic) Coulomb stress changes (ΔCFS_{cum}) due to earthquakes younger than the most recent event and applied the resulting values to the time-dependent probability calculations. Results from the probability calculations predict high percentages of occurrence for the Brigham City and Salt Lake City segments, due to their long elapsed times (>1-2 kyr) when compared to the Weber, Provo, and Nephi segments (< 1 kyr). We also found that

the Brigham City, Salt Lake City, and Provo segments have accumulated ΔCFS_{cum} larger than 10 bar, whereas the Weber segment has experienced a stress drop of 5 bar.

Our results indicate that the ΔCFS_{cum} resulting from earthquakes postdating the youngest events on the segments significantly affect the probability calculations only for the Brigham City, Salt Lake City, and Provo segments. In particular, the probability of occurrence of a large earthquake in the next 50 years on these three segments may be underestimated if a time-independent approach, or a time-dependent approach that does not consider ΔCFS, is adopted.

3.2 Introduction

Physical models based on Coulomb stress changes (ΔCFS) have been implemented in statistical probabilistic fault-based seismic hazard models for different regions such as Japan, Turkey, California, and Italy [*Toda et al.*, 1998; *Stein*, 1999; *Parsons*, 2005; *Console et al.*, 2008; *Pace et al.*, 2014]. These studies have shown that static stress changes may significantly alter the probability of future earthquake occurrence, but such results are subject to large uncertainties associated with the quantity and quality of information concerning input parameters. In Japan, Turkey and in the region around the San Andreas fault in California these uncertainties are minimized by the existence of abundant data on large historical, instrumental and paleoseismological earthquakes [*Toda et al.*, 1998; *Stein*, 1999; *Parsons*, 2005].

If we want to better understand and minimize the uncertainties in this kind of approach, then a study region rich in both geologic and paleoseismological data must be chosen. In this study we focus on the Wasatch fault zone (WFZ), a normal fault zone located at the eastern boundary of the Basin and Range Province (BRP) (Figure 3.1). The WFZ has been the focus of at least 25 published paleoseismological investigations

in the last ~20 years [*Personius et al.*, 2012], and at least 24 large, surface-faulting earthquakes have been detected on its five main central segments [*DuRoss et al.*, 2016, and references therein]. In addition several geodetic studies [*Friedrich et al.*, 2003; *Chang et al.*, 2006; *Hammond et al.*, 2009] have shown that, despite the absence of large historical earthquakes, the WFZ is characterized by higher deformation rates (~ 2 mm/yr) when compared to the central B&R and the WBR. Therefore the WFZ is an ideal study region for time-dependent probabilistic seismic hazard analysis, first because of its richness in both geologic and geodetic data, and second because it represents a possible source of risk for the ~2 millions of people living along the Wasatch Front.

A time-dependent approach to calculating probabilities of future large earthquakes on five central segments of the WFZ had already been adopted by *McCalpin and Nishenko* [1996]. These authors estimated high probabilities of $M \geq 7$ earthquakes on the Brigham City and Salt Lake City segments for the next 50 and 100 years, and relatively low probabilities on the other three segments (Weber, Provo, Nephi), which have experienced large earthquakes between 600 and 1100 years B.P. *Chang and Smith* [2002] introduced for the first time the effect of stress changes on probabilistic seismic hazard analysis of the Salt Lake City segment of the central WFZ. *McCalpin and Nishenko* [1996] however based their study on relatively old paleoseismological data, and did not include any paleoseismological earthquakes as sources of stress changes. Because past events may have modified the stress accumulated on the WFZ, they would most likely have an effect on time-dependent probabilistic seismic hazard calculations. *Chang and Smith* [2002] took in consideration only the effect of possible future events on adjacent segments (Weber and Provo), and did not take into account probability changes due to paleoseismological earthquakes.

In order to evaluate the possible influence of ΔCFS on a probabilistic seismic hazard model for the central WFZ, here we use paleoseismological data to compute the probability of single-segment earthquakes occurring on five segments (Brigham City, Weber, Salt Lake City, Provo, and Nephi) of the central WFZ. We then model the cumulative (coseismic + postseismic) Coulomb stress changes (ΔCFS_{cum}) due to several paleoseismological events on the WFZ and surrounding faults, and we include it in the probabilistic seismic hazard calculations. Finally, we compare the two probabilistic models, one including and the other not including ΔCFS, and discuss the impact of the chosen physical and statistical parameters on our results. We show that regardless of any uncertainties in this approach, ΔCFS_{cum} strongly affects the time-dependent probability of a large earthquake on the Brigham City, Salt Lake City and Provo segments.

3.3 Late Holocene history of the central WFZ and surrounding faults

The WFZ is located on the boundary between the extensional Basin and Range province to the west and the more stable Colorado Plateau to the east (Figure 3.1). It extends north - south for ~ 350 km, from southern Idaho to central Utah, and it accommodates ~ 50% of the deformation across the eastern Basin and Range [*Chang et al.*, 2006]. Based on geomorphic, structural, and paleoseismological studies, the WFZ has been divided into ten segments [*Machette et al.*, 1992; *McCalpin and Nishenko*, 1996], six of which (Brigham City, Weber, Salt Lake City, Provo, Nephi, Levan) define the central WFZ (Figure 3.1). All these segments show evidence of late Holocene activity and are considered capable of $M \geq 7$ single-segment ruptures, supporting the characteristic earthquake model [*Schwartz and Coppersmith*, 1984]. Studies have been carried out as well on some active faults that surround the WFZ as well. In particular,

recent events have been identified on the East Great Salt Lake fault and on the West Valley fault zone [*Dinter and Pechmann*, 2005; *DuRoss and Hylland*, 2015]. In the following sections we introduce the available geologic and paleoseismological data for the central WFZ, the East Great Salt Lake fault and the West Valley fault zone. In particular we describe the faults used as sources or receivers for Coulomb stress calculations, and the ones for which probability calculations were computed.

3.3.1 Paleoseismological data

In order to model Coulomb stress changes and to compute probability calculations here we use only data from paleoseismological investigations. All the faults described in the following subsections were used as source faults for ΔCFS calculations. However we compute probability calculations just for five segments of the central WFZ (Brigham City, Weber, Salt Lake City, Provo, Nephi). This is due to the fact that in only for these five segments enough paleoseismrological data are available for this purpose.

3.3.1.1 Central WFZ: Brigham City segment

Based on reinterpretation of previous studies, and data from new trench-sites, *Personius et al.* [2012] found evidence for at least four surface-rupturing events in the last ~ 6000 years (Table 3.1). The latest earthquake on the Brigham City segment is dated 2400 ± 300 years B.P., which represents the oldest most recent event among the ones documented for the six segments of the central WFZ (Table 3.1). A younger event (~1100 years B.P.) has been identified by *DuRoss et al.* [2012] on the southern part of the segment. According to the available data, the authors concluded that this may be an evidence for a spillover rupture from the adjacent Weber segment.

3.3.1.2 Central WFZ: Weber segment

The Weber segment is characterized by a mostly linear fault trace (Figure 3.1). Data from four trench-sites [*Swan et al.,* 1980, 1981; *McCalpin et al.*, 1994; *Nelson et al.*, 2006; *DuRoss et al.*, 2009] were re-evaluated by *DuRoss et al.* [2011] in order to define a chronology of surface-rupturing earthquakes for the entire segment. These authors concluded that five surface-rupturing earthquakes occurred on the Weber segment in the last ~ 6000 years (Table 3.1), with the most recent event dated 600 ± 100 B.P. In addition, a partial rupture on the southern part of the Brigham City segment may have been the result of a spill-over from the penultimate earthquake (1100±600 years B.P.) that occurred on the Weber segment [*DuRoss et al.,* 2012].

3.3.1.3 Central WFZ: Salt Lake City segment

The Salt Lake City segment (Figure 3.1) is the most complex segment in the central WFZ. It is divided in three subsections, from north to south: the Warm Springs, East Bench, and Cottonwood sections separated by left steps [*Personius and Scott*, 1992; *DuRoss and Hylland*, 2015]. In a recent work *DuRoss and Hylland* [2015] integrated data from previous paleoseismological investigations [*Swan et al.*, 1980; *Black et al.*, 1996; *McCalpin*, 2002] and concluded that at least seven surface-rupturing events occurred on the Salt Lake City segment in the last ~ 10000 years, the latest of which is dated 1340 ± 160 years B.P. In the other hand *McCalpin* [2002], based onan high resolution stratigrapgic record, interpreted a period of seismic quiescence on the Salt Lake City segment between about 17 and 9 ka. There is some uncertainty concerning the rupture lengths in these earthquakes, and concerning the overall behavior of this segment, because of the complexity of the structure and the less-than-ideal resolution of the data [*DuRoss and Hylland*, 2015].

3.3.1.4 Central WFZ: Provo segment

The Provo segment is the longest segment (~ 70 km) of the central WFZ and has a nearly continuous surface trace. (Figure 3.1). Several paleoseismological studies have been carried out on this segment, including a ~12 m deep, ~105 m long "megatrench" located in its southern part [*Olig et al.,* 2011]. Integrated data from different sites [*DuRoss et al.,* 2016] show evidence for at least five surface-rupturing earthquakes on the Provo segment, with the most recent event at 600 ± 50 years B.P. (Table 3.1).

3.3.1.5 Central WFZ: Nephi segment

The Nephi segment is composed of two strands, a more complex northern strand which is separated from the Provo segment by a ~8 km wide right step, and a more linear southern strand that terminates near the town of Nephi (Figure 3.1). Paleoseismological data from several trench sites shows evidence for at least six surface-rupturing events in the last ~6000 years (Table 3.1) [*DuRoss et al.,* 2014; 2016; *Crone et al.,* 2014]. Due to the structural complexity of this segment, the possible interaction of ruptures on the two strands with the adjacent Provo segment is still unclear. Recent studies from *Bennett et al.* [2014; 2015] suggest a complex rupture for the most recent event on the Nephi segment (200 ± 70 years B.P.). This rupture scenario includes the southernmost strand of the Nephi segment, the southern part of the northern strand, and a spillover onto the southern part of the Provo segment.

3.3.1.6 Central WFZ: Levan segment

Unlike the other segments of the WFZ, the Levan segment has very limited paleoseismological data. In fact, only two late Holocene events have been recognized by a relatively old study from *Jackson* [1991], with the latest event dated at 1000 ± 100 years B.P. The limited data available precludes the inclusion of this segment in probability calculations.

3.3.1.7 West Valley fault zone

The antithetic West Valley fault zone consists mainly of two subparallel main faults, known as the Granger fault and the Taylorsville fault (Figure 3.1). These faults, together with the Salt Lake City segment of the WFZ, form an intra-basin graben in the northern part of the Salt Lake Valley [*DuRoss and Hylland*, 2015]. Recent studies have shown evidence for at least three earthquakes in the last 6000 years, with the latest dated at 1400 ± 700 years B.P. [*Hylland et al.*, 2014; *DuRoss and Hylland*, 2014, 2015]. These events have ages similar to those of the Salt Lake City segment. Therefore *DuRoss and Hylland* [2014, 2015], also based on mechanical and geometric models, hypothesized possibly synchronous ruptures of the West Valley fault zone and the Salt Lake City segment.

3.3.1.8 Great Salt Lake fault

Located beneath the Great Salt Lake (Figure 3.1), this is a west-dipping normal fault. Several seismic profiles crossing it evidence two main active segments, the Fremont segment in the north, and the Antelope segment in the south [*Dinter and Pechmann*, 2005]. Radiocarbon dating of hanging wall deposits revealed a relatively

young surface-rupturing event on the Antelope segment, dated at 586 ± 200 years B.P. [*Dinter and Pechmann*, 2005].

3.3.2 Slip rates

Knowledge of the tectonic loading acting on the faults is necessary for the implementation of ΔCFS in probabilistic seismic hazard calculations. In order to calculate tectonic loading, we need the slip rate of all faults involved.

Slip rates are derived from either geodetic or geologic data. Rates are usually not in agreement between these two types, due to the difference in the timescale observation, and to the different parameters that are recorded by each method [*Friedrich et al.*, 2003; *Malservisi et al.*, 2003; *Chang et al.*, 2006].

We use here geological displacement rates based on mean vertical displacements measured from the paleoseismological data available for the five main segments of the central WFZ (Table 3.1) [*DuRoss et al.*, 2016]. This choice is justified by the fact that geological data are characterized by a better resolution along the segments of the central WFZ when compared to geodetic data.

3.4 Methods

3.4.1 Probabilistic seismic hazard calculations

Time-dependent seismic hazard approaches are based on the assumption that the probability of occurrence of an earthquake in a given time period depends on the time since the last event, as the fault is loaded to failure by plate motions. Several probability distributions have been used, for example lognormal, Weibull, and Brownian passage time (BPT) [*Fitzenz and Nyst*, 2015]. Lately, the BPT model has been preferred [*Field*

et al., 2015] because a BPT distribution has a hazard rate that tends towards a constant at long elapsed times, and it is considered to better approximate the elastic rebound theory [*Matthews et al.*, 2002]. The other models instead either monotonically increase (Weibull), or decrease asymptotically to zero (lognormal). Here we use the BPT distribution to calculate the conditional probability of occurrence of a characteristic earthquake on each of the five main segments of the central WFZ in the next 50 years. The BPT probability is given by *Matthews et al.*, [2002] as:

$$P(t \leq T \leq t + \Delta T) = \int_t^{t+\Delta T} \sqrt{\left(\frac{T_m}{2\pi\alpha^2 u^3}\right)} e^{\left(-\frac{(u-T_m)^2}{2\alpha^2 T_m u}\right)} du \qquad [3.1]$$

$$\mathrm{P}(\mathrm{T_{elap}} \leq \mathrm{T} \leq \mathrm{T_{elap}} + \Delta\mathrm{T} | \mathrm{T} > \mathrm{T_{elap}}) = \frac{\mathrm{P}(\mathrm{T_{elap}} \leq \mathrm{T} \leq \mathrm{T_{elap}} + \Delta\mathrm{T})}{1 - \mathrm{P}(0 \leq \mathrm{T} \leq \mathrm{T_{elap}})} \qquad [3.2]$$

Where T_m is either the mean recurrence time, or the time between maximum expected earthquakes of similar size on the individual source faults. α is the aperiodicity value (or coefficient of variation, CV, defined as the standard deviation of the recurrence time over the mean), T_{elap} is the time elapsed since the last event on the source fault, ΔT is the time-window examined (in our case 50 years), and T represents the actual position of the fault in the BPT curve.

In order to compare our results with a time-independent approach, we calculate for each fault segment the time-independent Poissonian probability of occurrence of a characteristic earthquake which is given by:

$$\mathrm{P_{poiss}} = 1 - \mathrm{e}^{-\mathrm{t}/\mathrm{Tm}} \qquad [3.3]$$

Where t is the observation period (50 years), and T_m is the mean recurrence time. In the next sections we will examine the approaches adopted to define the average recurrence time (T_m), the coefficient of variation (CV), and the maximum magnitude (M_{max}) expected for each of the five main segments of the central WFZ.

3.4.1.1 Average recurrence time (T_m) and coefficient of variation (CV)

We used the paleoseismological data described in section 3.3.1 (Table 3.1) as input for the open source Matlab® *FiSH* code *Recurrence Parameters* (*RP*) [*Pace et al.*, 2016] to calculate T_m and CV for the Brigham City, Weber, Salt Lake City, Provo, and Nephi segments of the central WFZ. *RP* uses a Monte Carlo approach for determining earthquake recurrence parameters from paleoseismological catalogs, as proposed by *Parsons* [2008]. The results of the simulation are then presented as arithmetic mean of the recurrence time (T_m) and its coefficient of variation (CV). *RP* also presents the results assuming that the events follow three different probability distributions (Poisson, BPT, Weibull).

3.4.1.2 Maximum expected magnitude (M_{max})

The size of the maximum expected earthquake is a required input in both time-dependent and Poissonian earthquake probability calculations. Here we use the *FiSH* tool *Moment Budget* (MB) [*Pace et al.*, 2016] to define the characteristic maximum magnitude (M_{max}) and the relative standard deviation for each of the five segment of the central WFZ. The code uses different empirical and analytical relationship based on subsurface length, rupture area, seismic moment, and aspect ratio [*Wells and Coppersmith*, 1994], to calculate four values of M_{max} and the relative standard deviation. Then the code calculates the sum of the different M_{max} values treated as probability density functions (SumD), and defines a mean M_{max} and a standard

deviation that will be used in the probability calculations. These values, the time elapsed since the last event (T_{elap}), T_m and CV are in turn used as input for the *FiSH* tool *Activity Rates* (AR) [*Pace et al.*, 2016], the code that we used to calculate BPT and Poissonian earthquake probabilities.

3.4.2 Coulomb stress changes calculations

The concept of Coulomb stress change (ΔCFS) has been extensively applied in the past two decades to explore the spatial and temporal relationships among active faults [e.g., *King et al.*, 1994; *Stein et al.*, 1994, 1997; *Harris and Simpson*, 1998; *Stein*, 1999; *Parsons et al.*, 2000; *Marsan*, 2003; *Ma et al.*, 2005; *Toda et al.*, 2008].

The change in Coulomb failure stress (ΔCFS) due to an earthquake on a source fault is:

$$\Delta CFS = \Delta\tau - \mu'(\Delta\sigma_n) \qquad [3.4]$$

Where $\Delta\tau$ is the change in shear stress for receiver faults calculated on the orientation and kinematics of either optimally oriented faults, or specified faults. μ' is the coefficient of effective friction, and $\Delta\sigma_n$ is the change in normal stress. Positive changes encourage faulting and thus increase the likelihood of an earthquake, while negative changes inhibit faulting and decrease the likelihood of an earthquake.

A combination of time-independent static (coseismic) and time-dependent quasi-static (postseismic) modeling is often used to explain earthquake interactions at different time-scales [*Freed*, 2005]. Postseismic calculations take into account the redistribution of Coulomb stress due to viscoelastic relaxation of the lower crust and the upper mantle, which is thought to play an important role in earthquake triggering at

time-scales longer than 5 years [e.g. *Chéry et al*., 2001; *Pollitz et al.,* 2003; *Lorenzo-Martín et al*., 2006; *Ali et al*., 2008; *Shan et al.,* 2013; *Verdecchia and Carena,* 2015]. In our case, we operate at a earthquake-cycle time-scale (~1000 years), and then we consider both coseismic and postseismic stress changes. Here in fact, we calculate the cumulative (coseismic + postseismic) Coulomb stress changes (ΔCFS_{cum}) accumulated by each of the five studied segments of the central WFZ during the time between their most recent event and the present-day. Our approach is based on the fact that after a characteristic earthquake the stress on the segment responsible for the event is dropped to zero, and the subsequent events on neighboring faults may modify its state of stress. For instance if we consider that the most recent event on the Brigham City segment was ~ 2400 years B.P., all the younger events on the surrounding segments and faults may have brought the Brigham City segment closer or not to failure.

Once that ΔCFS_{cum} for each segment has been defined, it can then be applied to the time-dependent earthquake probability calculations. This could be done in two ways as explained by *Stein et al.* [1997] and *Toda et al.* [1998]. The first requires a modification of T_m:

$$T'_m = T_m - (\Delta CFS/\dot{\tau}) \qquad [3.5]$$

Whereas the second option requires a modification of T_{elap}

$$T'_{elap} = T_{elap} + (\Delta CFS/\dot{\tau}) \qquad [3.6]$$

Where $\dot{\tau}$ is the tectonic loading.

We computed the tectonic loading by using the late Holocene slip rate values discussed in section 3.3.2. We extended the fault plane to a depth of 150 km in to the upper mantle, locked the fault between the surface and 15 km depth, and allowed the fault to slip freely between 15 and 150 km depth. The stress is thus transferred to the locked part of the fault [*Stein et al.*, 1997; *Cowie et al.*, 2013]. We calculated tectonic loading for each of the five studied segments of the central WFZ with the software *Coulomb 3.3* [*Toda et al.*, 2011], which is based on an elastic half-space. We used instead the multilayered viscoelastic half-space based code *PSGRN/PSCMP* [*Wang et al.*, 2006] to calculate coseismic and postseismic ΔCFS. *PSGRN/PSCMP* requires a rheologic model of the lithosphere as an input. We used the rheologic model defined by *Chang et al.* [2013] for the Intermountain Seismic Belt. These authors, based on trilateration and GPS data from 1973 to 2000, inferred a Maxwell rheology with 16 km of elastic upper and middle crust, 14 km of viscous lower crust, and 70 km of viscous upper mantle, with viscosity values of 10^{21} Pa s and 10^{19} Pa s respectively. Finally a range of effective friction coefficient (μ') between 0.2 and 0.8 is usually considered in studies of earthquake interactions [e.g. *Shan et al.*, 2013; *Verdecchia and Carena*, 2015]. Because the influence on the results of this parameter is not the focus of this study, we use an average single value of μ' equal to 0.4 in both ΔCFS_{cum} and tectonic loading calculations

3.4.3 Fault geometry and slip models for paleoseismological earthquakes

The ΔCFS distribution due to an earthquake depends on the geometry and slip models of source faults, and on the geometry and kinematics of receiver faults. When we model paleoseismological earthquakes, these parameters are usually characterized by a number of uncertainties due to the quality and density of the available

paleoseismological data. For each of the studied five segments of the central WFZ, vertical displacement data for each event exist at multiple locations [*DuRoss*, 2008; *DuRoss et al.*, 2016, and references therein], therefore we used these data to better constrain the slip distribution of the earthquakes in our models. For the Levan segment, the West Valley fault zone, and the Great Salt Lake fault, we used the measured coseismic offsets [*Jackson*, 1991; *DuRoss and Hylland*, 2015; *Dinter and Pechmann*, 2005] to built a laterally-tapered slip distribution, with maximum values at the center of the fault. For the WFZ, the dip angle and its possible changes with depth are debated, and several fault geometries based on different data types have been proposed in the past 20 years. Paleseismological data [*McCalpin et al.*, 1994] and earthquake moment tensors [*Doser and Smith*, 1989] indicate a high-angle (~70°), planar geometry. Conversely, seismic reflection data indicate a listric geometry (6°-30°) soling into an older low-angle fault, likely a reactivated thrust fault, at shallow depths [*Smith and Bruhn*, 1994; *Velasco et al.*, 2010]. Based on thickness of the sedimentary fill in the Salt Lake Valley and the projected position of the preextension paleosurface, *Friedrich et al.* [2003] inferred an average dip of ~20° - 30° for the active trace at depth, in agreement with the seismic reflection data [*Smith and* Bruhn, 1994]. We adopt a planar geometry and a 50° dip angle for the WFZ, in following the 50° ± 10° value proposed by the *Basin and Range Province Earthquake Working Group* [*Lund*, 2012], and consistent with analyses of large historical Basin and Range earthquakes. We set the locking depth at 15 km, based on the maximum depth of seismicity in the area [*Arabasz et al.*, 1992].

3.5 Results

Starting with the Brigham City segment, we modeled the ΔCFS_{cum} accumulated by each of the five segments of the central WFZ in the period of time starting from their most recent event to present-day. Afterwards, we computed the conditional probability of occurrence of a characteristic earthquake on these segments, and we then recalculated the conditional probability by adding the effect of ΔCFS_{cum} to the equation. Because the most recent event on the Nephi segment is the youngest among the studied earthquakes, this segment of the central WFZ has not been affected by Coulomb stress changes, and therefore the time-dependent probability calculated for the Nephi segment is the only one to which ΔCFS_{cum} does not apply.

3.5.1 Cumulative ΔCFS in the central WFZ

The most recent event on the Brigham City segment is the oldest of all the most recent events identified on any of the central WFZ segments (Table 3.1). Figure 3.1a shows that the largest positive ΔCFS_{cum} (~11 bar) (Table 3.2) on the Brigham City segment is located in its southern part. This is due to the effect of the most recent and the penultimate events on the adjacent Weber segment. The other source faults are too far to have a significant effect on the static stress field on the Brigham City segment (Figure 3.2a).

For the Weber segment due to the uncertainties in dating events, we explored two different scenarios: (1) Provo and Great Salt Lake most recent events are older than the most recent event on the Weber segment, and (2) the latest rupture on the Weber segment is older than the Provo and Great Salt Lake most recent events (Figure 3.2b). In the first case only the most recent event on the Nephi segment is part of the model with no effects on the Weber segment. In the second case, however, the most recent

event on the Great Salt Lake fault transfers negative ΔCFS_{cum} (-5.7 bar) (Table 3.2) on the Weber segment, whereas the Provo segment is too far to produce an effect on it (Figure 3.2b).

The most recent events on the Weber and Provo segments, and on the Great Salt Lake fault, strongly affect the Salt Lake City segment. These earthquakes produced positive stress changes larger than 10 bar (Table 3.2) in the northern and southern parts of the Salt Lake City segment (Figure 3.2c).

Finally the Nephi segment, which produced the youngest of all the paleoseismological earthquakes in the central WFZ, transferred significant positive ΔCFS_{cum} (12.5 bar) (Table 3.2) to the Provo segment, with maximum values concentrated in the region where the fault bends nearly 90° from a NNW-SSE to a NNE-SSW direction (Figure 3.2d).

3.5.2 Conditional probabilitiy for the central WFZ segments

Results from Monte Carlo simulations of paleoseismological data show similar values of recurrence time (T_m) for the five studied segments of the central WFZ, ranging from 1068 years for the Nephi segment to 1333 years for the Salt Lake City segment (Figures 3.3 to 3.7, Table 3.1). Although all the segments present values of the coefficient of variation (CV) smaller than one, some small differences are noticeable among segments. Based on the results from the Monte Carlo simulations carried out using *Recurrence Parameters*, we determined a range of CV between 0.1 and 0.4 for the Brigham City and Weber segments (Figures 3.3 and 3.4, Table 3.1), between 0.3 and 0.5 for the Salt Lake City segment (Figure 3.5, Table 3.1), between 0.3 and 0.6 for the Provo segment (Figure 3.6, Table 3.1), and between 0.2 and 0.5 for the Nephi segment (Figure 3.7, Table 3.1). The maximum magnitudes (M_{max}) calculated for each

of the five segments range from a minimum of 7.0 ± 0.2 for the Brigham City, Salt Lake City and Nephi segments to a maximum of 7.2 ± 0.2 for the Provo segment (Figure 3.8, Table 3.1). Using T_m, CV, and M_{max} as input parameters we determined the conditional (BPT) probability of a characteristic earthquake (M_{max} ± sd) for each segment of the central Wasatch fault for the next fifty years.

Our results show that the highest time-dependent probability of occurrence is for the Brigham City and Salt Lake City segments. For the first it ranges between 79% (CV = 0.1) and 12% (CV = 0.4) (Figure 3.9a, Table 3.3), whereas for the second it is between 6% (CV = 0.5) and 9% (CV = 0.3) (Figure 3.11a, Table 3.3). In both cases the time-independent probability is lower than the time-dependent one (Figures 3.9a and 3.11a, Table 3.3). The Provo segment has a BPT probability that ranges between 0.8% (CV = 0.3) and 3.9% (CV = 0.6) (Figure 3.12a, Table 3.3), and the for the Weber segment we computed time-dependent probability between 0.0% and 2.1% (Figure 3.10a, Table 3.3). In the case of the Provo and Weber segments instead, the variations between time-dependent and time-independent probability are comparable. Both the Provo and the Weber segments have a Poissonian probability of 3.5%. Finally, we determined a BPT probability very close to zero for the Nephi segment, against the 4.1% computed with a Poissonian approach (Figure 3.13, Table 3.3).

3.5.3 The effect of ΔCFS_{cum}

As already mentioned in section 3.4.2 (Equations 3.5 and 3.6), the implementation of ΔCFS in probabilistic seismic hazard models requires the knowledge of the tectonic loading ($\dot{\tau}$) acting on the studied faults. On the basis of late Holocene slip rates, we calculated values of tectonic loading for the central WFZ that range

between 0.036 bar/year (Salt Lake City segment) and 0.051 bar/year (Provo segment) (Figure 3.14, Table 3.2).

Of the five segments, the Brigham City segment has the highest probability of producing a characteristic earthquake in the next fifty years. The choice of whether we include ΔCFS by changing the elapsed time (T_{elap}) or the recurrence time (T_m) has a significant effect on the resulting probability. For this segment, the probability change is very small when T_{elap} is modified, whereas it may be 13% to 39% higher when the T_m is modified (Figure 3.9, Table 3.3). The Weber segment is the only one that has been affected by negative rather than positive ΔCFS_{cum}. Probability decreases (from 2.1% to 1.1%) are however only significant for CV equal to 0.4 (Figure 3.10, Table 3.3). Like for the Brigham City segment, the ΔCFS_{cum} impact on the earthquake probability for the Salt Lake City segment is heavily dependent on the approach used. By modifying T_{elap}, we calculated a 30% increase in the probability (from 9% to 11.5%) for CV equal to 0.3, but a 70% increase (from 9% to 15.5%) can be obtained by modifying T_m instead (Figure 3.11, Table 3.3).

According to our results, the largest effect of introducing ΔCFS_{cum} is for the Provo segment, where the probability increases up to five times (Figure 3.12, Table 3.3). The largest probability values for this segment (5.9%) is the result of a model with CV equal to 0.6 and an approach based on modification of T_m (Figure 3.12, Table 3.3).

3.6 Discussion

3.6.1 Significance of observed stress patterns on the central Wasatch Fault Zone

Because of the geometry of the fault network, high values of positive ΔCFS_{cum} ($\geq$ 10 bar) accumulate on the Brigham City, Salt Lake City, and Provo segments due to

the effect of earthquakes on their along-strike neighbors (Figure 3.2a, c, d). Negative ΔCFS_{cum} instead is transferred between parallel faults, as we can observe for the pair Great Salt Lake fault-Weber segment (Figure 3.2b). Antithetic structures like the West Valley fault zone may encourage faulting on the Weber segment, but this effect is negligible compared to that of the other faults nearby (Great Salt Lake fault and Salt Lake City segment).

An important parameter that can change our results is the temporal order of the modeled paleoevents. As already described in section 3.5.1 these uncertainties only affect the results on the Weber segment for which we examined two different scenario strongly depended on the absolute order of occurrence of the earthquakes on the Great Salt Lake fault, Provo segment, and Weber segment. Both scenarios are equally possible and therefore we do not choose one over the other.

In cases like ours, where faults terminations are very close to one another, the estimated extent of the coseismic rupture could affect the final results. Because here we modeled paleoseismological events, the information about rupture termination is strongly dependent on the number of sites available along each fault segment. Rupture extents are relatively well-known for the Brigham City [*DuRoss et al*., 2012; *Personius et al*., 2012] and Weber [*DuRoss et al.*, 2011; 2012] segments. The southern extent of the penultimate event on the Weber segment (1100 ± 600 years B.P.), which is modeled here as potential stress source for the Brigham City segment, is unclear [*DuRoss et al.*, 2016]. However, whether the southern part of the Weber segment is included in the rupture model of this event is not important, as it would not significantly change the amount of ΔCFS_{cum} accumulated on the adjacent Brigham City segment. On the other hand, according to the uncertainties in dating the penultimate event on the Weber segment, *DuRoss et al.* [2011] suggested that its southern part may have produced a

partial rupture of the Weber segment at ~ 900 years B.P. If this is the case, this event may have further increased the stress on the adjacent Salt Lake City segment.

The rupture behavior of the Salt Lake City segment is particularly complex. Whereas the most recent event (1300 ± 200 years B.P.) has been identified on the southernmost section (Cottonwood) of the segment, there is no trace of this earthquake in a trench site located in the East Bench section, and no data exist for the northernmost Warm Springs section [*Du Ross and Hylland,* 2015]. Two different scenarios have therefore been proposed by *DuRoss and Hylland* [2015]. In the first the most recent event ruptured both the Cottonwood and East Bench section, but in the East Bench the event could not be identified due to the position of the trench site, located at the northernmost extent of the rupture. In the second scenario, the Cottonwood rupture represents a spillover of a large event originated on the Provo segment. Although paleoearthquakes age ranges strongly support the first scenario, there is no evidence for excluding the second scenario. Modeling ΔCFS_{cum} with the second scenario for the most recent event on the Salt Lake City segment would result in a high value of ΔCFS_{cum} on the East Bench and Warm Springs sections, and negative ΔCFS_{cum} on the Cottonwood section.

The most recent event on the Nephi segment has also produced a complex surface rupture with a possible spill-over on the adjacent Provo segment [*Bennett et al.*, 2014; 2015] as we described in section 3.3.1.5. Some doubts however exist on the age of the event detected on the southernmost part of the northern strand of the Nephi segment (Santaquin site) [*DuRoss et al.*, 2008]. In our model, this part of the Nephi segment ruptures as part of the Nephi most recent event (~ 250 years B. P.). Another possible scenario arises if the event on the Santaquin site is actually older and of age similar to that of the most recent event on the Provo segment (~ 600 years B. P.). In this

second case, the southernmost part of the northern strand of the Nephi segment would represent a spill-over of the Provo segment earthquake. In either case, the amount of ΔCFS_{cum} accumulated on the Provo segment due to the Nephi most recent event would not change.

Finally, for the Levan segment, the West Valley fault zone, and the Great Salt Lake fault, for which limited data are available, we constrained the length of the rupture by applying an empirical relationship between event coseismic displacement and magnitude [*Wells and Coppersmith*, 1994].

3.6.2 Influence of the coefficient of variation (CV) on earthquake probabilities

The choice of the coefficient of variation (CV), defined as the standard deviation of the recurrence times over their mean, can have a significant influence on time-dependent probability calculations. Several studies acknowledge that the coefficient of variation for earthquake recurrence intervals are poorly constrained (e.g. *Ellsworth et al.*, 1999; *Visini and Pace*, 2014), and small differences in the value can lead to order of magnitude differences in earthquake probability forecast.

Based on results of Monte Carlo simulations of the available paleoseismological data (Figures 3.3 to 3.7), we decided to consider a range of values of CV for each studied segment of the central WFZ (Table 3.1). The largest impact of CV is evident in the probability calculated for the Brigham City segment. In fact, we noticed difference in probability up to 70% between CV = 0.1 and CV= 0.4. This is due to the fact that CV = 0.1 (periodic sequence) predicts significantly larger probabilities compared to other values (0.2, 0.3, 0.4), when $T_{elap} >> T_m$ (Figure 3.9). As already shown in section 3.5.2 and Table 3.3, the effect of CV on our final results is significant for all the five segments of the central WFZ. Therefore, we believe that all the values of CV

considered in this work are equally possible and thus choosing a single CV value for the entire central WFZ or even for each individual segment might not be the best solution.

3.6.3 Applying ΔCFS to probabilistic seismic hazard analysis: results from different methods

In section 3.4.2 we describe two different methods commonly used to integrate ΔCFS in time-dependent probability calculations. In the first, Coulomb stress changes affect the recurrence time (T_m) whereas in the second the elapsed time since the last event (T_{elap}) is modified. Although *Stein et al.* [1997] concluded that the two methods yield similar results, this is not true in cases when the T_{elap} is significantly smaller or larger than T_m [*Parsons*, 2005; *Console et al.*, 2008]. In our study this is particularly evident in the Brigham City segment. Here T_{elap} is more than twice T_m (Table 3.1), leading to large differences in probabilities calculated using the two different methods (Table 3.3). However we found this discrepancy also when T_m is similar to T_{elap} as for example in the case of the Salt Lake City segment. Here the probabilities calculated using the first method are significantly larger than the ones predicted by modifying T_{elap} (15.4% against 11.5% for CV = 0.3) (Table 3.3). Finally we did not find any obvious difference for the Weber and Provo segment, for which T_{elap} is nearly half of T_m.

As already discussed by *Parsons* [2005] and *Console et al.* [2008], there is no justification for choosing one method over another. The results from both methods should be considered as part of the uncertainties intrinsic to the integration of ΔCFS and probabilistic seismic hazard calculations. Here, in order to define a single probability of occurrence with its uncertainties, we calculated for each segment both the average and the standard deviation between the probability values in which ΔCFS is

implemented (Table 3.3). Another more conservative option, would be to consider only the highest probability, which in our specific case corresponds to a probability calculated including ΔCFS with modified T_m (Table 3.3).

3.6.4 Model limitations

The oversimplification of a model due to the lack of geological and seismological data in some regions is exemplified by the coseismic slip distribution that had to be adopted in our physical models. Because we are dealing with paleoseismological events, we modeled a tapered slip distribution constrained using the data available from each trench site. This is of course different from the more realistic heterogeneous distribution, but it is still the most reasonable assumption in these cases, where no instrumental or historical data are available. In section 3.4.3 we explored two competing models for the dip angle of the central WFZ: high angle, planar versus shallow listric. A reasonable question for this analysis is the influence of fault geometry on the ΔCFS calculations. *Verdecchia and Carena* [2016] (Chapter 2 of this thesis) compared stress patterns produced by normal faults with different geometries (high angle planar surface vs. listric surface), and concluded that for normal faults the maximum values of coseismic ΔCFS do not change significantly when a constant-dip model and a more complex model are compared.

Another simplification that may affect our results concerns the rheology of the lithosphere used in calculating postseismic ΔCFS. We have used a rheologic model that does not account for horizontal heterogeneities, which in this particular region might in fact exist between the footwall and the hanging wall of the central WFZ. Future work with finite elements instead of dislocation models should be carried out in order to better define the impact of lateral heterogeneities on postseismic ΔCFS.

The last important consideration comes from the statistical model used to calculate the probability of large earthquakes on the central WFZ. We calculate probabilities of a single-segment rupture, excluding any possible spillovers or multisegment ruptures. Paleoearthquakes chronology on the central WFZ generally supports the characteristic earthquake model, but uncertainties in the timing and amount of displacement of the paleoseismological events have strongly suggested the possibility of different scenarios [*Lund*, 2005; 2006; *DuRoss*, 2008, *DuRoss et al.*, 2016]. This has been confirmed by recent paleoseismological investigations [*Crone et al.*, 2014; *DuRoss et al.*, 2012; 2014; *Bennett et al.*, 2014; 2015], which have documented complex coseismic ruptures for the most recent events on the Weber and Nephi segments. We think therefore that more detailed models based on different rupture scenario should be explored in the future, to better characterize the seismic hazard along the WFZ.

3.7 Conclusions

In order to better understand the effect that ΔCFS may have on time-dependent probability calculations, we applied this methods to a well-studied active fault zone (central Wasatch Fault Zone). Here, using paleoseismological data, we modeled the present-day coseismic and postseismic ΔCFS accumulated on the five most studied segment of the central WFZ since their last events. We also calculated the probability of large earthquakes on these segments for the next 50 years, and then added ΔCFS in the same probability calculation, to verify whether it produces any significant changes in probability.

Our results show that, either we consider or not ΔCFS in the probability calculations, higher values of occurrence are predicted for the Brigham City and Salt

Lake City segments. In addition ΔCFS_{cum} models show that the Brigham City, the Salt Lake City, and the Provo segments have accumulated respectively 11.3, 10.8, and 12.5 bar of cumulative ΔCFS.

Finally by integrating the two models we observed a significant increase in probability for the Brigham City, Salt Lake City, and Provo segment when the effect of paleoseismological events is implemented in the probability calculations. This results indicates that the seismic hazard connected with single-segment ruptures on the central WFZ might be underestimated if the effects of stress changes are not considered.

Table 3.1. Input parameters used for probability calculations in the central WFZ.

Segment	Paleoevents[a] (years)	T_m (years)	CV	T_{elap} (years)	Slip Rate[b] (mm/yr)	Length (km)	M_{max} (± 1σ)
Brigham City	B1: 2400 ± 300 B2: 3500 ± 200 B3: 4500 ± 500 B4: 5600 ± 600	1127	0.1 - 0.4	2465	1.6	41	7.0 ± 0.2
Weber	W1: 600 ± 100 W2: 1100 ± 600 W3: 3100 ± 300 W4: 4500 ± 300 W5: 5900 ± 500	1267	0.1 - 0.4	665	1.8	58	7.1 ± 0.2
Salt Lake City	S1: 1300 ± 200 S2: 2200 ± 200 S3: 4100 ± 200 S4: 5300 ± 200	1333	0.3 - 0.5	1365	1.3	45	7.0 ± 0.2
Provo	P1: 600 ± 50 P2: 1500 ± 400 P3: 2200 ± 400 P4: 4700 ± 300 P5: 5900 ± 1000	1268	0.3 - 0.6	665	2.0	70	7.2 ± 0.2
Nephi	N1: 200 ± 70 N2: 1200 ± 80 N3: 2400 ± 100 N4: 4000 ± 90 N5: 4700 ± 500 N6: 5700 ± 800	1068	0.2 - 0.5	265	1.8	44	7.0 ± 0.2

[a]Per-segment earthquake timing, based on integration of site earthquake data younger than 7 ka (*DuRoss et al.*, 2016). [b]Mean vertical slip rate, based on mean vertical displacement per segment divided by mean recurrence time (*DuRoss et al.*, 2016).

Table 3.2. Calculated ΔCFS and its integration in time-dependent parameters.

Segment	Source Earthquakes[a]	ΔCFS_{cos}[b] (bar)	ΔCFS_{cum}[b] (bar)	$\dot{\tau}$ (bar/year)	$T_{elap}+\Delta CFS_{cum}$ (years)	$T_m+\Delta CFS_{cum}$ (years)
Brigham City	W1, W2, S1, P1, N1, LV, WV, GSL	5.7	11.3	0.045	2716	876
Weber	S1, P1, N1, GSL	-7.1	-5.2	0.049	559	1373
Salt Lake City	W1, W2, P1, N1, LV, GSL	4.7	10.8	0.036	1665	1036
Provo	W1, N1, GSL	10.5	12.5	0.051	910	1023
Nephi	/	0.0	0.0	0.048	265	1068

[a]Details in Table 3.1. [b]Maximum ΔCFS located anywhere on the fault plane.

Table 3.3. Probability of a single-segment rupture for the next 50 years, calculated on each of the five main segment of the central WFZ.

Segment	CV	P_{50}Poisson	P_{50}BPT	P_{50}BPT+ΔCFS_{cum} (T'_{elap})	P_Change[a] (T'_{elap})	P_{50}BPT+ΔCFS_{cum} (T'_{m})	P_Change[a] (T'_{m})	P_{50}BPT+ΔCFS_{cum}[b] (Avg ± sd)
Brigham City	0.1	3.9%	78.8%	80.0%	1.01	89.0%	1.13	39.9% ± 29.5%
	0.2		34.1%	35.2%	1.03	44.3%	1.3	
	0.3		18.5%	18.9%	1.02	24.2%	1.31	
	0.4		12.0%	12.1%	1.01	15.5%	1.39	
Weber	0.1	3.5%	0.0%	0.0%	1.0	0.0%	1.0	0.4% ± 0.6%
	0.2		0.0%	0.0%	1.0	0.0%	1.0	
	0.3		0.8%	0.2%	0.28	0.4%	0.5	
	0.4		2.1%	1.1%	0.53	1.4%	0.68	
Salt Lake City	0.3	3.3%	8.9%	11.5%	1.3	15.4%	1.72	10.4% ± 3%
	0.4		7.3%	8.5%	1.16	11.2%	1.52	
	0.5		6.3%	6.8%	1.08	8.8%	1.4	
Provo	0.3	3.5%	0.8%	3.8%	4.94	3.3%	4.23	4.8% ± 0.9%
	0.4		2.1%	4.8%	2.26	4.8%	2.3	
	0.5		3.2%	5.1%	1.58	5.6%	1.75	
	0.6		3.9%	5.1%	1.3	5.9%	1.5	
Nephi	0.2	4.2%	0.0%	0.0%	1.0	0.0%	1.0	0.1% ± 0.1%
	0.3		0.0%	0.0%	1.0	0.0%	1.0	
	0.4		0.0%	0.0%	1.0	0.0%	1.0	
	0.5		0.3%	0.3%	1.0	0.3%	1.0	

[a]Probability change with respect to P_{50}BPT (in which stress changes are not implemented). [b]Average and standard deviation calculated between the probabilities in which stress changes are implemented.

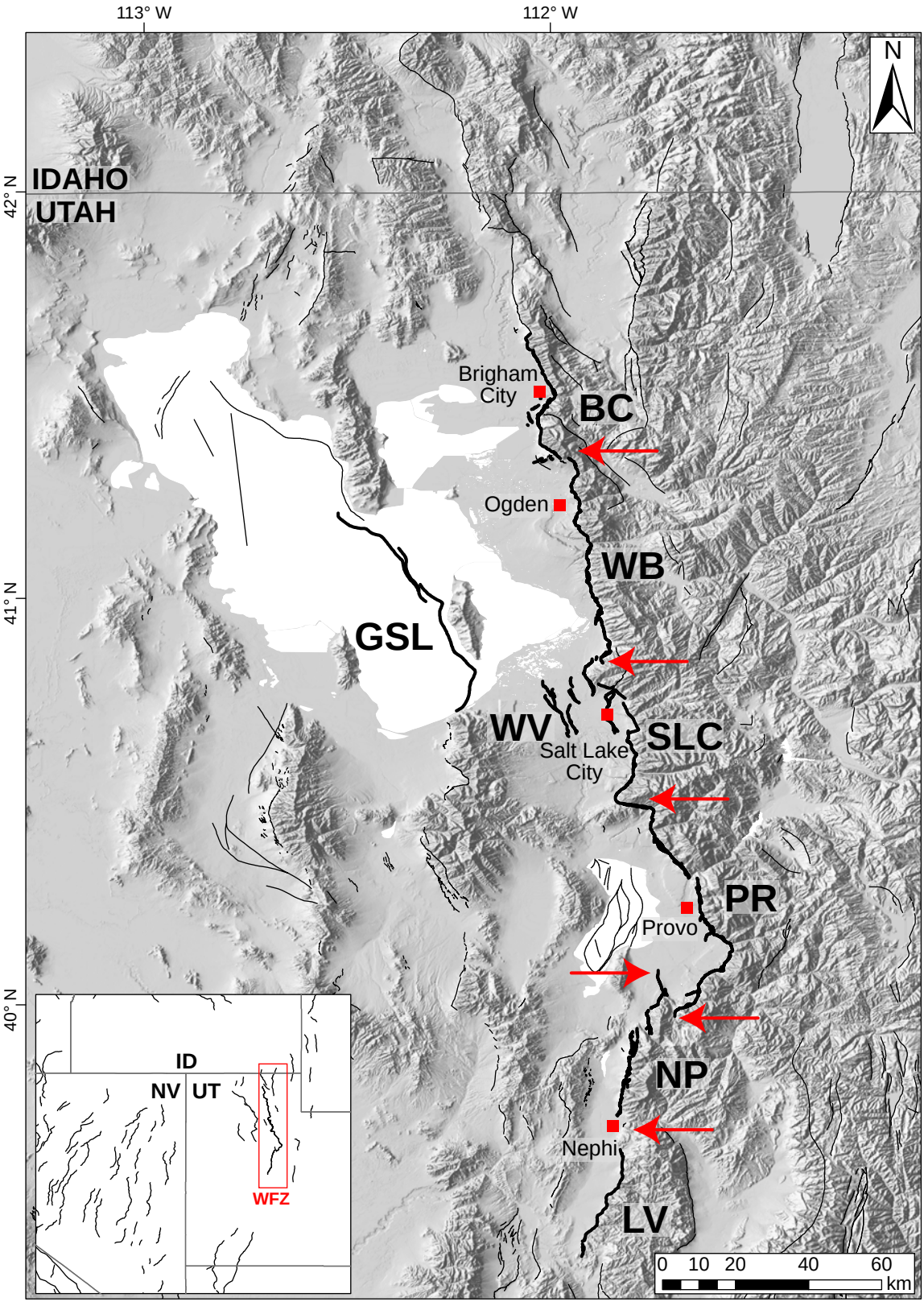

Figure 3.1. Map of Quaternary active faults in north-central Utah and south Idaho [*Black et al.*, 2003]. Thick black lines are the segments of the central WFZ. Red arrows indicate segment boundaries. BC=Brigham City segment, WB=Weber segment, SLC=Salt Lake City segment, PR=Provo segment, NP=Nephi segment, LV=Levan segment, GSL=Great Salt Lake fault, WV=West Valley fault zone.

Figure 3.2. Cumulative ΔCFS calculated over the time between the most recent event of the receiver fault and present-day, on the kinematics of (a) the Brigham City segment (BC), (b) the Weber segment (WB), (c) the Salt Lake City segment (SLC), (d) the Provo segment (PR). Thick white lines are source faults; thick yellow lines are receiver faults; dashed black lines represent the depth-countour of the receiver fault at calculation depth. NP=Nephi segment, LV=Levan segment, GSL=Great Salt Lake fault, WV=West Valley fault zone.

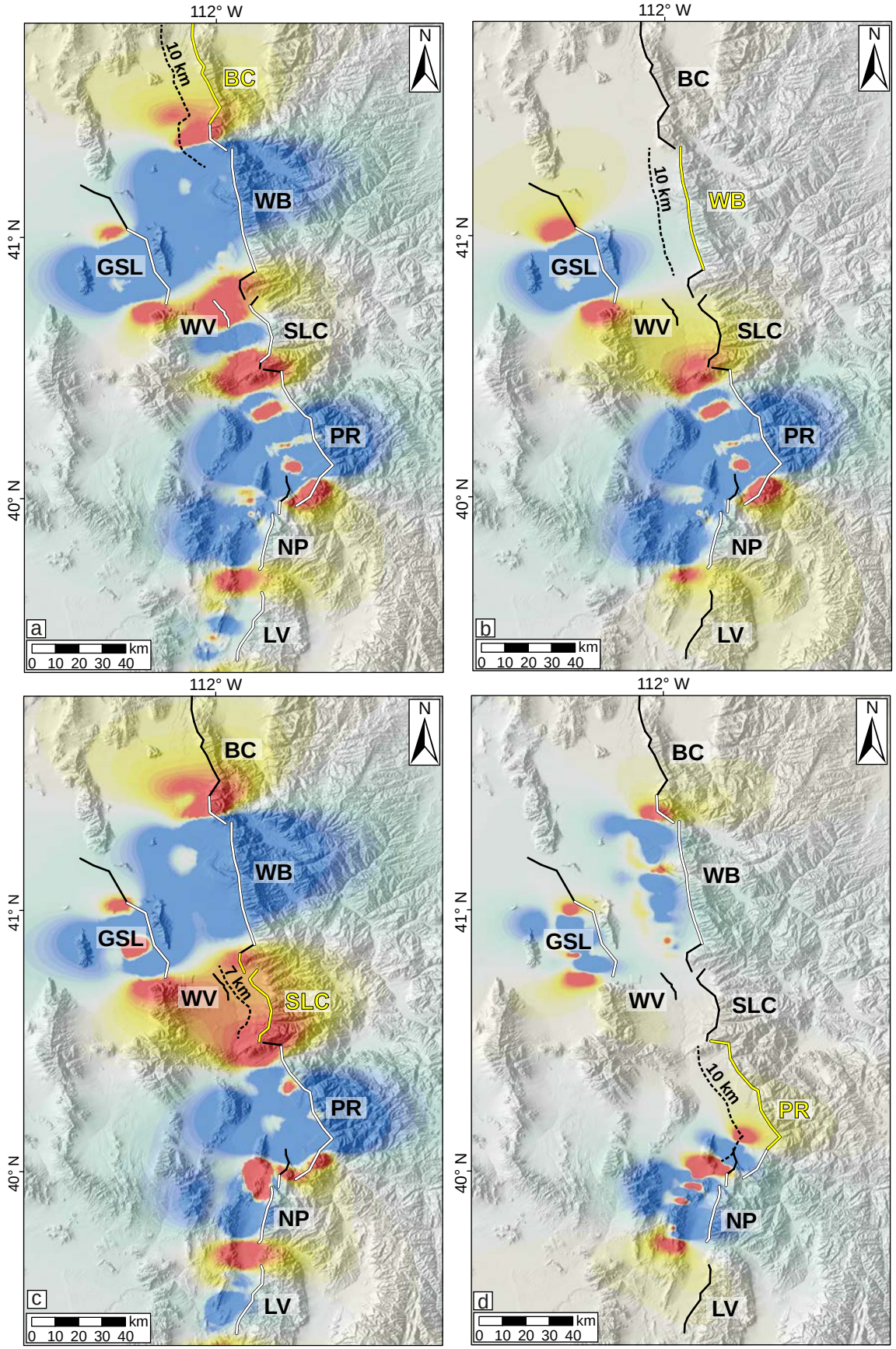
112° W
41° N
40° N
N
BC
WB
GSL
WV
SLC
PR
NP
LV
10 km
7 km
a
b
c
d
km
0 10 20 30 40
ΔCFS(bar)
<-10
-5
0
5
>10

Figure 3.2

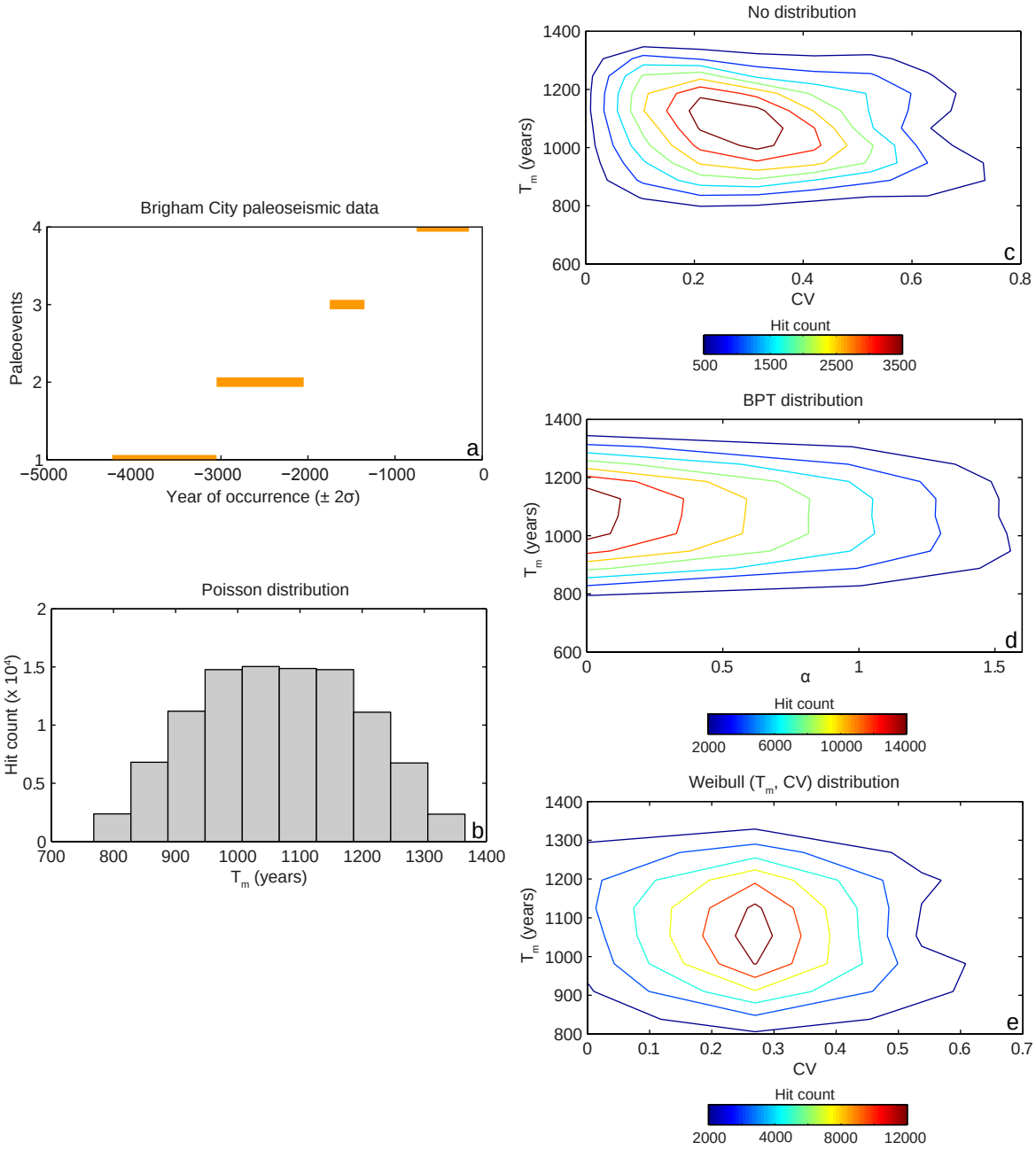

Figure 3.3. (a) Paleoseismological data for the Brigham City segment, and results from the Monte Carlo simulations showed for (b) time-independent and (c, d, e) time-dependent parameters. In c, d, and e the number of matches to the observed paleoseismological sequence are contoured vs. recurrence interval (T_m) and coefficient of variation (α, CV).

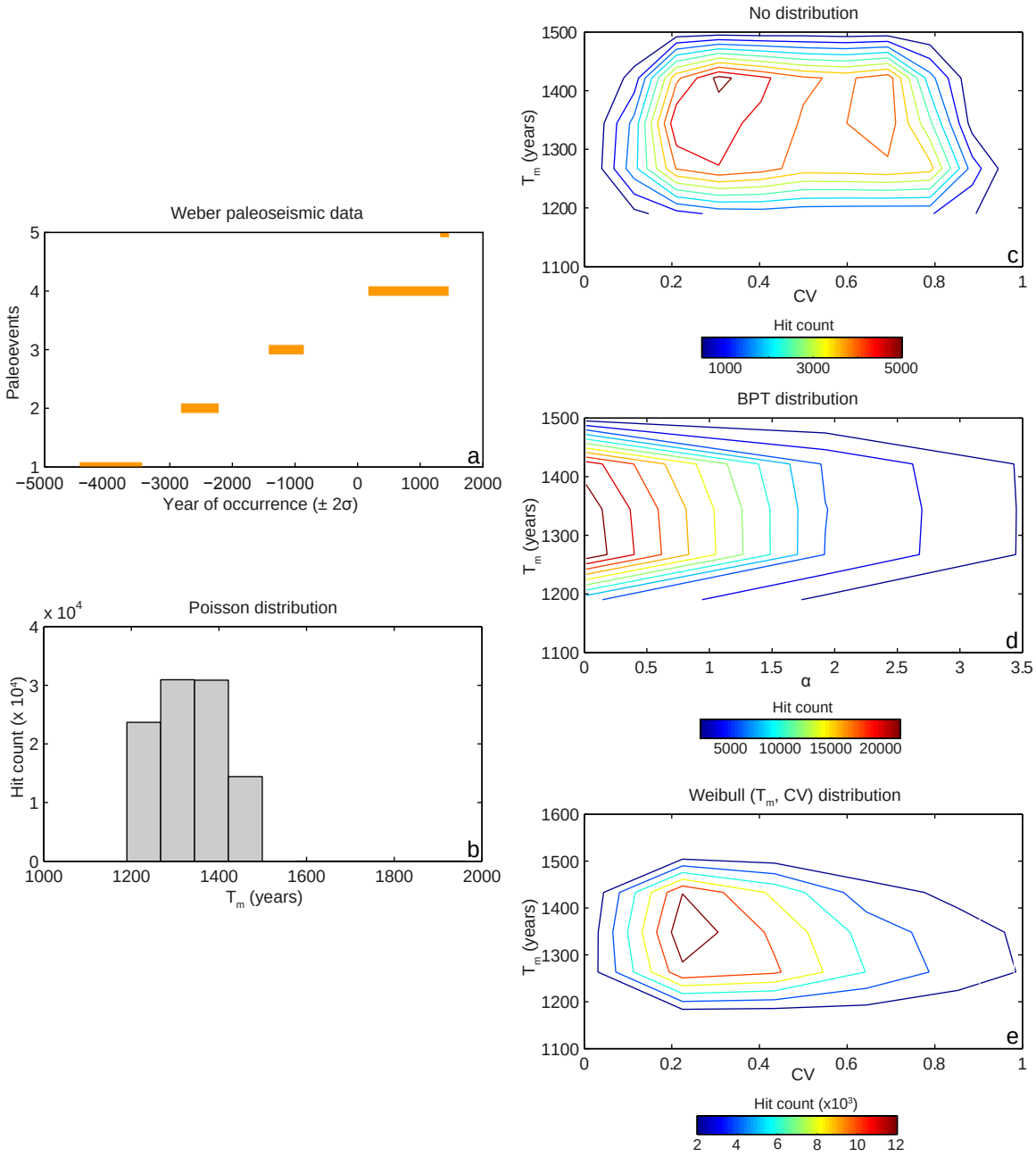

Figure 3.4. (a) Paleoseismological data for the Weber segment, and results from the Monte Carlo simulations showed for (b) time-independent and (c, d, e) time-dependent parameters. In c, d, and e the number of matches to the observed paleoseismological sequence are contoured vs. recurrence interval (T_m) and coefficient of variation (α, CV).

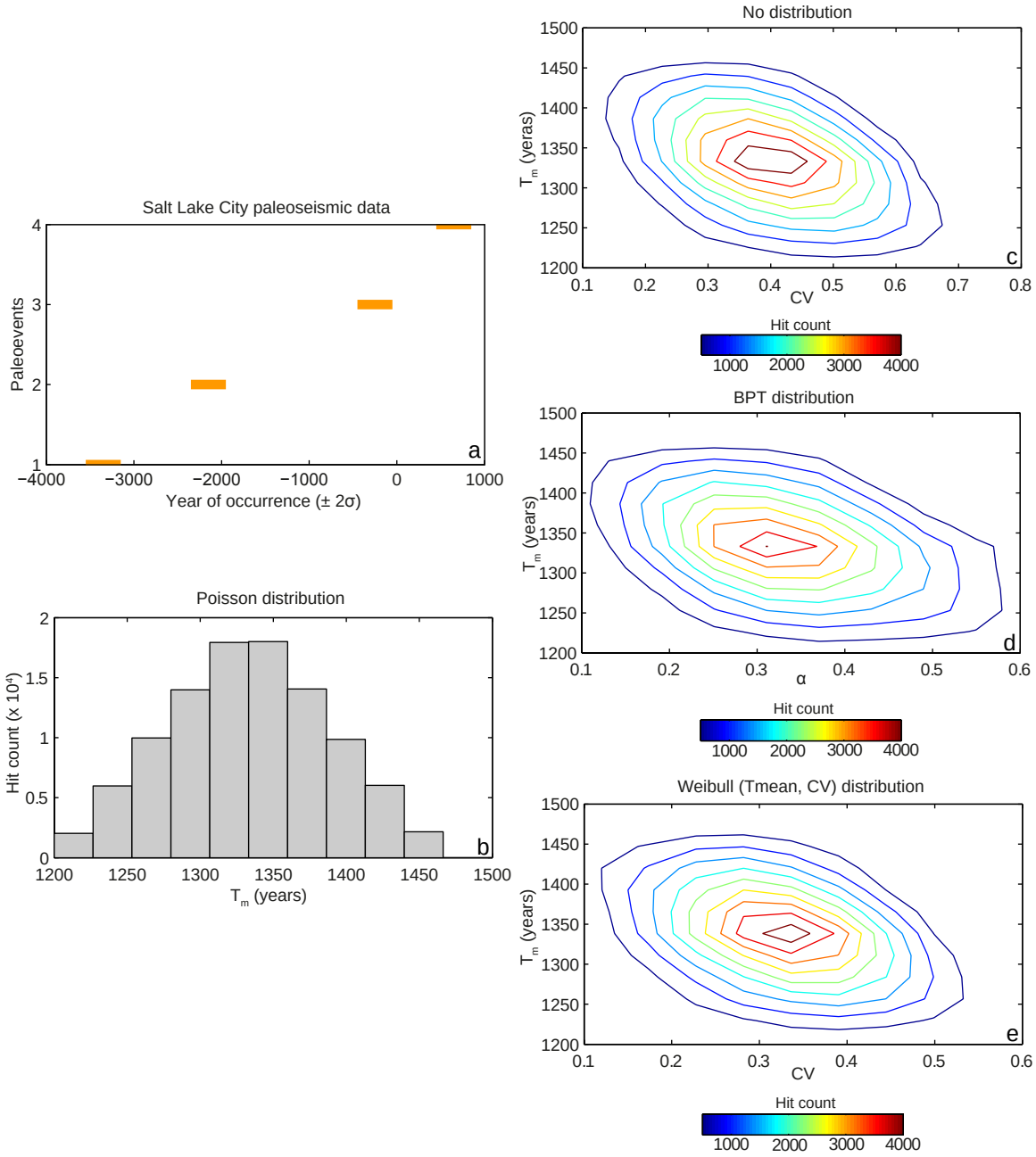

Figure 3.5. (a) Paleoseismological data for the Salt Lake City segment, and results from the Monte Carlo simulations showed fro (b) time-independent and (c, d, e) time-dependent parameters. In c, d, and e the number of matches to the observed paleoseismological sequence are contoured vs. recurrence interval (T_m) and coefficient of variation (α, CV).

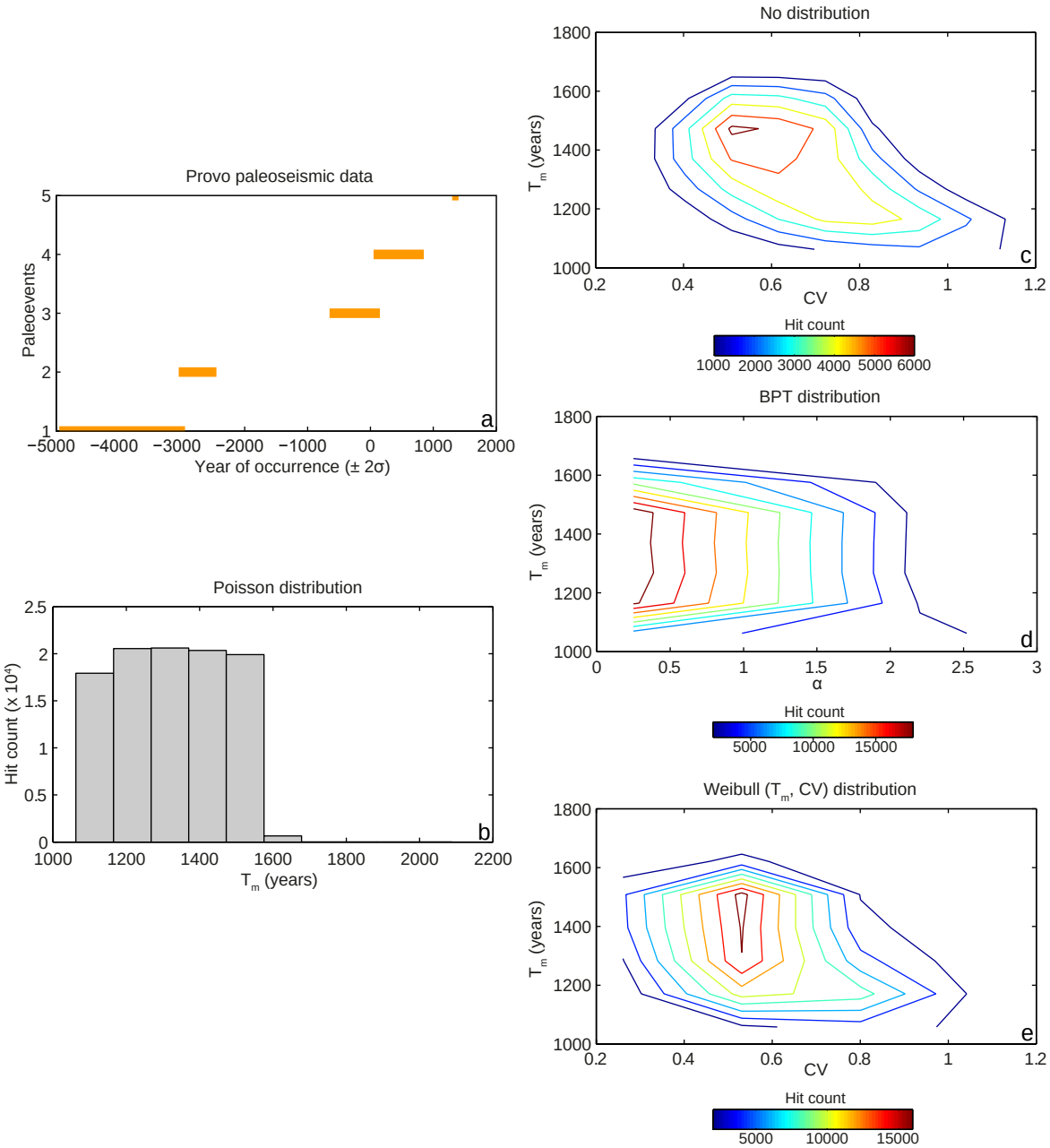

Figure 3.6. (a) Paleoseismological data for the Provo segment, and results from the Monte Carlo simulations showed for (b) time-independent and (c, d, e) time-dependent parameters. In c, d, and e the number of matches to the observed paleoseismological sequence are contoured vs. recurrence interval (T_m) and coefficient of variation (α, CV).

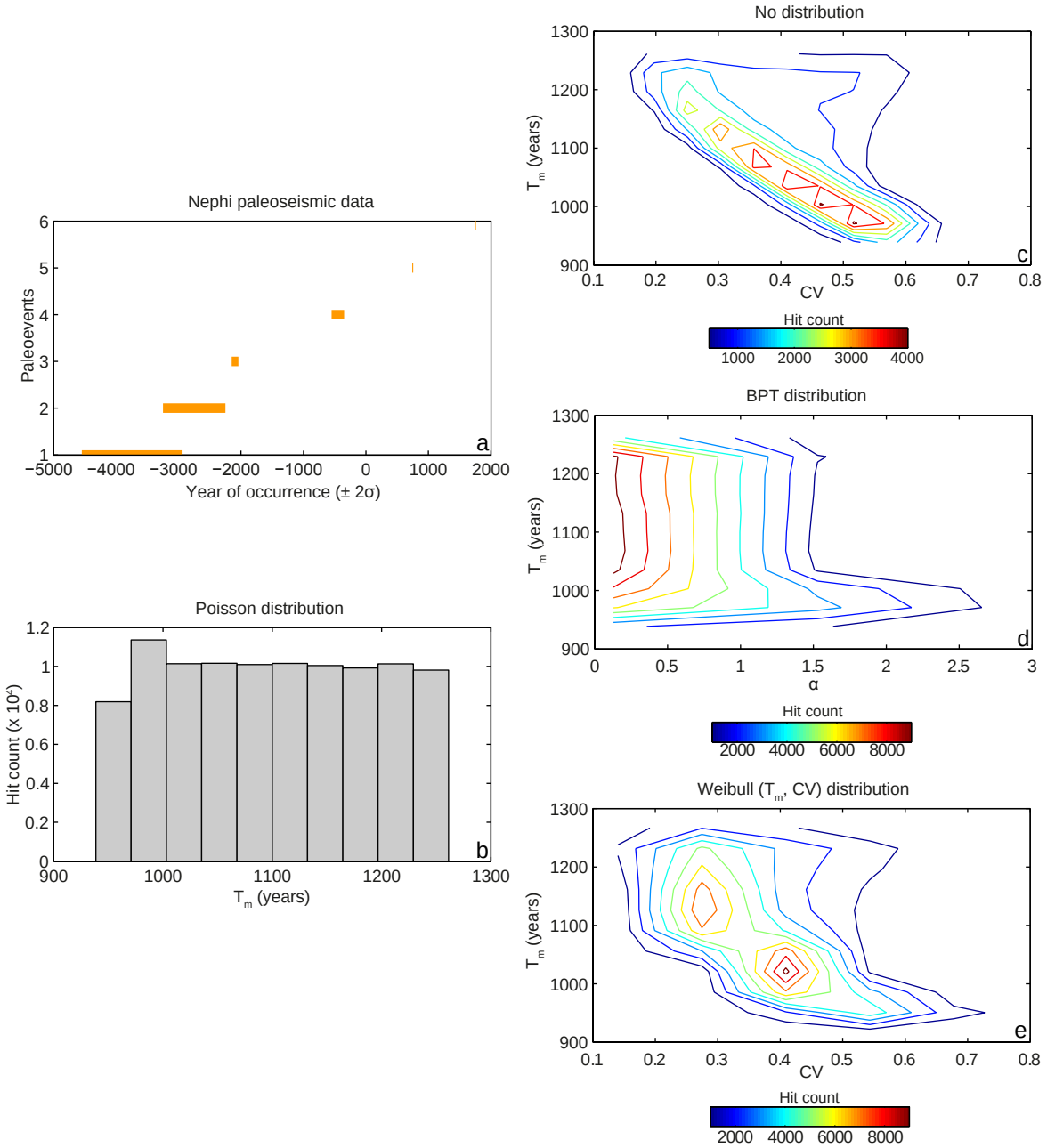

Figure 3.7. (a) Paleoseismological data for the Nephi segment, and results from the Monte Carlo simulations showed for (b) time-independent and (c, d, e) time-dependent parameters. In c, d, and e the number of matches to the observed paleoseismic sequence are contoured vs. recurrence interval (T_m) and coefficient of variation (α, CV).

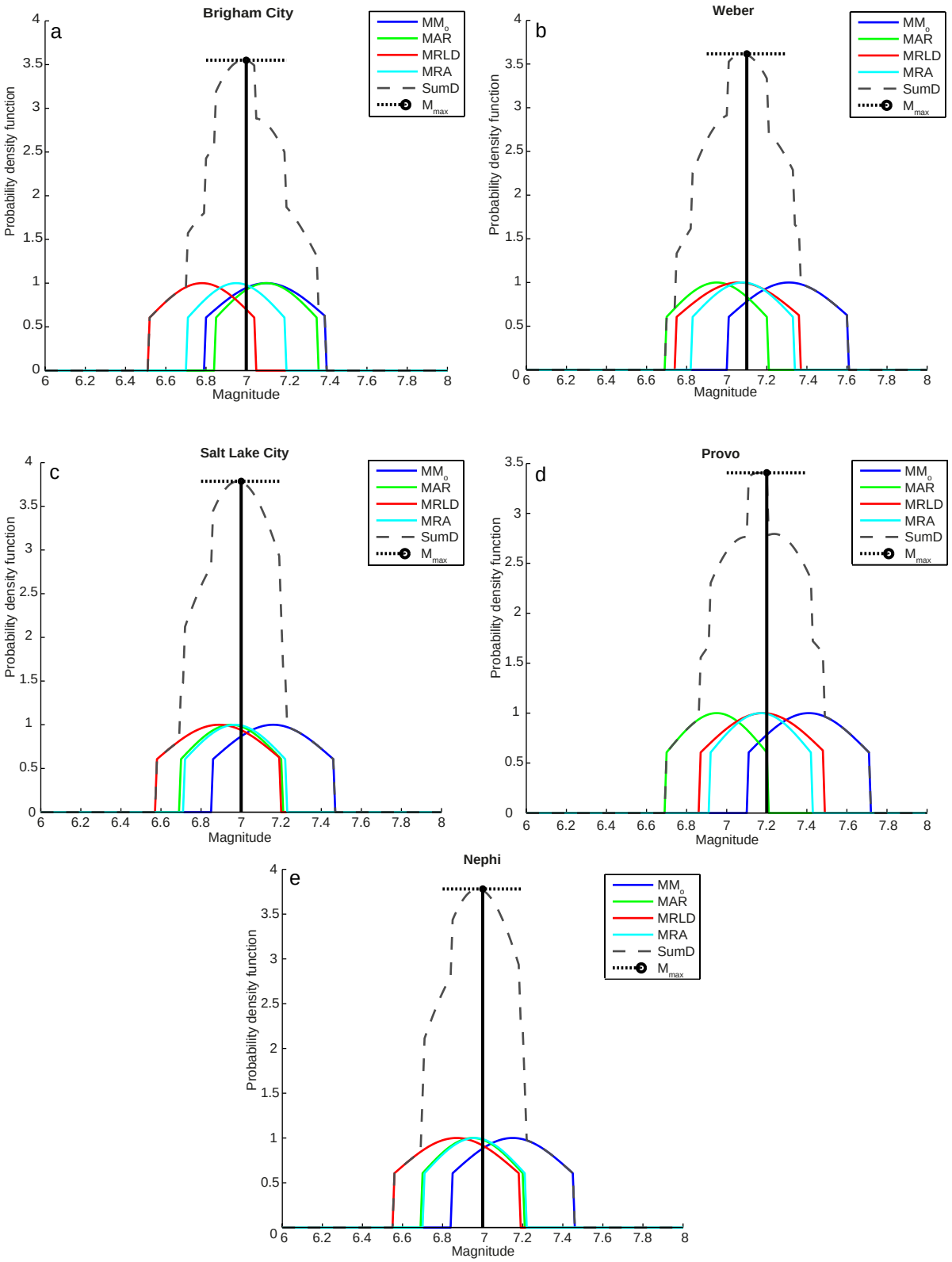

Figure 3.8. Magnitude distribution calculated for each of the five studied segments of the central WFZ. The dashed black line (SumD) represents the summation of the M_{max} values based on seismic moment (M_o), aspect ratio (AR), subsurface lenght (RLD), and rupture area (RA). The vertical black line represents the central value of the Gaussian fit of the summed probability density curves (M_{max}), and its standard deviation is given by the horizontal black dotted line.

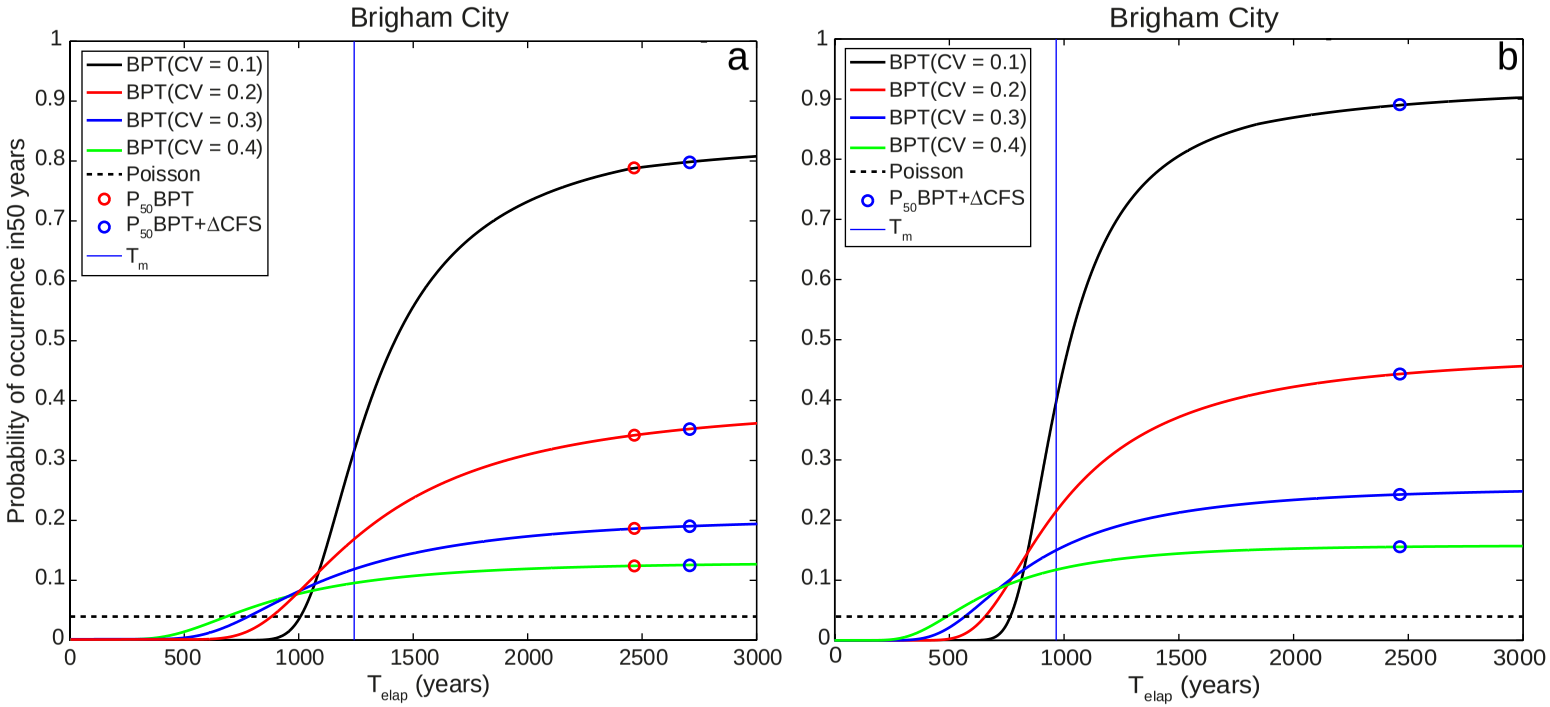

Figure 3.9. BPT probability curves calculated for the Brigham City segment for the next 50 years using different values of CV. Red circles represents the BPT probability when ΔCFS is not considered. Blue circles represents BPT probability when ΔCFS is considered using (a) the approach based on modified T_{elap}, and (b) the approach based on modified T_m. Dashed black line is the time-indipendent Poisson probability.

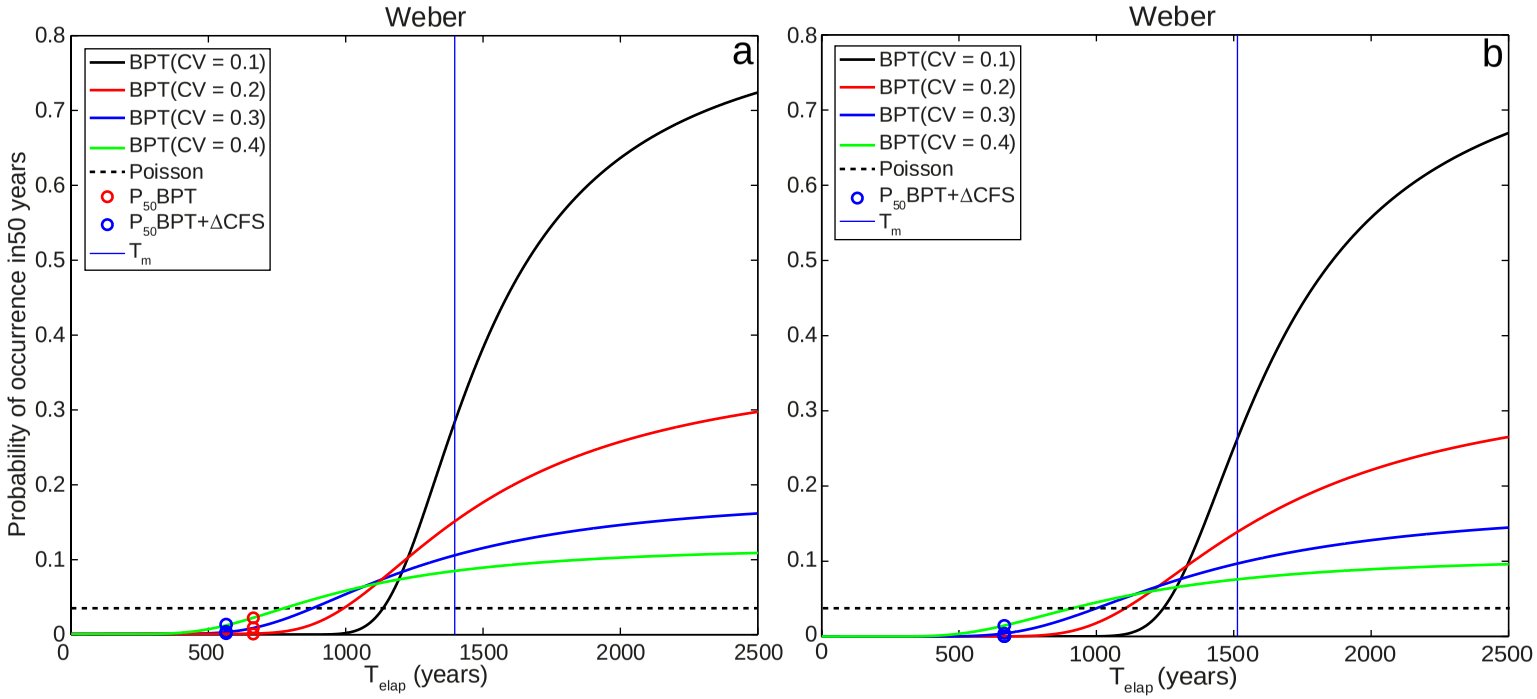

Figure 3.10. BPT probability curves calculated for the Weber segment for the next 50 years using different values of CV. Red circles represents the BPT probability when ΔCFS is not considered. Blue circles represents BPT probability when ΔCFS is considered using (a) the approach based on modified T_{elap}, and (b) the approach based on modified T_m. Dashed black line is the time-indipendent Poisson probability.

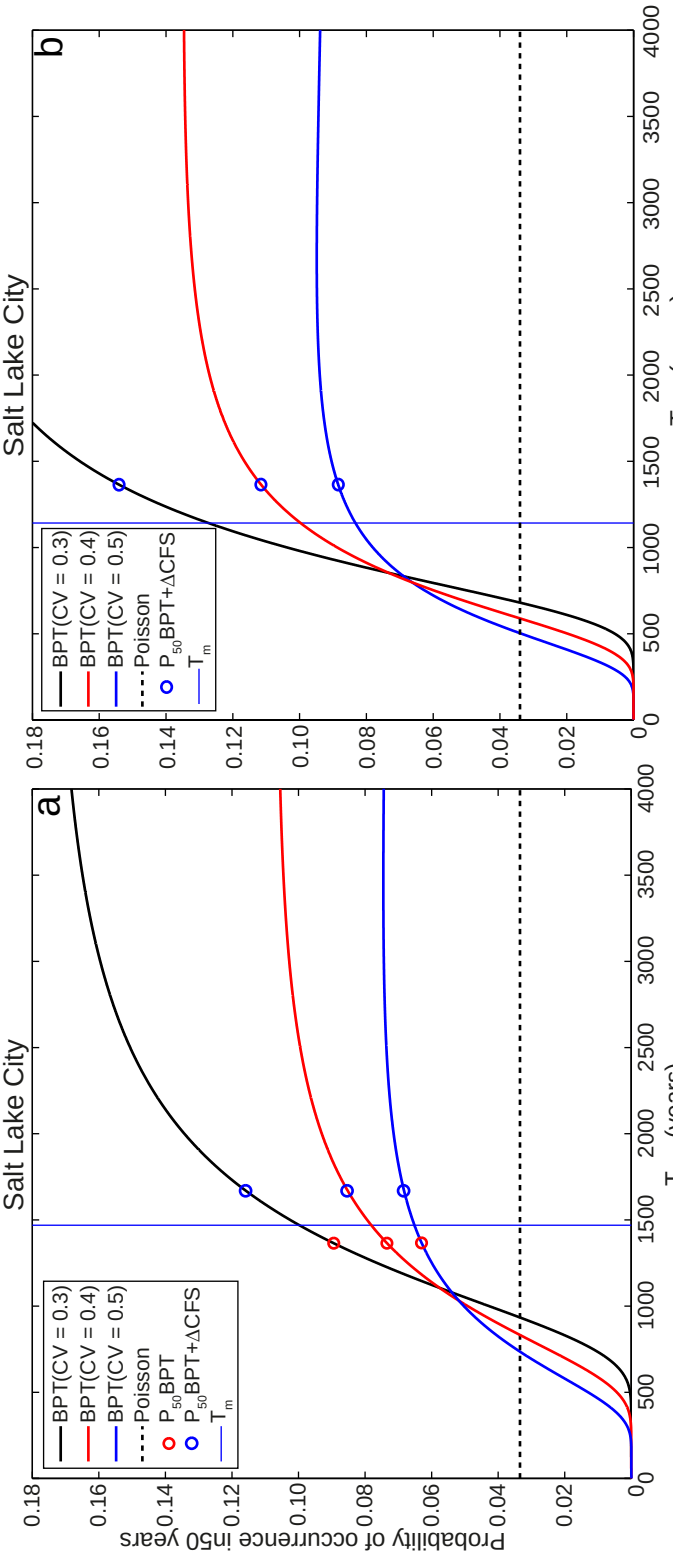

Figure 3.11. BPT probability curves calculated for the Salt Lake City segment for the next 50 years using different values of CV. Red circles represents the BPT probability when ΔCFS is not considered. Blue circles represents BPT probability when ΔCFS is considered using (a) the approach based on modified T_{elap}, and (b) the approach based on modified T_m. Dashed black line is the time-indipendent Poisson probability.

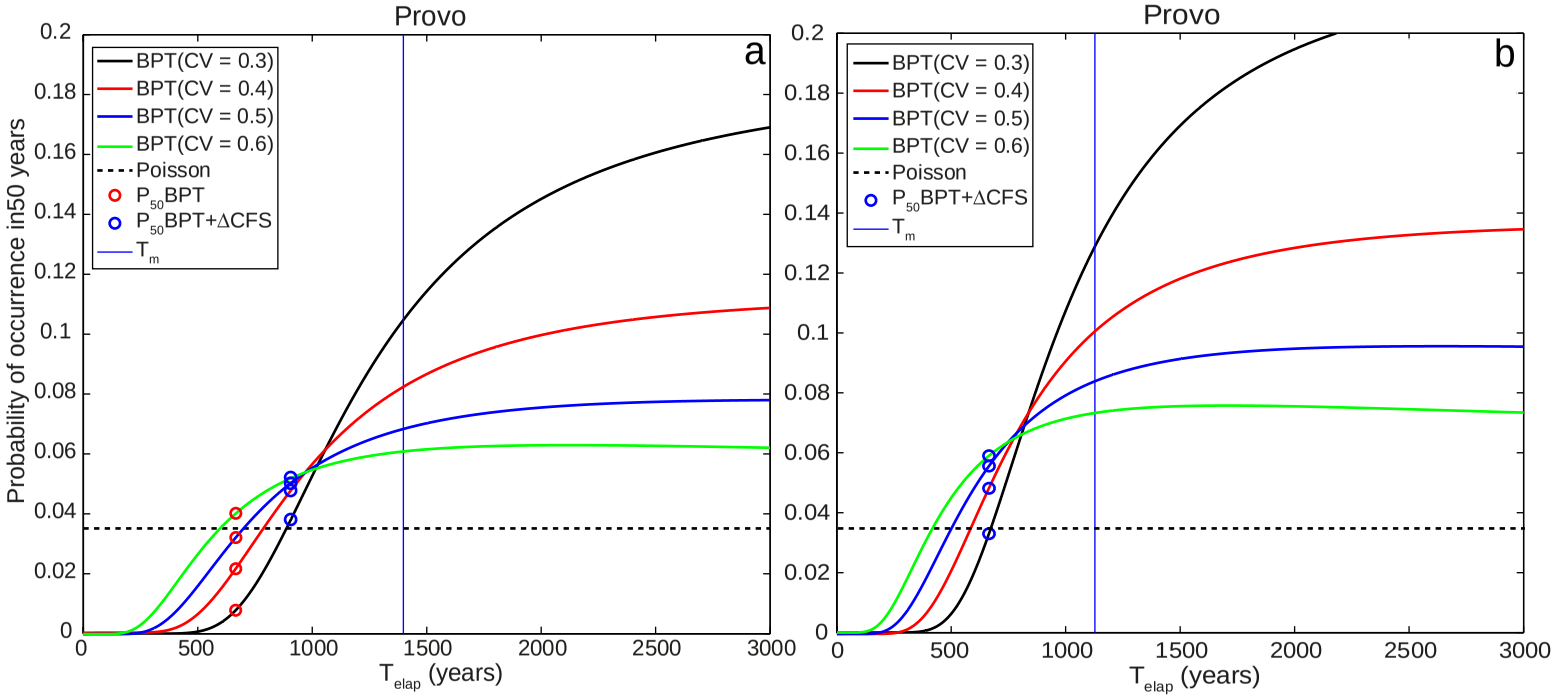

Figure 3.12. BPT probability curves calculated for the Provo segment for the next 50 years using different values of CV. Red circles represents the BPT probability when ΔCFS is not considered. Blue circles represents BPT probability when ΔCFS is considered using (a) the approach based on modified T_{elap}, and (b) the approach based on modified T_m. Dashed black line is the time-indipendent Poisson probability.

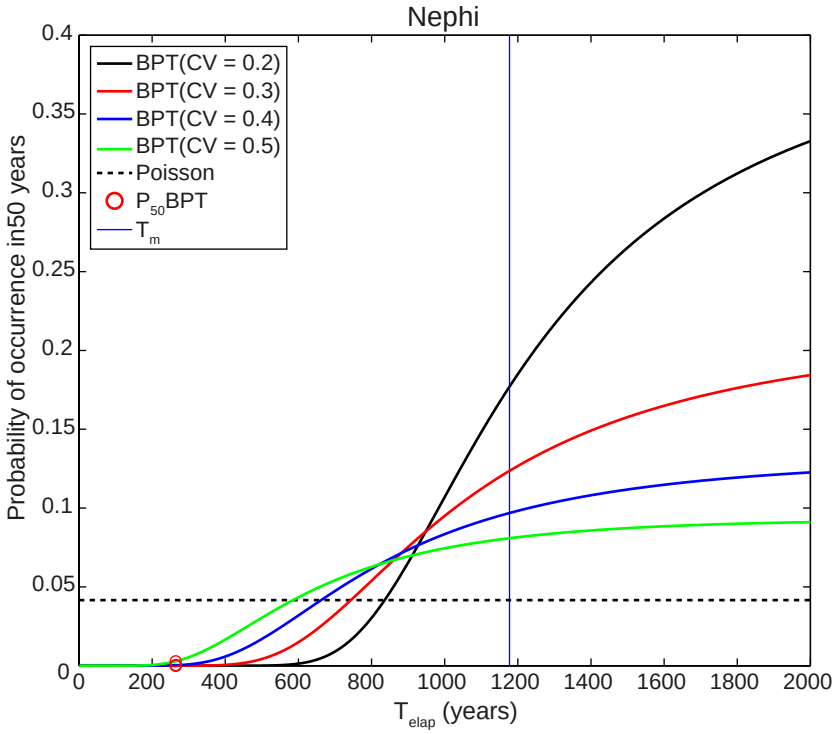

Figure 3.13. BPT probability curves calculated for the Nephi segment for the next 50 years using different values of CV. Red circles represents the BPT probability. Dashed black line is the time-indipendent Poisson probability.

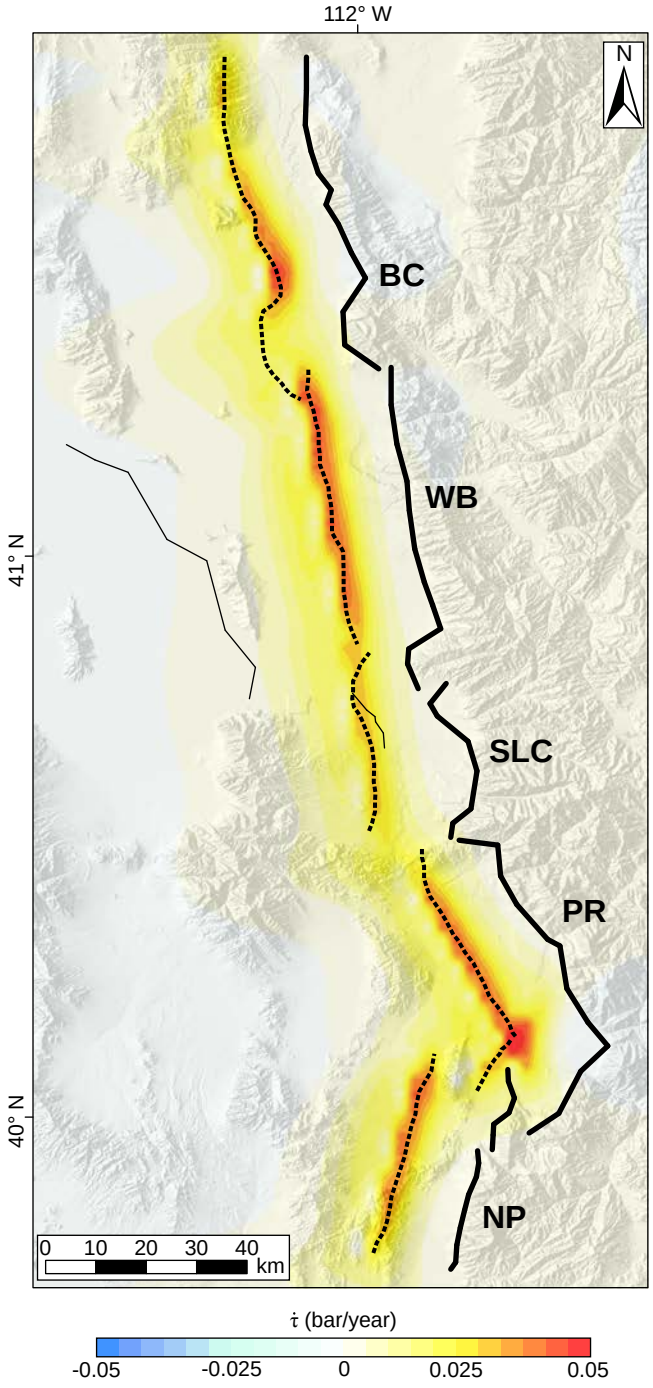

Figure 3.14. Tectonic loading ($\dot{\tau}$) calculated on the main orientation and kinematics (176° strike, 50° dip, and -90° rake) of the central WFZ at 13 km depth. Dashed black lines represent the 13 km contours of the central segments of the WFZ. BC=Brigham City segment, WB=Weber segment, SLC=Salt Lake City segment, PR=Provo segment, NP=Nephi segment.

Bibliography

Abbott, R. E., Louie, J. N., Pullammanappallil, S., and Caskey, S. J., 2001, Geophysical confirmation of low-angle normal slip on the historically active Dixie Valley fault, Nevada: Journal of Geophysical Research, v. 106, no. B3, p. 4169-4181.

Aki, K., 1979, Characterization of barriers on an earthquake fault: Journal of Geophysical Research: Solid Earth, v. 84, no. B11, p. 6140-6148.

Ali, S. T., Freed, A. M., Calais, E., Manaker, D. M., and McCann, W. R., 2008, Coulomb stress evolution in Northeastern Caribbean over the past 250 years due to coseismic, postseismic and interseismic deformation: Geophysical Journal International, v. 174, no. 3, p. 904-918.

Amos, C. B., Brownlee, S. J., Rood, D. H., Fisher, G. B., Bürgmann, R., Renne, P. R., and Jayko, A. S., 2013, Chronology of tectonic, geomorphic, and volcanic interactions and the tempo of fault slip near Little Lake, California, Geological Society of America Bulletin, v. 125, no. 7/8, p. 1187-1202.

Arabasz, W. J., Pechmann, J., and Brown, E., 1992, Observational seismology and the evaluation of earthquake hazards and risk in the Wasatch Front area, Utah: US Geological Survey Professional Paper, v. 1500.

Bacon, S. N., and Pezzopane, S. K., 2007, A 25,000-year record of earthquakes on the Owens Valley fault near Lone Pine, California: Implications for recurrence intervals, slip rates, and segmentation models: Geological Society of America Bulletin, v. 119, no. 7-8, p. 823-847.

Bailey, R., 1989, Geologic map of Long Valley Caldera, Mono-Inyo craters volcanic chain and vicinity, Eastern California, scale 1: 62,500, 11 pp: US Geol. Surv. Geophys. Invest. Map I—1993.

Bassin, C., 2000, The current limits of resolution for surface wave tomography in North America: Eos Trans. AGU.

Beanland, S., and Clark, M. M., 1994, The Owens Valley fault zone, eastern California, and surface faulting associated with the 1872 earthquake: U.S. Geological Survey Bullettin, no. 1892, 32 pp.

Bell, J. W., and Katzer, T., 1990, Timing of late Quaternary faulting in the 1954 Dixie Valley earthquake area, central Nevada: Geology, v. 18, no. 7, p. 622-625.

Bell, J. W., DePolo, C. M., Ramelli, A. R., Sarna-Wojcicki, A. M., and Meyer, C., 1999, Surface faulting and paleoseismic history of the 1932 Cedar Mountain earthquake area, west-central Nevada, and implications for modern tectonics of the Walker Lane: Geological Society of America Bulletin, v. 111, no. 6, p. 791-807.

Bell, J. W., Caskey, S. J., Ramelli, A. R., and Guerrieri, L., 2004, Pattern and rates of faulting in the central Nevada seismic belt, and paleoseismic evidence for prior beltlike behavior: Bulletin of the Seismological Society of America, v. 94, no. 4, p. 1229-1254.

Bennett, R., Wernicke, B., Davis, J., Elosegui, P., Snow, J., Abolins, M., House, M., Stirewalt, G., and Ferrill, D., 1997, Global Positioning System constraints on fault slip rates in the Death Valley region, California and Nevada: Geophysical research letters, v. 24, no. 23, p. 3073-3076.

Bennett, R., Wernicke, B., Niemi, N., Friedrich, A., and Davis, J., 2003, Contemporary strain rates in the northern Basin and Range province from GPS data: Tectonics, v. 22, no. 2.

Bennett, S., DuRoss, C., Reitman, N., Devore, J., Hiscock, A., Gold, R., Briggs, R., and Personius, S., Using Paleoseismic Trenching and LiDAR Analysis to Evaluate Rupture Propagation Through Segment Boundaries of the Central Wasatch Fault Zone, Utah, *in* Proceedings AGU Fall Meeting Abstracts 2014, Volume 1, p. 08.

Bennett, S., Gold, R., and DuRoss, C., 2015, Evidence for non-persistent rupture terminations at central Wasatch Fault Zone segment boundaries, Utah: Seismological Research Letters, v. 86, no. 2B.

Berry, M. E., 1997, Geomorphic analysis of late Quaternary faulting on Hilton Creek, Round Valley and Coyote warp faults, east-central Sierra Nevada, California, USA: Geomorphology, v. 20, no. 1, p. 177-195.

Bird, P., and Kong, X., 1994, Computer simulations of California tectonics confirm very low strength of major faults: Geological Society of America Bulletin, v. 106, no. 2, p. 159-174.

Black, B. D., Lund, W. R., Schwartz, D. P., Gill, H. E., and Mayes, B. H., 1996, Paleoseismic investigation on the Salt Lake City segment of the Wasatch fault zone at the South Fork Dry Creek and Dry Gulch sites, Salt Lake County, Utah, Special Studies, 92, 22 pp., Utah Geological Survey, Salt Lake City.

Bormann, J. M., Surpless, B. E., Caffee, M. W., and Wesnousky, S. G., 2012, Holocene Earthquakes and Late Pleistocene Slip-Rate Estimates on the Wassuk Range Fault Zone, Nevada: Bulletin of the Seismological Society of America, v. 102, no. 4, p. 1884-1891.

Briggs, R. W., and Wesnousky, S. G., 2004, Late Pleistocene fault slip rate, earthquake recurrence, and recency of slip along the Pyramid Lake fault zone, northern Walker Lane, United States: Journal of Geophysical Research: Solid Earth, v. 109, no. B8.

Brogan, G. E., Kellogg, K. S., Terhune, C. L., and Slemmons, D., 1991, Late quaternary faulting along the Death Valley-Furnace Creek fault system, California and Nevada: Geological Survey, Denver, CO (United States).

Brothers, D. S., Kent, G. M., Driscoll, N. W., Smith, S. B., Karlin, R., Dingler, J. A., Harding, A. J., Seitz, G. G., and Babcock, J. M., 2009, New constraints on deformation, slip rate, and timing of the most recent earthquake on the West Tahoe–Dollar Point Fault, Lake Tahoe Basin, California: Bulletin of the Seismological Society of America, v. 99, no. 2A, p. 499-519.

Carena, S., and Moder, C., 2009, The strength of faults in the crust in the western United States: Earth and Planetary Science Letters, v. 287, no. 3, p. 373-384.

Carena, S., and Suppe, J., 2002, Three-dimensional imaging of active structures using earthquake aftershocks: the Northridge thrust, California: Journal of structural geology, v. 24, no. 4, p. 887-904.

Carena, S., Suppe, J., and Kao, H., 2002, Active detachment of Taiwan illuminated by small earthquakes and its control of first-order topography: Geology, v. 30, no. 10, p. 935-938.

Carena, S., Suppe, J., and Kao, H., 2004, Lack of continuity of the San Andreas Fault in southern California: Three-dimensional fault models and earthquake scenarios: Journal of Geophysical Research: Solid Earth, v. 109, no. B4.

Caskey, S., and Wesnousky, S., 1997, Static stress changes and earthquake triggering during the 1954 Fairview Peak and Dixie Valley earthquakes, Central Nevada: Bulletin of the Seismological Society of America, v. 87, no. 3, p. 521-527.

Caskey, S., Wesnousky, S., Zhang, P., and Slemmons, D., 1996, Surface faulting of the 1954 Fairview Peak (MS 7.2) and Dixie Valley (MS 6.8) earthquakes, central Nevada: Bulletin of the Seismological Society of America, v. 86, no. 3, p. 761-787.

Caskey, S. J., Bell, J. W., Ramelli, A. R., and Wesnousky, S. G., 2004, Historic surface faulting and paleoseismicity in the area of the 1954 Rainbow Mountain-Stillwater earthquake sequence, central Nevada: Bulletin of the Seismological Society of America, v. 94, no. 4, p. 1255-1275.

Chang, W. L., and Smith, R. B., 2002, Integrated seismic-hazard analysis of the Wasatch Front, Utah: Bulletin of the Seismological Society of America, v. 92, no. 5, p. 1904-1922.

Chang, W. L., Smith, R. B., Meertens, C. M., and Harris, R. A., 2006, Contemporary deformation of the Wasatch Fault, Utah, from GPS measurements with implications for interseismic fault behavior and earthquake hazard: Observations and kinematic analysis: Journal of Geophysical Research: Solid Earth, v. 111, no. B11.

Chang, W. L., Smith, R. B., and Puskas, C. M., 2013, Effects of lithospheric viscoelastic relaxation on the contemporary deformation following the 1959 Mw 7.3 Hebgen Lake, Montana, earthquake and other areas of the intermountain seismic belt: Geochemistry, Geophysics, Geosystems, v. 14, no. 1, p. 1-17.

Chéry, J., Carretier, S., and Ritz, J.-F., 2001, Postseismic stress transfer explains time clustering of large earthquakes in Mongolia: Earth and Planetary Science Letters, v. 194, no. 1, p. 277-286.

Chiaraluce, L., Ellsworth, W., Chiarabba, C., and Cocco, M., 2003, Imaging the complexity of an active normal fault system: The 1997 Colfiorito (central Italy) case study: Journal of Geophysical Research: Solid Earth, v. 108, no. B6.

Console, R., Murru, M., Falcone, G., and Catalli, F., 2008, Stress interaction effect on the occurrence probability of characteristic earthquakes in Central Apennines: Journal of Geophysical Research: Solid Earth, v. 113, no. B8.

Cowie, P., Scholz, C., Roberts, G. P., Walker, J. F., and Steer, P., 2013, Viscous roots of active seismogenic faults revealed by geologic slip rate variations: Nature Geoscience, v. 6, no. 12, p. 1036-1040.

Crone, A. J., Personius, S. F., DuRoss, C. B., Machette, M. N., and Mahan, S. A., 2014, History of Late Holocene Earthquakes at the Willow Creek Site and on the Nephi Segment, Wasatch Fault Zone, Utah, Utah Geological Survey.

Das, S., and Henry, C., 2003, Spatial relation between main earthquake slip and its aftershock distribution: Reviews of Geophysics, v. 41, no. 3.

Dawson, T. E., McGill, S., and Rockwell, T., 2003, Irregular recurrence of paleoearthquakes along the central Garlock fault near El Paso Peaks, California: Journal of Geophysical Research: Solid Earth, v. 108, no. B7.

Del Pardo, C., Smith-Konter, B. R., Serpa, L. F., Kreemer, C., Blewitt, G., and Hammond, W. C., 2012, Interseismic deformation and geologic evolution of the Death Valley Fault Zone: Journal of Geophysical Research: Solid Earth, v. 117, no. B6.

DeMets, C., Gordon, R. G., and Argus, D. F., 2010, Geologically current plate motions: Geophysical Journal International, v. 181, no. 1, p. 1-80.

Deng, J., and Sykes, L. R., 1997, Evolution of the stress field in southern California and triggering of moderate-size earthquakes: A 200-year perspective: Journal of Geophysical Research: Solid Earth, v. 102, no. B5, p. 9859-9886.

Densmore, A. L., and Anderson, R. S., 1997, Tectonic geomorphology of the Ash Hill fault, Panamint valley, California: Basin Research, v. 9, no. 1, p. 53-63.

DePolo, C. M., 1989, Seismotectonics of the White Mountain fault system, eastern California and western Nevada: MS thesis, 354 pp., Univ. of Nevada, Reno.

DePolo, C. M., 1998, A reconnaissance technique for estimating the slip rates of normal-slip faults in the Great Basin, and application to faults in Nevada, USA, University of Nevada, unpublished Ph.D. dissertation, 199 p.

DePolo C. M., 2006, Estimating uncertainties of seismic hazard parameters for Nevada faults, formation of a Nevada Quaternary Fault Working Group, and gaining consensus fault parameters, U.S. Geological Survey, NEHRP final technical report, award 06HGAG0126.

DePolo, C. M., and Anderson, J., 2000, Estimating the slip rates of normal faults in the Great Basin, USA: Basin Research, v. 12, no. 3-4, p. 227-240.

DePolo, C. M., Peppin, W. A., and Johnson, P. A., 1993, Contemporary tectonics, seismicity, and potential earthquake sources in the white mountains seismic gap, west-central Nevada and east-central California, USA: Tectonophysics, v. 225, no. 4, p. 271-299.

Dingler, J. A., 2007, New geophysical approaches to study neotectonics and associated geohazards, PhD Thesis, University of California, San Diego.

Dingler, J., Kent, G., Driscoll, N., Babcock, J., Harding, A., Seitz, G., Karlin, B., and Goldman, C., 2009, A high-resolution seismic CHIRP investigation of active normal faulting across Lake Tahoe Basin, California-Nevada: Geological Society of America Bulletin, v. 121, no. 7-8, p. 1089-1107.

Dinter, D., and Pechmann, J., 2005, Segmentation and Holocene displacement history of the Great Salt Lake fault, Utah, in Proceedings Volume, Basin and Range Province Seismic Hazard Summit II, W., R., Lund (Editor), Utah Geological Survey Miscellaneous Publication.

Dixon, T. H., Miller, M., Farina, F., Wang, H., and Johnson, D., 2000, Present-day motion of the Sierra Nevada block and some tectonic implications for the Basin and Range province, North American Cordillera: Tectonics, v. 19, no. 1, p. 1-24.

Dixon, T. H., Norabuena, E., and Hotaling, L., 2003, Paleoseismology and Global Positioning System: Earthquake-cycle effects and geodetic versus geologic fault slip rates in the eastern California shear zone: Geology, v. 31, no. 1, p. 55-58.

Dokka, R. K., and Travis, C. J., 1990, Late Cenozoic strike-slip faulting in the Mojave desert, California: Tectonics, v. 9, no. 2, p. 311-340.

Doser, D. I., 1985, Source parameters and faulting processes of the 1959 Hebgen Lake, Montana, earthquake sequence: Journal of Geophysical Research: Solid Earth, v. 90, no. B6, p. 4537-4555.

Doser, D. I., 1986, Earthquake processes in the Rainbow Mountain-Fairview Peak-Dixie Valley, Nevada, Region 1954-1969: Journal of Geophysical Research-Solid Earth, v. 91, p. 12572-12586.

Doser, D. I., 1988, Source parameters of earthquakes in the Nevada seismic zone, 1915–1943: Journal of Geophysical Research: Solid Earth, v. 93, no. B12, p. 15001-15015.

Doser, D. I., and Smith, R. B., 1989, An assessment of source parameters of earthquakes in the Cordillera of the western United States: Bulletin of the Seismological Society of America, v. 79, no. 5, p. 1383-1409.

DuRoss, C. B., 2008, Holocene vertical displacement on the central segments of the Wasatch fault zone, Utah: Bulletin of the Seismological Society of America, v. 98, no. 6, p. 2918-2933.

DuRoss, C. B., and Hylland, M. D., 2014, Evaluating surface faulting chronologies of graben-bounding faults in Salt Lake Valley, Utah: New paleoseismic data from the Salt Lake City segment of the Wasatch fault zone and the West Valley fault zone, in Paleoseismology of Utah, C. B. DuRoss and M. D. Hylland (Editors), v. 24, Utah Geological Survey Special Studies, no. 149, 71 pp.

DuRoss, C. B., and Hylland, M. D., 2015, Synchronous Ruptures along a Major Graben-Forming Fault System: Wasatch and West Valley Fault Zones, Utah: Bulletin of the Seismological Society of America.

DuRoss, C. B., McDonald, G. N., and Lund, W. R., 2008, Paleoseismic Investigation of the Northern Strand of the Nephi Segment of the Wasatch Fault Zone at Santaquin, Utah, in Paleoseismology of Utah, W. R. Lund (Editor), v. 17, Utah Geological Survey Special Studies, no. 123, 33 pp.

DuRoss, C. B., Personius, S. F., Crone,A. J., McDonald, G. N., and Lidke, D. J., 2009, Paleoseismic investigation of the northern Weber segment of the Wasatch fault zone at the Rice Creek trench site, North Ogden, Utah, in Paleoseismology of Utah, W. R. Lund (Editor), Utah Geological Survey Special Studies, v. 18, no. 130, 37 pp.

DuRoss, C. B., Personius, S. F., Crone, A. J., Olig, S. S., and Lund, W. R., 2011, Integration of paleoseismic data from multiple sites to develop an objective earthquake chronology: Apllication to the Weber segment of the Wasatch fault zone, Utah, Bulletin of the Seismological Society of America, 101(6), p. 2765-2781.

DuRoss, C. B., Personius, S. F., Crone,A. J., McDonald, G. N., and Briggs, R. W., 2012, Late Holocene earthquake history of the Brigham City segment of the Wasatch fault zone at the Hansen Canyon, Kotter Canyon, and Pearson Canyon trench sites, Box Elder County, Utah, in Paleoseismology of Utah, W. R. Lund (Editor), Utah Geological Survey Special Studies, v. 22, no. 142, 62 pp.

DuRoss, C. B., Hylland, M. D., Hiscock, A., Beukelman, G., McDonald, G. N.,Erickson, B., McKean, A., Personius, S. F., Briggs, R., Gold, R., Angster, S., King, R., Crone, A. J. and Mahan, S. A., 2014, Paleoseismic investigation to detrmine the Mid-Holocene chronology of surface-faulting earthquakes on the Nephi segment of the Wasatch Fault Zone, Utah and Juab counties, Utah, *U.S. Geological Survey, NEHRP final technical report,* award G12AP20076.

DuRoss, C. B., Personius, S. F., Crone, A. J., Olig, S. S., Hylland, M. D., Lund, W. R., and Schwartz, D. P., 2016, Fault Segmentation: New Concepts from the Wasatch Fault Zone, Utah, USA: Journal of Geophysical Research: Solid Earth.

Ellsworth, W. L., Matthews, M. V., Nadeau, R. M., Nishenko, S. P., Reasenberg, P. A., and Simpson, R. W., 1999, A physically based earthquake recurrence model for estimation of long-term earthquake probabilities, U.S. Geological Survey Open-FIle Report, 99-522.

Field, E.H., Biasi, G.P., Bird, P., Dawson, T.E., Felzer, K.R., Jackson, D.D., Johnson, K.M., Jordan, T.H., Madden, C., Michael, A.J., Milner, K.R., Page, M.T., Parsons, T., Powers, P.M., Shaw, B.E., Thatcher, W.R., Weldon, R.J., II, and Zeng, Y., 2013, Uniform California earthquake rupture forecast, version 3 (UCERF3)—The time-independent model: U.S. Geological Survey Open-File Report 2013–1165, 97 p., California Geological Survey Special Report 228, and Southern California Earthquake Center Publication 1792, http://pubs.usgs.gov/of/2013/1165/.

Field, E. H., Biasi, G. P., Bird, P., Dawson, T. E., Felzer, K. R., Jackson, D. D., Johnson, K. M., Jordan, T. H., Madden, C., and Michael, A. J., 2015, Long-term time-dependent probabilities for the third Uniform California Earthquake Rupture Forecast (UCERF3): Bulletin of the Seismological Society of America, v. 105, no. 2A, p. 511-543.

Fitzenz, D. D., and Nyst, M., 2015, Building Time-Dependent Earthquake Recurrence Models for Probabilistic Risk Computations: Bulletin of the Seismological Society of America.

Frankel, K. L., Brantley, K. S., Dolan, J. F., Finkel, R. C., Klinger, R. E., Knott, J. R., Machette, M. N., Owen, L. A., Phillips, F. M., and Slate, J. L., 2007a, Cosmogenic 10Be and 36Cl geochronology of offset alluvial fans along the northern Death Valley fault zone: Implications for transient strain in the eastern California shear zone: Journal of Geophysical Research: Solid Earth, v. 112, no. B6.

Frankel, K. L., Dolan, J. F., Finkel, R. C., Owen, L. A., and Hoeft, J. S., 2007b, Spatial variations in slip rate along the Death Valley-Fish Lake Valley fault system determined from LiDAR topographic data and cosmogenic 10Be geochronology: Geophysical Research Letters, v. 34, no. 18.

Frankel, K. L., Dolan, J. F., Owen, L. A., Ganev, P., and Finkel, R. C., 2011, Spatial and temporal constancy of seismic strain releas along an evolving segment of the Pacific-North America plate boundary, Earth and Planetary Scinece Letters, 304, p. 565-576.

Frankel, K. L., Owen, L. A., Dolan, J.F., Knott, J. R., Lifton, Z. M., Finkel, R. C., and Wasklewicz, T., 2016, Timing and rates of Holocene normal faulting along the Black Mountains fault zone, Death Valley, USA, Lithosphere, 8(1), p. 3-22.

Freed, A. M., 2005, Earthquake triggering by static, dynamic, and postseismic stress transfer: Annu. Rev. Earth Planet. Sci., v. 33, p. 335-367.

Freed, A. M., Ali, S. T., and Bürgmann, R., 2007, Evolution of stress in Southern California for the past 200 years from coseismic, postseismic and interseismic stress changes: Geophysical Journal International, v. 169, no. 3, p. 1164-1179.

Freed, A. M., and Bürgmann, R., 2004, Evidence of power-law flow in the Mojave desert mantle: Nature, v. 430, no. 6999, p. 548-551.

Friedrich, A. M., Wernicke, B. P., Niemi, N. A., Bennett, R. A., and Davis, J. L., 2003, Comparison of geodetic and geologic data from the Wasatch region, Utah, and implications for the spectral character of Earth deformation at periods of 10 to 10 million years: Journal of Geophysical Research: Solid Earth, v. 108, no. B4.

Ganev, P. N., Dolan, J. F., Frankel, K. L., and Finkel, R. C., 2010, Rates of extension along the Fish Lake Valley fault and transtensional deformation in the Eastern California shear zone–Walker Lane belt: Lithosphere, v. 2, no. 1, p. 33-49.

Gold, R., Briggs, R., Crone, A., and Gosse, J., 2013, Late Quaternary Slip-Rate Variations along the Warm Springs Valley Fault System, Northern Walker Lane, California–Nevada Border: Bulletin of the Seismological Society of America, v. 103, no. 1, p. 542-558.

Gold, R. D., Briggs, R. W., Personius, S. F., Crone, A. J., Mahan, S. A., and Angster, S. J., 2014, Latest Quaternary paleoseismology and evidence of distributed dextral shear along the Mohawk Valley fault zone, northern Walker Lane, California: Journal of Geophysical Research: Solid Earth, v. 119, no. 6, p. 5014-5032.

Gourmelen, N., and Amelung, F., 2005, Postseismic mantle relaxation in the central Nevada seismic belt: Science, v. 310, no. 5753, p. 1473-1476.

Haddon, E. K., Amos, C. B., Zielke, O., Jayko, A. S., and Bürgmann, R., 2016, Surface slip during large Owens Valley earthquakes, Geochemistry, Geophysics, Geosystem, 17, p. 2239-2269.

Hammond, W. C., Kreemer, C., and Blewitt, G., 2009, Geodetic constraints on contemporary deformation in the northern Walker Lane: 3. Central Nevada seismic belt postseismic relaxation: Geological Society of America Special Papers, v. 447, p. 33-54.

Hammond, W. C., Kreemer, C., Blewitt, G., and Plag, H. P., 2010, Effect of viscoelastic postseismic relaxation on estimates of interseismic crustal strain accumulation at Yucca Mountain, Nevada: Geophysical Research Letters, v. 37, no. 6.

Hanks, T. C., 1977, Earthquake stress drops, ambient tectonic stresses and stresses that drive plate motions: Pure and Applied Geophysics, v. 115, p. 441-458.

Hardebeck, J. L., and Hauksson, E., 2001, Crustal stress field in southern California and its implications for fault mechanics: Journal of Geophysical Research B, v. 106, no. B10, p. 21859-21882.

Hardebeck, J. L., and Michael, A. J., 2004, Stress orientations at intermediate angles to the San Andreas Fault, California: Journal of Geophysical Research: Solid Earth, v. 109, no. B11.

Harris, R. A., and Simpson, R. W., 1998, Suppression of large earthquakes by stress shadows: A comparison of Coulomb and rate-and-state failure: Journal of Geophysical Research: Solid Earth, v. 103, no. B10, p. 24439-24451.

Harris, R. A., Simpson, R. W., and Reasenberg, P. A., 1995, Influence of static stress changes on earthquake locations in southern California.

Hetland, E., and Hager, B., 2003, Postseismic relaxation across the central Nevada seismic belt: Journal of Geophysical Research: Solid Earth, v. 108, no. B8.

Hill, D. P., 2006, Unrest in Long Valley Caldera, California, 1978–2004, *in* Troise, D., ed., Mechanisms of Activity and Unrest at Large Calderas, D. Troise et al. (Editor), Geological Society Special Pubblication, no.269, p. 1-24.

Hill, D. P., Langbein, J. O., and Prejean, S., 2003, Relations between seismicity and deformation during unrest in Long Valley Caldera, California, from 1995 through 1999: Journal of Volcanology and Geothermal Research, v. 127, no. 3, p. 175-193.

Hill, D. P., Pollitz, F., and Newhall, C., 2002, Earthquake-volcano interactions: Physics Today, v. 55, no. 11, p. 41-47.

Hodgkinson, K. M., Stein, R. S., and King, G. C., 1996, The 1954 Rainbow Mountain-Fairview Peak-Dixie Valley earthquakes: A triggered normal faulting sequence: Journal of Geophysical Research: Solid Earth, v. 101, no. B11, p. 25459-25471.

Hough, S. E., and Hutton, K., 2008, Revisiting the 1872 Owens Valley, California, Earthquake: Bulletin of the Seismological Society of America, v. 98, no. 2, p. 931-949.

Hsu, Y.-J., Avouac, J.-P., Yu, S.-B., Chang, C.-H., Wu, Y.-M., and Woessner, J., 2009, Spatio-temporal slip, and stress level on the faults within the western foothills of Taiwan: Implications for fault frictional properties: Pure and applied geophysics, v. 166, no. 10-11, p. 1853-1884.

Hubert-Ferrari, A., Barka, A., Jacques, E., Nalbant, S. S., Meyer, B., Armijo, R., Tapponnier, P., and King, G. C., 2000, Seismic hazard in the Marmara Sea region following the 17 August 1999 Izmit earthquake: Nature, v. 404, no. 6775, p. 269-273.

Hylland, M. D., DuRoss, C. B., McDonald, G. N., Olig, S. S., Oviatt, C. G., Mahan, S. A., Crone, A. J. and Personius, S. F., 2014, Late Quaternary paleoseismology of theWest Valley fault zone, Utah: Insights from the Baileys Lake trench site, in Evaluating

Surface Faulting Chronologies of Graben-Bounding Faults in Salt Lake Valley, Utah: New Paleoseismic Data from the Salt Lake City Segment of the Wasatch Fault Zone and the West Valley Fault Zone, in Paleoseismology of Utah, C. B. DuRoss and M. D. Hylland (Editors), Vol. 24, Utah Geological Survey Special Studies, 149, 41–71.

Iaffaldano, G., Bunge, H.-P., and Dixon, T. H., 2006, Feedback between mountain belt growth and plate convergence: Geology, v. 34, no. 10, p. 893-896.

Jackson, M., 1991, The number and timing of Holocene paleoseismic events on the Nephi and Levan segments, Wasatch fault zone, Utah, in Paleoseismology of Utah, W. R. Lund (Editor), vo. 3, Utah Geological Survey Special Studies, 78, 23 pp.

Johanson, I. A., Fielding, E. J., Rolandone, F., and Bürgmann, R., 2006, Coseismic and postseismic slip of the 2004 Parkfield earthquake from space-geodetic data: Bulletin of the Seismological Society of America, v. 96, no. 4B, p. S269-S282.

Johnson, K. M., Hilley, G. E., and Bürgmann, R., 2007, Influence of lithosphere viscosity structure on estimates of fault slip rate in the Mojave region of the San Andreas fault system: Journal of Geophysical Research: Solid Earth, v. 112, no. B7.

Julian, B. R., and Sipkin, S. A., 1985, Earthquake processes in the Long Valley caldera area, California: Journal of Geophysical Research: Solid Earth, v. 90, no. B13, p. 11155-11169.

Kanamori, H., and Anderson, D. L., 1975, Theoretical basis of some empirical relations in seismology: Bulletin of the Seismological Society of America, v. 65, no. 5, p. 1073-1095.

King, G., and Cocco, M., 2001, Fault interaction by elastic stress changes: New clues from earthquake sequences: Advances in Geophysics, v. 44, p. 1.

King, G. C., Stein, R. S., and Lin, J., 1994, Static stress changes and the triggering of earthquakes: Bulletin of the Seismological Society of America, v. 84, no. 3, p. 935-953.

Kirby, E., Burbank, D. W., Reheis, M., and Phillips, F., 2006, Temporal variations in slip rate of the White Mountain fault zone, eastern California: Earth and Planetary Science Letters, v. 248, no. 1, p. 168-185.

Klinger, R., 1999, Tectonic geomorphology along the Death Valley fault system—Evidence for recurrent late Quaternary activity in Death Valley National Park, in Proceedings Proceedings of Conference on Status of Geologic Research and Mapping, Death Valley National Park: US Geological Survey Open-File Report, p. 99-153.

Klinger, R. E., and Piety, L. A., 2000, Late Quaternary tectonic activity on the Death Valley and Furnace Creek faults, Death Valley, California: Geologic and Geophysical Characterization Studies of Yucca Mountain, Nevada, A Potential High-Level Radioactive-Waste Repository, p. 1-16.

Klinger, R. E., and Piety, L. A., 2001, Holocene faulting and slip rates along the Black Mountains fault zone near Mormon Point. in Quaternary and Late Pliocene geology of the Death Valley region: recent observations and tectonics, stratigraphy, and lake cycles, edited by M. N. Machette, M. L. Johnson and J. L. Slate, U.S. Geological Survey Open-File Reports, 01-51, pp. 245-270.

Koehler, R. D., and Wesnousky, S. G., 2011, Late Pleistocene regional extension rate derived from earthquake geology of late Quaternary faults across the Great Basin, Nevada, between 38.5°N and 40°N latitude, Geological Society of America Bulletin, v 123, p. 631-650.

Langbein, J., Dzurisin, D., Marshall, G., Stein, R., and Rundle, J., 1995, by modeling two-color geodimeter and leveling data: Journal of Geophysical Research, v. 100, no. B7, p. 12,487-412,495.

Lee, J., Garwood, J., Stockli, D. F., and Gosse, J., 2009, Quaternary faulting in Queen Valley, California-Nevada: Implications for kinematics of fault-slip transfer in the eastern California shear zone–Walker Lane belt: Geological Society of America Bulletin, v. 121, no. 3-4, p. 599-614.

Lee, J., Rubin, C. M., and Calvert, A., 2001, Quaternary faulting history along the Deep Springs fault, California: Geological Society of America Bulletin, v. 113, no. 7, p. 855-869.

Lifton, Z. M., 2013, Understanding an evolving diffuse plate boundary with geodesy and geochronology, PhD Thesis, Georgia Institute of Technology, Atlanta.

Lifton, Z. M., Frankel, K. L., and Newman, A. V., 2015, Latest Pleistocene and Holocene slip rates on the Lone Moutain fault: Evidence for accelerating slip in the Silver Peak-Lone Mountain extensional complex, Tectonics, 34.

Lorenzo-Martín, F., Roth, F., and Wang, R., 2006, Elastic and inelastic triggering of earthquakes in the North Anatolian Fault zone: Tectonophysics, v. 424, no. 3, p. 271-289.

Lund, W. R., 2005, Consensus preferred recurrence-interval and vertical slip-rate estimates: Review of Utah paleoseismic-trenching data by the Utah Quaternary Fault Parameters Working Group, Utah Geological Survey, v. 134.

Lund, W. R., 2006, Basin and Range Province Earthquake Working Group seismic-hazard recommendations to the US Geological Survey National Seismic Hazard Mapping Program: Utah Geological Survey Open-File Report 477, 23 p.

Lund, W. R., 2012, Basin and Range Province Earthquake Working Group II—Recommendations to the US Geological Survey National Seismic Hazard Mapping Program for the 2014 update of the National Seismic Hazard Maps: Utah Geological Survey Open-File Report 591, 17 p.

Ma, K. F., Chan, C. H., and Stein, R. S., 2005, Response of seismicity to Coulomb stress triggers and shadows of the 1999 Mw= 7.6 Chi-Chi, Taiwan, earthquake: Journal of Geophysical Research: Solid Earth, v. 110, no. B5.

Machette, M. N., Personius, S. F., and Nelson, A. R., 1992, Paleoseismology of the Wasatch fault zone: A summary of recent investigations, interpretations, and conclusions, in Assessment of Regional Earthquake Hazards and Risk along the Wasatch Front, Utah, P. L. Gori and W. W. Hays (Editor), U.S. Geological Survey Professional Paper, 1500-A-J, A1-A71.

Machette, M. N., Martinez, C. N., Crone, A. J., Haller, K. M., and D'Addezio, G., 1999, Geologic and Seismic Hazards Investigations of the Cow Creek Area, Death Valley National Park, California, Citeseer.

Madden, E. H., Maerten, F., and Pollard, D. D., 2013, Mechanics of nonplanar faults at extensional steps with application to the 1992 M 7.3 Landers, California, earthquake, Journal of Geophysical Research: Solid Earth, 118, p. 3249-3263.

Madugo, C. M., Dolan, J. F., and Hartleb, R. D., 2012, New paleoearthquake ages from the western Garlock fault: Implications for regional earthquake occurrence in southern California: Bulletin of the Seismological Society of America, v. 102, no. 6, p. 2282-2299.

Malservisi, R., Dixon, T. H., La Femina, P. C., and Furlong, K. P., 2003, Holocene slip rate of the Wasatch fault zone, Utah, from geodetic data: Earthquake cycle effects: Geophysical Research Letters, v. 30, no. 13.

Marsan, D., 2003, Triggering of seismicity at short timescales following Californian earthquakes: Journal of Geophysical Research: Solid Earth, v. 108, no. B5.

Matthews, M. V., Ellsworth, W. L., and Reasenberg, P. A., 2002, A Brownian model for recurrent earthquakes: Bulletin of the Seismological Society of America, v. 92, no. 6, p. 2233-2250.

McAuliffe, L. J., Dolan, J. F., Kirby, E., Rollins, C., Haravitch, B., Alm, S., and Rittenour, T. M., 2013, Paleoseismology of the southern Panamint Valley fault: Implications for regional earthquake occurrence and seismic hazard in southern California: Journal of Geophysical Research: Solid Earth, v. 118, no. 9, p. 5126-5146.

McCalpin, J. P., 2002, Post-Bonneville paleoearthquake chronology of the Salt Lake City segment, Wasatch fault zone, Utah, in Paleoseismology of Utah, Utah Geol. Surv. Misc. Pub. 02-9, vol. 11, edited by W. R. Lund, 46 pp., Utah Geological Survey, Salt Lake City, Utah.

McCalpin, J. P., and Nishenko, S., 1996, Holocene paleoseismicity, temporal clustering, and probabilities of future large (M> 7) earthquakes on the Wasatch fault zone, Utah: Journal of Geophysical Research: Solid Earth, v. 101, no. B3, p. 6233-6253.

McCalpin, J. P., Forman, S. L., and Lowe, M., 1994, Reevaluation of Holocene faulting at the Kaysville site, Weber segment of the Wasatch fault zone, Utah: Tectonics, v. 13, no. 1, p. 1-16.

McClusky, S., Bjornstad, S., Hager, B. H., King, R., Meade, B., Miller, M., Monastero, F., and Souter, B., 2001, Present day kinematics of the eastern California shear zone from a geodetically constrained block model: Geophysical Research Letters, v. 28, no. 17, p. 3369-3372.

McGill, S. F., and Sieh, K., 1991, Surficial offsets on the central and eastern Garlock fault associated with prehistoric earthquakes: Journal of Geophysical Research: Solid Earth, v. 96, no. B13, p. 21597-21621.

Meade, B. J., Klinger, Y., and Hetland, E. A., 2013, Inference of Multiple Earthquake-Cycle Relaxation Timescales from Irregular Geodetic Sampling of Interseismic Deformation: Bulletin of the Seismological Society of America, v. 103, no. 5, p. 2824-2835.

Mendoza, C., and Hartzell, S. H., 1988, Aftershock patterns and main shock faulting: Bulletin of the Seismological Society of America, v. 78, no. 4, p. 1438-1449.

Nalbant, S. S., Hubert, A., and King, G. C., 1998, Stress coupling between earthquakes in northwest Turkey and the north Aegean Sea: Journal of Geophysical Research: Solid Earth, v. 103, no. B10, p. 24469-24486.

Nelson, A. R., Lowe, M., Personius, S., Bradley, L.-A., Forman, S. L., Klauk, R., and Garr, J., 2006, Holocene earthquake history of the northern Weber segment of the Wasatch fault zone, Utah, in Paleoseismology of Utah, v. 13, W. R. Lund (Editor), Utah Geological Survey Miscellaneous Publication, 05-8, 39 pp.

Nostro, C., Stein, R. S., Cocco, M., Belardinelli, M. E., and Marzocchi, W., 1998, Two-way coupling between Vesuvius eruptions and southern Apennine earthquakes, Italy, by elastic stress transfer: Journal of Geophysical Research, v. 103, no. 24, p. 487-424.

Oldow, J., Late Cenozoic displacement partitioning in the northwestern Great Basin, *in* Proceedings Structure, Tectonics and Mineralization of the Walker Lane, Stewart, J., ed., Walker Lane Symposium Proceedings Volume, Geological Society of Nevada, Reno, NV1992, p. 17-52.

Olig, S., McDonald, G., Black, B., DuRoss, C., Lund, W., Hylland, M., Simon, D., Giraud, R., and Christenson, G., 2011, Extending the paleoseismic record of the Provo segment of the Wasatch fault zone, Utah: Final Techical Report to: US Geological Survey, National Earthquake Hazards Reduction Program, award 02HQGR0109.

Oskin, M., Peng, L., Shelef, M., Strane, M., Gurney, E., Singer, B.,and Zhang, X., 2008, Elevated shera zone loading during an earthquakecluster in eastern California, Geology. 36(6), p. 507-510.

Oswald, J. A., and Wesnousky, S. G., 2002, Neotectonics and Quaternary geology of the Hunter Mountain fault zone and Saline Valley region, southeastern California: Geomorphology, v. 42, no. 3, p. 255-278.

Pace, B., Bocchini, G. M., and Boncio, P., 2014, Do static stress changes of a moderate-magnitude earthquake significantly modify the regional seismic hazard? Hints from the L'Aquila 2009 normal-faulting earthquake (Mw 6.3, central Italy): Terra Nova, v. 26, no. 6, p. 430-439.

Pace, B., Visini, F., and Peruzza, L., 2016, FiSH: MATLAB Tools to Turn Fault Data into Seismic-Hazard Models: Seismological Research Letters.

Papadimitriou, E. E., and Sykes, L. R., 2001, Evolution of the stress field in the northern Aegean Sea (Greece): Geophysical Journal International, v. 146, no. 3, p. 747-759.

Parsons, T., 2005, Significance of stress transfer in time-dependent earthquake probability calculations: Journal of Geophysical Research: Solid Earth, v. 110, no. B5.

Parsons, T., 2008, Monte Carlo method for determining earthquake recurrence parameters from short paleoseismic catalogs: Example calculations for California: Journal of Geophysical Research: Solid Earth, v. 113, no. B3.

Parsons, T., Toda, S., Stein, R. S., Barka, A., and Dieterich, J. H., 2000, Heightened odds of large earthquakes near Istanbul: An interaction-based probability calculation: Science, v. 288, no. 5466, p. 661-665.

Peltzer, G., and Rosen, P., 1995, Surface displacement of the 17 May 1993 Eureka Valley, California, earthquake observed by SAR interferometry: Science, v. 268, no. 5215, p. 1333.

Personius, S. F., DuRoss, C. B., and Crone, A. J., 2012, Holocene Behavior of the Brigham City Segment: Implications for Forecasting the Next Large-Magnitude Earthquake on the Wasatch Fault Zone, Utah: Bulletin of the Seismological Society of America, v. 102, no. 6, p. 2265-2281.

Personius, S. F., and Scott, W. E., 1992, Surficial geologic map of the Salt Lake City segment and parts of adjacent segments of the Wasatch fault zone, Davis, Salt Lake, and Utah counties, Utah, U.S. Geological Survey Miscellaneous Investment Series, Map I-2106, scale 1:50000.

Petersen, M. D., Bryant, W. A., Cramer, C. H., Cao, T., Reichle, M. S., Frankel, A. D., Lienkaemper, J. J., McCrory, P. A., and Schwartz, D. P., 1996, Probabilistic seismic hazard assessment for the state of California: California Dept. of Conservation Division of Mines and Geology, U.S. Geological Survey Open-File Report, 96-706, 1-64.

Petersen, M. D., Moschetti, M. P., Powers, P. M., Mueller, C. S., Haller, K. M., Frankel, A. D., Zeng, Y., Rezaeian, S., Harmsen, S. C., and Boyd, O. S., 2014, Documentation for the

2014 update of the United States national seismic hazard maps: US Geological Survey Open-File Report 2014-1091, 2331-1258.

Pollitz, F. F., 2003, Transient rheology of the uppermost mantle beneath the Mojave Desert, California: Earth and Planetary Science Letters, v. 215, no. 1, p. 89-104.

Pollitz, F., Vergnolle, M., and Calais, E., 2003, Fault interaction and stress triggering of twentieth century earthquakes in Mongolia: Journal of Geophysical Research: Solid Earth, v. 108, no. B10.

Prejean, S., Ellsworth, W., Zoback, M., and Waldhauser, F., 2002, Fault structure and kinematics of the Long Valley Caldera region, California, revealed by high-accuracy earthquake hypocenters and focal mechanism stress inversions: Journal of Geophysical Research: Solid Earth, v. 107, no. B12.

Priestley, K. F., Smith, K. D., and Cockerham, R. S., 1988, The 1984 Round Valley, California earthquake sequence: Geophysical Journal International, v. 95, no. 2, p. 215-235.

Ramelli, A. R., and Bell, J. W., 2009, Spatial and temporal patterns of fault slip rates on the Genoa fault, *U.S. Geological Survey, NEHRP final technical report*, award G09AP00020.

Ramelli, A. R., Bell, J. W., and Yount, J. C., 1999, Large-magnitude, late Holocene earthquakes on the Genoa fault, west-central Nevada and eastern California: Bulletin of the Seismological Society of America, v. 89, no. 6, p. 1458-1472.

Reasenberg, P. A., and Simpson, R. W., 1992, Response of regional seismicity to the static stress change produced by the Loma Prieta earthquake: Science, v. 255, no. 5052, p. 1687-1690.

Reheis, M., 1991, Geologic map of late Cenozoic deposits and faults in the western part of the Rhyolite Ridge 15'Quadrangle, Esmeralda County, Nevada, U. S. Geological Survey Miscellaneous Investigations, Map I-2183, 1 sheet, scale 1:24000.

Reheis, M., 1994, Logs of trenches across the central part of the Fish Lake Valley fault zone: Mono County, California: US Geological Survey Miscellaneous Field Studies Map MF-2266, v. 1.

Reheis, M. C., and Dixon, T. H., 1996, Kinematics of the eastern California shear zone: Evidence for slip transfer from Owens and Saline Valley fault zones to Fish Lake Valley fault zone: Geology, v. 24, no. 4, p. 339-342.

Reheis, M. C., and Sawyer, T. L., 1997, Late Cenozoic history and slip rates of the fish lake valley, emigrant peak, and deep springs fault zones, Nevada and California: Geological Society of America Bulletin, v. 109, no. 3, p. 280-299.

Reheis, M.C., Slate, J. L., and Sawyer, T. L., 1995, Geologic map of late Cenozoic deposits and faults in parts of the Mt. Barcroft, Piper Peak, and Soldier Pass 15' quadrangles,

Esmeralda County, Nevada, and Mono County, California: U.S. Geological Survey Miscellaneous Investigations Map I-2464, 2 sheets.

Sarmiento, A. C., Wesnousky, S. G., and Bormann, J. M., 2011, Paleoseismic Trenches across the Sierra Nevada and Carson Range Fronts in Antelope Valley, California, and Reno, Nevada: Bulletin of the Seismological Society of America, v. 101, no. 5, p. 2542-2549.

Savage, J., 1983, A dislocation model of strain accumulation and release at a subduction zone: Journal of Geophysical Research: Solid Earth, v. 88, no. B6, p. 4984-4996.

Savage, J., and Clark, M., 1982, Magmatic resurgence in Long Valley caldera, California: Possible cause of the 1980 Mammoth Lakes earthquakes: Science, v. 217, no. 4559, p. 531-533.

Sawyer, T. L., and Bryant, W. A., compilers, 1995, Fault number 42, Silver Lake fault, in Quaternary fault and fold database of the United States: U.S. Geological Survey website, http://earthquakes.usgs.gov/hazards/qfaults.

Sawyer, T. L. and Reheis, M. C., 1997, Holocene paleoseismicity, recurrence intervals, rupture segments, and seismic potential of the Fish Lake Valley fault zone, Nevada and California, Proceedings volume Basin and Range province seismic-hazards summit, W. R. Lund (Editor), Miscellaneous Publication 98-2, Utah Geological Survey, 1998.

Sawyer, T. L., and Reheis, M. C., 1999, Seismic potential of the Fish Lake Valley fault zone, Nevada and California (p. 150-151), in Proceedings Proceedings of Conference on Status of Geologic Research and Mapping, Death Valley National Park: US Geological Survey Open-File Report, 1999, p. 99-153.

Sawyer, T. L., Briggs, R. W., and Ramelli, A. R., 2013, Paleoseismic investigation of the Mohawk Valley fault zone, Sierra County, northeastern California, 33 pp., NEHRP Final Technical Report.

Schaff, D. P., Bokelmann, G. H., Beroza, G. C., Waldhauser, F., and Ellsworth, W. L., 2002, High-resolution image of Calaveras Fault seismicity: Journal of Geophysical Research: Solid Earth, v. 107, no. B9.

Scharer, K. M., Biasi, G. P., and Weldon, R. J., 2011, A reevaluation of the Pallett Creek earthquake chronology based on new AMS radiocarbon dates, San Andreas fault, California: Journal of Geophysical Research: Solid Earth, v. 116, no. B12.

Scholz, C. H., 2002, The mechanics of earthquakes and faulting, Cambridge university press, New Yotk.

Scholz, C. H., 2010, Large earthquake triggering, clustering, and the synchronization of faults: Bulletin of the Seismological Society of America, v. 100, no. 3, p. 901-909.

Schwartz, D. P., and Coppersmith, K. J., 1984, Fault behavior and characteristic earthquakes: Examples from the Wasatch and San Andreas fault zones: Journal of Geophysical Research: Solid Earth, v. 89, no. B7, p. 5681-5698.

Shan, B., Xiong, X., Wang, R., Zheng, Y., and Yang, S., 2013, Coulomb stress evolution along Xianshuihe–Xiaojiang Fault System since 1713 and its interaction with Wenchuan earthquake, May 12, 2008: Earth and Planetary Science Letters, v. 377, p. 199-210.

Simkin, T., Tilling, R. I., Vogt, P. R., Kirby, S. H., Kimberly, P., and Stewart, D. B., 2006, World map of volcanoes, earthquakes, impact craters, and plate tectonics, Geologic Investigation Map I-2800: This Dynamic Planet, published by U.S. Geological Survey.

Smith, K. D., and Priestley, K. F., 1988, The foreshock sequence of the 1986 Chalfant, California, earthquake: Bulletin of the Seismological Society of America, v. 78, no. 1, p. 172-187.

Smith, K. D., and Priestley, K. F., 2000, Faulting in the 1986 Chalfant, California, sequence: Local tectonics and earthquake source parameters: Bulletin of the Seismological Society of America, v. 90, no. 4, p. 813-831.

Smith, R. B., and Bruhn, R. L., 1984, Intraplate extensional tectonics of the eastern Basin-Range: Inferences on structural style from seismic reflection data, regional tectonics, and thermal-mechanical models of brittle-ductile deformation: Journal of Geophysical Research: Solid Earth, v. 89, no. B7, p. 5733-5762.

Smith-Konter, B., and Sandwell D., 2009, Stress evolution of the San Andreas fault system: Recurrence interval versus locking depth, Geophysical Research Letters, 36, L13304.

Sohn, M. F., Knott, J. R., and Mahan, S. A., 2014, Paleoseismology of the Southern Section of the Black Mountains and Southern Death Valley Fault Zones, Death Valley, United States: Environmental & Engineering Geoscience, v. 20, no. 2, p. 177-198.

Stein, R. S., 1999, The role of stress transfer in earthquake occurrence: Nature, v. 402, no. 6762, p. 605-609.

Stein, R. S., Barka, A. A., and Dieterich, J. H., 1997, Progressive failure on the North Anatolian fault since 1939 by earthquake stress triggering: Geophysical Journal International, v. 128, no. 3, p. 594-604.

Stein, R. S., and Barrientos, S. E., 1985, Planar high-angle faulting in the basin and range: Geodetic analysis of the 1983 Borah Peak, Idaho, earthquake: Journal of Geophysical Research: Solid Earth, v. 90, no. B13, p. 11355-11366.

Stein, R. S., King, G. C., and Lin, J., 1994, Stress triggering of the 1994 M= 6.7 Northridge, California, earthquake by its predecessors: Science, v. 265, no. 5177, p. 1432-1435.

Stein, S., and Liu, M., 2009, Long aftershock sequences within continents and implications for earthquake hazard assessment: Nature, v. 462, no. 7269, p. 87-89.

Stewart, J., 1988, Tectonics of the Walker Lane belt, western Great Basin: Mesozoic and Cenozoic deformation in a zone of shear: Metamorphism and crustal evolution of the western United States, W. G. Ernst (Editor), v. 7, p. 683-713.

Suppe, J., 2007, Absolute fault and crustal strength from wedge tapers: Geology, v. 35, no. 12, p. 1127-1130.

Suppe, J., Huang, M.-H., and Carena, S., 2009, Mechanics of thrust belts and the weak-fault/strong-crust problem: Trabajos de geología, v. 29, no. 29.

Surpless, B., and Kroeger, G., 2015, The unusual temporal and spatial slip history of the Wassuk Range normal fault, western Nevada (USA): Implications for seismic hazard and Walker Lane deformation: Geological Society of America Bulletin, v. 127, no. 5-6, p. 737-758.

Swan, F., Schwartz, D., Hanson, K., Knuepfer, P., and Cluff, L., 1981, Study of earthquake recurrence intervals on the Wasatch fault at the Kaysville site, Utah:,U.S. Geological Survey Open-File Report, 81-228, 30 pp.

Swan, F., Schwartz, D. P., and Cluff, L. S., 1980, Recurrence of moderate to large magnitude earthquakes produced by surface faulting on the Wasatch fault zone, Utah: Bulletin of the Seismological Society of America, v. 70, no. 5, p. 1431-1462.

Thatcher, W., 1995, Microplate versus continuum descriptions of active tectonic deformation: Journal of Geophysical Research: Solid Earth, v. 100, no. B3, p. 3885-3894.

Thatcher, W., and Pollitz, F. F., 2008, Temporal evolution of continental lithospheric strength in actively deforming regions: GSA TODAY, v. 18, no. 4/5, p. 4.

Thatcher, W., and Savage, J., 1982, Triggering of large earthquakes by magma-chamber inflation, Izu Peninsula, Japan: Geology, v. 10, no. 12, p. 637-640.

Thio, H. K., and Kanamori, H., 1995, Moment-tensor inversions for local earthquakes using surface waves recorded at TERRAscope: Bulletin of the Seismological Society of America, v. 85, no. 4, p. 1021-1038.

Tizzani, P., Battaglia, M., Zeni, G., Atzori, S., Berardino, P., and Lanari, R., 2009, Uplift and magma intrusion at Long Valley caldera from InSAR and gravity measurements: Geology, v. 37, no. 1, p. 63-66.

Toda, S., Lin, J., Meghraoui, M., and Stein, R. S., 2008, 12 May 2008 M= 7.9 Wenchuan, China, earthquake calculated to increase failure stress and seismicity rate on three major fault systems: Geophysical Research Letters, v. 35, no. 17.

Toda, S., Stein, R. S., Reasenberg, P. A., Dieterich, J. H., and Yoshida, A., 1998, Stress transferred by the 1995 Mw= 6.9 Kobe, Japan, shock: Effect on aftershocks and future earthquake probabilities: Journal of Geophysical Research: Solid Earth, v. 103, no. B10, p. 24543-24565.

Toda, S., Stein, R. S., Sevilgen, V., and Lin, J., 2011, Coulomb 3.3 graphic-rich deformation and stress-change software for earthquake, tectonic, and volcano research and teaching-user guide: U.S. Geological Survey Open File Report, 2011-1060, 63 pp.

Townend, J., and Zoback, M., 2004, Regional tectonic stress near the San Andreas fault in central and southern California: Geophysical Research Letters, v. 31, no. 15.

Turner, R., Koehler, R., Briggs, R., and Wesnousky, S., 2008, Paleoseismic and slip-rate observations along the Honey Lake fault zone, northeastern California, USA: Bulletin of the Seismological Society of America, v. 98, no. 4, p. 1730-1736.

Valoroso, L., Chiaraluce, L., Piccinini, D., Di Stefano, R., Schaff, D., and Waldhauser, F., 2013, Radiography of a normal fault system by 64,000 high-precision earthquake locations: The 2009 L'Aquila (central Italy) case study: Journal of Geophysical Research: Solid Earth, v. 118, no. 3, p. 1156-1176.

Velasco, M. S., Bennett, R. A., Johnson, R. A., and Hreinsdóttir, S., 2010, Subsurface fault geometries and crustal extension in the eastern Basin and Range Province, western US: Tectonophysics, v. 488, no. 1, p. 131-142.

Verdecchia, A., and Carena, S., 2015, One hundred and fifty years of Coulomb stress history along the California-Nevada border, USA: Tectonics, v. 34, no. 2, p. 213-231.

Verdecchia, A., and Carena, S., 2016, Coulomb stress evolution in a diffuse plate boundary: 1400 years of earthquakes in eastern California and western Nevada, USA, Tectonics, 35(8), p. 1793-1811..

Visini, F., and Pace, B., 2014, Insights on a key parameter of earthquake forecasting, the coefficient of variation of the recurrence time, using a simple earthquake simulator: Seismological Research Letters, v. 85, no. 3, p. 703-713.

Waldhauser, F., and Schaff, D. P., 2008, Large-scale relocation of two decades of Northern California seismicity using cross-correlation and double-difference methods: Journal of Geophysical Research: Solid Earth, v. 113, no. B8.

Wallace, R. E., 1978, Patterns of faulting and seismic gaps in the Great Basin province, in Proceedings of Conference IV, Methodology for identifying seismic gaps and soon-to-break gaps, May 25-27, U.S. Geological Survey Open File Reports, p. 858-868.

Wallace, R. E., 1984a, Fault scarps formed during the earthquakes of October 2, 1915, in Pleasant Valley, Nevada, and some tectonic implications, in Faulting related to the 1915 Earthquakes in Pleasant Valley, Nevada, U.S. Geological Survey Professional Paper, 1274-A, p. A1-A33.

Wallace, R. E., 1984b, Patterns and timing of late Quaternary faulting in the Great Basin province and relations to some regional tectonic features, Journal of Geophysical Research, 89, p. 5763-5769.

Wallace, R. E., 1987, Grouping and migration of surface faulting and variations in slip rates on faults in the Great Basin province: Bulletin of the Seismological Society of America, v. 77, no. 3, p. 868-876.

Wang, J., Xu, C., Freymueller, J. T., Li, Z., and Shen, W., 2014, Sensitivity of Coulomb stress change to the parameters of the Coulomb failure model: A case study using the 2008 M_w 7.9 Wenchuan earthquake, Journal of Geophysical Research: Solid Earth, 119, p. 3371-3392.

Wang, R., Lorenzo-Martín, F., and Roth, F., 2006, PSGRN/PSCMP—a new code for calculating co-and post-seismic deformation, geoid and gravity changes based on the viscoelastic-gravitational dislocation theory: Computers & Geosciences, v. 32, no. 4, p. 527-541.

Wells, D. L., and Coppersmith, K. J., 1994, New empirical relationships among magnitude, rupture length, rupture width, rupture area, and surface displacement: Bulletin of the seismological Society of America, v. 84, no. 4, p. 974-1002.

Wesnousky, S. G., 2005, Active faulting in the Walker Lane: Tectonics, v. 24, no. 3.

Wesnousky, S. G., and Caffee, M., 2011, Range-bounding normal fault of Smith Valley, Nevada: Limits on age of last surface-rupture earthquake and Late Pleistocene rate of displacement, Bulletin of the Seismological Society of America, 101, p. 1431-1437.

Wesnousky, S. G., Bormann, J. M., Kreemer, C., Hammond, W. C., and Brune, J. N., 2012, Neotectonics, geodesy, and seismic hazard in the Northern Walker Lane of Western North America: Thirty kilometers of crustal shear and no strike-slip?: Earth and Planetary Science Letters, v. 329, p. 133-140.

Willis, C. J., Weldon II, R. J., and Bryant, W. A., 2008, Appendix A: California fault parameters for the National Seismic Hazard Maps and Working Group on California Earthquake Probabilities, U.S. Geological Survey Open-File Report, 2007-1437A.

Zhang, P., Ellis, M., Slemmons, D., and Mao, F., 1990, Right-lateral displacements and the holocene slip rate associated with prehistoric earthquakes along the southern Panamint Valley fault zone: Implications for southern Basin and Range tectonics and coastal California deformation: Journal of Geophysical Research: Solid Earth, v. 95, no. B4, p. 4857-4872.